Efim Pelinovsky
Christian Kharif
(Eds.)

Extreme Ocean Waves

Springer

Extreme Ocean Waves

Efim Pelinovsky • Christian Kharif
Editors

Extreme Ocean Waves

Springer

Editors

Efim Pelinovsky
Russian Academy of Sciences
Inst. Appl. Physics
Ul'yanov str. 46
Nizhny Novgorod
Russia 603950
pelinovsky@hydro.appl.sci-nnov.ru

Christian Kharif
IRPHE
Technopole de
Chateau-Gombert
49 rue F. Joliot Curie
13384 Marseille
BP 146 France
kharif@irphe.univ-mrs.fr

ISBN 978-1-4020-8313-6 e-ISBN 978-1-4020-8314-3

Library of Congress Control Number: 2008928129

Printed on acid-free paper

9 8 7 6 5 4 3 2 1

springer.com

Preface

Extreme wave events occurring in seas and oceans almost every week are reported. There are a number of physical mechanisms that focus the water wave energy into a small area and produce the occurrence of extreme waves called freak or rogue waves. These events may be due to wave instability (modulation or Benjamin-Feir instability), chaotic behavior, dispersion (frequency modulation), refraction (presence of variable currents or bottom topography), soliton interactions, etc. These giant waves are a real danger to ships and platforms, causing accidents resulting in human loss. There are several examples of such events which occurred in 2007. The freak surge striking East Anglia and Kent (UK) on November 12 missed the high tide by minutes and forced the emergency services to evacuate more than 1,000 people from their homes. Strong waves struck a group of 15 picnickers who had waded far into the sea on October 15 at the Gadani beach about 40 km southwest of Karachi (Pakistan). On October 1, nine houses were destroyed and 77 families displaced when strong waves hit the coastal Davao City (Phillipine). The heavy rain and freak tides on August 31 damaged and in some cases destroyed banks and walls along the Saigon River (Vietnam). A 7–10-m wave hit many people in Mostaganem (Algeria) killing 12 on August 3. One man was killed by a freak wave while fishing on the rocks off the coast of Scotland (UK) on August 2. He was swept out to sea. A tourist was killed by a giant wave as freak weather hit the French Mediterranean island of Corsica on May 30. Great damage was caused to a large passenger ferry "L'Enez Sun III" in the English Channel near Island Sein on May 19. Such events occur in the English Channel each year. The ferry "La Déesse des Flots" was hit by a freak wave of 10 m on August 3, 2006 near the French coast (Barfleur). The wave, estimated as 12 m high crashed into the "Pont-Aven", the flagship of the British Ferries fleet on May 22, 2006, near the French port of Roscoff. The wave was of 12 m and five passengers were injured. Of course, this list is not exhaustive. According to the Lloyds "World Fleet Statistics", the number of fatalities per year during 1978–2001 is estimated at 300–600.

Extreme waves have been intensively studied in the past few years, and the European Geophysical Union organizes every year a special section on extreme waves. This book, "Extreme Ocean Waves", contains invited papers written mainly

on the basis of works presented during the General Assembly of the European Geosciences Union in Vienna (April 2007). The formation of freak waves in deep water is investigated numerically in the paper "Freak Waves: Peculiarities of Numerical Simulations" by V.E. Zakharov, A.I. Dyachenko and A.O. Prokofiev. They assume that unusual waves are formed due to modulational instability of nonlinear wave field. Physical and statistical properties of rogue wave generation in deep water are studied using various models of nonlinear water waves in the paper "Rogue Waves in High-order Nonlinear Schrödinger Models" by C.M. Schober and A. Calini. They demonstrate that a chaotic sea state appears to be an important mechanism for both generation and increased likelihood of rogue waves. The occurrence of extreme waves in shallow water is investigated in the paper "Non-Gaussian Properties of Shallow Water Waves in Crossing Seas" by A. Toffoli, M. Onorato, A.R. Osborne and J. Monbaliu. They show that the interaction of two crossing wave trains generates steep and high amplitude peaks, thus enhancing the deviation of the surface elevation from the Gaussian statistics. The existence of various shapes of rogue waves in shallow water is discussed in the paper "Modeling of Rogue Wave Shapes in Shallow Water" by T. Talipova, C. Kharif and J.P. Giovanangeli. They point out that the variable-polarity shape of a rogue wave is more probable than only one crest or one trough. The possibility of the appearance of freak waves on a beach is analysed in the paper "Runup of Long Irregular Waves on Plane Beach" by I. Didenkulova, E. Pelinovsky and A. Sergeeva. It is shown that the average runup height of waves with a wide spectrum is higher than that of waves with a narrow spectrum. Special analysis of nonlinear resonances between water waves is given in the paper "Symbolic Computation for Nonlinear Wave Resonances" by E. Kartashova, C. Raab, CH. Feurer, G. Mayrhofer, and W. Schreiner. They discuss the important role of nonlinear resonances in the wave dynamics that can be used to simplify the governing equations. The relation between observations and freak wave theories is examined in the paper "Searching for Factors that Limit Observed Extreme Maximum Wave Height Distributions in the North Sea" by G. Burgers, F. Koek, H. de Vries and M. Stam. Their observations indicate that steepness is a limiting factor for extreme wave height and at shallow water locations, extreme waves are not as frequently observed as at deep water locations. Average wave conditions, their variations, and extreme wave storms in the northern Baltic Sea are studied, based on long-term time series in the paper "Extremes and Decadal Variations of the Northern Baltic Sea Wave Conditions" by T. Soomere. Significant wave heights of more than 4 m occur in this area of the Baltic Sea with a probability of about 1% and the overall recorded maximum is 7.8 m. Data of storm surges induced by cyclones in Guadeloupe, Lesser Antilles are given in the paper "Extreme Waves Generated by Cyclones in Guadeloupe" by N. Zahibo, I. Nikolkina and I. Didenkulova, in particular, the results of the field survey of the passing of Hurricane Dean of category 5, which occurred in August 2007 in the Caribbean Sea. Waves of huge amplitudes can appear in the deepest layers of the ocean and the possible shapes of such waves in two-layer fluid is described in the paper "An Analytical Model of Large Amplitude Internal Solitary Waves" by N.I. Makarenko and J.L. Maltseva.

The book is written for specialists in the fields of fluid mechanics, applied mathematics, nonlinear physics, physical oceanography and geophysics, and also for students learning these subjects.

Efim Pelinovsky
Christian Kharif

Contents

Contributors

Gerrit Burgers
Royal Netherlands Meteorological Institute, P.O. Box 201, NL-3730 AE De Bilt, The Netherlands, burgers@knmi.nl

Annalisa Calini
Department of Mathematics, College of Charleston, Charleston, SC 29424, USA, calinia@cofc.edu

Hans de Vries
Royal Netherlands Meteorological Institute, De Bilt, The Netherlands, jwdv@knmi.nl

Ira Didenkulova
Institute of Cybernetics, Tallinn, University of Technology, Tallinn, Estonia; Laboratory of Tropical and Atmospheric Physics; Department of Physics, University of Antilles Guyane, Guadeloupe (F.W.I.), France; Department of Applied Mathematics, Nizhny Novgorod State Technical University, Nizhny Novgorod, Russia; Department of Nonlinear Geophysical Processes, Institute of Applied Physics, Russian Academy of Sciences, Nizhny Novgorod, Russia, dii@hydro.appl.sci-nnov.ru

A.I. Dyachenko
Landau Institute for Theoretical Physics, 2 Kosygina str., Moscow 119334, Russia, alexd@itp.ac.ru

Ch. Feurer
Research Institute for Symbolic Computation (RISC), Johannes Kepler University Linz, Altenbergerstr. 69, 4040 Linz, Austria

J.-P. Giovanangeli
IRPHE Technopôle de Château − Gombert, 13384 Marseille cedex 13, France, giovanangeli@irphe.univ-mrs.fr

E. Kartashova
Research Institute for Symbolic Computation (RISC), Johannes Kepler University Linz, Altenbergerstr. 69, 4040 Linz, Austria,
elena.kart@gmx.at

Christian Kharif
IRPHE, Technopole de, Chateau-Gombert, 49 rue F. Joliot Curie
13384 Marseille, BP 146 France
kharif@irphe.univ-mrs.fr

Frits Koek
Royal Netherlands Meteorological Institute, De Bilt, The Netherlands,
koek@knmi.nl

Nikolay I. Makarenko
Lavrentyev Institute of Hydrodynamics, Novosibirsk 630090, Russia,
makarenko@hydro.nsc.ru

Janna L. Maltseva
Lavrentyev Institute of Hydrodynamics, Novosibirsk 630090, Russia,
maltseva@hydro.nsc.ru

G. Mayrhofer
Research Institute for Symbolic Computation (RISC), Johannes Kepler University Linz, Altenbergerstr. 69, 4040 Linz, Austria

J. Monbaliu
Katholieke Universiteit Leuven, Leuven, Belgium,
jaak.monbaliu@bwk.kuleuven.be

Irina Nikolkina
Laboratory of Tropical and Atmospheric Physics, Department of Physics, University of Antilles Guyane, Guadeloupe (F.W.I.), France; Department of Applied Mathematics, Nizhny Novgorod State Technical University, Nizhny Novgorod, Russia, irina.nikolkina@caramail.com

M. Onorato
Universitá di Torino, Torino, Italy, onorato@ph.unito.it

A.R. Osborne
Universitá di Torino, Torino, Italy, al.osborne@gmail.com

Efim Pelinovsky
Russian Academy of Sciences, Inst. Appl. Physics, Ul'yanov str. 46
Nizhny Novgorod, Russia 603950
pelinovsky@hydro.appl.sci-nnov.ru

A.O. Prokofiev
Landau Institute for Theoretical Physics, 2 Kosygina str., Moscow 119334, Russia

C. Raab
Research Institute for Symbolic Computation (RISC), Johannes Kepler University Linz, Altenbergerstr. 69, 4040 Linz, Austria

Constance M. Schober
Department of Mathematics, University of Central Florida, Orlando, FL 32816, USA, cschober@mail.ucf.edu

W. Schreiner
Research Institute for Symbolic Computation (RISC), Johannes Kepler University Linz, Altenbergerstr. 69, 4040 Linz, Austria

Anna Sergeeva
Institute of Applied Physics, Nizhny Novgorod, Russia, a.sergeeva79@mail.ru

Tarmo Soomere
Institute of Cybernetics at Tallinn University of Technology, Tallinn, Estonia, soomere@cs.ioc.ee

Martin Stam
Royal Netherlands Meteorological Institute, De Bilt, The Netherlands, stam@knmi.nl

T. Talipova
Institute of Applied Physics RAS, 46 Uljanov str. Nizhny Novgorod 603950 Russia, tata@hydro.appl.sci-nnov.ru

A. Toffoli
Katholieke Universiteit Leuven, Leuven, Belgium, toffoli.alessandro@gmail.com

Narcisse Zahibo
Laboratory of Tropical and Atmospheric Physics, Department of Physics, University of Antilles Guyane, Guadeloupe (F.W.I.), France, nzahibo@bakanik.univ-ag.fr

V.E. Zakharov
Department of Mathematics, University of Arizona, Tucson, AZ, 857201, USA; Waves and Solitons LLC, W. Sereno Dr., Gilbert, AZ, 85233, USA, zakharov@math.arizona.edu

Freak Waves: Peculiarities of Numerical Simulations

V.E. Zakharov, A.I. Dyachenko, and A.O. Prokofiev

Abstract Numerical simulation of evolution of nonlinear gravity waves is presented. Simulation is done using two-dimensional code, based on conformal mapping of the fluid to the lower half-plane. We have considered two problems: (i) modulation instability of wave train and (ii) evolution of nonlinear Shrödinger equation solitons with different steepness of carrier wave. In both cases we have observed formation of freak waves.

1 Introduction

Waves of extremely large size, alternatively called freak, rogue, or giant waves, are a well-documented hazards for mariners (see, for instance Smith 1976; Dean 1990; Chase 2003). These waves are responsible for loss of many ships and many human lives. Freak waves could appear in any place of the world ocean (see Earle 1975; Mori et al. 2002; Divinsky et al. 2004); however, in some regions they are more probable than in the others. One of the regions where freak waves are especially frequent is the Agulhas current of the South-East coast of South Africa (see Grundlingh 1994; Gutshabash and Lavrenov 1986; Irvine and Tilley 1988; Lavrenov 1998; Mallory 1974). In the paper by Peregrine (1976) it was suggested that in areas of strong current such as the Agulhas, giant waves could be produced when wave action is concentrated by reflection into a caustic region. According to this

V.E. Zakharov
Department of Mathematics, University of Arizona, Tucson, AZ, 857201, USA
and
Waves and Solitons LLC, W. Sereno Dr., Gilbert, AZ, 85233, USA
zakharov@math.arizona.edu

A.I. Dyachenko and A.O. Prokofiev
Landau Institute for Theoretical Physics, 2 Kosygina str., Moscow, 119334, Russia
alexd@itp.ac.ru

E. Pelinovsky, C. Kharif (eds.) *Extreme Ocean Waves*, 1–29.

theory, a variable current acts analogously to an optic lens to focus wave action. The caustic theory of freak waves was supported since that time by works of many authors. Among them were Smith (1976), Gutshabash and Lavrenov (1986), Irvine and Tilley (1988), Sand et al. (1990), Gerber (1987, 1993), Kharif and Pelinovsky (2003). The statistics of caustics along with application to calculation of the freak wave formation probability was studied in the paper of White and Fornberg (1998).

In our opinion, connection between freak wave generation and caustics for swell or wind-driven sea is the indisputable fact. However, this is not the end of the story. Focusing of ocean waves by an inhomogeneous current is a pure linear effect. Meanwhile, there is no doubts that freak waves are essentially nonlinear objects. They are very steep. In the last stage of their evolution, the steepness becomes infinite, forming a "wall of water." Before this moment, the steepness is higher than that for the limiting Stokes wave. Moreover, a typical freak wave is a single event (see, for instance Divinsky et al. 2004. Before breaking it has a crest, three–four (or even more) times higher than the crests of neighbor waves. The freak wave is preceded by a deep trough or "hole in the sea." A characteristic life time of a freak wave is short – ten of wave periods or so. If the wave period is 15 s, this is just few minutes. Freak wave appears almost instantly from a relatively calm sea. Sure, these peculiar features of freak waves cannot be explained by a linear theory. Focusing of ocean waves creates only preconditions for formation of freak waves, which is a strongly nonlinear effect.

It is natural to associate appearance of freak waves with the modulation instability of Stoke's waves. This instability is usually called after Benjamin and Feir; however, it was first discovered by Lighthill (1965). The theory of instability was developed independently by Benjamin and Feir (1967) and by Zakharov (1967). Feir (1967) was the first who observed the instability experimentally in 1967.

Slowly modulated weakly nonlinear Stokes wave is described by nonlinear Shrödinger equation (NLSE), derived by Zakharov (1968). This equation is integrable (see Zakharov and Shabat 1972) and is just the first term in the hierarchy of envelope equations describing packets of surface gravity waves. The second term in this hierarchy was calculated by Dysthe (1979), the next one was found a few years ago by Trulsen and Dysthe (1996). The Dysthe equation was solved numerically by Ablovitz and his collaborates (see Ablovitz et al. 2000, 2001).

Since the first work of Smith (1976), many authors tried to explain the freak wave formation in terms of NLSE and its generalizations, like Dysthe equation. A vast scientific literature is devoted to this subject. The list presented below is long but incomplete: Peregrine (1983); Peregrine et al. (1988), Tanaka (1990), Trulsen and Dysthe (1996), Trulsen and Dysthe (1997), Trulsen (2000), Trulsen et al. (2000), Ablovitz et al. (2000), Onorato et al. (2000, 2001, 2002).

One cannot deny some advantages achieved by the use of the envelope equations. Results of many authors agree to one important point: nonlinear development of modulation instability leads to concentration of wave energy in a small spatial region. On the one hand, this is a "hint" regarding possible formation of freak wave. On the other hand, it is clear that the freak wave phenomenon cannot be explained in terms of envelope equations. Indeed, NLSE and its generalizations are derived by

expansion in series on powers of parameter $\lambda \simeq 1/Lk$, where k is a wave number, L is a length of modulation. For real freak wave $\lambda \sim 1$ and any "slow modulation expansion" fails. However, the analysis in the framework of the NLS-type equations gives some valuable information about formation of freak waves.

Modulation instability leads to decomposition of initially homogeneous Stokes wave into a system of envelope solitons (more accurately speaking, quasi-solitons Zakharov and Kuznetsov (1998); Zakharov et al. (2004)). This state can be called "solitonic turbulence," or, more exactly "quasisolitonic turbulence." In the framework of pure NLSE, solitonic turbulence is "integrable." Solitons are stable, and they scatter on each other elastically. However, even in this simplest scenario, spatial distribution of wave energy displays essential intermittency. More exact Dysthe equation is not integrable. In this model solitons can merge, and this effect increases spatial intermittency and leads to establishing of chaotic intense modulations of energy density. So far this model cannot explain formation of freak waves with $\lambda \sim 1$.

This effect can be explained if the envelope solutions of a certain critical amplitude are unstable and can collapse. In the framework of 1D focusing NLSE solitons are stable; thus solitons instability and the collapse must have a certain threshold in amplitude. Instability of a soliton of large amplitude and further collapse could be a proper theoretical explanation of the freak wave origin.

This scenario was observed in numerical experiment on the heuristic one-dimensional Maida-McLaughlin Tabak (MMT) model (see Majda et al. 1997) of one-dimensional wave turbulence (Zakharov et al. (2004)). At a proper choice of parameters this model mimics gravity waves on the surface of deep water. In the experiments described in the cited paper, instability of a moderate amplitude monochromatic wave leads first to creation of a chain of solitons, which merge due to inelastic interaction into one soliton of a large amplitude. This soliton sucks energy from neighbor waves, becomes unstable, and collapse up to $\lambda \sim 1$, producing the freak wave. We believe that this mechanism of freak wave formation is universal.

The most direct way to prove validity of the outlined above scenario for freak wave formation is a direct numerical solution of Euler equation, describing potential oscillations of ideal fluid with a free surface in a gravitational field. This solution can be made by the methods published in several well-known articles (Dommermuth and Yue (1987); West et al. (1987); Clamond and Grue (2001)). Here we use another method, based on conformal mapping. It should be mentioned that idea to exploit conformal mapping for unsteady flows was presented in Ovsyannikov (1973) and later in Meison et al. (1981), Chalikov and Sheinin (1998). Method used in this article has origin in Dyachenko et al. (1996), has been using in Zakharov et al. (2002), and was finally formulated in Dyachenko (2001). This method is applicable in $1+1$ geometry; it includes conformal mapping of fluid bounded by the surface to the lower half-plane together with "optimal" choice of variables, which guarantees well-posedness of the equations (Dyachenko 2005) and existence of smooth, unique solution of the equations for a finite time (Shamin 2006). Here we would like to stress that one of the main goal of this paper is to demonstrate effectiveness of the conformal variables to simulate exact 2D potential flow with a free boundary. Earlier, fully nonlinear numerical experiments regarding wave breaking, freak wave

formation, comparison with weakly nonlinear model (such as Nonlinear Shrodinger equation) were done in the papers Dold and Peregrine (1986), Tanaka (1990), Banner and Tian (1998), Henderson et al. (1999), Clamond and Grue (2002). On the other hand, using conformal approach we have studied in the paper Zakharov et al. (2002) the nonlinear stage of modulation instability for Stokes waves of steepness $\mu = ka \simeq 0.3$ and $\mu = 0.1$.

In the present article we perform similar experiment for waves of steepness $\mu \simeq 0.15$. This experiment could be considered as a simulation of a realistic situation. If a typical steepness of the swell is $0.06 \div 0.07$, in caustic area it could easily be 2–3 times more. In the new experiment, we start with the Stokes wave train, perturbed by a long wave with 20 times less amplitude. We observe development of modulation instability and finally the explosive formation of the freak wave that is pretty similar to waves observed in natural experiments.

2 Basic Equations

Suppose that incompressible fluid covers the domain

$$-\infty < y < \eta(x,t). \tag{1}$$

The flow is potential, hence

$$V = \nabla\phi, \qquad \nabla V = 0, \qquad \nabla^2\phi = 0. \tag{2}$$

Let $\psi = \phi|_{y=\eta}$ be the potential at the surface and $H = T + U$ be the total energy. The terms

$$T = -\frac{1}{2}\int_{-\infty}^{\infty} \psi\phi_n \,\mathrm{d}x, \tag{3}$$

$$U = \frac{g}{2}\int_{-\infty}^{\infty} \eta^2(x,t)\,\mathrm{d}x \tag{4}$$

are correspondingly kinetic and potential parts of the energy, g is a gravity acceleration, and ϕ_n is a normal velocity at the surface. The variables ψ and η are canonically conjugated; in these variables Euler equation of hydrodynamics reads

$$\frac{\partial\eta}{\partial t} = \frac{\delta H}{\delta\psi}, \qquad \frac{\partial\psi}{\partial t} = -\frac{\delta H}{\delta\eta}. \tag{5}$$

One can perform the conformal transformation to map the domain that is filled with fluid

$$-\infty < x < \infty, \qquad -\infty < y < \eta(x,t), \qquad z = x + iy$$

in z-plane to the lower half-plane

$$-\infty < u < -\infty, \qquad -\infty < v < 0, \qquad w = u + iv$$

in w-plane. Now, the shape of surface $\eta(x,t)$ is presented by parametric equations

$$y = y(u,t),\ x = x(u,t),$$

where $x(u,t)$ and $y(u,t)$ are related through Hilbert transformation

$$y = \hat{H}\left(x(u,t) - u\right), \qquad x(u,t) = u - \hat{H}y(u,t). \tag{6}$$

Here

$$\hat{H}(f(u)) = PV\frac{1}{\pi}\int_{-\infty}^{\infty}\frac{f(u')\,\mathrm{d}u'}{u'-u}.$$

Equations (5) minimize the action,

$$S = \int L\,\mathrm{d}t, \tag{7}$$

$$L = \int \psi\frac{\partial\eta}{\partial t}\,\mathrm{dx} - H. \tag{8}$$

Lagrangian L can be expressed as follows,

$$L = \int_{-\infty}^{\infty}\psi(y_t x_u - x_t y_u)\,\mathrm{d}u + \frac{1}{2}\int_{-\infty}^{\infty}\psi\hat{H}\psi_u\,\mathrm{du} - \frac{g}{2}\int_{-\infty}^{\infty}y^2 x_u\,\mathrm{du}$$
$$+\int_{-\infty}^{\infty}f\left(y-\hat{H}(x-u)\right)\mathrm{du}\,. \tag{9}$$

Here f is the Lagrange multiplier, which imposes the relation (6). Minimization of action in conformal variables leads to implicit equations (see Dyachenko et al. (1996))

$$y_t x_u - x_t y_u = -\hat{H}\psi_u$$
$$\psi_t y_u - \psi_u y_t + g y y_u + \hat{H}(\psi_t x_u - \psi_u x_t + g y x_u) = 0. \tag{10}$$

System (10) can be resolved with respect to the time derivatives. Omitting the details, we present only the final result

$$Z_t = \mathrm{i}UZ_u,$$
$$\Phi_t = \mathrm{i}U\Phi_u - B + \mathrm{i}g(Z-u). \tag{11}$$

Here

$$\Phi = 2\hat{P}\psi \tag{12}$$

is a complex velocity potential, U is a complex transport velocity:

$$U = 2\hat{P}\left(\frac{-\hat{H}\psi_u}{|z_u|^2}\right) \tag{13}$$

and

$$B = \hat{P}\left(\frac{|\Phi_u|^2}{|z_u|^2}\right) = \hat{P}\left(|\Phi_z|^2\right). \tag{14}$$

In (12), (13), and (14) $\hat{P}$ is the projector operator generating a function that is analytical in a lower half-plane

$$\hat{P}(f) = \frac{1}{2}\left(1 + i\hat{H}\right) f.$$

In (11)

$$z(w) \to w, \qquad \Phi(w) \to 0, \qquad \text{at } v \to -\infty.$$

All functions z, Φ, U, and B are analytic ones in the lower half-plane $v < 0$.

Recently, we found that (11) were derived in Ovsyannikov (1973), and we call them here Ovsyannikov's equations, OE. Implicit equations (10) were not known until 1994, so we call them DKSZ-equations.

Note, (10) can be used to obtain the Lagrangian description of surface dynamics. Indeed, from (10) one can get

$$\Psi = \partial^{-1}\hat{H}(y_t x_u - x_t y_u). \tag{15}$$

Plugging (15) to (8) one can express Lagrangian L only in terms of surface elevation. This result was independently obtained by Balk (1996). In Dyachenko (2001) (11) were transformed to a simple form, which is convenient both for numerical simulation and analytical study. By introducing new variables

$$R = \frac{1}{Z_w}, \quad V = \mathrm{i}\Phi_z = \mathrm{i}\frac{\Phi_w}{Z_w} \tag{16}$$

one can transform system (11) into the following one:

$$\begin{aligned} R_t &= \mathrm{i}(UR_w - RU_w), \\ V_t &= \mathrm{i}(UV_w - RB_w) + g(R-1). \end{aligned} \tag{17}$$

Now complex transport velocity U and B

$$\begin{aligned} U &= \hat{P}(V\bar{R} + \bar{V}R), \\ B &= \hat{P}(V\bar{V}). \end{aligned} \tag{18}$$

Thereafter, we call (17) and (18) Dyachenko equations, DE.

Both DKSZ-equations (10) and OE (11) have the same constants of motion

$$H = -\int_{-\infty}^{\infty} \Psi\hat{H}\Psi_u \,\mathrm{d}u + \frac{g}{2}\int_{-\infty}^{\infty} y^2 x_u \,\mathrm{d}y, \tag{19}$$

the same total mass of fluid

$$M = \int_{-\infty}^{\infty} y x_u \,\mathrm{d}u, \tag{20}$$

and the same horizontal momentum

$$P_x = \int_{-\infty}^{\infty} \Psi y_u \, \mathrm{d}u. \tag{21}$$

The Dyachenko equations (17) and (18) have the same integrals. To express them in terms of R and V, one has to perform the integration

$$Z = u + \int_{-\infty}^{u} \frac{\mathrm{d}u}{R}, \qquad \Phi = -i \int_{-\infty}^{u} \frac{V}{R} \, \mathrm{d}u. \tag{22}$$

3 Numerical Instability with Respect to Small Scale Perturbation

The problem of stability of the equations of motion of the fluid with a free surface goes back to the famous work of Taylor (1950). He has found the relationship between the growth rate of the interface instability, the wave-length of the perturbation, and the gravity acceleration. Today we would say that Taylor instability is the manifestation of the ill-posedness of the Cauchy problem for the case when gravity acceleration is directed out of the fluid.

The problem of well-posedness of the Cauchy problem for the potential irrotational flows with a free surface was studied in many papers. First time it was studied by Nalimov in Nalimov (1974).

3.1 Instability of Φ-Z Equations

Let us consider (11) with (13) and (14). Stability of the large-scale solution with respect to short-scale perturbation will be considered. Let this large-scale solution have subscripts 0, namely, $\Phi_0(w,t)$ and $Z_0(w,t)$. Obviously, perturbed solution is the following:

$$\Phi = \Phi_0 + \delta\Phi, \qquad Z = Z_0 + \delta Z. \tag{23}$$

Characteristic wavenumber k of $\delta\Phi$ and δZ is much larger than characteristic wavenumber k_0 of Φ_0 and Z_0. Let us expand arguments of U and B in (13 and 14) up to the first order in $\delta Z'$ and $\delta\Phi'$:

$$\begin{aligned} \frac{\mathrm{i}\Phi'}{Z'\bar{Z}'} + \text{c.c.} &\simeq \frac{\mathrm{i}\Phi_0'}{Z_0'\bar{Z}_0'} + (\bar{\Phi}_0' - \Phi_0') \frac{\mathrm{i}\delta Z'}{Z_0'^2 \bar{Z}_0'} + \frac{\mathrm{i}\delta\Phi'}{\bar{Z}_0' Z_0'} + \text{c.c.} \\ \frac{\Phi'}{Z'} \frac{\bar{\Phi}'}{\bar{Z}'} &\simeq \frac{\Phi_0'}{Z_0'} \frac{\bar{\Phi}_0'}{\bar{Z}_0'} - \frac{\Phi_0'}{Z_0'} \frac{\bar{\Phi}_0'}{\bar{Z}_0'} \frac{\delta Z'}{Z_0'} + \frac{\bar{\Phi}_0'}{\bar{Z}_0'} \frac{\delta\Phi'}{Z_0'} + \text{c.c.} \end{aligned} \tag{24}$$

Now we can calculate U and B:

$$U \simeq U_0 + \frac{\mathrm{i}}{Z_0'^2 \bar{Z}_0'} \left(\bar{\Phi}_0' - \Phi_0'\right) \delta Z' + \frac{\mathrm{i}\delta\Phi'}{\bar{Z}_0' Z_0'},$$

$$B \simeq B_0 - \frac{\Phi_0'}{Z_0'} \frac{\bar{\Phi}_0'}{\bar{Z}_0'} \frac{\delta Z'}{Z_0'} + \frac{\bar{\Phi}_0'}{\bar{Z}_0' Z_0'} \delta\Phi'. \tag{25}$$

When deriving (25) we have to calculate projector of (24). To do this we deal with products like $A_0 \delta Z'$ and $A_0 \delta \bar{Z}'$. It is easy to see that due to the scale separation of A_0 and δZ the following relations are valid:

$$\hat{P}(A_0 \delta Z') \simeq A_0 \delta Z',$$

$$\hat{P}(A_0 \delta \bar{Z}') \simeq 0. \tag{26}$$

Now we are ready to write down the linearized equations for perturbations.

$$\delta Z_t = \mathrm{i}\left(U_0 - \frac{\mathrm{i}}{Z_0' \bar{Z}_0'} \left(\Phi_0' - \bar{\Phi}_0'\right)\right) \delta Z' - \frac{\delta\Phi'}{\bar{Z}_0'},$$

$$\delta\Phi_t = \frac{\Phi_0'^2}{Z_0'^2 \bar{Z}_0'} \delta Z' + \mathrm{i}\left(U_0 + \frac{\mathrm{i}(\Phi_0' + \bar{\Phi}_0')}{Z_0' \bar{Z}_0'}\right) \delta\Phi' + \mathrm{i}g\delta Z. \tag{27}$$

Now we treat all functions with subscript $\ldots_0$ in (27) as constants. This is so-called "method of frozen coefficient," which is widely used in analysis of numerical schemes.

Let δZ and $\delta\Phi \sim \exp(\mathrm{i}\omega t - \mathrm{i}ku)$. Then the following dispersion relation can be derived:

$$\omega = kV_\mathrm{D} \pm \sqrt{gk \frac{1}{\bar{Z}_0'}}. \tag{28}$$

Here V_D has a meaning of Doppler frequency shift and is equal to

$$V_\mathrm{D} = \frac{\Psi_0'}{Z_0' \bar{Z}_0'} - \hat{H} \frac{\hat{H}\Psi_0'}{Z_0' \bar{Z}_0'}. \tag{29}$$

So, from (28) immediately follows that for gravity waves ω has imaginary part, which *grows as a function of k*:

$$\gamma = \frac{1}{2}\sqrt{gk} \frac{\eta_x'}{\sqrt{X'}}.$$

It means that large scale solution is unstable with respect to the perturbation.

This instability takes place only in the numerics when dealing with Ovsyannikov equations.

3.2 Stability of R-V Equations

Doing similar analysis for *R-V* equations one can easily derive the following set of equations for perturbations:

$$\begin{aligned}\delta R_t &= V_{\mathrm{D}}\delta R' - \mathrm{i}|R_0|^2\delta V' + b_{11}\delta R + b_{12}\delta V,\\ \delta V_t &= V_{\mathrm{D}}\delta V' + b_{21}\delta R + b_{22}\delta V,\end{aligned} \tag{30}$$

with

$$\begin{aligned}b_{11} &= -\mathrm{i}(U_0' + R_0\bar{V}_0' - R_0'\bar{V}_0),\\ b_{12} &= \mathrm{i}(\bar{R}_0R_0' - R_0\bar{R}_0'),\\ b_{21} &= g + \mathrm{i}(\bar{V}_0V_0' - B_0') = g + \tilde{g},\\ b_{22} &= \mathrm{i}(\bar{R}_0V_0' - R_0\bar{V}_0').\end{aligned} \tag{31}$$

Coefficient $b_{21} = g + \tilde{g}$ is pure real. Indeed,

$$\begin{aligned}\tilde{g} - \bar{\tilde{g}} &= \mathrm{i}(\bar{V}_0V_0' - B_0' + V_0\bar{V}_0' - \bar{B}_0'),\\ &= i\frac{\partial}{\partial u}(V_0\bar{V}_0 - B_0 - \bar{B}_0) = 0.\end{aligned}$$

Applying "method of frozen coefficient" one can obtain the following dispersion relation:

$$\omega = kV_{\mathrm{D}} + \mathrm{i}\Omega \pm \frac{1}{|Z_0'|}\sqrt{(g+\tilde{g})k - \Omega^2}. \tag{32}$$

while

$$\Omega = \frac{\mathrm{i}}{2}\left(\frac{\bar{V}_0'}{Z_0'} - \frac{V_0'}{\bar{Z}_0'}\right),$$

$$\tilde{g} = \mathrm{i}(\bar{V}_0V_0' - B_0').$$

Note, V_D, Ω, and $\tilde{g}$ are pure real values.

Although ω in (32) has imaginary part, *it doesn't grow as a function of k* (of course, if $\tilde{g}$ does not exceed g). This property makes the system of equation (17) numerically stable with respect to small scale perturbation.

4 Freak Waves as a Result of Modulation Instability

Here we study modulation instability of uniform wave train of Stokes wave numerically. For time integration the standard Runge–Kutta method of the fourth order was used.

Question of great interest is the nonlinear stage of the instability. Here and everywhere below we do simulation in periodic domain $L = 2\pi$ and

$$g = 1.$$

Wavetrain of the amplitude a with wavenumber k_0 is unstable with respect to large scale modulation δk. Growth rate of the instability γ is

$$\gamma = \frac{\omega_0}{2}\left(\left(\frac{\delta k}{k_0}\right)^2 (ak_0)^2 - \frac{1}{4}\left(\frac{\delta k}{k_0}\right)^4\right)^{\frac{1}{2}}. \tag{33}$$

Here ω_0 is the linear dispersion relation for gravity wave

$$\omega_0 = \sqrt{gk_0}.$$

- The shape of Stokes progressive wave is given by

$$y = \frac{c^2}{2g}\left(1 - \frac{1}{|Z_u|^2}\right),$$

  while Φ is related to the surface as

$$\Phi = -c(Z-u), \qquad V = \mathrm{i}c(R-1).$$

  The amplitude of the wave h/L is the parameter for initial condition. (For the sharp peaked limiting wave $h/L \simeq 0.141$).
- Put 100 such waves with small perturbation in the periodic domain of 2π.

In such a way we prepared initial wave train with the steepness $\mu \simeq 0.095$. Main Fourier harmonic of this wave train is $k = 100$. Similar problem was studied in Song and Banner (2002). But instead of long wavetrain they studied evolution of small group of waves.

For perturbation small value for Fourier harmonic with $k_p = 1$ was set. So, that

$$R_k = R_k^{\text{unperturbed}} + 0.05R_{100}\exp^{-\mathrm{i}k_p u}.$$

Surface profile of this initial condition is shown in Fig. 1.

Fourier spectrum of the initial condition is shown in Fig. 2.

After sufficient large time, which is more than 1,300 wave periods, one can observe freak wave formation, as it is shown in Fig. 3. Freak wave grows from mean level of waves to its maximal value for several wave periods, than vanishes or breaks.

Detailed view at the freak wave at the moment of maximal amplitude is shown in Fig. 4. This set of experiments is similar to that of Dold and Peregrine (1986), Tanaka (1990). The difference is that we were able to increase the accuracy of the simulation, and consider much longer wavetrains. Also (due to using conformal mapping) we can simulate breaking with multivalued surface profile. Accuracy in the simulation is very important because the freak wave appears in a very subtle

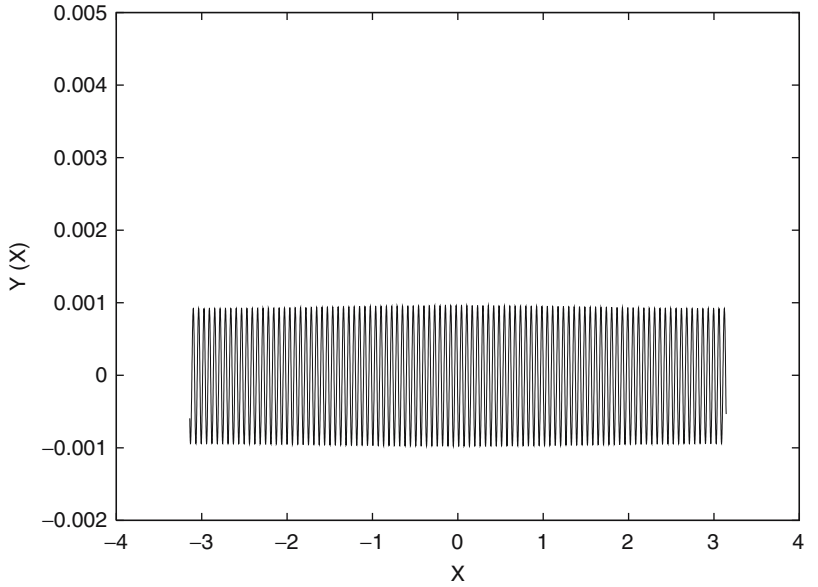

Fig. 1 Initial profile of the wave train

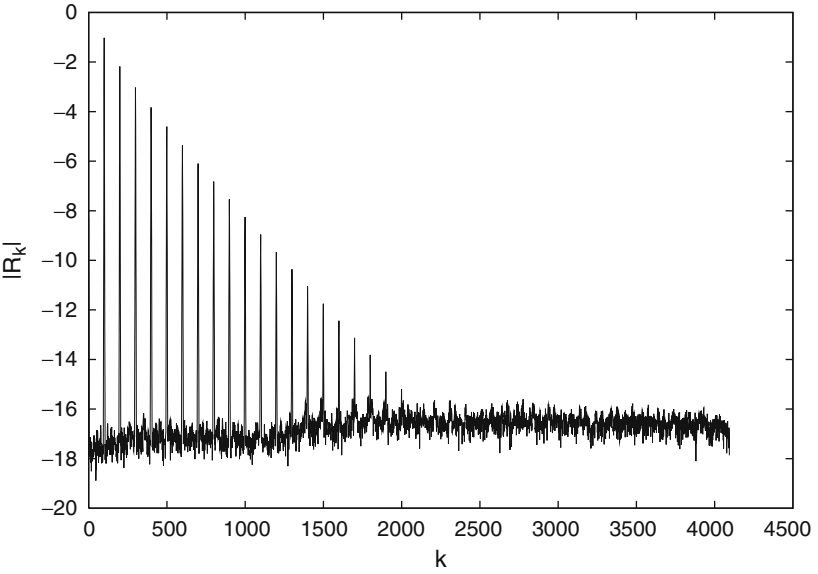

Fig. 2 Fourier coefficients $|R_k|$ for initial condition ($\mu \simeq 0.095$)

manner on the phase relations between Fourier harmonics of the surface. Moreover, for shorter wavetrains, threshold of modulation instability increases and breaking does not happen even for large steepness. In our experiments we have observed

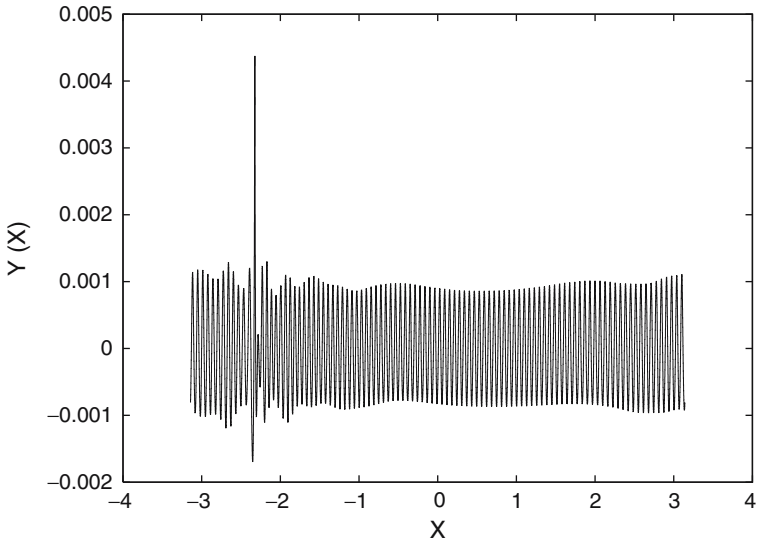

Fig. 3 Freak wave on the surface profile. $T = 802.07$

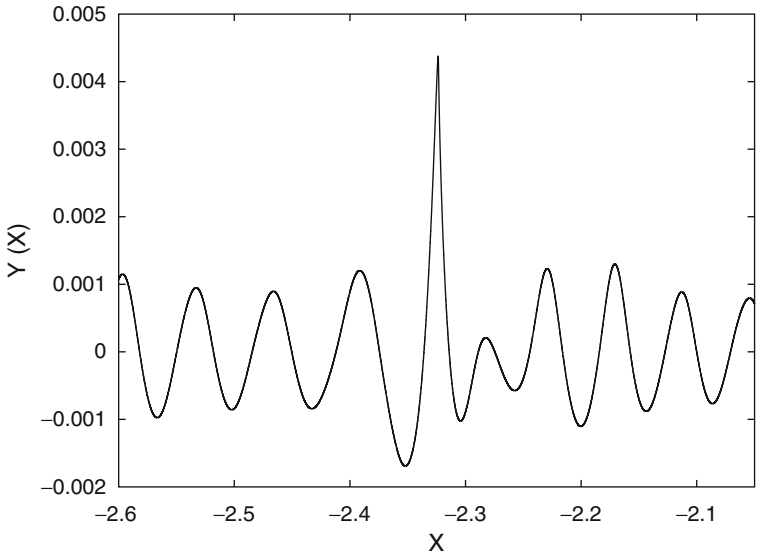

Fig. 4 Zoom in surface profile at $T = 802.07$

threshold of steepness for wave breaking a little less than in Tanaka (1990), but above $\mu = 0.1$. Still, surface profile from Tanaka (1990) (Fig. 5) is very similar to the picture in Fig. 4 with $\mu = 0.095$.

During numerical simulation of the final stage of freak wave formation, resolution must be increased to resolve high curvature of the surface profile. To do this we

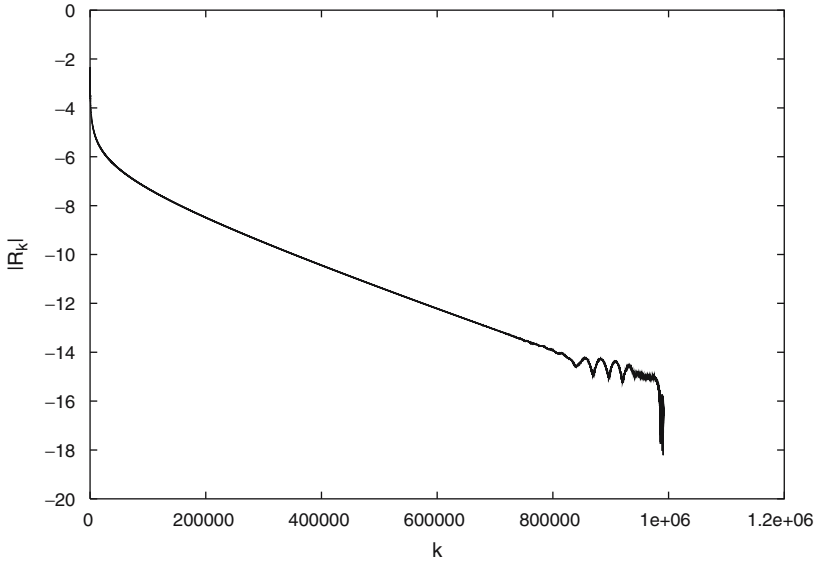

Fig. 5 Fourier coefficients $|R_k|$ at $T = 802.07$

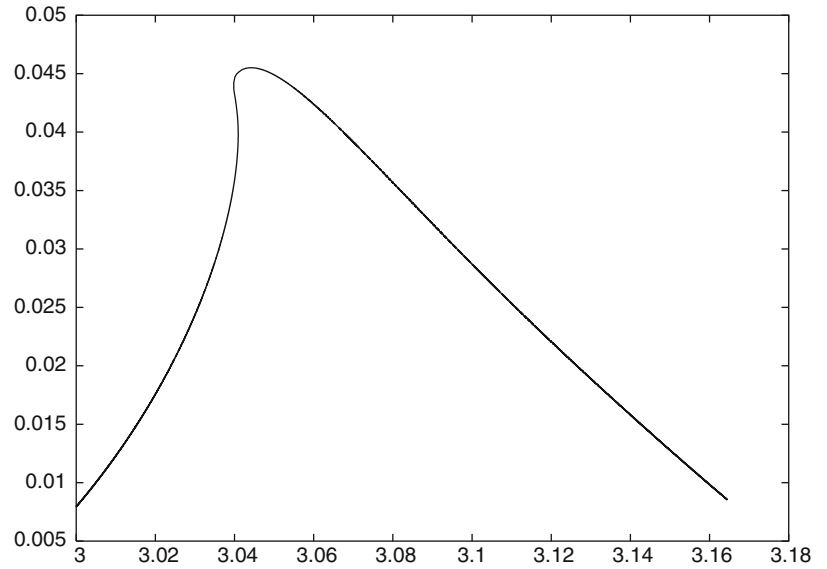

Fig. 6 Profile of breaking wave

have been increasing number of Fourier harmonics, which reached 2^{20} at the end ($T = 802.07$). Fourier coefficients of R_k are shown in Fig. 5.

If amplitude of the wave train is large, then freak wave may eventually break. Such a picture is presented in the Fig. 6, which corresponds to the other numerical simulation with the initial steepness $\mu \simeq 0.14$.

5 Exact Equations and Nonlinear Shrödinger Approximation

Evolution of weakly nonlinear Stokes wavetrain can be described by nonlinear Shrödinger equation (*NLSE*), derived by Zakharov (1968). This equation is integrable (see Zakharov and Shabat 1972) and is just the first term in the hierarchy of envelope equations describing packets of surface gravity waves. The second term in this hierarchy was calculated by Dysthe (1979), the next one was found a few years ago by Trulsen and Dysthe (1996). The Dysthe equation was solved numerically by Ablovitz and his collaborates (see Ablovitz et al. 2000).

Since the first work of Smith (1976), many authors tried to explain the freak wave formation in terms of NLSE and its generalizations, like Dysthe equation. A vast scientific literature is devoted to this subject. The list presented below is long but incomplete: Ablovitz et al. (2000), Onorato et al. (2000, 2001, 2002), Peregrine (1983); Peregrine et al. (1988), Trulsen and Dysthe (1996, 1997), Trulsen (2000), Trulsen et al. (2000), Clamond and Grue (2002).

One cannot deny some advantages achieved by the use of the envelope equations. Results of many authors agree in one important point: nonlinear development of modulation instability leads to concentration of wave energy in a small spatial region. This is a "hint" regarding possible formation of freak wave. On the other hand, it is clear that the freak wave phenomenon cannot be explained in terms of envelope equations. Indeed, NLSE and its generalizations are derived by expansion in series on powers of parameter $\lambda \simeq 1/Lk$, where k is a wave number and L is a length of modulation. For real freak wave $\lambda \sim 1$ and any slow modulation expansion fails. At this point interesting question rises: what happens to NLSE approximation when increasing the steepness of the carrier wave? In particular, we study "exact" soliton solutions for NLSE placed in the exact equations (17).

Such type of problem was considered in the Henderson et al. (1999), but with low resolution, and small length of periodic carrier. Also in Clamond and Grue (2002) numerical solutions for envelope equation was compared with "almost" exact equations.

For (17) NLSE model can be derived for the envelope of R.

$$R = 1 + R_1 \, \mathrm{e}^{-\mathrm{i}k_0 u - \omega_0 t} + \cdots$$

$$\mathrm{i}R_{1t} + \frac{1}{8}\frac{\omega_0}{k_0^2} R_{1uu} + \frac{1}{2}\omega_0 k_0^2 |R_1|^2 R_1 = 0.$$

Initial conditions consist of "linear wave carrier" $\mathrm{e}^{-\mathrm{i}k_0 u}$, modulated in accordance with soliton solution for NLSE:

$$\begin{aligned} R(u) &= 1 + s_0 \frac{\mathrm{e}^{-\mathrm{i}k_0 u}}{\cosh(\lambda k_0 u)}, \\ V(u) &= -\mathrm{i}c_0 s_0 \frac{\mathrm{e}^{-\mathrm{i}k_0 u}}{\cosh(\lambda k_0 u)}. \end{aligned} \tag{34}$$

Here s_0 is the steepness of the carrier wavetrain, c_0 is the phase velocity of the carrier.

First comparison of fully nonlinear model for water wave with NLSE was done in Clamond and Grue (2002) for the wave carrier with the steepness $\mu \simeq 0.091$. For such steepness there was a good agreement between two models, but only for the short time. After finite time weakly nonlinear model (*NLSE*) ceases to be valid.

In our work we want to study the situation with larger and smaller steepness to find out how NLSE approximation breaks.

5.1 Small Steepness

First experiment was intended to observe how NLSE works. In the initial conditions (34) we used

$$s_0 \simeq 0.07, \qquad \lambda = 0.1, \qquad k_0 = 100.$$

Initial surface of fluid is shown in Fig. 7.

After couple of thousands wave periods, soliton changes a little as it is seen in Fig. 8. Also in the Figs. 9 and 10 Fourier spectra of the soliton at both moments of time are presented.

So, one can see that for the steepness $\mu \leq 0.07$ NLSE model is quite reasonable.

Another numerical experiment showing effective simulation with (17) along with applicability NLSE model for moderate steepness, $\mu \simeq 0.085$, is the collision of two solitons.

In Fig. 11 initial condition is shown. Moment of collision is shown in the Fig. 12 and detailed view showing carrier wavetrain under the envelope is in the Fig. 13.

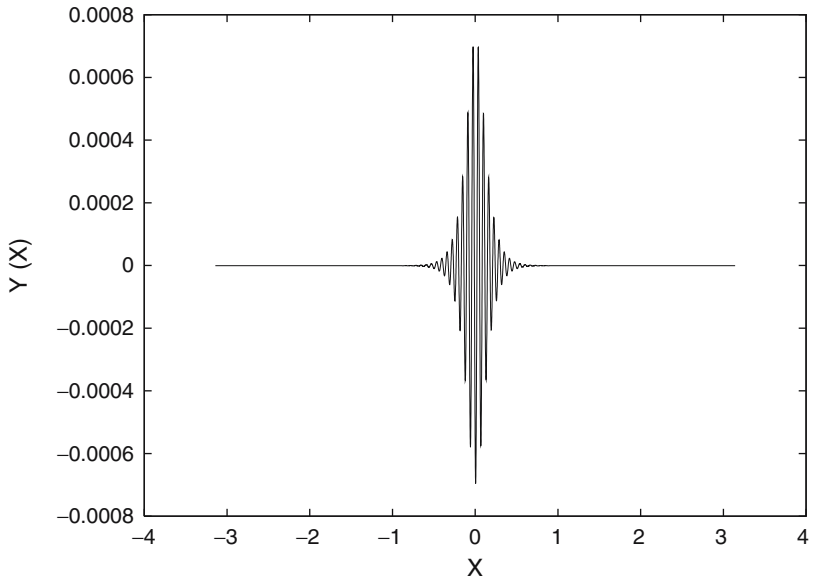

Fig. 7 Initial surface profile like for NLSE soliton with $\mu \simeq 0.07$

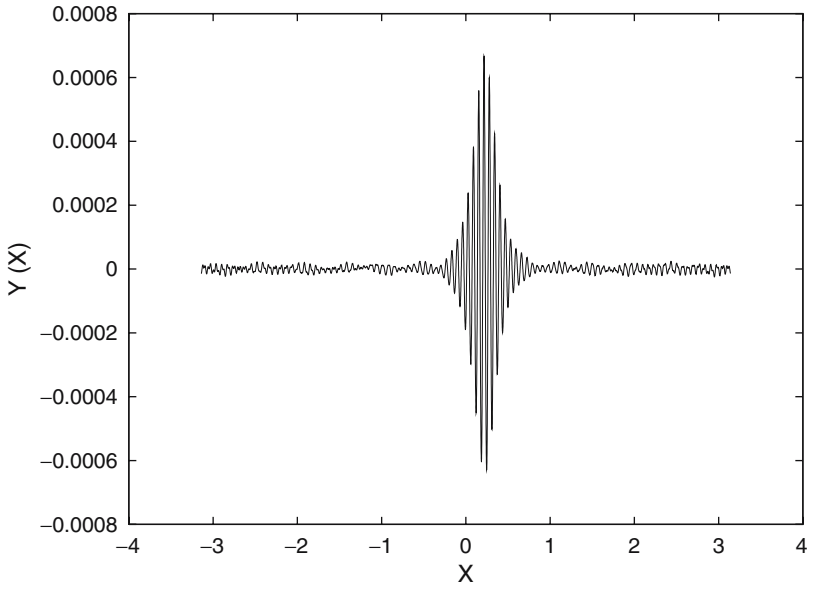

Fig. 8 Surface profile like for NLSE soliton with $\mu \simeq 0.07$ at $T = 1,500$

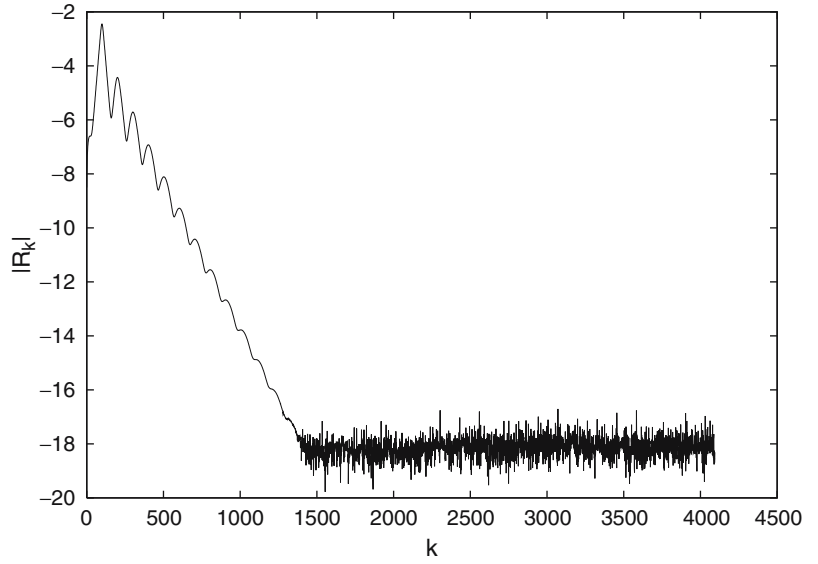

Fig. 9 Fourier harmonics of the initial soliton with $\mu \simeq 0.07$

After second collision (recall that boundary conditions are periodic) solitons are plotted in Fig. 14. Fourier spectra of these two solitons at the moments of time $T = 0.05,\ 30.8,$ and 250.0 are shown in Figs. 15–17.

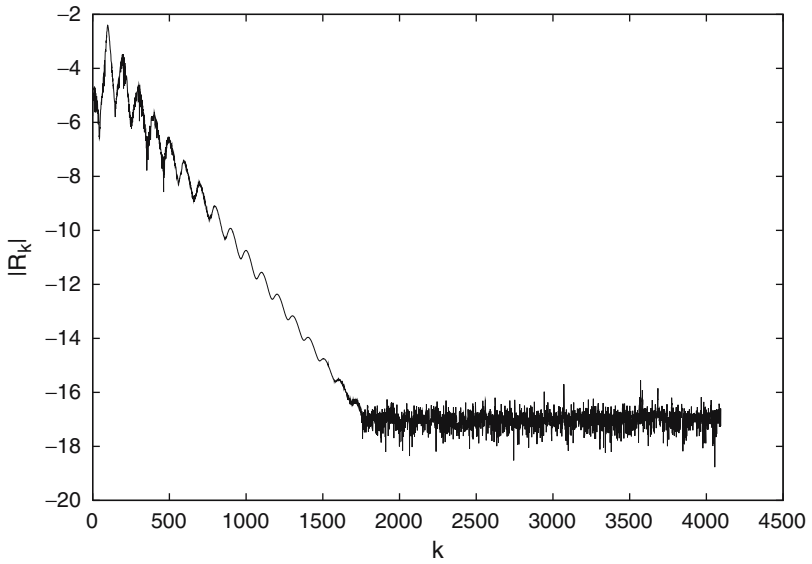

Fig. 10 Fourier harmonics of the soliton with $\mu \simeq 0.07$ at $T = 1,500$

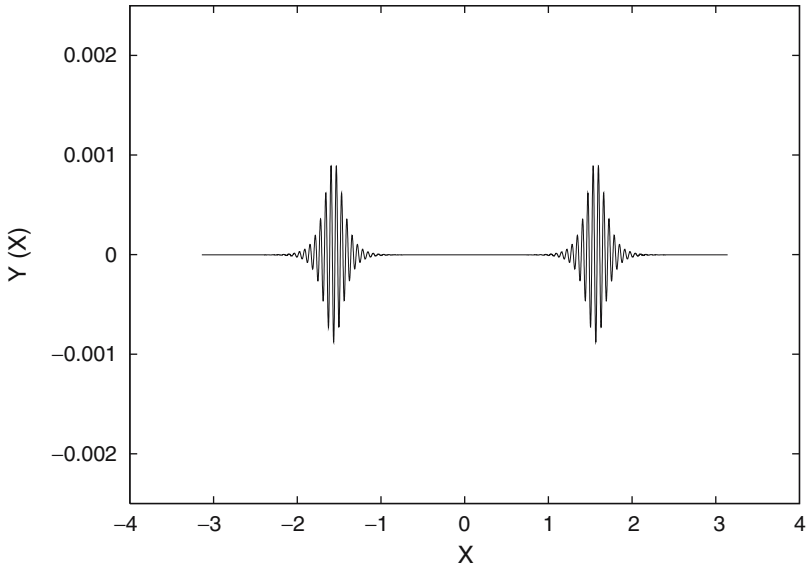

Fig. 11 Initial surface profile of two NLSE solitons with $\mu \simeq 0.085$

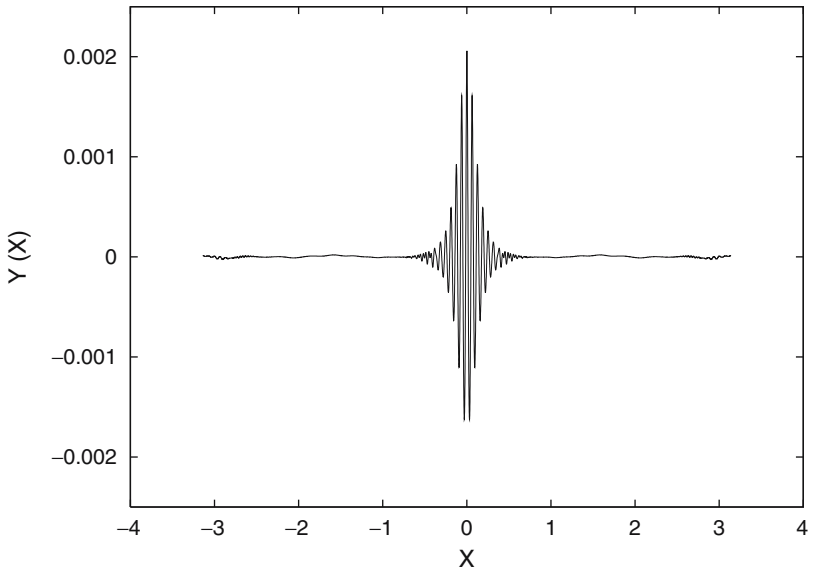

Fig. 12 Two NLSE solitons with $\mu \simeq 0.085$. collide at $T = 30.8$

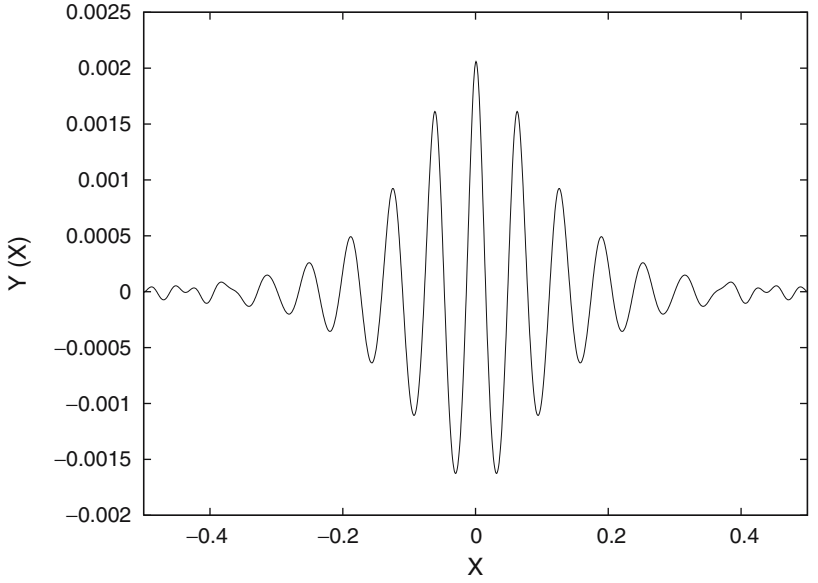

Fig. 13 Detailed view of two colliding NLSE solitons with $\mu \simeq 0.085$ at $T = 30.8$

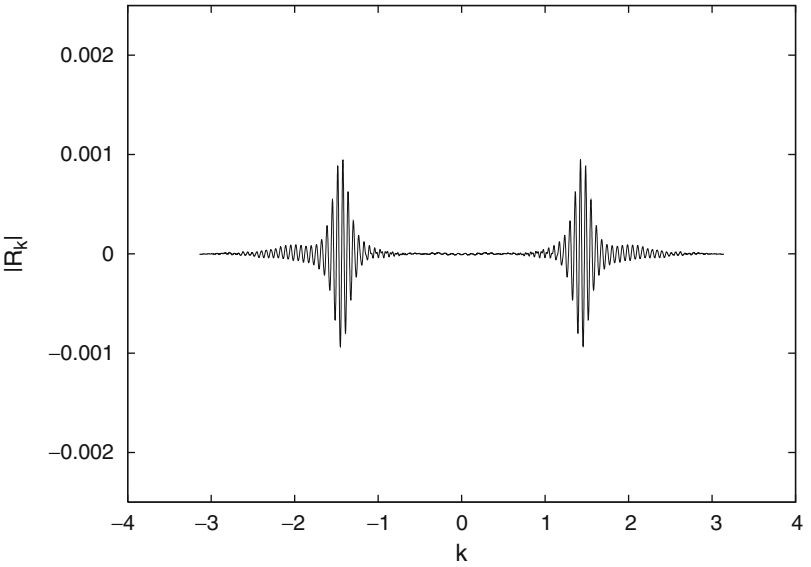

Fig. 14 Two *NLSE* solitons with $\mu \simeq 0.085$ after two collisions at $T = 250.0$

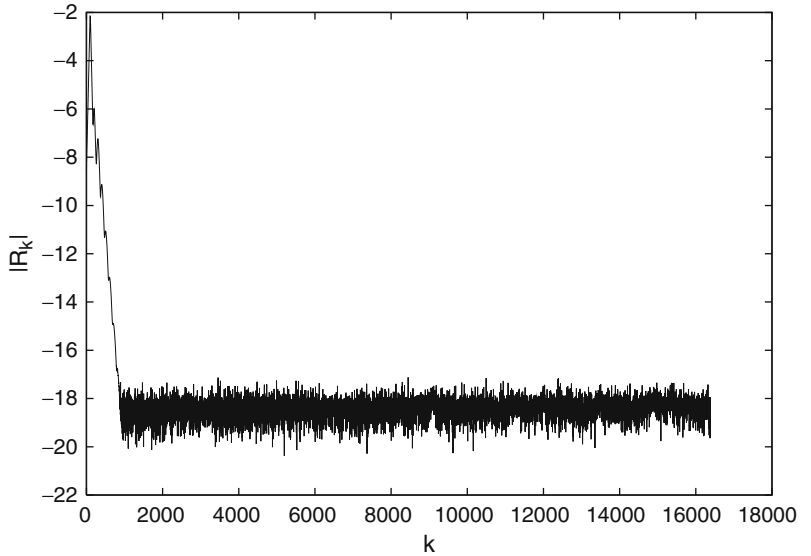

Fig. 15 Fourier spectrum of the initial surface profile of two NLSE solitons with $\mu \simeq 0.085$

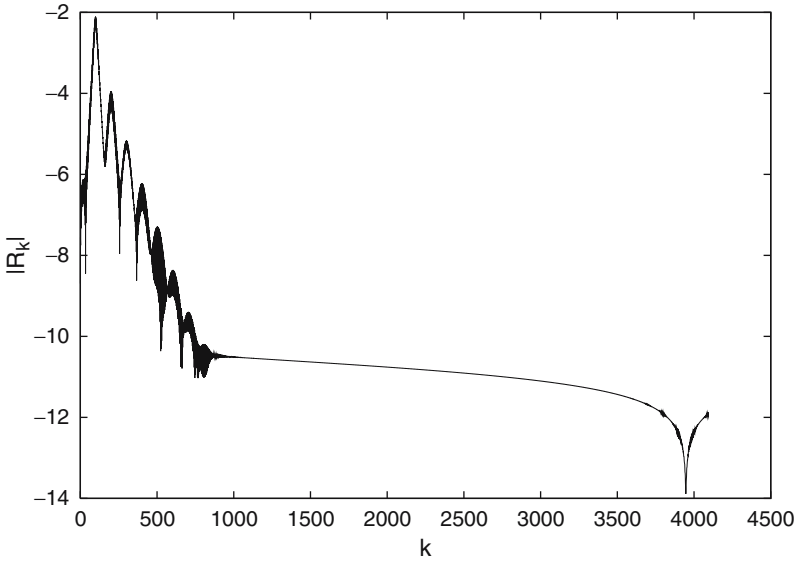

Fig. 16 Fourier spectrum of two colliding NLSE solitons with $\mu \simeq 0.085$ at $T = 30.8$

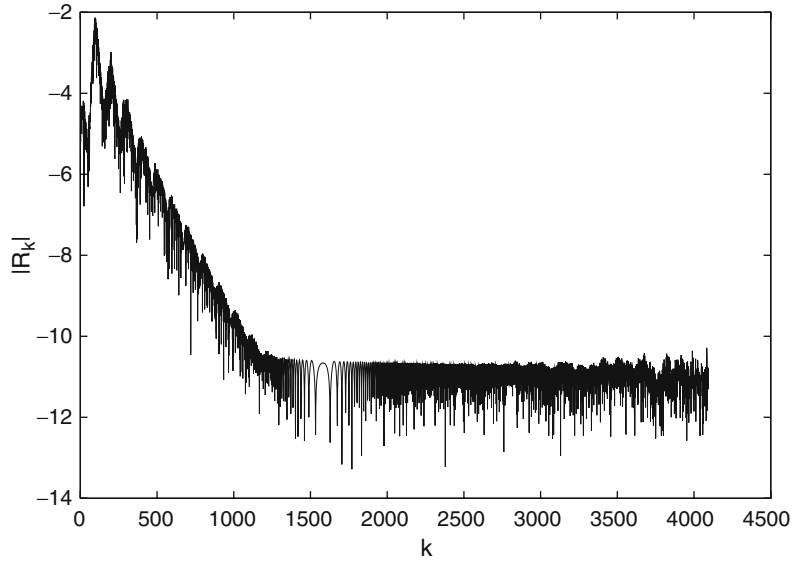

Fig. 17 Fourier spectrum of two NLSE solitons with $\mu \simeq 0.085$ at $T = 250.0$

5.2 Large Steepness

Now let us turn to the higher steepness of the carrier,

$$\mu = 0.1.$$

In the Fig. 18 there is initial condition. Again, after couple of thousand wave periods, soliton changes a little as it is seen in Fig. 19. In Figs. 20 and 21 Fourier spectra of the soliton at both moments of time are presented.

From this pictures one can see that for steepness $\mu \simeq 0.10$ some corrections to the NLSE model are desirable. Dysthe equations are exactly intended for that situation.

But what happens when further increasing the steepness? Below we consider the case of the steepness of the carrier

$$\mu = 0.14.$$

In the Fig. 22 there is initial condition. Very fast, after couple of dozen wave periods, soliton drastically changes as it is seen in Fig. 23. One can see freak wave at the surface (in Fig. 24). In the Figs. 25 and 26 Fourier spectra of the soliton at both moments of time are presented. They demonstrate the quality of the numerical simulation. The tail of the spectrum in Fig. 26 shows that the resolution decreases (aliasing errors "go up"); however, the simulation remains stable.

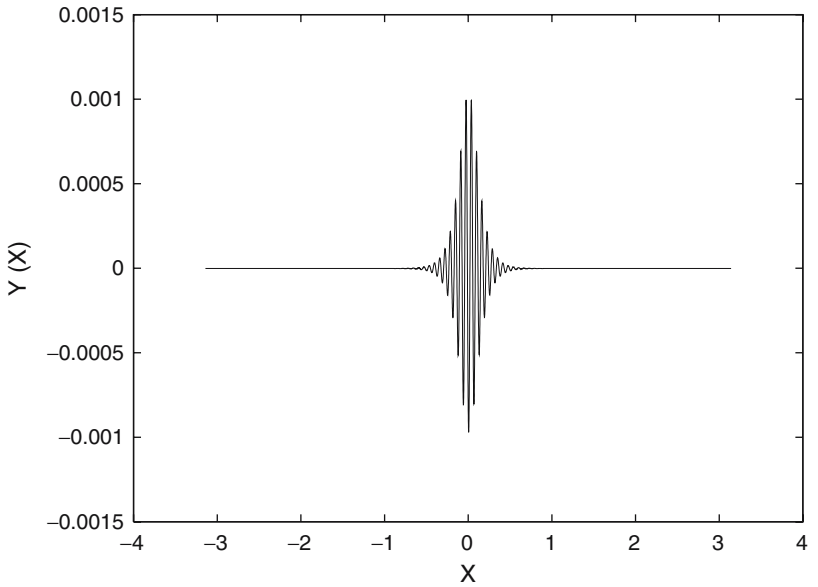

Fig. 18 Initial surface profile like for NLSE soliton with $\mu \simeq 0.10$

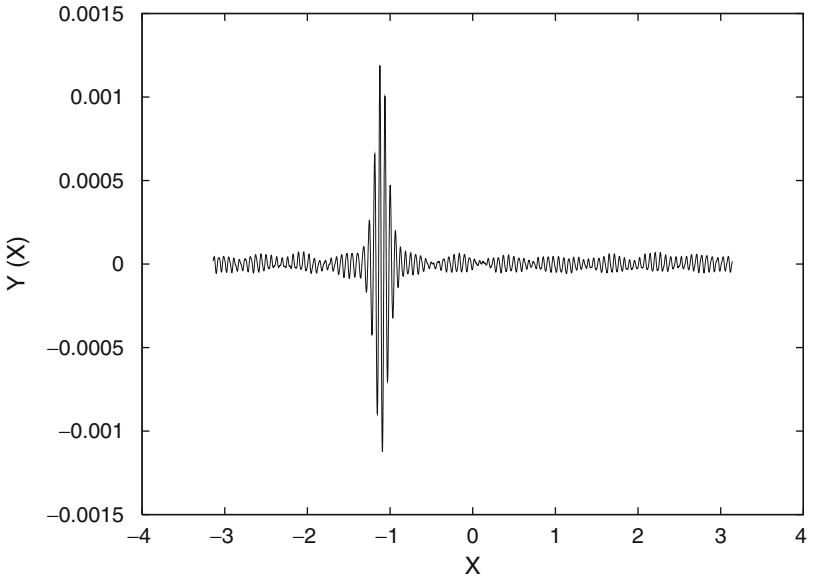

Fig. 19 Surface profile like for NLSE soliton with $\mu \simeq 0.10$ at $T = 2,345$

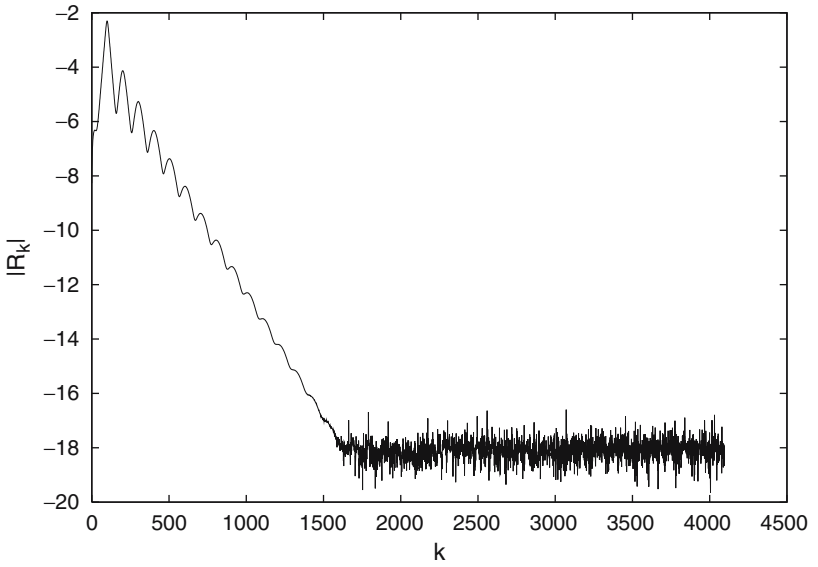

Fig. 20 Fourier harmonics of the initial soliton with $\mu \simeq 0.10$

From the last case, with the steepness $\mu = 0.14$, one can see that envelope approximation completely fails. Such event as one single crest (freak wave) can not be described in terms of wave envelope.

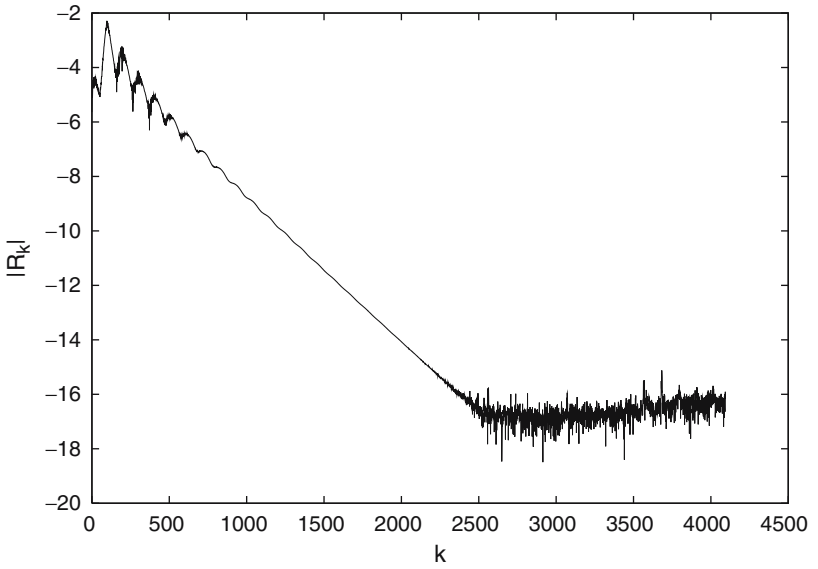

Fig. 21 Fourier harmonics of the soliton with $\mu \simeq 0.10$ at $T = 2,345$

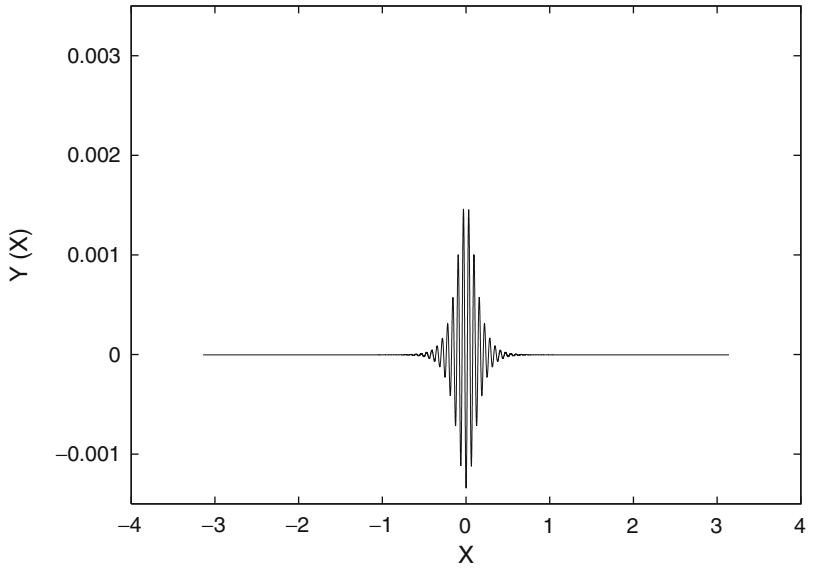

Fig. 22 Initial surface profile like for NLSE soliton with $\mu \simeq 0.14$

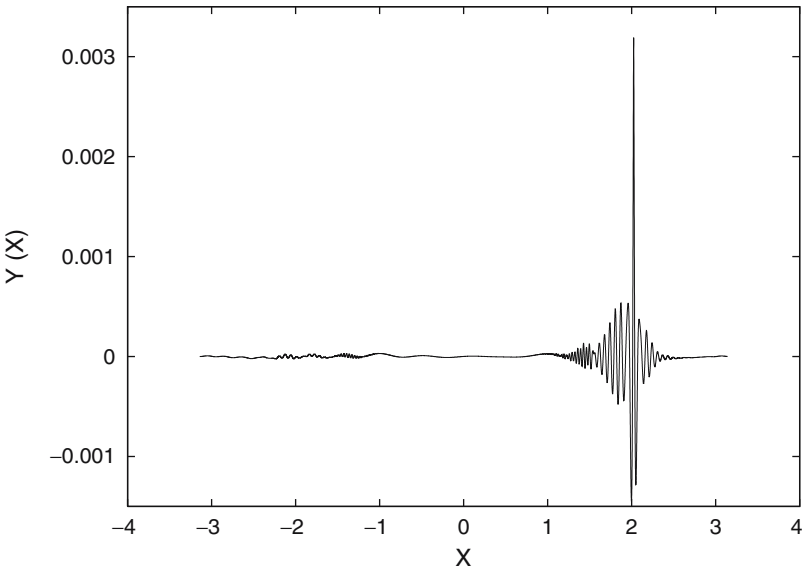

Fig. 23 Surface profile like for NLSE soliton with $\mu \simeq 0.14$ at $T = 38.4$

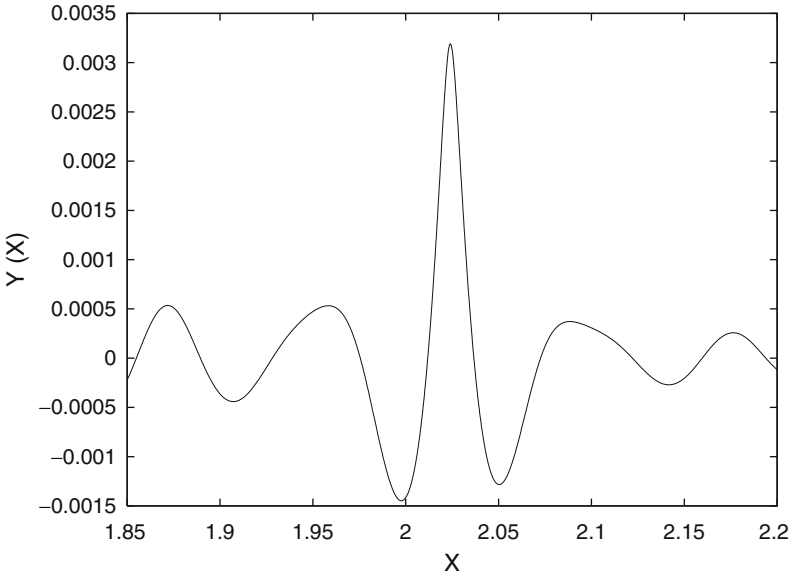

Fig. 24 Zoomed surface profile near freak wave $\mu \simeq 0.14$ at $T = 38.4$

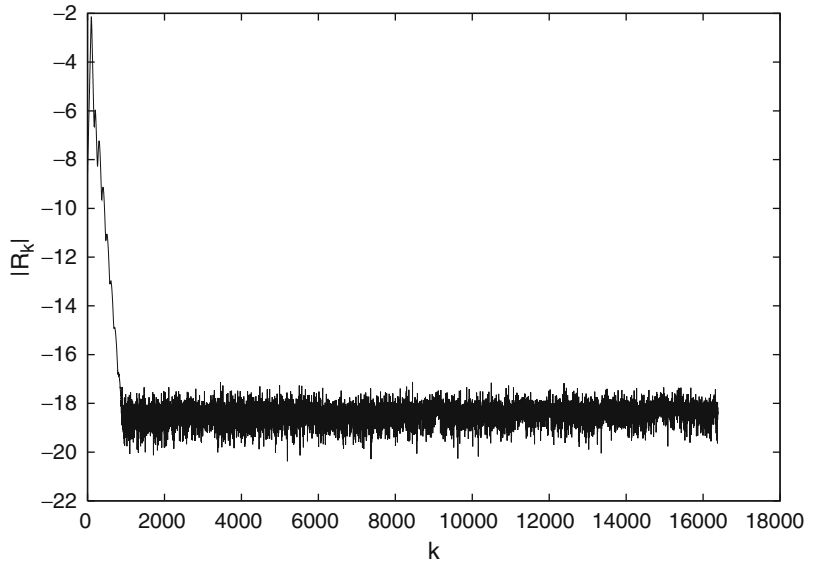

Fig. 25 Fourier harmonics of the initial soliton with $\mu \simeq 0.14$

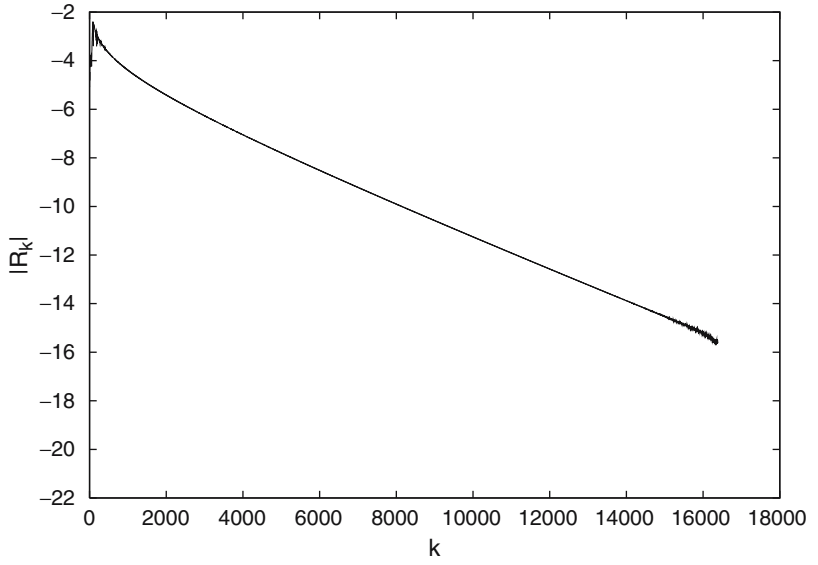

Fig. 26 Fourier harmonics of the soliton with $\mu \simeq 0.14$ at $T = 38.4$

6 Do Freak Waves Appear from Quasisolitonic Turbulence?

Let us summarize the results of our numerical experiments. Certainly, they reproduce the most apparent features of freak waves: single wave crests of very high amplitude, exceeding the significant wave height more than three times, appear from "nowhere" and reach full height in a very short time, less than ten periods of surrounding waves. The singular freak wave is proceeded by the area of diminished wave amplitudes. Nevertheless, the central question about the physical mechanism of freak waves origin is still open.

In our experiments, the freak wave appears as a result of development of modulation instability, and it takes a long time for the onset of instability to create a freak wave. Indeed, the level of perturbation in our last experiment is relatively high. The 2–3 inverse growth-rate is enough to reach the state of full-developed instability, when the initial Stokes wave is completely decomposed. Meanwhile, the freak wave appears only after 15th inverse growth-rates of instability. What happens after developing of instability but before formation of freak wave?

During this relatively long period of time, the state of fluid surface can be characterized as quasisolitonic turbulence, which consists of randomly located quasisolitons of different amplitudes moving with different group velocities. Numerical study of interaction of envelope soliton was done in Clamond and Grue (2002). Such interaction leads to formation of wave with large amplitude. Here we can think in terms of quasisolitonic turbulence. Such turbulence was studied in the recent work of Zakharov et al. (2004) in a framework of so-called defocusing MMT model:

$$\mathrm{i}\frac{\partial \Psi}{\partial t} = \left|\frac{\partial}{\partial x}\right|^{1/2}\Psi + \left|\frac{\partial}{\partial x}\right|^{3/4}\left(\left|\left|\frac{\partial}{\partial x}\right|^{3/4}\Psi\right|^{2}\left|\frac{\partial}{\partial x}\right|^{3/4}\Psi\right). \tag{35}$$

This is a heuristic model description of gravity surface waves in deep water. In this model, quasi-solitons of small amplitude are stable, interact inelastically, and can merge. Above some critical level quasi-solitons of large amplitude are unstable. They collapse in finite time forming very short wave pulses, which can be considered as models of freak waves. Equation 35 has the exact solution:

$$\begin{aligned}\Psi &= A\,\mathrm{e}^{\mathrm{i}kx-\mathrm{i}\omega t}\\ \omega &= k^{1/2}\left(1+k^{5/2}A^{2}\right).\end{aligned} \tag{36}$$

This solution can be constructed as a model of the Stokes wave and is unstable with respect to modulation instability. Development of this instability was studied numerically. On the first stage, the unstable monochromatic wave decomposes to a system of almost equal quasi-solitons. Then, the quasi-solitonic turbulence is formed: quasi-solitons move chaotically, interact with each other, and merge. Finally they create one large quasi-soliton, which exceeds threshold of instability and collapses, creating a freak wave.

One can think that a similar scenario of freak wave formation is realized in a real sea. We like to stress that the key point in this scenario is the quasi-solitonic turbulence and not the Stokes wave. The Stokes wave is just a "generator" of this turbulence. The quasisolitonic turbulence can appear as a result of instability of narrow spectral distributions of gravity waves.

The formulated above concept is so far a hypothesis, which has to be confirmed by future numerical experiments.

Acknowledgments This work was supported by the US Army Corps of Engineers Grant W912BU-07-P-0231, by ONR Grant N00014-06-C-0130, by NSF Grant DMS 0404577, by RFBR Grant 06-01-00665, 07-01-92165, by the Program "Fundamental Problems in Nonlinear Dynamics" from the RAS Presidium, and by Grant "Leading Scientific Schools of Russia."

References

Ablovitz MI, Hammack D, Henderson J, Scholder CM (2000) Modulated periodic stokes waves in deep water. Phys Rev Lett:887–890

Ablovitz MI, Hammack D, Henderson J, Scholder CM (2001) Long-time dynamics of the modulational instability of deep water. Phys D 152–153:416–433

Balk A (1996) A Lagrangian for water waves. Phys Fluids 8:416–420

Banner M, Tian X (1998) On the determination of the onset of wave breaking for modulating surface gravity waves. J Fluid Mech 367:107–137

Benjamin TB, Feir JE (1967) The disintegration of wave trains on deep water: Part 1. Theory. J Fluid Mech 27:417–430

Chase(2003) http://bell.mma.edu/achase/NS-221-Big-Wave.html

Chalikov D, Sheinin D (1998) Direct modeling of one-dimensional nonlinear potential waves. In: Perrie W (ed) Nonlinear ocean waves: Advances in fluid mechanics, vol 17. Computation Mechanics Publications, MA, pp 89–110

Clamond D, Grue J (2001) A fast method for fully nonlinear-wave computations. J Fluid Mech 447:337–355

Clamond D, Grue J (2002) Interaction between envelope solitons as a model for freak wave formation: Part 1. Long time interaction. C.R.Mecanique 330:575–580

Dean RG (1990) Freak waves: A possible explanation. In: Torum A, Gudmestad OT (eds) Water w ave kinetics. Kluwer, Dordrecht, pp 609–612

Divinsky VD, Levin BV, Lopatikhin LI, Pelinovsky EN, Slyunyaev AV (2004) A freak wave in the Black sea: Observations and simulation. Doklady Earth Sci 395:438–443

Dold JW (1992) An efficient surface integral algorithm applied to unsteady gravity waves. J Comput Phys 103:90–115

Dold JW, Peregrine DH (1986) Water-wave modulation. In: Proceedings of 20th International Conference on Coastal Engineering. vol 1, Chap 13, pp 163–175

Dommermuth DG, Yue DKP (1987) A high-order spectral method for the study of nonlinear gravity waves. J Fluid Mech 184:267–288

Dyachenko AI, Kuznetsov EA, Spector MD, Zakharov VE (1996) Analytical description of the free surface dynamics of an ideal fluid (canonical formalism and conformal mapping). Phys Lett A 221:73–79

Dyachenko AI (2001) On the dynamics of an ideal fluid with free surface. Doklady Math 63:115–118

Dyachenko AI, Zakharov VE (2005) Modulation instability of stokes wave - Freak wave. JETP Lett 81(6):255–259

Dyachenko AI (2005) Instability in the numeric models of free surface hydrodynamics. In: International conference on Frontiers of Nonlinear Physics, St.Petersburg-Nizhny Novgorod, Russia, 2–9 August 2005

Dysthe KB (1979) Note on a modification to the nonlinear Schrodinger equation for application to deep water waves. Proc R Soc Lond
Ser A 369:105–114

Earle MD (1975) Extreme wave conditions during Hurricane Camille. J Geophys Res 80:377–379

Feir JE (1967) Discussion: Some results from wave pulse experiments. Proc R Soc Lond A 299:54–58

Gerber M (1987) The Benjamin-Feir instability of a deep water s
tokes wave packet in the presence of a non-uniform medium. J Fluid Mech 176:311–332

Gerber M (1993) The interaction of deep water gravity waves and an annular current: Linear theory. J Fluid Mech 248:153–172

Grundlingh ML (1994) Evidence of surface wave enhancement in the southwest Indian Ocean from satellite altimetry. J. Geophys. Res. 99:7917–7927

Gutshabash YS, Lavrenov IV (1986) Swell transformation in the Cape Agulhas current. Izv Atmos Ocean Phys 22 494–497

Henderson KLD, Peregrine DH, Dold JW (1999) Unsteady water wave modulations: Fully nonlinear solutions and comparison with nonlinear Schrodinger equation. Wave Motion 29:341–361

Irvine DE, Tilley DG (1988) Ocean wave directional spectra and wave-current interaction in the Agulhas from the shuttle imaging radar-B synthetic aperture radar. J Geophys Res 93:15389–15401

Kharif C, Pelinovsky E (2003) Physical mechanisms of the rogue wave phenomena. Eur J Mech B: Fluids 22:603–634

Lavrenov IV (1998) The wave energy concentration at the Agulhas current of South Africa. Nat Hazards 17:117–127

Lighthill M.J. (1965) Contribution to the theory of waves in nonlinear dispersive systems. J Inst Math Appl 1:269–306

Majda A, McLaughlin D, Tabak A (1997) one-dimensional model for dispersive wave turbulence. J Nonlinear Sci 7:9–44

Mallory JK (1974) Abnormal waves on the south-east of South Africa. Inst Hydrog Rev 51:89–129

Meison D, Orzag S, Izraely M (1981) Applications of numerical conformal mapping. J Comput Phys 40:345–360

Mori N, Liu PC, Yasuda T (2002) Analysis of freak wave measurements in the sea of Japan. Ocean Eng 29:41399–41414

Nalimov VI (1974) The Cauchy-Poisson problem. (Russian) Dinamika Sploshnoi Sredy, Vyp. 18. Dinamika Zidkost. so Svobod Granicami:104–210

Onorato M, Osborne AR, Serio M, Damiani T (2001) Occurence of freak waves from envelope equation in random ocean wave simulations. In: Olagnon M, Athanassoulis GA (eds) Rogue waves 2000: Brest, France, Ifremer,
pp 181–192

Onorato M, Osborne AR, Serio M (2000) The nonlinear dynamics of rogue waves and holes in deep-water gravity wave trains. Phys Lett A 275:386–393

Onorato M, Osborne AR, Serio M, Bertone S (2001) Freak waves in random oceanic sea states. Phys Rev Lett 86:5831–5834

Onorato M, Osborne AR, Serio M (2002) Extreme wave events in directional, random oceanic sea states. Phys Fluids 14:L25–L28

Ovsyannikov LV (1973) Dinamika sploshnoi sredy, M.A. Lavrent'ev Institute of hydrodynamics Sib. Branch USSR Acad Sci, No.15, pp 104–125

Peregrine DH (1976) Interaction of water waves and currents. Adv Appl Mech 16:9–117

Peregrine DH (1983) Water waves, nonlinear Schrodinger equations and their solutions. J Aust Math Soc B 25:16–43

Peregrine DH, Skyner D, Stiassnie M, Dold N (1988) Nonlinear effects on focused water waves. In: Proceedings of 21th international conference on coastal engineering, vol 1, chap 54, pp 732–742

Sand SE, Hansen NE, Klinting P, Gudmestad OT, Sterndorff MJ (1990) Freak wave kinematics. In: Torum A, Gudmestad OT (eds) Water wave kinematics, Kluwer, Dodrecht, pp 535–549

Shamin RV (2006) On the existence of smooth solutions to the Dyachenko equations governing free-surface unsteady ideal fluid flows. Doklady Math 73(1):112–113

Smith, R. Giant waves, Fluid Mech. 77 (1976), 417–431

Song J, Banner ML (2002) On determining the onset and strength of breaking for deep water waves: Part 1. Unforced irrotational wave groups. J Phys Oceanogr 32:2541–2558

Tanaka M (1990) Maximum amplitude of modulated wavetrain. Wave Motion 12:559–568

Taylor G (1950) The Instability of liquid surfaces when accelerated in a direction perpendicular to their Planes. I. Proc R Soc Lond A 201:192–196

Trulsen K, Dysthe KB (1996) A modified nonlinear Schrodinger equation for broader bandwidth gravity waves on deep water. Waves Motion 24:281–289

Trulsen K, Dysthe KB (1997) Freak waves – A three-dimensional wave simulation. In: Proceedings of 21st symposium on naval hydrodynamics, 1997, pp 550–558 http://www.nap.edu/books/0309058791/html/550.html

Trulsen K (2001) Simulating the spatial evolution of a measured time series of a freak wave. In: Olagnon M, Athanassoulis GA (eds) Rogue waves 2000: Brest, France, November 2000, Ifremer, pp 265–274

Trulsen K, Kliakhandler I, Dysthe KB, Velarde MG (2000) On weakly nonlinear modulation of waves on deep water. Phys Fluids 12:2432–2437

West B, Brueckner K, Janda R, Milder D, Milton R (1987) A new numerical method for surface hydrodynamics. J Geophys Res C 92(11):11803–11824

White BS, Fornberg B (1998) On the chance of freak waves at sea. J Fluid Mech 355:113–138

Zakharov VE (1967) Stability of nonlinear waves in dispersive media. J Teor Prikl Fiz 51 (1966) 668–671 (in Russian); Sov Phys JETP 24:455–459

Zakharov VE (1968) Stability of periodic waves of finite amplitude on a surface of deep fluid. J Appl Mech Tech Phys 9:190–194

Zakharov VE, Shabat AB (1972) Exact theory of two-dimensional self-focusing and one-dimensional self-modulation of waves in nonlinear media. Sov Phys JETP 34:62–69

Zakharov VE, Kuznetsov EA (1998) Optical solitons and quasisolitons. JETP 86:1035–1046

Zakharov VE, Dyachenko AI, Vasilyev OA (2002) New method for numerical simulation of non-stationary potential flow of incompressible fluid with a free surface. Eur J Mech B Fluids 21:283–291

Zakharov VE, Dias F, Pushkarev AN (2004) One-dimensional wave turbulence. Phys Rep 398: 1–65

Rogue Waves in Higher Order Nonlinear Schrödinger Models

Annalisa Calini and Constance M. Schober

Abstract We discuss physical and statistical properties of rogue wave generation in deep water from the perspective of the focusing Nonlinear Schrödinger equation and some of its higher order generalizations. Numerical investigations and analytical arguments based on the inverse spectral theory of the underlying integrable model, perturbation analysis, and statistical methods provide a coherent picture of rogue waves associated with nonlinear focusing events. Homoclinic orbits of unstable solutions of the underlying integrable model are certainly candidates for extreme waves, however, for more realistic models such as the modified Dysthe equation two novel features emerge: (a) a chaotic sea state appears to be an important mechanism for both generation and increased likelihood of rogue waves; (b) the extreme waves intermittently emerging from the chaotic background can be correlated with the homoclinic orbits characterized by maximal coalescence of their spatial modes.

1 Introduction

Among the various mechanisms for wave amplification under different physical conditions, the Benjamin–Feir (BF) instability and nonlinear self-focusing are often proposed in relation to rogue wave generation in deep water. In particular, the work of Henderson et al. (1999) suggests that excitation of certain breather-like solutions of the focusing nonlinear Schrödinger (NLS) equation

$$\mathrm{i}u_t + u_{xx} + 2|u|^2 u = 0, \tag{1}$$

A. Calini
Department of Mathematics, College of Charleston, Charleston, SC 29424, USA
calinia@cofc.edu

C.M. Schober
Department of Mathematics, University of Central Florida, Orlando, FL 32816, USA
cschober@mail.ucf.edu

E. Pelinovsky, C. Kharif (eds.) *Extreme Ocean Waves*, 31–51.

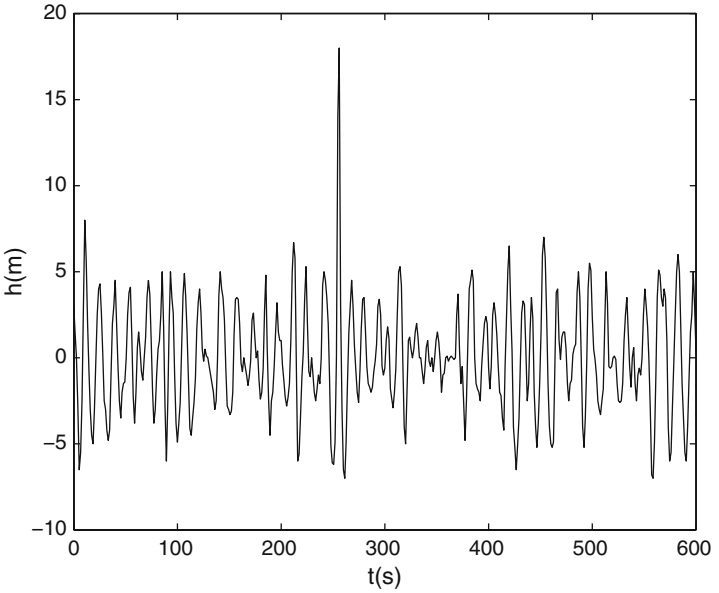

Fig. 1 Time series of the surface elevation of the 1995 New Year Wave Event

triggers the formation of rogue waves. Trulsen and Dysthe's analysis (Trulsen and Dysthe 1997a) of the sea state during the famous New Year Wave event recorded at the North Sea Draupner Platform in 1995 (see Fig. 1) shows a weakly nonlinear wave train with a relatively narrow frequency bandwidth, thus supporting the use of the focusing NLS equation as a basic model for studying rogue waves in deep water.

A stability analysis of solutions of the NLS equation shows that low frequency modes may become unstable and that the number of unstable modes increases with the amplitude of the carrier wave. Homoclinic orbits of unstable NLS solutions, including those of an unstable Stokes wave, exhibit many of the properties observed in rogue waves (Osborne 2000; Calini and Schober 2002; Karjanto 2006). However, generic homoclinic orbits of unstable solutions of the NLS equation are unlikely to be physically observable in more realistic models of deep water wave dynamics (for example, those described by higher order generalizations of the NLS equation). It is thus important to develop criteria for rogue wave formation for general sea states, to investigate whether proximity to unstable solutions of the integrable model can be correlated to rogue wave generation, and to determine the robustness of the homoclinic orbits under physically meaningful perturbations.

A more realistic description of deep water wave dynamics is provided by the modified Dysthe (MD) equation,

$$\begin{aligned} &\mathrm{i}u_t + u_{xx} + 2|u|^2 u + \mathrm{i}\varepsilon^{1/2}\left(\frac{1}{2}u_{xxx} - 6|u|^2 u_x + u^2 u_x^* - 2u\mathrm{i}\left[H\left(|u|^2\right)\right]_x\right) \\ &\quad + \varepsilon\,\frac{5}{16}u_{4x} + \mathrm{i}\varepsilon^{3/2}\,\frac{7}{32}u_{5x} = 0, \end{aligned}$$

introduced by Trulsen and Dysthe (1996, 1997a) by retaining higher order terms in the asymptotic expansion of the surface wave displacement. (Here $H(f)$ denotes the Hilbert transform of the function f.)

Laboratory experiments conducted in conjunction with numerical simulations by the Schober and her collaborators (Ablowitz et al. 2000, 2001), established that, for higher order generalizations of the NLS equations, the generic long-time dynamics of initial data near an unstable Stokes wave with two unstable modes is chaotic. Further numerical investigations of the MD equation revealed that for a general class of such initial data, high amplitude coherent structures arise intermittently above the chaotic background (Calini and Schober 2002). Remarkably, these emerging coherent structures are structurally similar to maximal homoclinic orbits of the unperturbed Stokes wave with coalesced spatial phases (which are also the homoclinic orbits of maximal amplitude). Such optimally phase modulated homoclinic solutions of the NLS equation appear to be the only homoclinic solutions which persist under perturbations, their persistence being independent of phase selection of the initial conditions (Calini and Schober 2002; Schober 2006). In other words, a chaotic sea state due to proximity to unstable NLS solutions appears to increase the occurrence of rogue waves, enhance focusing effects, and select, among homoclinic solutions, those that are good candidates for modeling physically observable rogue waves.

To analyze this phenomenon in more detail, we regard the MD equation as a perturbation of the NLS equation. A combination of tools from the integrable theory of the NLS equation, and a formal extension of the Melnikov method for perturbations of Hamiltonian systems with homoclinic structures are used to address both structural and statistical properties of the observed rogue waves.

In Sect. 2, we review elements of the periodic theory for the integrable NLS equation, the analytical construction of homoclinic solutions (from low-dimensional to maximal homoclinic manifolds) of the unstable Stokes wave, and discuss wave amplification due to phase coalescence, as well as the relation between phase singularities, wave compression, and wave amplification.

In Sect. 3, we study the effects of homoclinic chaos on rogue wave generation, and discuss numerical simulations of the MD equation (8) and its restriction to spatially symmetric wave trains (see e.g. Fig. 5b.) "Noisy" rogue waves emerge intermittently above a chaotic background: we discuss how the likelihood of rogue wave occurrence as well as wave focusing are found to increase in the chaotic regime.

In Sect. 4, we present a formal Melnikov-type calculation aimed at explaining the persistence of optimally phase modulated homoclinic orbits during the perturbed chaotic dynamics. These persisting coherent structures are thus natural candidates for the physically observable rogue waves.

The remaining sections use a statistical approach (in combination with the periodic theory of the integrable NLS), to develop a criterion for rogue wave prediction, and a statistical description of rogue waves associated with homoclinic chaos in both the NLS and MD models.

In Sect. 5, we discuss rogue wave generation for random sea states characterized by the Joint North Sea Wave Project (JONSWAP) power spectrum. The JONSWAP

spectrum was introduced to describe developing sea states with ongoing nonlinear wave–wave interactions (Ochi 1998; Bridges and Derks 1999). A spectral quantity, the "splitting distance" between simple periodic points of the Floquet spectrum of an initial condition in a neighborhood of an unstable NLS solution, is proposed as a measurement of the proximity in spectral space to unstable waves and homoclinic data. For regimes in which few (two or three) unstable modes are present, hundreds of realizations of JONSWAP type initial data show that, in both the pure NLS and the MD models, rogue waves develop for small splitting distance, and do not develop when the splitting distance is large (Islas and Schober 2005).

In the final section, a statistical interpretation of rogue waves in both the NLS and MD equations is provided. Using the third and fourth statistical moments of the wave elevation for sea states characterized by JONSWAP spectra with random phases, we examine dependence of skewness, kurtosis, and likelihood of rogue waves on the proximity to unstable waves and homoclinic data. Extensive numerical studies reveal that wave strength, skeweness, and kurtosis all increase as the spectral splitting distance decreases, thus supporting the claim that modulational instability is not only an important mechanism for rogue wave generation, but also a significant source of non-Gaussianity in the water wave statistics. Finally, consistent with the numerical and analytical studies described in the first part of this chapter, statistically, the NLS equation appears to under predict, as compared to the MD equation, both the strength and likelihood of rogue waves.

2 Background

As is well-known, the nonlinear Schrödinger (NLS) equation is equivalent to the solvability condition of the AKNS system, the pair of first-order linear systems (Zakharov and Shabat 1972):

$$\mathcal{L}^{(x)}\phi = 0, \qquad \mathcal{L}^{(t)}\phi = 0 \tag{2}$$

for a vector-valued function ϕ. The linear operators on the left-hand sides of (2) are

$$\mathcal{L}^{(x)} = \begin{pmatrix} \partial_x + \mathrm{i}\lambda & -u \\ u^* & \partial_x - \mathrm{i}\lambda \end{pmatrix}, \quad \mathcal{L}^{(t)} = \begin{pmatrix} \partial_t + \mathrm{i}(2\lambda^2 - |u|^2) & -2\lambda u - \mathrm{i}u_x \\ 2\lambda u^* - \mathrm{i}u_x^* & \partial_t - \mathrm{i}(2\lambda^2 - |u|^2) \end{pmatrix},$$

and depend on x and t through the NLS potential u and on the *spectral parameter* λ.

The nonlinear spectral decomposition of an NLS initial condition (or in general of an ensemble of JONSWAP initial data) is based on the inverse spectral theory of the NLS equation. For periodic boundary conditions $u(x+L,t) = u(x,t)$, the Floquet spectrum associated with an NLS potential u (i.e. the spectrum of the linear operator $\mathcal{L}^{(x)}$ at u) can be described in terms of the *Floquet discriminant* of u, defined as the trace of the transfer matrix of a fundamental matrix solution Φ of (2) over the interval $[0,L]$ (Ablowitz and Segur 1981):

$$\Delta(u;\lambda) = \text{Trace}\left(\Phi(x,t;\lambda)^{-1}\Phi(x+L,t;\lambda)\right).$$

Then, the Floquet spectrum is defined as the region

$$\sigma(u) = \{\lambda \in \mathbb{C} \,|\, \Delta(u;\lambda) \in \mathbb{R}, -2 \leq \Delta \leq 2\}.$$

Points of the *continuous spectrum* of u are those for which the eigenvalues of the transfer matrix have unit modulus, and therefore $\Delta(u;\lambda)$ is real and between 2 and -2; in particular, the real line is part of the continuous spectrum. Points of the L-periodic/antiperiodic *discrete spectrum* of u are those for which the eigenvalues of the transfer matrix are ± 1, equivalently $\Delta(u;\lambda) = \pm 2$. Points of the discrete spectrum which are embedded in a continuous band of spectrum have to be critical points for the Floquet discriminant (i.e., $\mathrm{d}\Delta/\mathrm{d}\lambda$ must vanish at such points).

Since the transfer matrix only changes by conjugation when we shift in x or t, Δ is independent of those variables. An important consequence of this observation is that the Floquet discriminant is invariant under the NLS flow, and thus encodes an infinite family of constants of motion (parametrized by λ).

The continuous part of Floquet spectrum of a generic NLS potential consists of the real axis and of complex bands terminating in *simple points* λ_j^s (at which $\Delta = \pm 2, \Delta' \neq 0$). The *N-phase potentials* are those characterized by a finite number of bands of continuous spectrum (or a finite number of simple points). Figure 2 shows the spectrum of a typical N-phase potential: complex critical points (usually *double points* of the discrete spectrum for which $\Delta' = 0$ and $\Delta'' \neq 0$), such as the one appearing in the figure, are in general associated with linear instabilities of u and label its homoclinic orbits (Ercolani et al. 1990). Figure 8a shows spectrum of an N-phase potential near the one shown in Fig. 2: the complex double point has split into a pair of simple points; such a potential possesses no linear unstable modes (simple points and real double points are in general associated with neutrally stable modes).

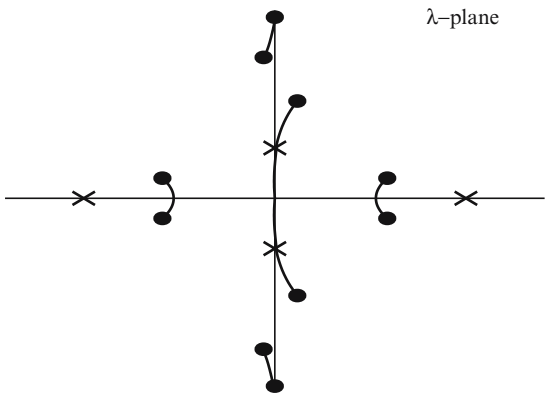

Fig. 2 Spectrum of an unstable N-phase solution. The simple periodic eigenvalues are labeled by *circles* and the double points by *crosses*

2.1 Homoclinic Solutions of the NLS Equation as Candidates for Rogue Waves

Modulationally unstable solutions of the NLS equation (e.g., N-phase solutions whose Floquet spectra have complex double points) have homoclinic orbits that can undergo large amplitude excursions away from their target solution. Such homoclinic orbits can be used as models of rogue waves.

An important (and the simplest) example of unstable NLS solution is the *plane* (or *Stokes*) *wave* potential

$$u_a(x,t) = a\mathrm{e}^{2\mathrm{i}a^2 t}. \tag{3}$$

Elementary Fourier analysis shows that the plane wave is unstable when its amplitude a is sufficiently large: in fact, for $0 < \pi n/L < a$, the solution of the linearized NLS equation about u_a has M linearly unstable modes (UMs) $\mathrm{e}^{\sigma_n t + 2\pi n x/L}$ with growth rates σ_n given by

$$\sigma_n^2 = \mu_n^2(\mu_n^2 - 4a^2), \quad \mu_n = 2\pi n/L,$$

where M is the largest integer satisfying $0 < M < aL/\pi$.

One can also check (see e.g., Calini and Schober 2002) that for $0 < \pi n/L < 0$ the Floquet spectrum of the plane wave potential u_a has exactly M complex double points, each "labelling" an associated unstable mode.

Using Bäcklund transformations (McLaughlin and Schober 1992; Matveev and Salle 1991) one can in principle construct the family of homoclinic orbits of an unstable NLS potential. In fact, this method gives explicit formulas for homoclinic orbits of N-phase solutions, although their expressions become rather complicated for $N > 2$. For NLS potentials with several unstable modes, iterated Bäcklund transformations will generate their entire stable and unstable manifolds, comprised of homoclinic orbits of increasing dimension up to the dimension of the invariant manifolds. Such higher-dimensional homoclinic orbits associated with two or more UMs are also known as *combination* homoclinic orbits.

A single (i.e., lowest dimensional) homoclinic orbit of the plane wave potential is given by

$$u(x,t) = a\mathrm{e}^{-2\mathrm{i}a^2 t}\,\frac{1 + 2\cos(px)\mathrm{e}^{\sigma_n t + 2\mathrm{i}\phi + \rho} + A\mathrm{e}^{2\sigma_n t + 4\mathrm{i}\phi + 2\rho}}{1 + 2\cos(px)\mathrm{e}^{\sigma_1 t + \rho} + A\mathrm{e}^{2\sigma_n t + 2\rho}}, \tag{4}$$

where $A = 1/\cos^2\phi$, $\sigma_n = \pm p\sqrt{4a^2 - p^2}$, $\phi = \sin^{-1}(p/2a)$, and $p = \mu_n = 2\pi n/L < a$ for some integer n. Each UM has an associated homoclinic orbit characterized by the mode $p = \mu_n$.

Figure 3 shows the space–time plot of the amplitude $|u(x,t)|$ of a homoclinic orbit with one UM, for $a = 0.5$, $L = 2\sqrt{2}$ and $p = 2\pi/L$. As $t \to \pm\infty$, (4) limits to the plane wave potential; in fact, the plane wave behavior dominates the dynamics of the homoclinic solution for most of its lifetime. As t approaches $t_0 = 0$, nonlinear focusing occurs due to the BF instability and the solution rises to a maximum height

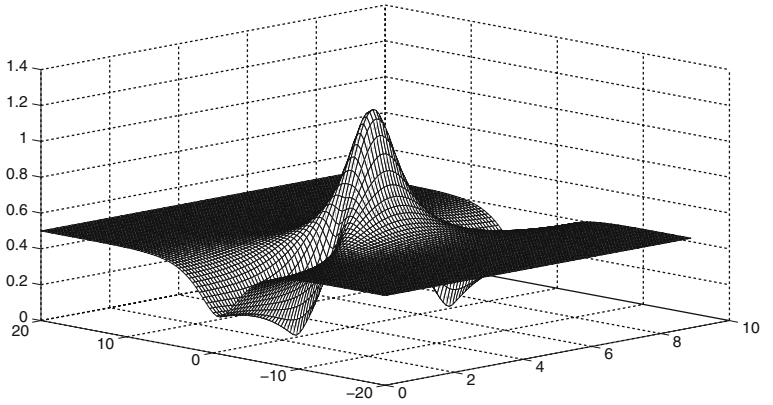

Fig. 3 Analytical rogue wave solution of the NLS corresponding to one UM

of $2.4a$. Thus, the homoclinic solution with one UM can be regarded as the simplest model of rogue wave.

An almost equally dramatic wave trough occurs close to the crest of the rogue wave as a result of wave compression due to wave dislocation. The amplitude amplification factor is given by

$$f = \frac{\max_{x\in[0,L],\,t\in\mathbb{R}}|u(x,t)|}{\lim_{t\to\pm\infty}|u(x,t)|} \approx 2.4. \tag{5}$$

In general, f depends upon the wavenumber of the modulation. As the wave number decreases, the amplification factor increases to the limiting value

$$f_{\max} = \lim_{\kappa\to 0^+} f(\kappa) = 3, \tag{6}$$

although the waves take longer to reach their maximum height since their growth rate is smaller (Akhmediev et al. 1988).

2.2 Phase Modulated Rogue Waves

As the number of UMs increases, the space–time structure of the homoclinic solutions becomes more complex. When two or more UMs are present the initial wave train can be phase modulated to produce additional focusing.

The family of homoclinic orbits of the plane wave potential with two UMs is given by an expression of the form

$$u(x,t) = a\mathrm{e}^{2\mathrm{i}a^2t}\,\frac{g(x,t)}{f(x,t)}, \tag{7}$$

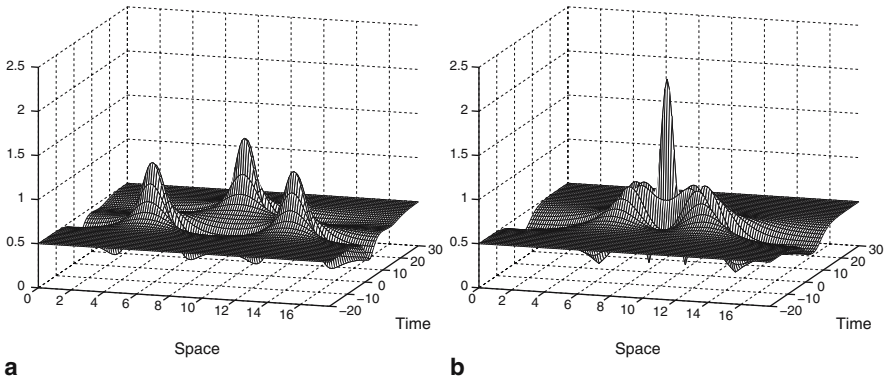

Fig. 4 Rogue wave solutions of the NLS corresponding to two unstable modes (**a**) without phase modulation ($\rho = -1$) and (**b**) with phase modulation ($\rho = -0.65$)

where the expression for $f(x,t)$ and $g(x,t)$ depend on the two spatial modes $\cos(2n\pi x/L)$, $\cos(2m\pi x/L)$, and on temporal exponential factors $\exp(\sigma_n t + \rho_n)$, $\exp(\sigma_m t + \rho_m)$, with growth rates $\sigma_l = \mu_l\sqrt{\mu_l^2 - 4a^2}$, $\mu_l = 2\pi l/L$. (The complete formulas can be found in Calini et al. (1996); Calini and Schober (2002).)

As in the one-UM case, this combination homoclinic orbit decays to the plane wave potential as $t \to \pm\infty$, and the associated rogue wave remains hidden beneath the background plane wave for most of its lifetime. The temporal separation of the two spatial modes depends upon a parameter ρ related to the difference $\rho_n - \rho_m$ in the temporal phases (Calini et al. 1996; Calini and Schober 2002).

In turn, ρ affects the amplitude amplification factor. Figure 4a, b shows the combination homoclinic orbit (7) obtained with all parameters set equal except for ρ. In Fig. 4a, $\rho = 0.1$, the modes are well separated, and the amplitude amplification factor is roughly 3. In Fig. 4b, the value of ρ is approximately -0.65, corresponding to the two UMs being simultaneously excited or coalesced. At such ρ-value the amplitude amplification factor is maximal and the rogue wave rises to a height of 4.1 times the height of the carrier wave (whose maximum height is 2.1).

Note that Fig. 4a shows focusing due to only weak amplitude modulation of the initial wave train; the growth in amplitude beginning at $t \approx -5$ and at $t \approx 10$ is due to the BF instability. However, in Fig. 4b focusing due to both amplitude and phase modulation occurs. The amplitude growth at $t \approx -5$ is due to the BF instability, while the additional very rapid focusing at $t \approx 3.4$ is due to the phase modulation. In general, it is possible to select the phases in a combination homoclinic orbit with N spatial modes so that any number n ($2 \le n \le N$) of modes coalesce at some fixed time.

3 Noisy Rogue Waves

The broad bandwidth modified NLS equation was introduced by Trulsen and Dysthe as a higher order asymptotic approximation of slowly modulated periodic wave trains in deep water, assuming that the wave slope ka (where k is the wave number, and a the size of the initial displacement) is $\mathcal{O}(\varepsilon)$, while the bandwidth $|\Delta k|/k$ and the quantity $(kh)^{-1}$ (where h is the water depth) are $\mathcal{O}(\varepsilon^{1/2})$. The resulting MD equation

$$\begin{aligned} &\mathrm{i}u_t + u_{xx} + 2|u|^2 u + \mathrm{i}\varepsilon^{1/2}\left(\frac{1}{2}u_{xxx} - 6|u|^2 u_x + u^2 u_x^* - 2u\mathrm{i}\left[H\left(|u|^2\right)\right]_x\right) \\ &\quad + \varepsilon\,\frac{5}{16}u_{4x} + \mathrm{i}\varepsilon^{3/2}\,\frac{7}{32}u_{5x} = 0, \end{aligned} \tag{8}$$

is the starting point of our numerical experiments, aimed at investigating the robustness of homoclinic solutions of the NLS equation, as well as the likelihood of rogue wave generation, when higher order terms are introduced in the wave dynamics.

We choose initial data for solutions with two and three UMs; for example, in the two-UM regime, the initial condition has the form

$$u(x,0) = a\left[1 + 4\mathrm{i}\left(\varepsilon_1 \sin\phi_1 \mathrm{e}^{\mathrm{i}\phi_1}\cos\left(\frac{2\pi x}{L}\right) + \varepsilon_2 \sin\phi_2 \mathrm{e}^{\mathrm{i}\phi_2}\cos\left(\frac{4\pi x}{L}\right)\right)\right],$$

where the parameters ϕ_i's are varied to explore a neighborhood of the unstable plane wave potential.

Figure 5a illustrates a striking rogue wave solution of (8) for $\varepsilon_1 = 10^{-4}$ and $\varepsilon_2 = 10^{-5}$. The solution rapidly becomes chaotic (around $t = 31$) and exhibits an irregular dynamics for a long time afterwards. At $t \approx 471.2$ a rogue wave rises from the plane wave state, developing a crest of amplitude approximately equal to four times the background wave height. The structure of this rogue wave is remarkably

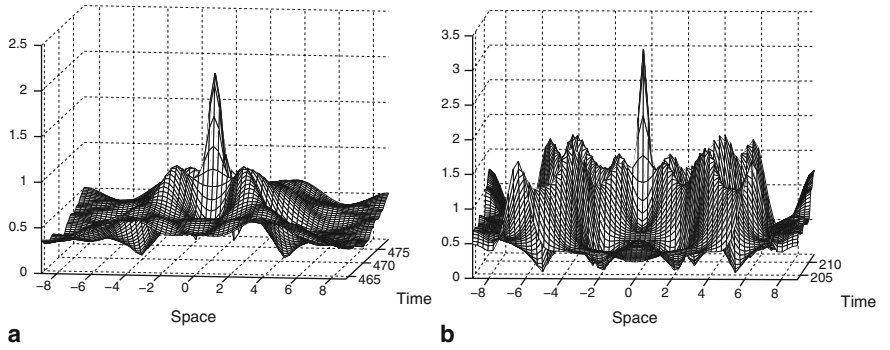

Fig. 5 Rogue waves solutions for the even MD equation when (**a**) two and (**b**) three unstable modes are present

similar to that of the combination homoclinic solution (7) with coalesced spatial modes obtained when $\rho = -0.65$. (Compare Fig. 5a with Fig. 4b.)

Numerical simulations of the MD equation in the three-UM regime show a similar phenomenon: after the onset of chaotic dynamics, rogue waves rise intermittently above the chaotic background (see Fig. 5b). At $t \approx 208$ a rogue wave develops with a wave amplitude amplification factor of almost five. Again, the emerging rogue wave is close to the optimally phase modulated NLS homoclinic solution in the three-UM regime.

Extensive numerical experiments were performed for both the full MD model and its restriction to spatially even potentials (see Sect. 4) in the two- and three-UM regime, varying both perturbation strength ε and the values of the parameters ϕ_is in the initial data. In all cases, the coalesced homoclinic NLS solution emerges generically as a structurally stable feature of the perturbed dynamics.

We observe how the chaotic regime produces additional focusing by effectively selecting optimal phase modulation, and how the chaotic dynamics singles out the maximally coalesced homoclinic solutions of the unperturbed NLS equation as physically observable rogue waves. Moreover, (see e.g., Fig. 5) larger amplitude waves, and more of them, are obtained for the MD equation, as also supported by the diagnostics developed in Sect. 5, correlating wave strengths in the NLS and MD models to proximity to homoclinic data. Thus, the underlying chaotic dynamics of the MD equation appears to increase the likelihood of rogue wave generation and to favor occurrence of large amplitude rogue waves, as compared to predictions obtained from the NLS equation.

4 Melnikov Analysis

To better understand the emergence of the coalesced homoclinic orbit in the chaotic dynamics described by the MD equation, we use perturbation methods to construct appropriate measurements of the splitting distance of the stable and unstable manifolds of a plane wave solution with two unstable modes. In this section, we briefly describe the main ingredients of the ensuing Melnikov analysis; the reader is referred to Calini and Schober (2002) for full details.

We consider the following restriction of the MD equation to spatially even potentials $u(x,t) = u(-x,t)$:

$$\mathrm{i}u_t + u_{xx} + 2|u|^2 u = \varepsilon u_{xxxx}. \tag{9}$$

Equation (9) can be regarded as a Hamiltonian dynamical system on an appropriate Sobolev space of even, periodic functions, with Hamiltonian functional $H_\varepsilon(u) = \int_0^L (|u_x| - |u|^4 - \varepsilon |u_{xx}|^2)\,\mathrm{d}x$, and an additional conserved functional given by the L^2-norm $I(u) = \int_0^L |u|^2\,\mathrm{d}x$.

For $\varepsilon = 0$, we consider a plane wave potential u_a with two UMs (equivalently, with two complex double points): linear analysis shows that u_a possesses two-dimensional stable and unstable eigenspaces and an infinite number of center modes (characterized by complex conjugate pairs of imaginary eigenvalues). Its center-stable and center-unstable invariant manifolds coincide and have codimension 2. (In fact, they are explicitly parametrized in terms of the homoclinic solution (7).)

When $\varepsilon \neq 0$, the plane wave potential persists as a solution of the perturbed equation, and its perturbed center-stable and center-unstable manifolds generically split. In finite-dimensional situations, invariant manifolds of unstable solutions can split under perturbation and intersect transversally. Such transversal intersections are often associated with chaotic behavior and with persistence of homoclinic orbits in the perturbed system. For PDEs the analogous situation is far more subtle, and rigorous analysis has been performed only in a handful of cases (Haller and Wiggins 1992; Li et al. 1996; Zeng 2000; Cai et al. 1995).

If we assume that the perturbed invariant manifolds split transversally, we need two independent measurements for their splitting distance (one for each direction transversal to the unperturbed invariant manifold). However, the perturbation is Hamiltonian, so the splitting occurs within the codimension 1 energy surface $H_\varepsilon = \text{const.}$, thus reducing the number of measurements to 1.

To define suitable measurements, we recall how the Floquet discriminant $\Delta(u;\lambda)$ of an NLS solution u, viewed as a functional on the NLS phase space, encodes an infinite family of constants of motion (Li and McLaughlin 1994). Given a solution u_c with a purely imaginary critical point λ^c (such as, for example, an unstable plane wave potential), regarding λ^c as a functional on a neighborhood $\mathcal{U}$ of u_c, the functional $F : \mathcal{U} \to \mathbb{C}$,

$$\boldsymbol{F}(u) := \Delta(\lambda^c(u);u) \tag{10}$$

is locally smooth, provided $\dfrac{\mathrm{d}^2\Delta}{\mathrm{d}\lambda^2}(\lambda,u) \neq 0\,, \forall\, u \in \mathcal{U}$. Then, the sequence

$$F_j(u) = \Delta(\lambda_j^c(u),u),$$

generated as λ_j^c varies among the critical points of the potential u, defines a natural family of constants of motion, which identify the critical level sets of u by labelling them in terms of the double points of its Floquet spectrum.

One of the main advantages of this representation of the constants of motion of the NLS equation is that the gradient of F_j can be explicitly expressed in terms of solutions of the AKNS system by means of the following remarkable formula (Li and McLaughlin 1994):

$$\frac{\delta F_j}{\delta \mathbf{u}}(u) = \mathrm{i}\frac{\sqrt{\Delta^2-4}}{W[\psi^+,\psi^-]} \left[\begin{array}{c} \psi_2^+\psi_2^- \\ -\psi_1^+\psi_1^- \end{array}\right]\Bigg|_{\lambda=\lambda^c}. \tag{11}$$

In (11), $\mathbf{u} = (u,u^*)$, $\psi^\pm(x,\lambda)$ are the Bloch eigenfunctions (common eigenfunctions of the operator $\mathcal{L}^{(x)}$ and the shift operator $(\mathcal{S}\psi)(x) = \psi(x+L)$), and W denotes the Wronskian.

We observe that $\delta F_j/\delta \mathbf{u}$ vanishes at a critical potential u_c (such as the plane wave solution), reflecting the fact that F_j is critical along the critical level set. On the other hand, if u_h is a homoclinic orbit of u_c, then $\delta F_j/\delta \mathbf{u}(u_h) \neq 0$; therefore $\delta F_j/\delta \mathbf{u}\,(u^h)$, $j = 1, \ldots M$, (M being the number of complex double points in the spectrum of u_c) define directions transversal to the homoclinic manifold.

Returning to the even restriction of the MD equation (9), the components of the splitting distance of the perturbed stable and unstable manifolds of a plane wave potential with two UMs along directions ∇F_j, $j = 1, 2$ are expressed in terms of the following Melnikov-type integrals:

$$d_j = \varepsilon M_j(\rho) + \mathcal{O}(\varepsilon^2), \qquad M_j(\rho) = \int_{-\infty}^{+\infty} \langle \nabla F_j, f \rangle \big|_{u=u_h} \, \mathrm{d}t, \tag{12}$$

where $f(\mathbf{u}) = (u_{xxxx}, u^*_{xxxx})$ is the vector of the perturbation, $<\ ,\ >$ is the standard inner product in $L^2([0,L],\mathbb{C})$, and u_h is the homoclinic orbit (7). Both measurements depend on parameter ρ, the same parameter that governs the temporal separation of the spatial modes of the unperturbed homoclinic orbit (7) (see Sect. 2.2).

Consistent with the dimensional count for the splitting distance, numerical evaluation of the two Melnikov integrals show that M_1 and M_2 are mutually proportional functions of the parameter ρ (i.e., a single measurement is sufficient). Figure 6 shows existence of a unique nondegenerate zero of M_1, suggesting that a transversal homoclinic structure persists under perturbation.

A truly remarkable fact, is that the nondegenerate zero of $M_1(\rho)$ coincides (up to order ε) with the value of ρ at which the two spatial modes of the homoclinic solution (7) coalesce, producing a homoclinic orbit of maximal amplitude. The same structure is observed as the recurring structurally stable feature of the chaotic dynamics. (see Fig. 5)

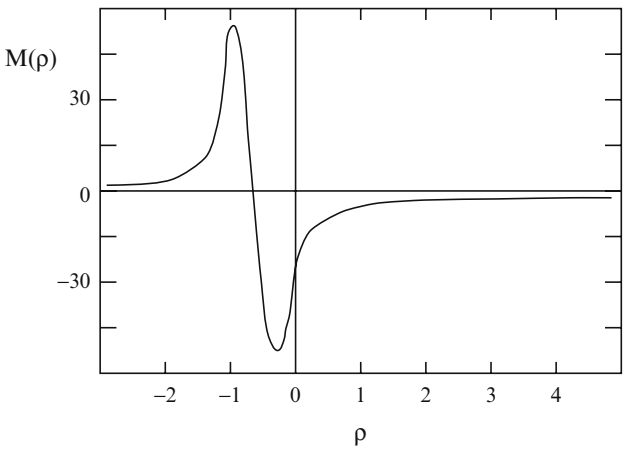

Fig. 6 Graph of the Melnikov integral M_1 as a function of parameter ρ. A transversal zero occurs at $\rho = -0.65$

A study of the analytical structure of single and combination homoclinic orbits, together with the numerical experiments and the Melnikov analysis, supports the following:

- Although homoclinic solutions of the NLS equation have many of the features of rogue waves, not all can be regarded as good candidates for modeling actual rogue waves, as not all are robust under perturbations that lead to more accurate physical models.
- For sea states characterized by a finite number of unstable modes, the homoclinic solutions that are robust under perturbation are the combination homoclinic orbits (1) with a maximal number of spatial modes excited (this should not be a surprise, since the lower-dimensional homoclinic solutions are linear unstable); and (2) for which the spatial modes are optimally coalesced.
- A chaotic sea state enhances the occurrence of rogue waves. One should note that a homoclinic solution of the NLS will rise over the background wave only once in its life time and for a relative brief time. However, in a chaotic evolution, the maximally coalesced homoclinic orbit will occur repeatedly, although in an unpredictable fashion.

5 Random Oceanic Sea States and the Proximity to Homoclinic Data

To study the generation of rogue waves in a random sea state, we consider initial data for the surface elevation to be of the form (Onorato 2001)

$$\eta(x,0) = \sum_{n=1}^{N} C_n \cos(k_n x - \phi_n), \tag{13}$$

where $k_n = 2\pi n/L$ and the random phases ϕ_n are uniformly distributed on $(0, 2\pi)$ and the spectral amplitudes, $C_n = \sqrt{2S(f_n)/L}$, are obtained from the JONSWAP spectrum (Ochi 1998):

$$S(f) = \frac{\alpha g^2}{(2\pi f)^5} \exp\left[-\frac{5}{4}\left(\frac{f_0}{f}\right)^4\right] \gamma^r, \qquad r = \exp\left[-\frac{1}{2}\left(\frac{f-f_0}{\sigma_0 f_0}\right)^2\right]. \tag{14}$$

Here f is spatial frequency, $f_n = k_n/2\pi$, f_0 is the dominant frequency, determined by the wind speed at a specified height above the sea surface, g is gravity, and $\sigma_0 = 0.07\ (0.9)$ for $f \le f_0$ $(f > f_0)$. In contrast to physical experiments, which monitor the surface evolution at a given spatial point (probe) in time, here we take time slices and examine the features in space.

JONSWAP spectra describe developing sea states since for $\gamma > 1$ the wave spectra continues to evolve through nonlinear wave-wave interactions for very long times and distances. As γ is increased, the spectrum becomes narrower about the dominant peak (see Fig. 7). In this sense, γ is considered the "peak-shape" parameter.

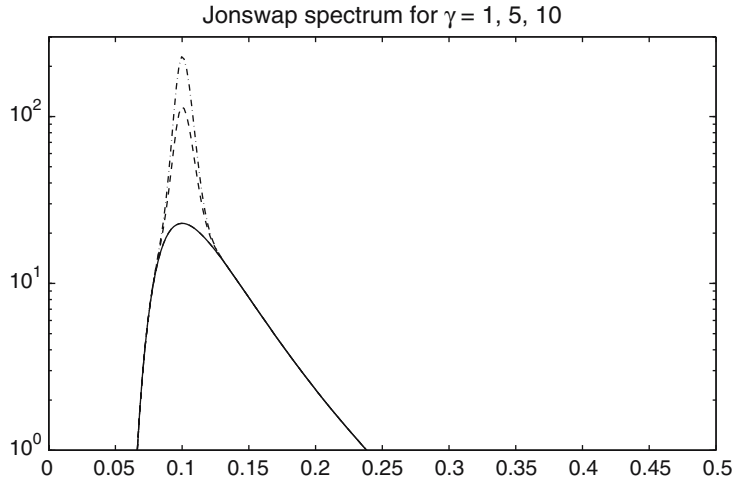

Fig. 7 The JONSWAP spectrum for $\gamma = 1$ (*solid line*), $\gamma = 5$ (*dashed line*), and $\gamma = 10$ (*dash-dot line*) with $f_0 = 0.1$ Hz and $\alpha = 0.0081$

The scale parameter α is related to the amplitude and energy content of the wavefield. Based on an "Ursell number," the ratio of the nonlinear and dispersive terms of the NLS equation (1) in dimensional form, the NLS equation is considered to be applicable for $2 < \gamma < 8$ (Onorato 2001). Typical values of alpha are $0.008 < \alpha < 0.02$.

In the numerical experiments, the NLS and MD equations are integrated using a pseudo-spectral scheme with 256 Fourier modes in space and a fourth-order Runge–Kutta discretization in time ($\Delta t = 10^{-3}$). The nonlinear mode content of the data is numerically computed using the direct spectral transform described above, i.e., the system of ODEs (2) is numerically solved to obtain the discriminant Δ. The zeros of $\Delta \pm 2$ are then determined with a root solver based on Muller's method (Ercolani et al. 1990). The spectrum is computed with an accuracy of $\mathcal{O}(10^{-6})$, whereas the spectral quantities we are interested in range from $\mathcal{O}(10^{-2})$ to $\mathcal{O}(10^{-1})$.

Under perturbation complex double points typically split into two simple points, $\lambda_{\pm}$, thus opening a gap in the band of spectrum (see Fig. 2). We refer to the distance between these two simple points, $\delta(\lambda_+, \lambda_-) = |\lambda_+ - \lambda_-|$, as the splitting distance. As mentioned, homoclinic solutions arise as an appropriate degeneration of a finite gap solution (Its et al. 1988), i.e. when the resulting double point, $\delta(\lambda_+, \lambda_-) \to 0$, is complex. Consequently, we can use δ to measure the proximity in the spectral plane to homoclinic data, i.e. to complex double points and their corresponding instabilities. Since the NLS spectrum is symmetric with respect to the real axis and real double points correspond to inactive modes, in subsequent plots only the spectrum in the upper half complex λ-plane will be displayed.

Our first step is to determine the spectrum of JONSWAP initial data given by (13) for various combinations of $\alpha = 0.008, 0.012, 0.016, 0.02$, and $\gamma = 1, 2, 4, 6, 8$. For each such pair (γ, α), we performed 50 simulations, each with a different set of

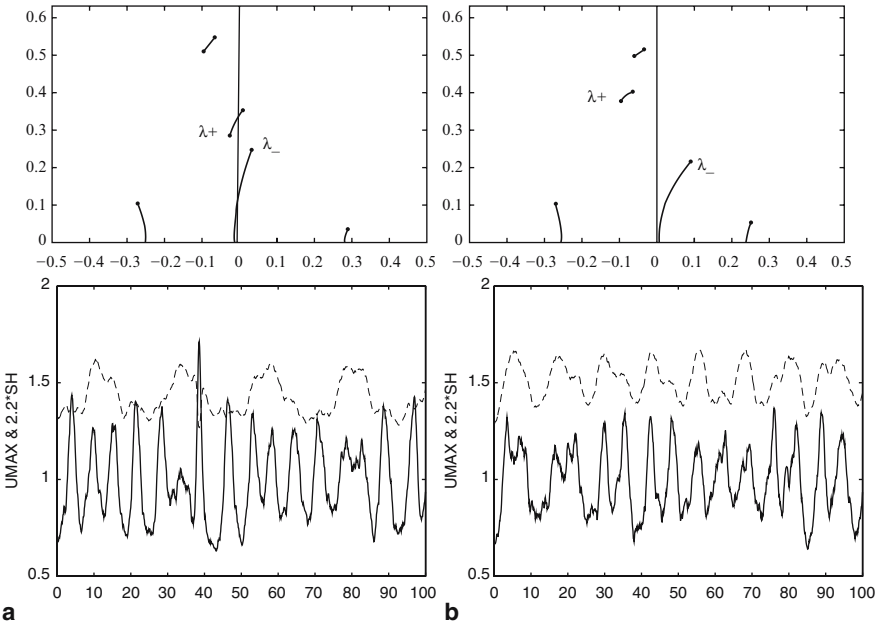

Fig. 8 Spectrum and evolution of $U_{\max}$ (**a**) "near" and (**b**) "far" from homoclinic data

randomly generated phases. As expected, the spectral configuration depends on the energy α and the enhancement coefficient γ. However, the extent of the dependence of features of the spectrum, such as the proximity to complex double points, upon the phases in the initial data is surprising.

Typical examples of the results are given in Fig. 8a, b which shows the numerically computed nonlinear spectrum of JONSWAP initial data when $\gamma = 4$ and $\alpha = 0.016$ for two different realizations of the random phases.

We find that JONSWAP data correspond to "semi-stable" N-phase solutions, i.e. JONSWAP data can be viewed as perturbations of N-phase solutions with one or more unstable modes (compare Fig. 2 with the spectrum of an unstable N-phase solution in Fig. 8). In Fig. 8a the splitting distance $\delta(\lambda_+, \lambda_-) \approx .07$, while in Fig. 8b $\delta(\lambda_+, \lambda_-) \approx .2$. Thus the JONSWAP data can be quite "near" homoclinic data as in Fig. 8a or "far" from homoclinic data as in Fig. 8b, depending on the values of the phases ϕ_n in the initial data. For all the examined values of α and γ we find that, when α and γ are fixed, as the phases in the JONSWAP data are varied, the spectral distance δ of typical JONSWAP data from homoclinic data varies.

Most importantly, irrespective of the values of the JONSWAP parameters α and γ, in simulations of the NLS equation (1) we find that extreme waves develop for JONSWAP initial data that are "near" NLS homoclinic data, whereas the JONSWAP data that are "far" from NLS homoclinic data typically do not generate extreme waves. Figure 8c, d shows the corresponding evolution of the maximum surface elevation, $U_{\max}$, obtained with the NLS equation. $U_{\max}$ is given by the solid curve

and as a reference, $2.2H_S$ (the threshold for a rogue wave) is given by the dashed curve. H_S is the significant wave height and is calculated as four times the standard deviation of the surface elevation. Figure 8c shows that when the nonlinear spectrum is near homoclinic data, $U_{\max}$ exceeds $2.2H_S$ (a rogue wave develops at $t \approx 40$). Figure 8d shows that when the nonlinear spectrum is far from homoclinic data, $U_{\max}$ is significantly below $2.2H_S$ and a rogue wave does not develop. As a result, we can correlate the occurrence of rogue waves characterized by JONSWAP spectrum with the proximity to homoclinic solutions of the NLS equation.

The results of hundreds of simulations of the NLS and MD equations consistently show that proximity to homoclinic data is a crucial indicator of rogue wave events. Figures 9 and 10 provide a synthesis of 200 random simulations of the NLS equation and of the MD equation for two perturbation strengths ($\varepsilon = 0.005$ and $\varepsilon = 0.01$) for JONSWAP initial data with different (γ, α) pairs (with $\gamma = 2, 4, 6, 8$, and $\alpha = 0.012, 0.016$). For each such pair (γ, α), we performed 25 simulations, each with a different set of randomly generated phases. We restrict our consideration to semi-stable N-phase solutions near to unstable solutions of the NLS with one UM. Each circle represents the strength of the maximum wave ($U_{\max}/H_S$) attained during one simulation as a function of the splitting distance $\delta(\lambda_+, \lambda_-)$. The results for the particular pair $(\gamma = 4, \alpha = 0.012)$ is represented with an asterisk. A horizontal line at $U_{\max}/H_S = 2.2$ indicates the reference strength for rogue wave formation. We identify two critical values $\delta_1(\varepsilon)$ and $\delta_2(\varepsilon)$ that clearly show that (a) if $\delta < \delta_1$ (near homoclinic data) rogue waves will occur; (b) if $\delta_1 < \delta < \delta_2$, the likelihood of obtaining rogue waves decreases as δ increases and, (c) if $\delta > \delta_2$ the likelihood of a rogue wave occurring is extremely small.

This behavior is robust. As α and γ are varied, the strength of the maximum wave and the occurrence of rogue waves are well predicted by the proximity to homoclinic solutions. The individual plots of the strength vs. δ for particular pairs

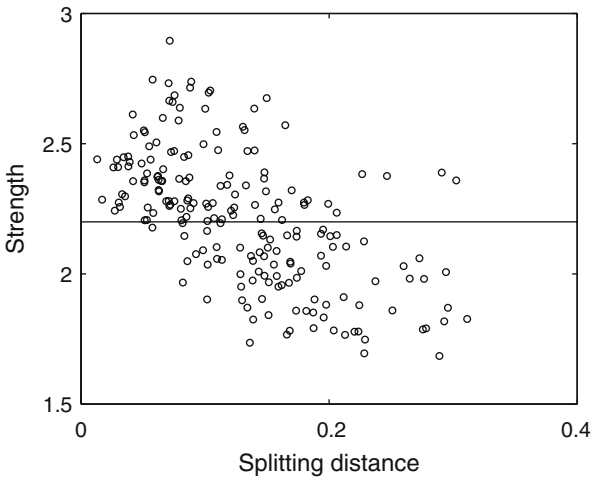

Fig. 9 Strength of $U_{\max}/H_S$ vs. the splitting distance $\delta(\lambda_+, \lambda_-)$ for solutions of the NLS equation

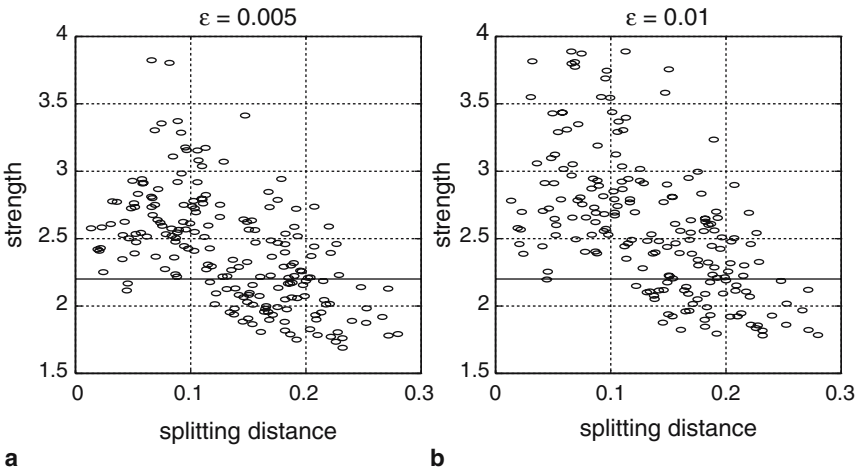

Fig. 10 Strength of $U_{\max}/H_S$ vs. the splitting distance $\delta(\lambda_+, \lambda_-)$ for solutions of the MD equation when (**a**) $\varepsilon = 0.005$ and (**b**) $\varepsilon = 0.01$

(γ, α) are qualitatively the same regardless of the pair chosen. As noted in Sect. 4 on the MD equation, enhanced focusing occurs in the chaotic regime. Figure 10 shows that as ε increases the average strength and the likelihood of rogue waves increases. Clarification on the likelihood of rogue waves through an examination of the kurtosis is provided in Sect. 6. These results give strong evidence of the relevance of homoclinic solutions of the NLS equation in investigating rogue wave phenomena for more realistic oceanic conditions and identifies the nonlinear spectral decomposition as a simple diagnostic tool for predicting the occurrence and strength of rogue waves.

6 Non-Gaussian Statistics and the Dependence of Kurtosis on the Proximity to Homoclinic Data

In (Longuet-Higgins 1952) the probability distribution of crest-to-trough wave heights was formulated to be given by the Rayleigh distribution when the wave spectrum is narrow banded and the phases in the reconstruction of the surface elevation are uniformly distributed. Various studies using experimental and field wave data have shown that this can be a reasonable assumption for water waves in the linear regime.

In the nonlinear regime, the relation of the probability density function of wave heights to the nonlinear parameters describing various sea states is not generally known. Simply assuming a Gaussian distribution can be risky. If the kurtosis is in fact much greater than that for the Gaussian distribution, then the probability of an extreme event will be underpredicted.

The main questions we address in this section are whether the modulational instability and the presence of coherent structures yield non-Gaussian statistics of surface gravity waves in the nonlinear regime and whether this can be captured by the spectral parameter δ. In our earlier work with the NLS equation, it appeared that homoclinic chaos increases the likelihood of rogue waves. After a short time, the waves become chaotic resulting in a sea state characterized by intermittent rogue waves. To more precisely quantify rogue wave events, in our current numerical experiments we monitor the evolution of the skewness, m_3, and the kurtosis, m_4, of the wavefield which are related to the third and fourth statistical moments of the probability density function of the surface elevation by

$$m_3(\eta) = \sum_{j=1}^{N} \frac{(\eta_j - \bar{\eta})^3}{N\sigma^3}, \qquad m_4(\eta) = \sum_{j=1}^{N} \frac{(\eta_j - \bar{\eta})^4}{N\sigma^4},$$

where σ is the standard deviation of the surface elevation, $\bar{\eta}$ is the average surface elevation and N is the number of data points sampled.

Skewness is a measure of the vertical asymmetry of the wavefield. Positive values indicate the wavefield is skewed above the average height, i.e., the crests are bigger than the troughs. Negative values indicate that the wavefield is skewed below the average height.

The kurtosis is a measure of whether the distribution for the wavefield is peaked or flat, relative to a Gaussian distribution and defines the contribution of large waves to the wavefield. The kurtosis for a Gaussian distribution is 3. Wavefields with high kurtosis (in excess of 3) tend to have a distinct peak near the mean, decline rapidly, and have heavy tails. That is, fewer observations or events cluster near the average and more observations populate the extremes either far above or far below the average compared to the bell curve of the normal distribution. For this reason, excess kurtosis much above 3 indicates that the contribution of large waves is significant and corresponds to a higher probability of a rogue wave event.

Figure 11a shows the plot of the kurtosis as a function of time for the analytical two unstable mode homoclinic solutions of the NLS (7) (the corresponding

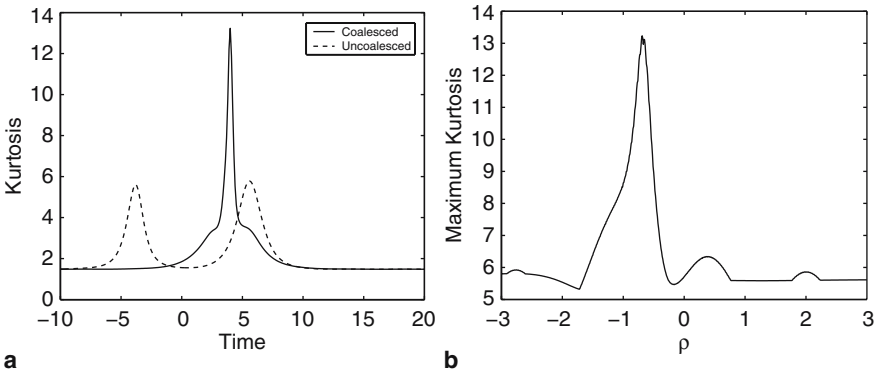

Fig. 11 For the two unstable mode homoclinic solution of NLS: (**a**) the evolution of the kurtosis for the coalesced and uncoalesced cases and (**b**) the maximum of the kurtosis as a function of ρ

waveforms are given in Fig. 4) in the uncoalesced case, $\rho = -1$, and in the coalesced case, $\rho = -0.65$. Here we are using the kurtosis as a formal tool to obtain a rough estimate of the peakedness of the waveform. In both cases, the kurtosis starts to increase with the onset of the BF instability and reaches a maximum when the instability saturates. In the uncoalesced case, there are two excursions in the kurtosis. In the coalesced case, the increased height achieved by the waveform is reflected in a significantly larger kurtosis. Figure 11b shows the plot of the maximum of the kurtosis of the two unstable mode homoclinic orbit, as a function of the phase parameter ρ. Interestingly, the maximum of the kurtosis is optimized by the robust coalesced homoclinic solution which also gives the zero of the Melnikov integrals and is persistent in the MD equation.

Janssen (2003) formulated the relation between the kurtosis of the surface elevation and the probability of rogue wave occurrence for $1D$ weakly non-Gaussian waves. A is the envelope of the wavetrain and ϕ the phase. The PDF of the envelope A follows from an integration of the joint probability distribution over the phase ϕ. The first term gives the Rayleigh distribution while the terms involving the skewness integrate to zero. The third term does give a contribution depending on the kurtosis and they find that the narrow-band approximation of the PDF of the envelope is

$$p(A) = A\mathrm{e}^{-(1/2)A^2}\left[1 + \frac{1}{3}m_4\left(1 - A^2 + \frac{1}{8}A^4\right)\right].$$

The probability of the occurrence of a rogue wave as a function of N (the number of waves) and the kurtosis is

$$\mathcal{P}_{\text{rogue}} = 1 - \exp\left[-\mathrm{e}^{-8}N\left(1 + 8m_4\right)\right].$$

In this way, as the kurtosis increases, the probability that rogue waves will occur increases. We examine the evolution of the skewness and kurtosis for three ranges of δ: (1) $\delta \leq 0.1$, (2) $0.1 < \delta < 0.2$, and (3) $\delta \geq 0.2$. The skewness and kurtosis is computed at each time step, first as an average over space and then averaging over the ensemble. As before, we begin by determining the nonlinear spectrum of the JONSWAP initial data for various combinations of (α, γ). We used a sufficient number of realizations of the random phases so that we would have 250 cases for each range of values of δ. Figure 12 provides the evolution of the skewness and kurtosis for three different values of the nonlinear spectral gap size δ. Both the skewness and kurtosis grows initially and then relax to their asymptotic value. The asymptotic value of the kurtosis is approximately (1) 3.5 when $\delta \leq 0.1$, (2) 3.2 when $0.1 < \delta < 0.2$, and (3) 3 when $\delta \geq 0.2$. It is clear in Fig. 12 the kurtosis is strongly dependent on δ and attains larger values for JONSWAP data closer to homoclinic data. The proximity to homoclinic data changes the wave statistics and increases the likelihood of rogue waves.

Using the inverse spectral theory of the NLS equation, we have shown that the development of extreme waves in random oceanic sea states characterized by JONSWAP power spectra is well predicted by the proximity to homoclinic data of the NLS equation. We observe that the modulational instability generates a significant

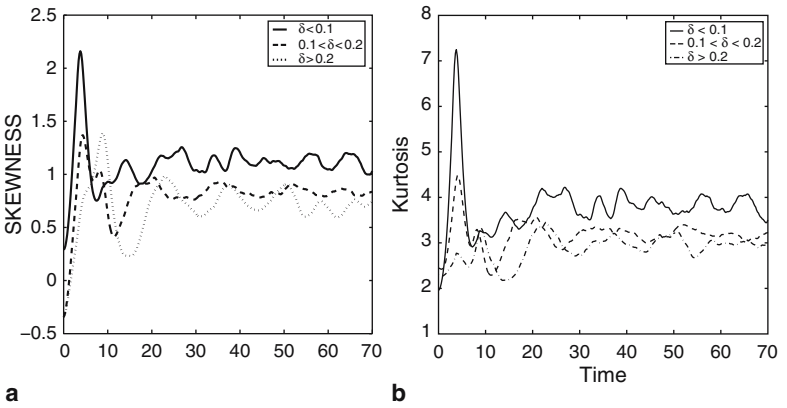

Fig. 12 Evolution of the (**a**) skewness and (**b**) kurtosis for JONSWAP initial data

deviation from Gaussianity. In particular we find (1) the kurtosis and wave strength are found to be strongly dependent on δ, the proximity to instabilities and homoclinic structures; (2) the likelihood of rogue waves increases for JONSWAP data near to homoclinic data of the NLS; (3) the NLS equation underpredicts, as compared to the MD equation, both the wave strength and likelihood of rogue waves.

References

Ablowitz MJ, Hammack J, Henderson D, Schober CM (2000) Modulated periodic stokes waves in deep water. Phys Rev Lett 84:887–890

Ablowitz MJ, Hammack J, Henderson D, Schober CM (2001) Long time dynamics of the modulational instability of deep water waves. Physica D 152–153:416–433

Ablowitz MJ, Segur H (1981) Solitons and the inverse scattering transform. SIAM, Philadelphia

Akhmediev NN, Korneev VI, Mitskevich NV (1988) *N*-modulation signals in a single-mode optical waveguide under nonlinear conditions. Sov Phys JETP 67:1

Bridges TJ, Derks G (1999) Unstable eigenvalues and the linearization about solitary waves and fronts with symmetry. Proc R Soc Lond A 455:2427

Cai D, McLaughlin DW, McLaughlin KTR (1995) The nonlinear Schrödinger equation as both a PDE and a dynamical system. Preprint.

Calini A, Schober CM (2002) Homoclinic chaos increases the likelihood of rogue waves. Phys Lett A 298:335–349

Calini A, Ercolani NM, McLaughlin DW, Schober CM (1996) Mel'nikov analysis of numerically induced chaos in the nonlinear Schrödinger equation. Physica D 89:227–260

Ercolani N, Forest MG, McLaughlin DW (1990) Geometry of the modulational instability. Part III: Homoclinic orbits for the periodic Sine-Gordon equation. Physica D 43:349–384

Haller G, Wiggins S (1992) Orbits homoclinic to resonances: The Hamiltonian case. Physica D 66:298–346

Henderson KL, Peregrine DH, Dold JW (1999) Unsteady water wave modulations: Fully nonlinear solutions and comparison with the nonlinear Schrödinger equation. Wave Motion 29:341

Islas A, Schober CM (2005) Predicting rogue waves in random oceanic sea states. Phys Fluids 17:1–4

Its AR, Rybin AV, Salle MA (1988) On the exact integration of the nonlinear Schrodinger equation. Theoret. and Math. Phys. 74(1): 20–32

Janssen P (2003) Nonlinear four-wave interactions and freak waves. J Phys Oceanogr 33:863–884

Karjanto N (2006) Mathematical aspects of extreme water waves. Ph.D. Thesis, Universiteet Twente

Li Y (1999) Homoclinic tubes in the nonlinear Schrödinger equation under Hamiltonian perturbations. Prog Theor Phys 101:559–577

Li Y, McLaughlin DW (1994) Morse and Mel'nikov functions for NLS Pde's discretized perturbed NLS systems. I. Homoclinic orbits. Commun Math Phys 612:175–214

Li Y, McLaughlin DW, Shatah J, Wiggins S (1996) Persistent homoclinic orbits for a perturbed nonlinear Schrödinger equation. Commun Pure Appl Math 49:1175–1255

Longuet-Higgins MS (1952) On the statistical distribution of the heights of sea waves. J Mar Res 11:1245

Matveev VB, Salle MA (1991) Darboux transformations and solitons. Springer, Berlin Heidelberg New York

McLaughlin DW, Schober CM (1992) Chaotic and homoclinic behavior for numerical discretizations of the nonlinear Schrödinger equation. Physica D 57:447–465

Ochi MK (1998) Ocean waves: The stochastic approach. Cambridge University Press, Cambridge

Osborne A, Onorato M, Serio M (2000) The nonlinear dynamics of rogue waves and holes in deep-water gravity wave trains. Phys Lett A 275:386

Onorato M, Osborne A, Serio M, Bertone S (2001) Freak wave in random oceanic sea states. Phys Rev Lett 86:5831

Schober C (2006) Melnikov analysis and inverse spectral analysis of rogue waves in deep water. Eur J Mech B Fluids 25:602–620

Trulsen K, Dysthe K (1996) A modified nonlinear Schrödinger equation for broader bandwidth gravity waves on deep water. Wave Motion 24:281

Trulsen K, Dysthe K (1997a) Frequency downshift in three-dimensional wave trains in a deep basin. J Fluid Mech 352:359–373

Trulsen K, Dysthe K (1997b) Freak waves – a three dimensional wave simulation. In: Rood EP (ed) Naval hydrodynamics. Proceedings of the 21st symposium on nature. Academic Press, USA

Zakharov VE, Shabat AB (1972) Exact theory of two-dimensional self-focusing and one-dimensional self-modulation of waves in nonlinear media. Sov Phys JETP 34:62–69

Zeng C (2000) Homoclinic orbits for a perturbed nonlinear Schrödinger equation. Commun Pure Appl Math 53:1222–1283

Zeng C (2000) Erratum: Homoclinic orbits for a perturbed nonlinear Schrödinger equation. Commun Pure Appl Math 53:1603–1605

Non-Gaussian Properties of Shallow Water Waves in Crossing Seas

A. Toffoli, M. Onorato, A.R. Osborne, and J. Monbaliu

Abstract The Kadomtsev–Petviashvili equation, an extension of the Korteweg–de Vries equation in two horizontal dimensions, is here used to study the statistical properties of random shallow water waves in constant depth for crossing sea states. Numerical simulations indicate that the interaction of two crossing wave trains generates steep and high amplitude peaks, thus enhancing the deviation of the surface elevation from the Gaussian statistics. The analysis of the skewness and the kurtosis shows that the statistical properties depend on the angle between the two wave trains.

1 Introduction

Sea states characterized by two spectral peaks with different mean directions, also known as mixed or crossing seas, are quite common in nature. Such conditions, for example, can be easily observed when the wind direction suddenly changes or a swell system coming from a distant source interferes with the local sea. A recent study by Toffoli et al. (2006a), based on data collected from January 1995 to April 1999 by the Lloyd's Marine Information Service (Bitner-Gregersen and Eknes 2001), has also revealed that a large percentage of ship accidents, reported as being due to bad weather conditions, has occurred in crossing sea states (see also Donelan and Magnusson 2005; Greenslade 2001).

In that respect, mixed sea conditions are suspected to enhance the probability of occurrence for extreme wave events (see, e.g., Lehner et al. 2005). For the case of

A. Toffoli and J. Monbaliu
Katholieke Universiteit Leuven, Leuven, Belgium
toffoli.alessandro@gmail.com, jaak.monbaliu@bwk.kuleuven.be

M. Onorato and A.R. Osborne
Universitá di Torino, Torino, Italy
onorato@ph.unito.it, al.osborne@gmail.com

E. Pelinovsky, C. Kharif (eds.) *Extreme Ocean Waves*, 53–69.

deep water, theoretical studies on the influence of a second spectral peak (Onorato et al. 2006; Shukla et al. 2006), which propagates with a mean direction that differs from the principal wave system, showed that waves can be unstable in mixed seas. Moreover, using second-order wave theory to simulate random time series of the sea surface, Toffoli et al. (2006b) have shown that crossing sea state conditions may modify the form of the wave crest distribution as an excess of large waves may occur when two wave systems coexist.

In the case of shallow water, Peterson et al. (2003) and Soomere and Engelbrecht (2005, 2006) have studied the interaction of multidirectional wave trains by considering soliton-like solutions of the Kadomtsev–Petviashvili equation (Kadomtsev and Petviashvili 1970), which can be thought as an extension of the Korteweg–de Vries equation in the case of propagation in the (x, y) plane. The most interesting feature that arises from the interaction of two noncollinear solitons results in the formation of a steep and high peak (Miles 1977a, 1977b). In particular, not only does its amplitude exceed the value predicted by linear theory, but also assumes values up to four times the amplitude of the incoming solitons.

Although directional, shallow water wave fields have recently been investigated (see, e.g., Herbers 2003; Janssen et al. 2006), the evolution of shallow water waves in crossing sea state conditions has not yet been addressed properly. The aim of the present study is to discuss the case of possible nonlinear interactions that may arise in shallow water when two sea states, with a certain frequency distribution and directional spreading, coexist. We mainly concentrate on the occurrence of extreme wave events and hence on the form of the probability density function of the surface elevation and its third- and fourth-order moments.

To accomplish this task, the Kadomtsev–Petviashvili equation has been simulated numerically. Our choice on such equation is not due to the fact that we believe that the Kadomtsev–Petviashvili equation is the most accurate theoretical approach to describe shallow water waves (higher order models based on the Boussinesq equations are surely more appropriate to describe different effects that take place in shallow water (Herbers, 2003)). We are motivated by the fact that the Kadomtsev–Petviashvili equation is the leading order equation in the shallow water expansion of the Euler equations where directionality is included. Our aim is to highlight a nonlinear mechanism described by the Kadomtsev–Petviashvili equation, that brings the statistical properties of the surface elevations far from the Gaussian behavior. The numerical solution of the Kadomtsev–Petviashvili equation, moreover, is fast. Therefore, this facilitates the performance of many numerical experiments considering different random phases, different degrees of nonlinearity, and different angles between the incoming wave systems. It should be mentioned, furthermore, that the bottom topography has an important role in the evolution of shallow water waves (Janssen et al. 2006). For convenience, however, we only discuss the case of flat bottom.

The paper is organized as follows: we first begin with a general description of the Kadomtsev–Petviashvili equation. In the following section we describe the numerical experiment. In Sect. 4, the skewness and the kurtosis of the simulated surface elevation are investigated as a function of the angle between the two wave systems.

A direct analysis of the sea surface and the concurrent probability density function is presented in Sect. 5. In Sect. 6, we discuss the statistical distribution of the wave height. Some concluding remarks are presented in Sect. 7.

2 The Kadomtsev–Petviashvili Equation

The Korteweg–de Vries (KdV) equation describes nonlinear waves that propagate in the x-direction. A periodic solution of such an equation is expressed by means of a Jacobian elliptic function, which is known as cnoidal wave (see, e.g., Johnson 1997). To express the degree of nonlinearity of KdV-like wave trains, the Ursell number (Ursell 1953) is often used:

$$Ur = \frac{3}{16}\frac{a\lambda^2}{\pi^2 h^3} = \frac{3}{4}\frac{ka}{k^3h^3}. \tag{1}$$

Small Ursell numbers indicate linear wave motion ($Ur \ll 1$); large values address to increasing nonlinear effects (Osborne and Petti 1994).

One of the major shortcomings of cnoidal wave theory is its one-dimensional nature, i.e., it describes long-crested waves. A real sea surface, however, has two horizontal dimensions, and waves can be both long and short crested. The y-dependence, for example, would not be trivial in the case of two crossing waves. To describe the evolution of weakly directional waves in shallow water, a two-dimensional generalization of the KdV equation was derived by Kadomtsev and Petviashvili (1970); hereafter, we shall refer to this equation as the KP equation. For an irrotational, inviscid fluid in constant depth, the KP equation can be obtained from the Euler equations, if the following assumptions are satisfied (see, e.g., Johnson 1997; Segur and Finkel 1985 for a review): (a) waves are of small amplitude, i.e., $\delta = a/h \ll 1$; (b) the water is shallow, i.e., $\beta = (kh)^2 \ll 1$; (c) the waves are weakly directional, i.e., $\zeta = (k_y/k_x)^2 \ll 1$, where k_x and k_y are the components of the wave number vector $\mathbf{k}$; (d) these three small effects are comparable, i.e., $\zeta \simeq O(\delta) \simeq O(\beta)$; (e) waves propagate only toward positive values of x. In dimensional form, the KP equation can be written as follows:

$$\frac{\partial}{\partial x}\left(\frac{\partial \eta}{\partial t} + \frac{3}{2}\frac{C_0}{h}\eta\frac{\partial \eta}{\partial x} + \frac{1}{6}h^2 C_0 \frac{\partial^3 x}{\partial x^3}\right) + \frac{1}{2}C_0\frac{\partial^2 \eta}{\partial y^2} = 0, \tag{2}$$

where $C_0 = \sqrt{gh}$ is the phase velocity, and h is the water depth.

Fornberg and Whitham (1978) developed a method for solving KdV-type wave equations. The method uses a pseudo-spectral treatment of the space dependence together with a leap-frog scheme in time. Here, we have extended this method to the KP equation to perform numerical simulations. Boundary conditions are assumed to be periodic and derivatives are performed using the Fast Fourier Transform (FFT)

algorithm. The number of grid points in physical space was set to 128×64. The numerical method has been successfully tested against analytical soliton solutions of the KP equation.

3 Numerical Experiment

A two-dimensional wave field is commonly described by a directional wave spectrum: $E(\omega,\vartheta) = S(\omega)D(\omega,\vartheta)$, where ω is the angular frequency and ϑ is the direction. Here, we use a JONSWAP spectral formulation (Komen et al. 1994) with dominant wavelength $\lambda_p = 76.5$ m, peak enhancement factor $\gamma = 3.3$ and Phillips parameter $\alpha = 0.004$ to model the wave energy in the frequency domain ($S(\omega)$); this corresponds to a significant wave height H_s of 1.7 m (calculated as four times the standard deviation). A $cos^{2s}(\vartheta/2)$ spreading function (see, e.g., Hauser et al. 2005) is then applied to model the energy in the directional domain ($D(\omega,\vartheta)$). The spreading coefficient s is expressed as a function of the angular frequency (Goda 2000):

$$s(\omega) = \left(\frac{\omega}{\omega_p}\right)^5 s_{\max} \qquad \text{if} \quad \omega \le \omega_p \tag{3}$$

$$s(\omega) = \left(\frac{\omega}{\omega_p}\right)^{-2.5} s_{\max} \qquad \text{if} \quad \omega > \omega_p \tag{4}$$

where ω_p is the peak frequency. For the present study, we have chosen the spreading coefficient such that at the peak frequency $s(\omega_p) = 25$, which corresponds to the directional spreading of a short-decay swell (Goda 2000). Such a spectrum, however, is unimodal, i.e., single peaked. To describe crossing sea conditions, which represent bimodal sea states, the wave field is defined by using two identical, aforementioned, single peaked spectra with different mean directions, i.e., $\vartheta_1 \neq \vartheta_2$. The resulting sea state, $\tilde{E}(\omega,\vartheta) = E(\omega,\vartheta-\vartheta_1) + E(\omega,\vartheta-\vartheta_2)$, is characterized by $\lambda_p = 76.5$ m, and $H_s = 2.4$ m. Note that in case $\vartheta_1 = \vartheta_2$, such a spectrum reduces to an unimodal energy distribution.

By means of the linear dispersion relation, the directional spectrum $\tilde{E}(\omega,\vartheta)$ is expressed as a function of the wave number vector $\mathbf{k} \equiv (k_x, k_y)$ (Tanaka 2001). For a typical, bimodal, wave number spectrum $\tilde{E}(\mathbf{k})$ used in this study, the two spectral peaks are assumed to be symmetric with respect to the x-direction, such that $\vartheta_1 = -\vartheta_2 = \vartheta^*$.

The spectrum $\tilde{E}(\mathbf{k})$ is then used to generate a random sea surface $\eta(x,y)$ at an initial time $t = 0$ s as a linear superposition of Fourier modes. It is straightforward to show that a linear surface, which will be our initial condition for the simulations, can be expressed as follows:

$$\eta(\mathbf{x}) = \sum_{i=1}^{N}\sum_{j=1}^{M} a_{ij}\, cos[(k_x)_i x + (k_y)_j y + \varepsilon_{ij}], \tag{5}$$

where $\mathbf{x} \equiv (x, y)$ is the position vector; ε_{ij} the random phase, which is selected from a uniform distribution in the interval $[0, 2\pi]$; N and M represent the number of wave numbers in the x and y-direction, respectively and a_{ij} is the spectral amplitude, which is calculated as follow:

$$a_{ij} = \sqrt{2\,\tilde{E}[(k_x)_i, (k_y)_j]\,\Delta k_x\,\Delta k_y}. \tag{6}$$

Note that the use of a determinist amplitude may not include all natural variability of waves. However, if a directional wave field is simulated, the addition of different directional components automatically restores this variability (Forristall 2000).

The summations in (5) are performed by means of a two-dimensional inverse Fast Fourier Transform. The input spectrum $\tilde{E}(\mathbf{k})$ is defined by using equally spaced wave numbers in both x and y-direction, i.e., Δk_x and Δk_y are constants; this automatically generates periodic boundaries, which are required for numerical simulations of the KP equation. The spatial domain is chosen such that the wave field measures 400 m in the x-direction and 200 m in the y-direction.

We now consider this linear surface in a shallow water environment at three different water depths. This defines three different degrees of nonlinearity as measured by the Ursell number, (1), where $a = H_s/2$ and $k = 2\pi/\lambda_\mathrm{p}$. The different water depths and the concurrent Ursell numbers are presented in Table 1. Under these conditions, the linear surface is then used as input in the KP model; the surface is let evolve in time according to (2) until it reaches a statistically stationary condition. The experiment is repeated for different values of the angles ϑ^* between a minimum of 0° (unimodal spectrum) up to a maximum of 45° with a step size of 2.5°. The spectral energy is kept constant, i.e. $H_s = \text{const.}$ and $\lambda_\mathrm{p} = \text{const.}$ for all repetitions of the numerical experiment.

For each time step, $\Delta t = 0.001$ s, the model produces a two-dimensional surface as output; the skewness and the kurtosis have been computed from the space series associated with each instant in time. For all spectral densities, the numerical experiment is repeated 500 times with different random phases; this should in principle stabilize the statistical information from the simulated samples. Furthermore, time series have been recorded at four different grid points of the physical domain, starting after the surface has reached a statistically stable condition.

Table 1 Water depths and degrees of nonlinearity: water depths h (m); relative water depth kh; and Ursell number Ur

h (m)	kh	Ur
7.00	0.57	0.39
6.00	0.49	0.62
5.00	0.41	1.10

4 Skewness and Kurtosis of the Simulated Surface Elevation

When the water depth is reduced, the nonlinear interaction becomes more and more relevant. The most obvious manifestation of this nonlinearity is the sharpening of the wave crests and the flattening of the wave troughs, which results in a departure from the Gaussian statistics. The deviation is usually expressed in terms of the skewness, λ_3, and kurtosis, λ_4, which represent the third- and fourth-order moments of the probability density function, respectively. The first expresses the vertical asymmetry of the wave profile and the second is an indication of extreme events. For waves in shallow water, $kh \ll 0$, it is therefore expected that $\lambda_3 > 0$ and $\lambda_4 > 3$, where 0 and 3 are the values of skewness and kurtosis for a Gaussian random process.

In Fig. 1, we show the skewness and kurtosis of the simulated surface elevation $\eta(x,y)$ as a function of time for a single peaked sea state, i.e., $\vartheta^* = 0^\circ$ and a degree of nonlinearity $Ur = 0.62$. Note that, since the physical phenomenon is considered a random process, the statistical properties of the wave field are retrieved by calculating average values at each time step over the collection of simulated samples (ensemble average).

The input, linear, surface evolves at each instant of time according to the KP equation; the statistical properties of the wave surface show a rapid and significant deviation from the Gaussian statistics. After about 600 s, the values of the skewness and kurtosis reach a stationary condition (cf. Pelinovsky and Sergeeva 2006). For the considered degree of nonlinearity ($Ur = 0.62$), for example, the moments tend to stabilize around the following values: $\lambda_3 \simeq 0.60$; $\lambda_4 \simeq 3.39$. As one would

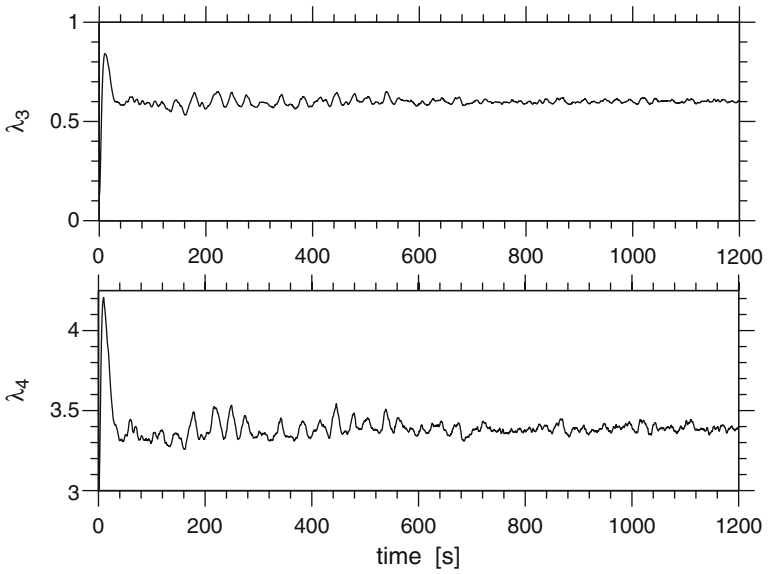

Fig. 1 Skewness (*upper panel*) and kurtosis (*lower panel*) as a function of time from numerical simulations with $\vartheta_1 = -\vartheta_2 = \vartheta^* = 0^\circ$ and $Ur = 0.62$

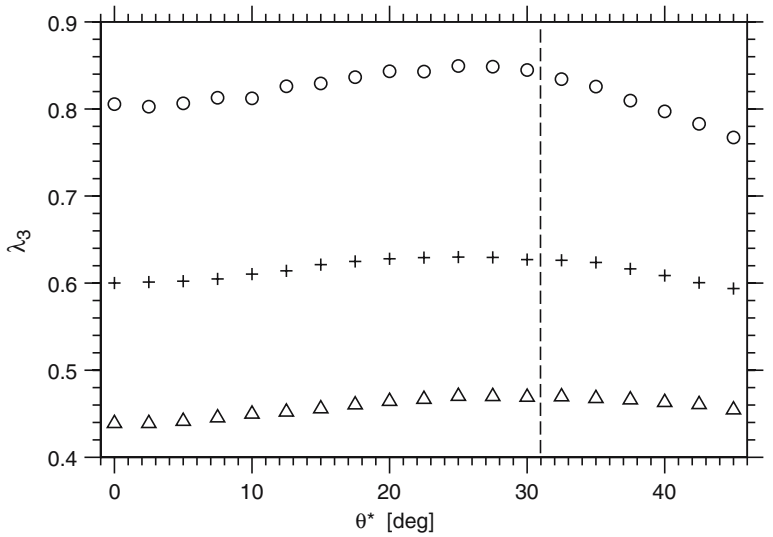

Fig. 2 Skewness (λ_3) as a function of the mean direction ($\vartheta_1 = -\vartheta_2 = \vartheta^*$) of the spectral peaks from numerical simulation: $Ur = 0.39$ (*triangle*); $Ur = 0.62$ (*plus*); and $Ur = 1.10$ (*circle*)

expect, the skewness and kurtosis vary in magnitude as the nonlinearity of the system changes: for $Ur = 0.39$, $\lambda_3 \simeq 0.44$ and $\lambda_4 \simeq 3.13$; for $Ur = 1.10$, $\lambda_3 \simeq 0.81$, and $\lambda_4 \simeq 3.87$. The vertical asymmetry (λ_3), however, assumes remarkably high values already at relatively low nonlinearity. A similar result was also obtained in unidirectional condition using the KdV equation by Pelinovsky and Sergeeva (2006).

We now investigate how the statistical properties of the simulated surfaces can change when two spectral peaks with different mean directions are considered. In Figs. 2 and 3, we show the skewness and kurtosis as a function of the angle ϑ^*. The existence of a second spectral peak results in an increase of the skewness and kurtosis as the angle between the spectra is increased. This enhancement, however, is almost nil when the systems are almost collinear ($\vartheta^* \leq 5^\circ$) and becomes more relevant as the wave trains assume well-separated directions. The maximum magnitudes of the third- and fourth-order moments are obtained for $\vartheta^* \approx 30^\circ$: (1) for $Ur = 0.39$, $\lambda_3 \simeq 0.47$ and $\lambda_4 \simeq 3.33$; (2) for $Ur = 0.62$, $\lambda_3 \simeq 0.63$ and $\lambda_4 \simeq 3.65$; (3) for $Ur = 1.10$, $\lambda_3 \simeq 0.85$ and $\lambda_4 \simeq 4.30$. It is important to remark that the energy remains constant and hence this variation is only due to the nonlinear interaction of intersecting wave trains. When $\vartheta^* > 30^\circ$, the increasing trend decreases. For low and moderate nonlinearity, the kurtosis approximately conserved the values found for $\vartheta^* \approx 30^\circ$; the skewness, in contrast, slowly decreases as ϑ^* approaches 45°. For high degrees of nonlinearity, however, both skewness and kurtosis show a decreasing trend for large ϑ^*. Note that the angle at which the statistical moments of the surface elevation maximize is to some extent consistent with the critical angle at which two noncollinear solitons with wavelength equal to λ_p and amplitude equal to $H_s/2$ produce an intersection peak with maximum height and length

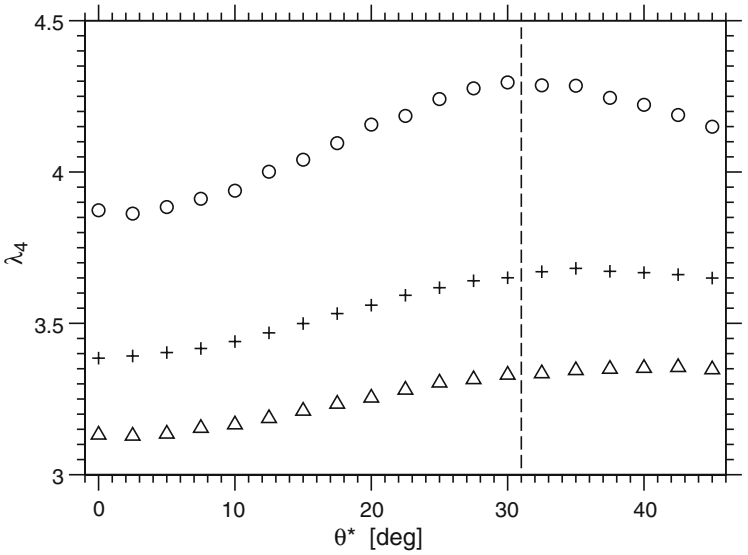

Fig. 3 Kurtosis (λ_4) as a function of the mean direction ($\vartheta_1 = -\vartheta_2 = \vartheta^*$) of the spectral peaks from numerical simulation: $Ur = 0.39$ (*triangle*); $Ur = 0.62$ (*plus*); and $Ur = 1.10$ (*circle*)

(Peterson et al. 2003). For $\vartheta^* > 30^\circ$, however, the condition of weak directionality, i.e., $\zeta = (k_y/k_x)^2 \ll 1$, is no longer respected: $\zeta > 0.34$ for $\vartheta^* > 30^\circ$. Therefore, the physical meaning of this critical angle is uncertain, and further investigations using the Euler equations as well as laboratory experiments are needed to confirm this finding.

It is now instructive to look at a normalized form of the skewness and kurtosis. In this respect, we define two additional parameters, which describe how much the skewness and kurtosis in bimodal systems differ from the one in unimodal conditions: $\lambda_3^* = \lambda_3/\lambda_{3,\,\vartheta^*=0}$; $\lambda_4^* = \lambda_4/\lambda_{4,\,\vartheta^*=0}$, where $\lambda_{3,\,\vartheta^*=0}$ and $\lambda_{4,\,\vartheta^*=0}$ are the skewness and kurtosis in unimodal condition, respectively. In Figs. 4 and 5, λ_3^* and λ_4^* are presented as a function of ϑ^*. For low nonlinearity, $Ur = 0.39$, the bimodality of the system produces waves which are about 8% more asymmetric than in unimodal conditions ($\lambda_3^* \simeq 1.08$). However, for higher nonlinearity, $Ur = 0.62$ and 1.10, the second spectral peak has a weaker effect on the skewness though the behavior is qualitatively identical; λ_3^* reaches, in fact, smaller values than in the case of lower nonlinearity ($\lambda_{3\,\max}^* \simeq 1.05$).

For a small degree of nonlinearity, $Ur = 0.39$, the kurtosis increases up to 7%; at such nonlinearity, the bimodality has an identical effect of both skewness and kurtosis, i.e., $\lambda_4^* \approx \lambda_3^*$. In contrast with the skewness, however, the effect of the second spectral peak on the kurtosis does not diminish at higher degrees of nonlinearity: $\lambda_{4\,\max}^* = 1.09$ for $Ur = 0.62$; $\lambda_{4\,\max}^* \simeq 1.11$ for $Ur = 1.10$. Note, in particular, the relevant enhancement of kurtosis at high degrees of nonlinearity, at which very large amplitudes may be expected.

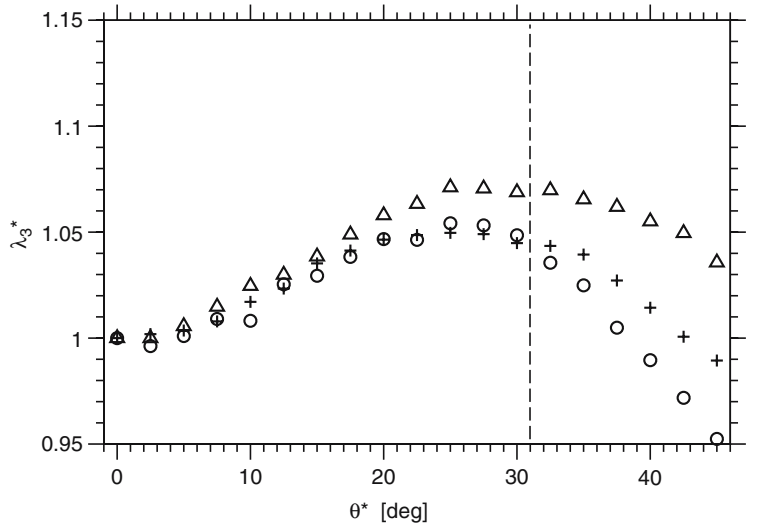

Fig. 4 Normalized skewness $\left(\lambda_3^* = \lambda_3/\lambda_{3(\vartheta^*=0)}\right)$ as a function of the mean direction ($\vartheta_1 = -\vartheta_2 = \vartheta^*$) of the spectral peaks from numerical simulation: $Ur = 0.39$ (*triangle*); $Ur = 0.62$ (*plus*); and $Ur = 1.10$ (*circle*)

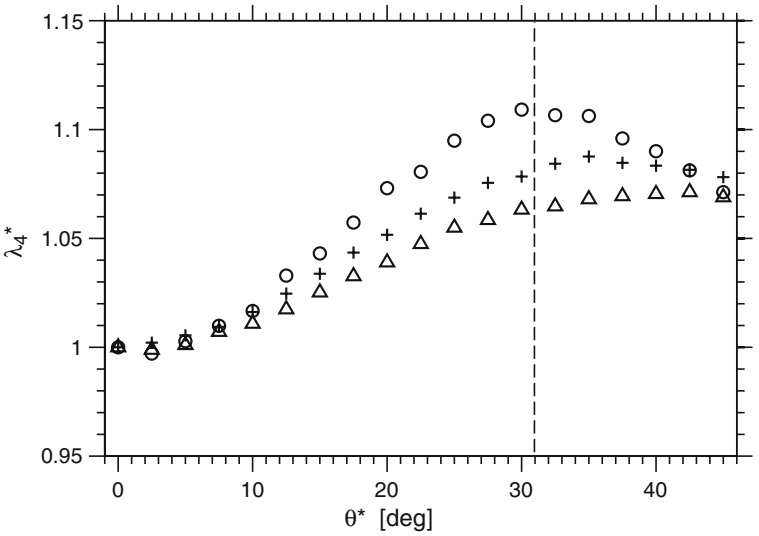

Fig. 5 Normalized kurtosis $\left(\lambda_4^* = \lambda_4/\lambda_{4(\vartheta^*=0)}\right)$ as a function of the mean direction ($\vartheta_1 = -\vartheta_2 = \vartheta^*$) of the spectral peaks from numerical simulation: $Ur = 0.39$ (*triangle*); $Ur = 0.62$ (*plus*); and $Ur = 1.10$ (*circle*)

5 Surface Elevation and Probability Density Function

As waves propagate into shallow water, a definite excess of steep crests and shallow troughs can be observed due to the increasing of nonlinearity; this is also expressed by the high values of the skewness and kurtosis observed in Figs. 2 and 3. In Figs. 6 and 7, we show, as an example, two-dimensional shallow water wave fields, which have been simulated by using unimodal ($\vartheta^* = 0°$) and bimodal ($\vartheta^* = 30°$) spectral conditions.

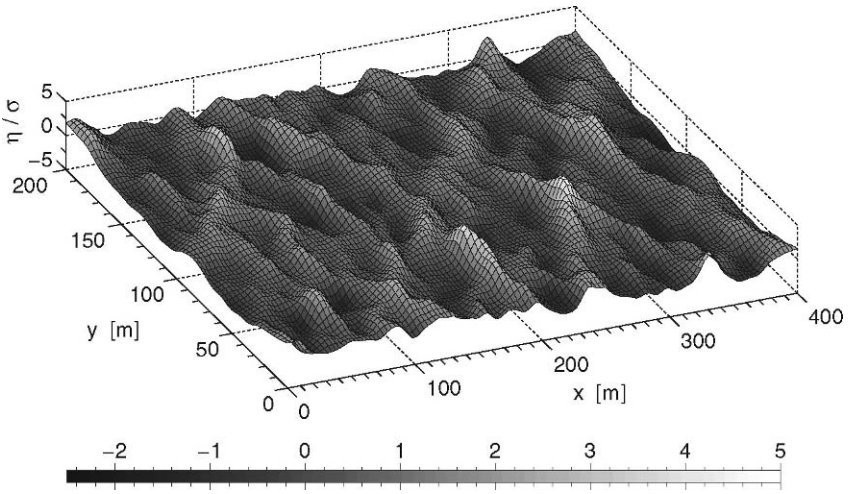

Fig. 6 Nonlinear sea surface (η/σ) from numerical simulations: $\vartheta^* = 0°$ (unimodal sea)

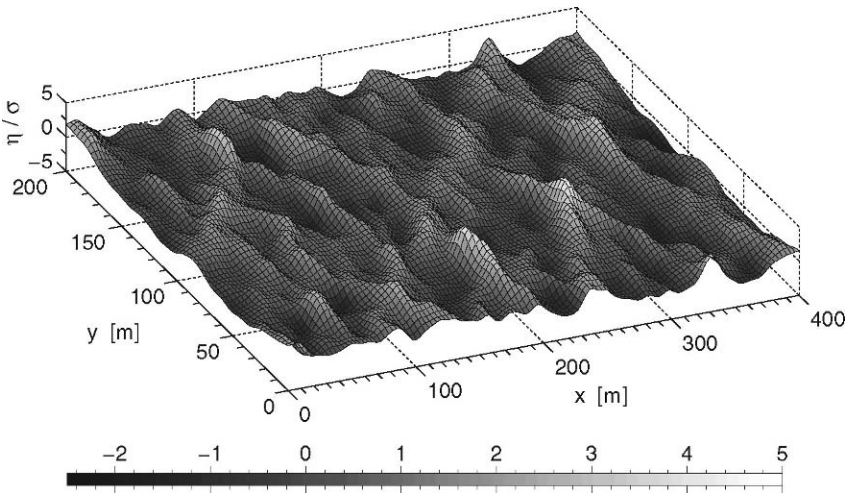

Fig. 7 Nonlinear sea surface (η/σ) from numerical simulations: $\vartheta^* = 30°$ (bimodal sea)

By using the KP equation, we observed that when two wave systems coexist, besides the sharpening of the wave crests and the flattening of the wave troughs, steep and large amplitude peaks arise in the intersecting region of two wave fronts similar to what was observed in the case of the two-soliton solution of the KP equations (see, e.g., Miles 1977a,1977b). Considering the case of two noncollinear solitons, the geometrical properties of these peaks have already been described in details by many authors (Peterson et al. 2003; Segur and Finkel 1985; Soomere and Engelbrecht 2005). It is important to note that the interaction peak of two noncollinear solitons can, in principle, propagate unaltered for infinite distance. In a dispersive system, however, the amplitude of the interaction peak arises and decreases within a distance of a few wavelengths: two up to three times the dominant wavelength in the case of not well-separated directions (e.g., $\vartheta^* \leq 20^\circ$); one dominant wavelength in case of well-separated directions (e.g., $\vartheta^* > 20^\circ$).

It is now instructive to investigate how the interaction peaks modify the probability density function for the surface elevation. In Figs. 8–10, we present, as an a example, the probability density function in unimodal ($\vartheta^* = 0^\circ$) and bimodal ($\vartheta^* = 30^\circ$) wave fields for different degrees of nonlinearity. The wave elevation is expressed in normalized form by using the standard deviation σ of the surface displacements. Note that the statistical distribution is calculated by only using the surface elevation $\eta(x,y)$ at the final time step of each random realization, because at this stage the surface can be assumed statistically stationary (see, e.g., Fig. 1). The distribution of the simulated elevation is compared with the normal probability density function, which describes linear (Gaussian) waves.

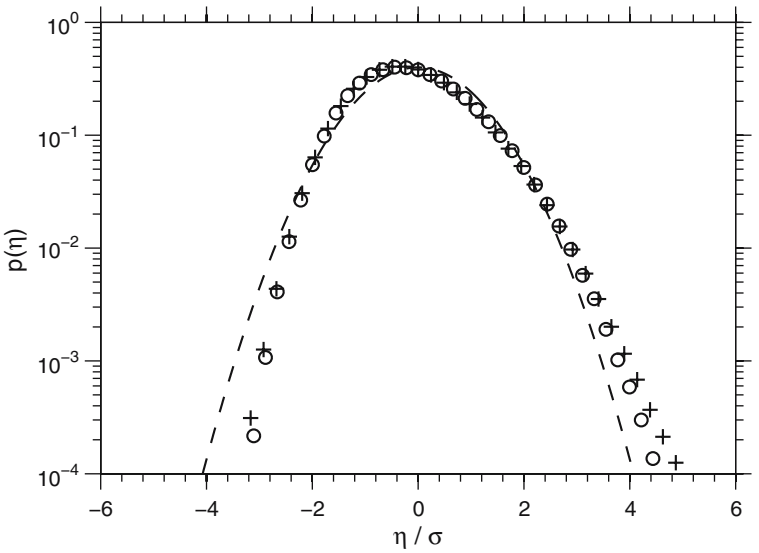

Fig. 8 Probability density function for a degree of nonlinearity $Ur = 0.39$: Gaussian distribution (*dashed line*); simulated unimodal sea (*circle*); simulated bimodal sea with $\vartheta^* = 30^\circ$ (*plus*)

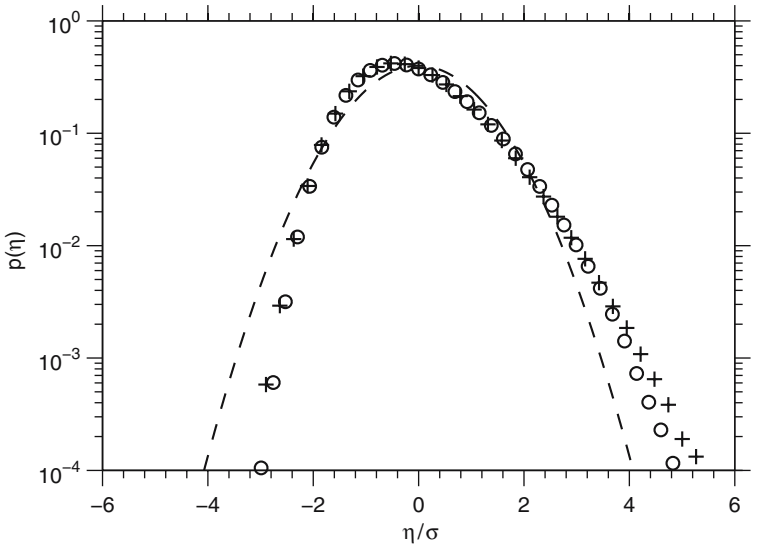

Fig. 9 Probability density function for a degree of nonlinearity $Ur = 0.62$: Gaussian distribution (*dashed line*); simulated unimodal sea (*circle*); simulated bimodal sea with $\vartheta^* = 30^\circ$ (*plus*)

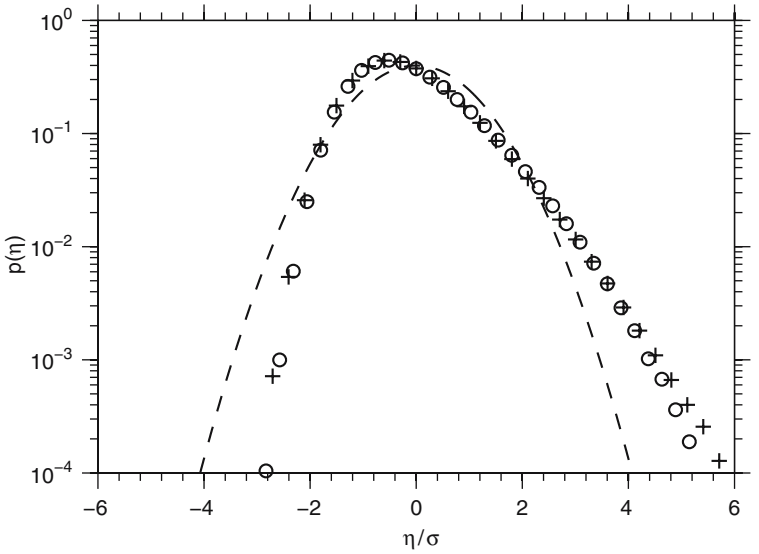

Fig. 10 Probability density function for a degree of nonlinearity $Ur = 1.10$: Gaussian distribution (*dashed line*); simulated unimodal sea (*circle*); simulated bimodal sea with $\vartheta = 30^\circ$ (*plus*)

We first look at the unimodal case $\vartheta^* = 0^\circ$. As one would expect, the form of the probability density function of simulated shallow water waves strongly deviates from the Gaussian statistics. The excess of sharp crests and shallow troughs results in a shift toward negative values of the peak of the distribution and a remarkable

deviation of its tails. When crossing waves are considered, on the other hand, the peaks arising at the intersection of the wave fronts produce a modification of the upper tail of the distribution. However, a significant deviation from the probability density function of unimodal wave fields only occurs at low probability levels ($p(\eta) < 0.001$). The interaction between two noncollinear wave systems, moreover, seems not to have any particular effect on the form of the lower tail of the distribution, which remains almost unchanged.

6 Wave Height Distribution

For an empirical analysis, the wave height H is normally defined as the difference in surface elevation between the crest and trough of an individual wave (trough-to-crest wave height). Although, it is straightforward to extract individual waves from time series (see, e.g., Goda 2000), it is not clear how to define them from a certain surface $\eta(x,y)$. In the following, therefore, we make use of the recorded time series to calculate the wave heights. In this respect, we assume that an individual wave is the portion of a wave record between two consecutive zero-downcrossings. In Fig. 11, the exceedance probability of the dimensionless wave height (the standard

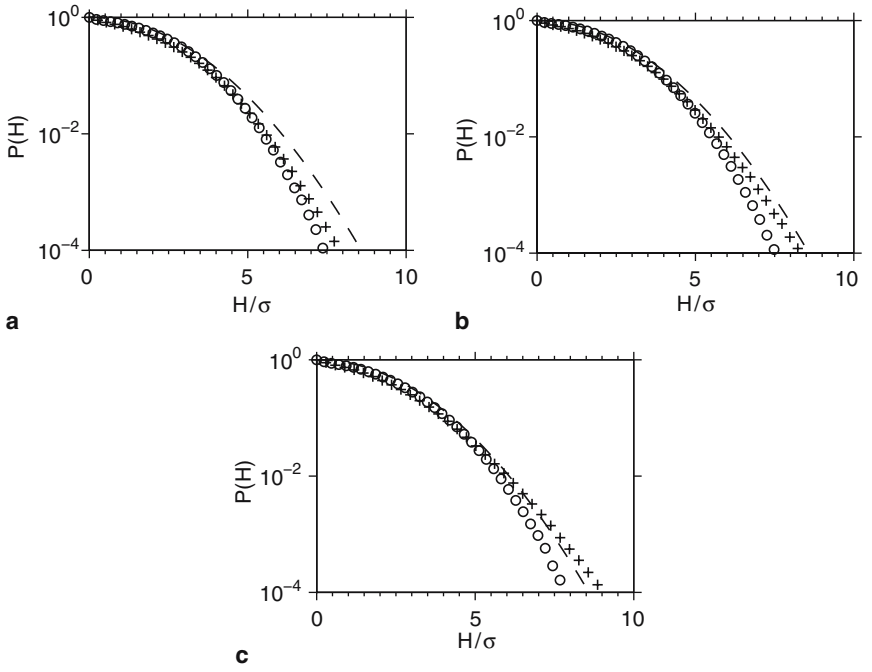

Fig. 11 Exceedance probability of wave height for different degree of nonlinearity: (**a**) $Ur = 0.39$; (**b**) $Ur = 062$; (**c**) $Ur = 1.10$. The unimodal, $\vartheta = 0°$ (*circle*), and bimodal, $\vartheta = 30°$ (*plus*), cases are compared with the Rayleigh distribution (*dashed line*)

deviation σ is used as normalizing factor) is presented for the unimodal and bimodal cases. For the latter, only the case with $\vartheta^* = 30^\circ$ is shown, because the wave height is expected to maximize for this angular condition. The statistical distribution of the simulated wave heights is then compared with the Rayleigh density function, which approximates the wave height distribution of Gaussian random processes (Longuet-Higgins, 1952).

We first consider the unimodal spectral conditions. The analysis shows that the simulated wave heights are systematically overestimated by the Rayleigh density function. Although this deviation may be attributed to the skew non-Gaussian nature of shallow water waves, it is more likely related to the finite bandwidth of the wave spectrum, and the difference in definition between the trough-to-crest wave height and the envelope-based representation, which is relevant for the Rayleigh distribution (Longuet-Higgins 1952; Tayfun 1981, 1980). When two spectral peaks coexist, however, the wave height increases. For a low degree of nonlinearity ($Ur = 0.39$), nevertheless, the bimodality of the wave spectrum does not lead to any significant deviation of the wave height distribution; as indicated in Fig. 11a, the tail of the distribution only slightly changes. When higher degrees of nonlinearity are taken into account, the interaction between noncollinear wave trains becomes more relevant and the wave height tends to be significantly higher than in unimodal conditions. As a result, the deviation of the tail of the distribution becomes more evident as the Ursell number is increased (Fig. 11b, c). For high nonlinearity ($Ur = 1.10$), furthermore, the tail of the distribution indicates that the wave height can overtake the value expected from the Rayleigh distribution.

The numerical model, which is here used to describe the elevation of shallow water waves, does not include wave breaking mechanisms. For a certain water depth and wavelength, however, there is a maximum height above which the waves become unstable and break. Since broken waves do not lose all of their energy, moreover, the heights of individual random waves after breaking can slightly modify the probability density function. To verify whether the wave breaking may affect the results presented herein, the limiting height for wave breaking, H_b, is compared with the wave height expected at low probability levels (i.e., $P(H) = 0.0001$). To this end, an estimation of the wave breaking height can be obtained as follows (see, e.g., Goda 2000): $H_\mathrm{b} = \gamma_\mathrm{b} h$, where the coefficient γ_b is typically between 0.7 and 0.9 for spilling breakers (Battjes 1974); in this study, we assume $\gamma_\mathrm{b} = 0.78$ as it is often used for coastal applications (Demirbilek and Vincent 2002).

According to the aforementioned definition, the following (dimensionless) wave breaking heights are to be expected: for $Ur = 0.39$, $H_\mathrm{b}/\sigma = 9.10$; for $Ur = 0.62$, $H_\mathrm{b}/\sigma = 7.80$; for $Ur = 1.10$, $H_\mathrm{b}/\sigma = 6.50$. The ratio of the wave height expected at low probability levels ($H_{0.0001}$) to the wave breaking height (H_b) is then presented in Fig. 12. It is evident that, for low degrees of nonlinearity ($Ur = 0.39$ in this study), the breaking limit is well above the largest wave height, which is obtained in crossing seas. Therefore, the wave breaking should not have any significant effects on the statistical properties of the surface elevation.

For a moderate nonlinearity ($Ur = 0.62$), the breaking limit approximately matches the wave height at the probability level $P(H) = 0.0001$ (see Fig. 12).

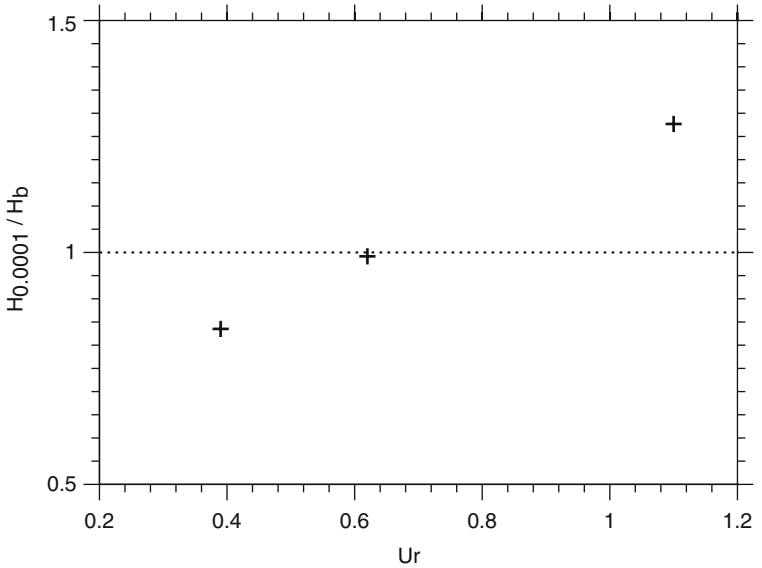

Fig. 12 Ratio of the simulated large wave height ($H_{0.0001}$) to wave breaking height (H_b) as a function of the Ursell number

However, since a very limited number of waves have been recorded to be higher than $H_{0.0001}$, we may expect that also for the case $Ur = 0.62$ the wave breaking does not affect the probability density function of wave elevation and wave height significantly. When $Ur > 0.62$, nevertheless, the breaking limit is rather small. Thus, wave heights at probability levels lower than 0.01 would break. As a result, the probability density function and the statistical moments would be significantly different than the ones obtained from the simulations.

7 Conclusions

The statistical properties of bimodal, shallow water wave fields have been discussed. A generalization of the Korteweg–de Vries equation in the (x, y) plane, the Kadomtsev–Petviashvili equation, has been used to describe two-dimensional waves in shallow water. The input spectra have been generated as a summation of two equivalent single-peaked spectra with different mean directions. We have used a JONSWAP spectral formulation to model the energy distribution in the frequency domain and a *cos-2s* function to model the directional domain. Considering several spectral cases with constant energy and different angles between the two peaks, many realizations have been simulated with different random phases. Different degrees of nonlinearity, as measured by the Ursell number, have been investigated.

Shallow water waves are characterized by an excess of high crests and shallow troughs, which produces a deviation from the Gaussian statistics. The simulated surface elevation, during single-peaked spectral conditions, shows a very skewed probability density function. When two noncollinear wave trains are considered in the wave field, their nonlinear interaction produces steep and high amplitude peaks. These peaks yield a modification of the upper tail of the probability density function for the surface elevation $\eta(x,y)$, which significantly deviates from the distribution of wave elevation in the unimodal condition. The coexistence of two spectral peaks, therefore, enhances the nonlinearity of the wave field, which results in an increase of the skewness and kurtosis. Whereas this enhancement is negligible for nearly collinear waves, the skewness and kurtosis reaches high values when the two spectral peaks have well separated directions. In particular, it has been observed that for $\vartheta^* \simeq 30^\circ$ their magnitudes maximize. Beyond the threshold $\vartheta^* \simeq 30^\circ$, the increasing trend of the skewness and kurtosis vanishes; for high degrees of nonlinearity, furthermore, skewness and kurtosis decrease. Formally speaking, the KP equation results from an expansion in which the directionality is a small parameter, therefore additional verification should be made with the Euler equations and laboratory experiments to confirm this finding.

It is important to mention that the model does not consider wave breaking. However, for a certain water depth and wavelength, waves can actually break. In this respect, the comparison between the wave height expected at low probability levels ($P(H) = 0.0001$) and the breaking limit has shown that wave breaking may only affect the statistical properties when large degree of nonlinearity ($Ur > 0.62$) and large angle ϑ^* are accounted for.

This work was carried out in the framework of the F.W.O. project G.0228.02 and G.0477.04., and the E.U. project SEAMOCS (contract MRTN-CT-2005-019374). The numerical simulations were performed by using the K.U. Leuven's High Performance Computing (HPC) facilities.

References

Battjes JA (1974) Surf similarity. In: Proceedings of the 14th international conference on coastal engineering, Copenhagen, Denmark

Bitner-Gregersen E, Eknes M (2001) Ship accidents due to bad weather. Technical Report 2001-1330, Det Norske Veritas

Demirbilek Z, Vincent L (2002) Water wave mechanics. In: Demirbilek Z, Vincent L (eds) Coastal engineering manual, Part II. Hydrodynamics, chap. II-1, Engineer manual 1110-2-1100. US Army Corps of Engineers, Washington, DC

Donelan M, Magnusson AK (2005) The role of meteorological focusing in generating rogue wave conditions. In: Proceedings of the 14th Aha Huliko a Hawaiian winter workshop, University of Hawaii at Manoa, USA, 24–28 January 2005

Fornberg B, Whitham GB (1978) A numerical and theoretical study of certain nonlinear wave phenomena. Philos Trans R Soc Lond Ser A 289:373–404

Forristall GZ (2000) Wave crests distributions: Observations and second-order theory. J Phys Ocean 30:1931–1943

Goda Y (2000) *Random seas and design on marine structures*. Advanced Series on Ocean engineering, vol. 15. World Scientific, Singapore

Greenslade DJM (2001) A wave modelling study of the 1998 sydney to hobart yacht race. Aust Met Mag 50:53–63

Hauser D, Kahma KK, Krogstad HE, Lehner S, Monbaliu J, Wyatt LW (eds) (2005) Measuring and analysing the directional spectrum of ocean waves. Cost Office, Brussels

Herbers THC, Orzech M, Elgar S, Guza RT (2007) Shoaling transformation of wave frequency-directional spectra. J Geophys Res 108(C1):doi:10.1029/2001JC001304

Janssen TT, Herbers THC, Battjes JA (2006) Generalized evolution equations for nonlinear surface gravity waves over two-dimensional topography. J Fluid Mech 552:393–418

Johnson RS (1997) A modern introduction to the mathematical theory of water waves. Cambridge University, Cambridge

Kadomtsev BB, Petviashvili VI (1970) On the stability of solitary waves in weakly dispersive media. Sov Phys Doklady 15:539–541

Komen GJ, Cavaleri L, Donelan M, Hasselmann K, Hasselmann H, Janssen PAEM (1994) Dynamics and modeling of ocean waves. Cambridge University, Cambridge

Lehner S, Günther H, Rosenthal W (2005) Extreme wave observations from radar data sets. In: Ocean waves measurements and analysis, Fifth international symposium WAVES 2005, Madrid, Spain, 3–7 July 2005, paper 69

Longuet-Higgins MS (1952) On the statistical distribution of the heights of sea waves. J Mar Res 11:1245–1266

Miles JW (1977a) Diffraction of solitary waves. Z Ang Math 28:889–902

Miles JW (1977b) Note on solitary wave on a slowly varying channel. J Fluid Mech 80:149–152

Onorato M, Osborne AR, Serio M (2006) Modulation instability in crossing sea states: A possible mechanism for the formation of freak waves. Phys Rev Lett 96:014503

Osborne AR, Petti M (1994) Laboratory-generated, shallow-water surface waves: analysis using the periodic, inverse scattering transform. Phys Fluids 6(5):1727–1744

Pelinovsky E, Sergeeva A (2006) Numerical modeling of the kdv random wave field. Eur J Mech B Fluids 25:425–434

Peterson P, Soomere T, Engelbrecht J, van Groesen E (2003) Soliton interaction as a possible model for extreme waves in shallow water. Nonlinear Proc Geophys 10:503–510

Segur H, Finkel A (1985) An analytical model of periodic waves in shallow water. Stud Appl Math 73:183–220

Shukla PK, Kaurakis I, Eliasson B, Marklund M, Stenflo L (2006) Instability and evolution of nonlinearly interacting water waves. Phys Rev Lett 97:094501

Soomere T, Engelbrecht J (2005) Extreme elevation and slopes of interacting solitons in shallow water. Wave Motion 41:179–192

Soomere T, Engelbrecht J (2006) Weakly two-dimensional interaction of solitons in shallow water. Eur J Mech B Fluids 25:636–648

Tanaka M (2001) A method of studying nonlinear random field of surface gravity waves by direct numerical simulations. Fluid Dyn Res 28:41–60

Tayfun AM (1981) Distribution of crest-to-trough wave heights. J Waterw Port C Ocean Eng 107(3):149–158

Tayfun MA (1980) Narrow-band nonlinear sea waves. J Geophys Res 85(C3):1548–1552

Toffoli A, Lefèvre JM, Bitner-Gregersen E, Monbaliu J (2006a) Towards the identification of warning criteria: Analysis of a ship accident database. Appl Ocean Res 27:281–291

Toffoli A, Onorato M, Monbaliu J (2006b) Wave statistics in unimodal and bimodal seas from a second-order model. Eur J Mech B Fluids 25:649–661

Ursell F (1953) The long wave paradox in the theory of gravity waves. Proc Camb Philos Soc 49:685–694

Modelling of Rogue Wave Shapes in Shallow Water

T. Talipova, Ch. Kharif, and J.-P. Giovanangeli

Abstract Various shapes of rogue waves are discussed within the framework of the mechanism of non-linear focusing of transient frequency modulated wave groups. A particular attention is paid to the formation of troughs in front of high crests. The conditions for appearance of the 'three sisters' are discussed too. It is important to emphasize that this mechanism is not too sensitive to the variation of the shape of transient frequency modulated wave groups. The variable-polarity shape of a rogue wave is more probable than only one crest or one trough, because the generation of the latter ones needs a specific phase relation between individual waves in the group.

1 Introduction

The interest in occurrence of abnormal huge waves on the sea surface has arisen a long time ago and the physical mechanisms generating these giant water waves are now well understood and documented (Kharif and Pelinovsky 2003). Rogue waves are observed everywhere, both in deep and shallow waters and sometimes even on beaches. The shapes of rogue waves are various. Sometimes they look like solitary waves, sometimes they appear as a group of waves (the 'three sisters') or as a wall of water (Mallory 1974; Torum and Gumestad 1990; Olagnon and Athanassoulis 2000; Chien et al. 2002; Rosenthal 2003). In some descriptions (see, Lavrenov 2003), a long shallow trough occurs in front of a very high crest (Fig. 1) and such a wave can be very dangerous for shipping.

Indeed, there is no unique representation of rogue wave shapes. In theory, until now main attention has been paid to the possible values reached by the amplitude or

T. Talipova
Institute of Applied Physics RAS, 46 Uljanov str. Nizhny Novgorod 603950 Russia
tata@hydro.appl.sci-nnov.ru

Ch. Kharif and J.-P. Giovanangeli
IRPHE Technopôle de Château – Gombert, 13384 Marseille cedex 13, France

E. Pelinovsky, C. Kharif (eds.) *Extreme Ocean Waves*, 71–81.

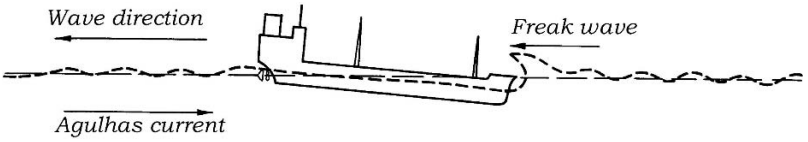

Fig. 1 Rogue wave collision with the 'Taganrorsky Zaliv' (from the book by Lavrenov (2003))

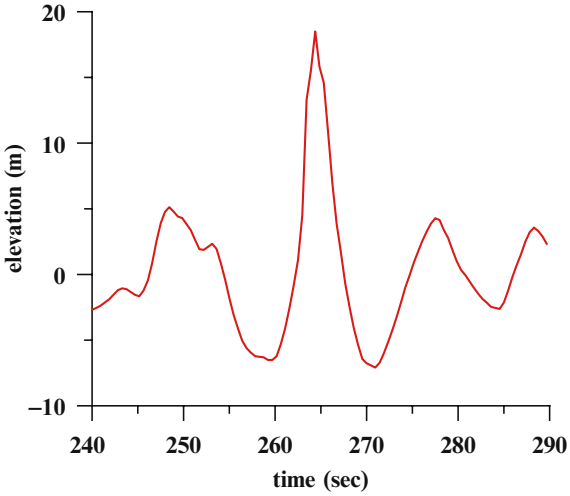

Fig. 2 The Draupner New Year wave (from the paper by Haver and Jan Andersen (2000))

height of freak waves, but not to their shapes. One attempt to explain the shape of the Draupner New Year wave (Fig. 2) from various non-linear water wave theories has been made in the paper by Walker et al. (2004).

Here, we discuss theoretical shapes of rogue waves in a basin of moderate depth due to the focusing of transient wave groups. As it is discussed in a review paper (Kharif and Pelinovsky 2003), various mechanisms of wave group focusing may be suggested by using (i) water wave amplitude and frequency variations in space due to wind action, (ii) non-linear modulational instability and (iii) sea current or sea bottom inhomogeneity. The simplest explanation of rogue wave occurrence due to transient group focusing may be described as follows (Kharif et al., 2001; Slunyaev et al., 2002). If initially short wave groups are located in front of longer wave groups having larger group velocities, then during the stage of evolution, longer waves will overtake shorter waves. A huge wave can occur at some fixed time because of the superposition of waves merging at a given location. Afterwards, the longer waves will be in front of the shorter waves and the amplitude of the highest wave will decrease. Such a mechanism has been reproduced in various laboratory tanks (Baldock and Swan 1996; Johannessen and Swan 2001; Brown and Jensen 2001; Clauss 2002; Shemer et al. 2006; Giovanangeli et al. 2005; Touboul et al. 2006; Kharif et al. 2008).

The elements of the non-linear dispersive theory of wave focusing are given in Sect. 2 and the results of the numerical model are described in Sect. 3.

2 Theoretical Model

The dynamics of non-linear long surface water waves on constant depth may be described by the Korteweg-de Vries equation (Dingemans 1996)

$$\frac{\partial \eta}{\partial t} + c\left(1 + \frac{3\eta}{2h}\right)\frac{\partial \eta}{\partial x} + \frac{ch^2}{6}\frac{\partial^3 \eta}{\partial x^3} = 0, \tag{1}$$

where η is the water surface elevation, h is the undisturbed water depth, $c = \sqrt{gh}$ is the linear speed of long surface wave and g is the gravity acceleration. Equation (1) may be reduced to dimensionless form (3) by the following transformations (2):

$$\zeta = \frac{\eta}{h}, \quad \tau = \frac{c}{h}t, \quad y = \frac{x - ct}{h}, \tag{2}$$

$$\frac{\partial \zeta}{\partial \tau} + \frac{3}{2}\zeta\frac{\partial \zeta}{\partial y} + \frac{1}{6}\frac{\partial^3 \zeta}{\partial y^3} = 0. \tag{3}$$

The effective process to generate transient wave group focusing in a rogue wave was suggested in a recent paper (Pelinovsky et al. 2000). It is based on the invariance of the Korteweg-de Vries equation (3) with respect to reversal of time and abscissa. It means that we may choose the expected form of freak wave $\zeta_{\mathrm{fr}}(x)$ as the initial condition for (3) and solve it for any time $t = T$. Solutions found analytically or numerically after reversal of abscissa $\zeta(-x)$ describes the wave train whose evolution may lead to the occurrence of waves of abnormal amplitude with the chosen shape $\zeta_{\mathrm{fr}}(x)$ and time $t = T$. From (3) solved within the framework of a deterministic approach, with zero boundary conditions when $|x|$ goes to ∞ and the shape of the abnormal wave described by positive pulse with amplitude A_0 and length L, we show that the process is controlled by the Ursell parameter (Kharif et al. 2000). Furthermore, it is shown in the paper by Pelinovsky et al. (2000) that for a single rogue wave the Ursell parameter satisfies the following condition:

$$\mathrm{Ur} = A_0 L^2 \ll 1. \tag{4}$$

The very steep wave appears due to the focusing of a group of waves of moderate amplitude. For the sake of simplicity this wave may be approximated by the δ-function

$$\varsigma_{\mathrm{f}}(y) = Q\delta(y). \tag{5}$$

The coefficient Q in (5) is equal to wave "mass"

$$M_{\mathrm{f}} = \int_{-\infty}^{\infty} \varsigma_{\mathrm{f}}(y)\mathrm{d}y = Q. \tag{6}$$

The potential energy of this wave is infinite formally. Within the framework of (3), which may be solved by using the method of inverse scattering transform (Drazin and Johnson 1993), the delta-pulse (5) evolves into a solitary wave

$$\varsigma_s = A_s \mathrm{sech}^2 \left[\gamma(y - (1 + A_s/2)\tau)\right], \tag{7}$$

with dimensionless amplitude A_s and inverse width γ

$$A_s = \frac{3}{4}Q^2 \qquad \gamma = \sqrt{\frac{3}{4}A_s} = \frac{3}{4}Q. \tag{8}$$

There is a dispersive tail spreading in space and damping in time. The solitary wave mass M_s and its energy E_s are conserved in time and equal to

$$M_s = \frac{A_s}{\gamma}\int_{-\infty}^{\infty} \mathrm{sech}^2 z \, \mathrm{d}z = \frac{2A_s}{\gamma} = 2Q, \tag{9}$$

$$E_s = \frac{A_s^2}{\gamma}\int_{-\infty}^{\infty} \mathrm{sech}^4 z \, \mathrm{d}z = \frac{4A_s^2}{3\gamma} = Q^3. \tag{10}$$

We emphasize that the solitary wave mass is larger than twice the rogue wave mass; therefore, incipient dispersive tail has negative mass

$$M_t = -Q. \tag{11}$$

The energy of dispersive tail goes to infinity as also the energy of the initial delta-pulse. Hence, if the solitary wave is deleted from the wavefield, the energy of dispersive tail is large enough to produce a wave of abnormal amplitude. Since dispersive tail mass is negative, it is reasonable to assume that the deep negative trough prevails in the rogue wave generation. Dispersive wave tail, especially with small amplitude, within the framework of the Korteweg-de Vries equation, evolves like the Airy function, and because its mass M_t, according to (11), is proportional to the mass of expected rogue wave Q, the waves in the dispersive tail contain the information about both time (or position) of rogue wave occurrence and rogue amplitude due to self-similarity of the Airy function.

When the initial rogue wave disturbance has negative polarity, solitary waves are not generated irrespective of the Ursell parameter value, and the whole energy goes into damping dispersive wave train. Let us mention that within the framework of an idealized problem, solitary waves prevent the formation of rogue waves whose amplitude has to be higher not only than the amplitude of the dispersive tail but also higher than solitary wave amplitudes, constant in time. Hence, it is reasonable to suggest that without solitary waves in dispersive tail, the formation of rogue wave of variable-polarity is more probable. In this case, the condition about the Ursell parameter is satisfied.

3 Numerical Model

The numerical integration of the Korteweg-de Vries equation (3) is based on a finite-difference scheme that satisfies the Courant criterion. The main goal of the numerical simulations is to analyse the conditions of variable-polarity rogue wave generation from transient wave groups without solitary waves.

Following Pelinovsky et al. (2000), we generate numerically transient wave groups from a short Gaussian pulse given by $A_f \exp(-y^2/L^2)$. The corresponding Ursell parameter is sufficiently small. The transient group corresponds to a solitary wave plus a damping dispersive wave train. After reversing of abscissa, this transient wave group focuses again into the rogue wave with the Gaussian pulse shape. This process is shown in Fig. 3 for two values of the Gaussian pulse amplitude 0.2 and 0.4 and the same width $L = 0.55$. In this case, the rogue wave occurs at $\tau = 2{,}000$. Amplitudes of generated rogue waves in both cases (Fig. 3b) are more than four times larger than the amplitude of the corresponding solitary waves in initial wave transient groups (Fig. 3a), and it is more than the criterion needed for the freak wave occurrence: the amplitude of the freak wave has to be more than twice the amplitude of background waves.

Note that amplitudes of generated solitary waves in both runs differ from one another by a factor of 4 (0.025–0.092), whereas the amplitudes of dispersive tails differ by a factor of 2. So, this simple numerical experiment confirms our theoretical conclusions that influence of amplitude of the dispersive tail on the amplitude of the rogue wave is strong (practically linear when the Ursell parameter is very weak).

Additional numerical simulations were run corresponding to truncated transient wave groups: the solitary wave has been ignored. Hence, we consider the mechanism of rogue wave formation directly from the dispersive tail alone. Results of

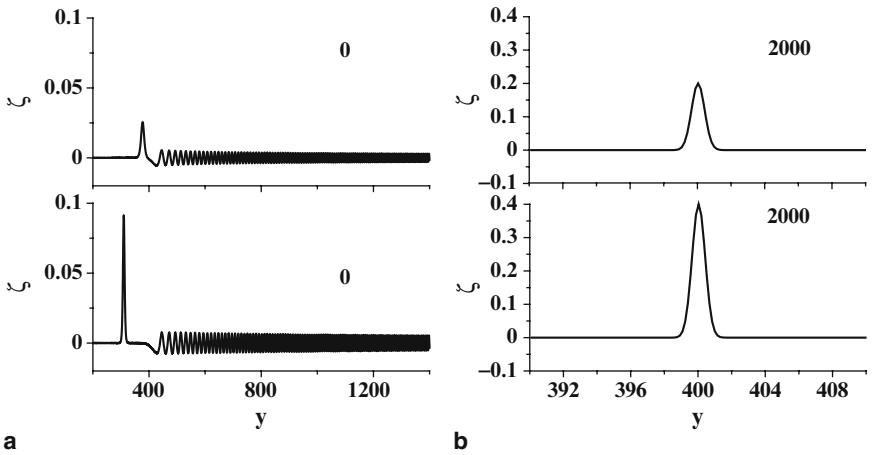

Fig. 3 Transient wave groups (**a**), leading to the formation of a Gaussian pulse of positive polarity (**b**) with amplitude values 0.2 (*black*) and 0.4 (*red*). The width is 0.55

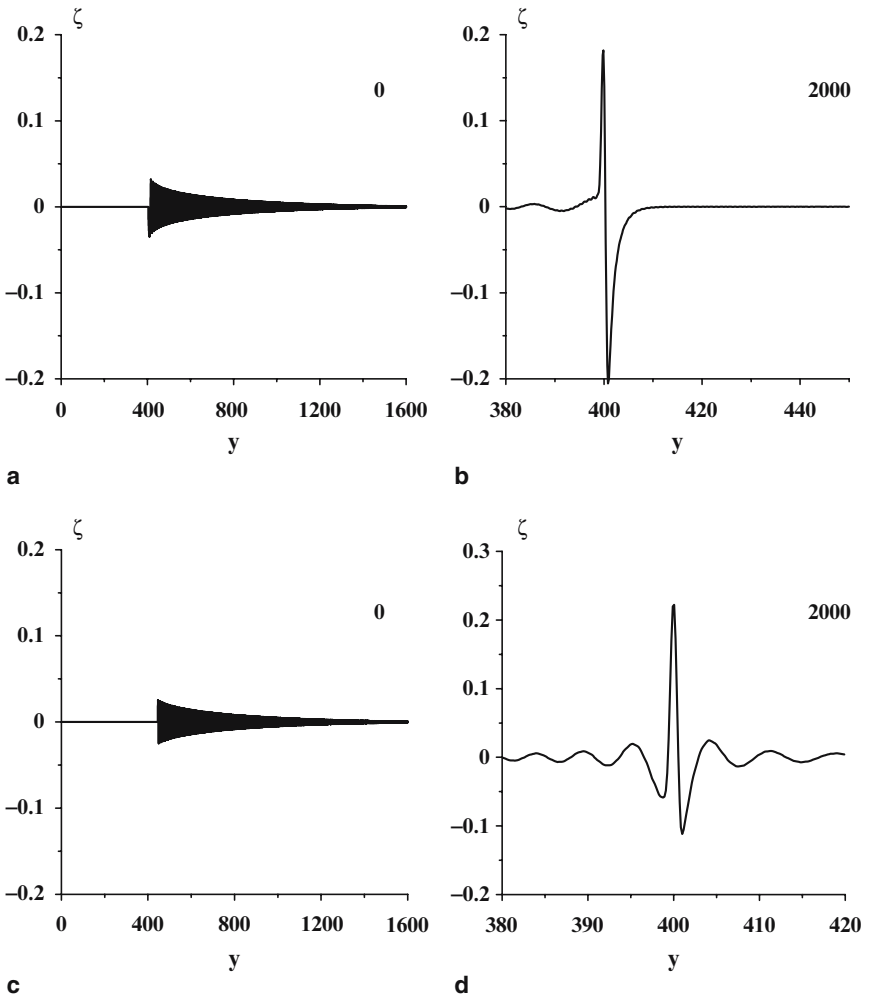

Fig. 4 (**a**) Initial dispersive wave train; (**b**) rogue wave generated by dispersive focusing; (**c**) initial wave train where one negative half-wave is deleted; (**d**) rogue wave generated by focusing of this wave train

these runs are shown in Fig. 4. Because of dispersive focusing of the tail (Fig. 4a), the variable-polarity high amplitude wave is generated (Fig. 4b) and its height (from trough to crest) is equal to 0.4, that is the same height as that of the rogue wave generated from the full wave group, including the solitary wave. The excess of wave height above the initial height of dispersive tail is about 6.7, and so such a wave satisfies the amplitude criterion of rogue wave occurrence. It is evident that the negative trough of the rogue wave is longer than the positive crest, and negative total mass described into Sect. 2 is conserved.

So the evolution of the dispersive tail allows us to explain the appearance of the long trough (which has a specific shape within the framework of an idealized model) ahead of the positive pulse as it is described in the book by Lavrenov (2003).

The amplitude of oscillations in the dispersive tail varies significantly with wave position, and the mass distribution here is very non-uniform. So, if we delete the last high-energy negative half-wave (Fig. 4c), the mass of the tail is modified significantly, and the rogue wave, which focuses from such a tail after reversing of abscissa, consists of one high peak and moderately deep troughs (Fig. 4d). It is interesting to note that the wave shape in Fig. 4d is similar to the New Year wave (Fig. 2). Despite the fact that the rogue wave height becomes smaller (0.33 against 0.4 in the previous case), the excess of wave height above the initial height of the dispersive tail is about 6.7 as in the previous case. Thus, the mass of dispersive wave train influences significantly the shape of the rogue wave, but in any case we obtain the variable-polarity rogue wave. A second series of numerical simulations has been performed corresponding to a Gaussian pulse of negative polarity. Its focusing leads to the occurrence of abnormal deep trough on the sea surface (Fig. 5). It is well known that during the evolution of such a pulse, solitary waves do not occur and the shape of the transient wave group is close to the Airy function profile, especially for small values of the amplitude. The maximal wave height (from trough to crest) in the tail in Fig. 4a is 0.1, while the pulse amplitude is 0.2. So, the amplitude criterion of rogue wave is satisfied in this case too.

The removal of back long negative half-wave from the wave train is shown in Fig. 5a (see Fig. 6a). The generation of a trough in front of the high positive pulse is observed (Fig. 6b). However, in this situation the trough with larger amplitude is behind the crest and following crests also. This is close to the wave packet often called in literature the three sisters. The decrease in elevation between the first

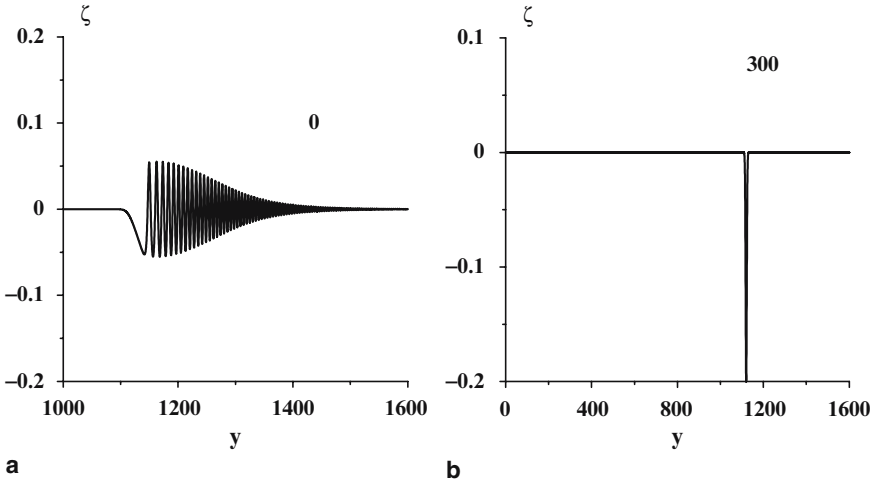

Fig. 5 (**a**) Initial wave train; (**b**) its transformation into a Gaussian pulse of negative polarity

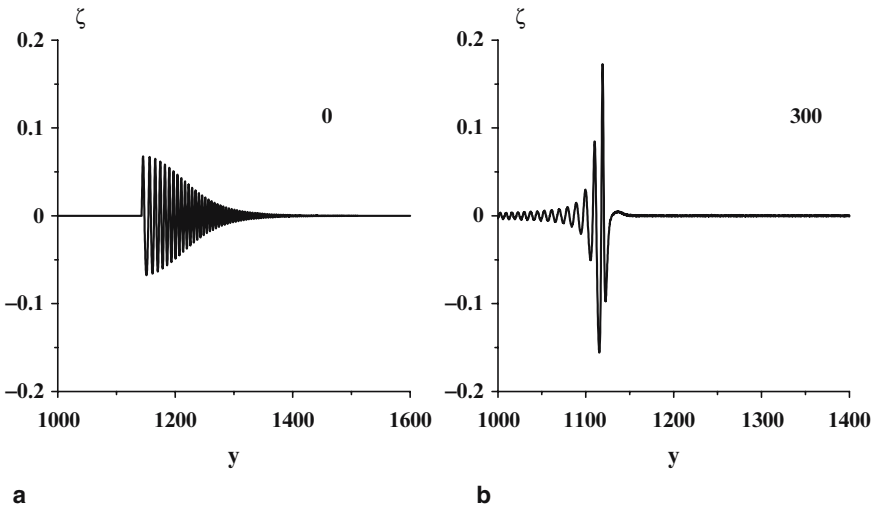

Fig. 6 (**a**) Initial wave train; (**b**) transformation into 'three sisters'

crest and following trough is equal to 0.33, that is more than three times the height of the initial dispersive wave train, and the amplitude criterion is satisfied. Thus, our assumption that any dispersive wave train without solitons may generate the variable-polarity rogue wave is confirmed by the evolution of this class of transient wave group also.

For the third series of numerical experiments, the rogue wave generation from a transient wave group has been chosen as a wave with a shape close to that shown in the book by Lavrenov (2003) (see Fig. 1). For this case, the solitary wave and dispersive wave tail used are shown in Fig. 6a. The evolution of this wavefield is the chosen 'Lavrenov's' rogue wave (Fig. 7b). We fixed its amplitude large enough to obtain a decrease in the elevation of the initial wave packet (Fig. 7a) more than three times.

The main characteristic feature observed in the wavefield of the dispersive train in comparison with cases shown above is a non-monotonic modulation, which may be interpreted as an almost linear interference of both wave trains generated by positive and negative parts of initial rogue wave in the direct simulation.

A more realistic situation has been suggested for the fourth series of runs. This situation is closed to experimental results obtained in the Hannover tank and described by Shemer et al. (2006). A dispersive wave tail shown in Fig. 8a has been obtained from the wave packet given in Fig. 4a multiplied by a Gaussian envelope $A_g \exp(-(y-b)^2/L^2)$, where $A_g = 1,\ b = 800,\ L = 200$. Evolution of this packet also leads to the generation of the three sisters (Fig. 8b) and the maximal wave height of this group is ten times larger than the maximal height of the initial wave packet.

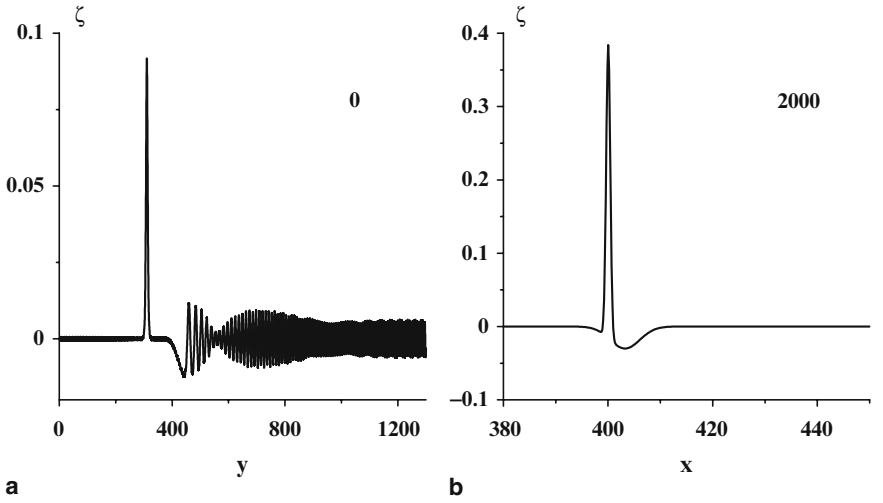

Fig. 7 (**a**) Initial wave packet; (**b**) transformation into 'Lavrenov's' wave

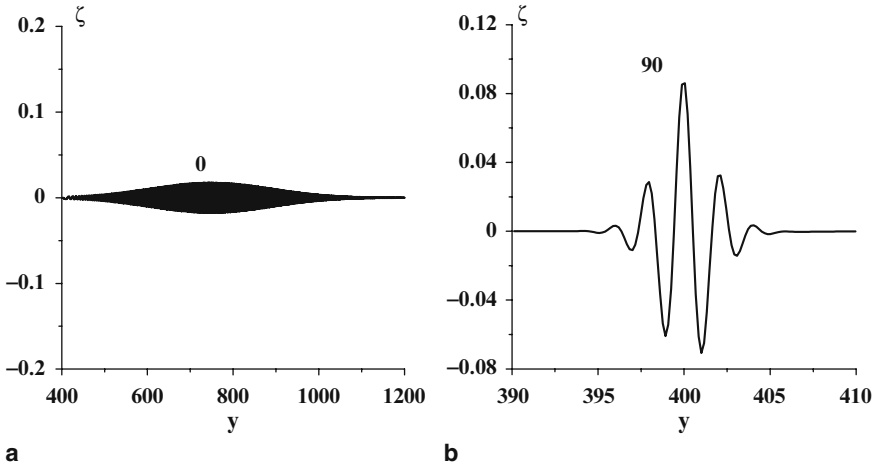

Fig. 8 (**a**) Initial wavefield; (**b**) transformation into 'three sisters'

4 Conclusions

Within the framework of non-linear-dispersive mechanism, relevant variety of shapes of rogue waves may be obtained, including the Lavrenov's wave, which consists of a huge crest and a long trough in front of it. It is important to emphasize that this mechanism is not too sensitive to the variation of the shape of transient wave groups. The optimal focusing of transient wave groups which requires a special phase relation gives the best conditions for rogue wave occurrence with huge

amplitude. Nevertheless, the amplitude criterion is satisfied for conditions of strong deformations of the wave group, initially leading to optimal focusing, as it is shown in this work. It is clear from this simple theory that we can always get any natural form of abnormal wave. Within the framework of this model the generation of the Lavrenov's wave and the three sisters is of equal probability. From our point of view, today in situ data of abnormal waves does not mark out any preferable shapes of rogue waves. The question about the more probable shapes of abnormal wave is an open question. It seems that the shape of a rogue wave in the form of a crest and a trough is more probable than only one crest or only one trough, because the generation of the latter ones needs a specific phase relation. In future, we study the shapes of rogue waves within the framework of direct numerical simulations of random wind wave fields.

Acknowledgements The authors devote this paper in memory of Igor Lavrenov who was one of the pioneers to investigate rogue wave dynamics. This work was partially supported by the grants of RFBR No 06-05-64232, 06-05-72011 (for TT) and INTAS No 06-1000013-9236.

References

Baldock TE, Swan C (1996) Extreme waves in shallow and intermediate water depths. Coast Eng 27:21–46

Brown MG, Jensen A (2001) Experiments on focusing unidirectional water waves. J Geophys Res 106(C8):16917–16928

Chien H, Kao CC, Chuang LZH (2002) On the characteristics of observed coastal freak waves. Coast Eng J 44(4):301–319

Clauss G (2002) Dramas of the sea: Episodic waves and their impact on offshore structures. Appl Ocean Res 24:147–161

Dingemans MW (1996) Water wave propagation over uneven bottoms. World Scientific, Singapore

Drazin PG, Johnson RS (1993) Solitons: An introduction. Cambridge University Press, Cambridge, England

Giovanangeli JP, Kharif C, Pelinovsky E (2005) Experimental study of the wind effect on the focusing of transient wave groups. In: Olagnon M, Prevosto M (eds) Rogue waves 2004 (Brest, France, 2000). Ifremer, France

Haver S, Jan Andersen O (2000) Freak waves: Rare realizations of a typical population or typical realizations of a rare population? In: Proceedings of the tenth international offshore and polar engineering conference, Seattle, USA

Johannessen TB, Swan C (2001) A laboratory study of the focusing of transient and directionally spread surface water waves. Proc R Soc Lond Ser A 457:971–1006

Mallory JK (1974) Abnormal waves on the south-east of South Africa. Inst Hydrod Rev 51:89–129

Kharif C, Pelinovsky E (2003) Physical mechanisms of the rogue wave phenomenon. Eur J Mech B Fluids 22:603–634

Kharif C, Pelinovsky E, Talipova T (2000) Formation de vagues géantes en eau peu profonde. Comptes Rendus de l'Academie des Sciences 328(serie IIb, 11):801–807

Kharif C, Pelinovsky E, Talipova T, Slunyaev A (2001) Focusing of nonlinear wave groups in deep water. JETP Lett 73(4):190–195

Kharif C, Giovanangeli JP, Touboul J, Grare L, Pelinovsky EN (2008) Influence of wind on extreme wave events: Experimental and numerical approaches. J Fluid Mech 594:209–247

Lavrenov IV (2003) Wind waves in ocean. Springer, Berlin Heidelberg New York

Olagnon M, Athanassoulis GA (eds) (2001) Rogue Waves 2000. Ifremer, France
Pelinovsky E, Talipova T, Kharif C (2000) Nonlinear dispersive mechanism of the freak wave formation in shallow water. Phys D 147(1–2):83–94
Rosenthal W (2003) MaxWave. Rogue waves: Forecast and impact on marine structures. GKSS Research Center, Geesthacht, Germany
Shemer L, Goulitski K, Kit E (2006) Steep transient waves in tank– Experiments and simulations. Proceedings of OMAE, 4–9 June 2006, Hamburg, Germany
Slunyaev A, Kharif C, Pelinovsky E, Talipova T (2002) Nonlinear wave focusing on water of finite depth. Phys D 173(1–2):77–96
Torum A, Gudmestad OT (eds) (1990) In: Water wave kinematics, Kluwer, Dordrecht
Touboul J, Giovanangeli JP, Kharif Ch, Pelinovsky E (2006) Experiments and simulations of freak waves under the action of wind. Eur J Mech B: Fluids 25(5):662–676
Walker DAG, Taylor PH, Eatock Taylor R (2004) The shape of large surface waves on the open sea and the Draupner new year wave. Appl Ocean Res 26:73–83

Runup of Long Irregular Waves on Plane Beach

Ira Didenkulova, Efim Pelinovsky, and Anna Sergeeva

Abstract Runup of irregular waves, modeled as superposition of Furrier harmonics with random phases, is studied in frames of nonlinear shallow water theory. The possibility of appearance of freak waves on a beach is analyzed. The distribution functions of runup characteristics are computed. An incident wave represents an irregular sea state with Gaussian spectrum. The asymptotic of probability functions in the range of large amplitudes for estimation of freak wave formation in the shore is studied. It is shown that average runup height of waves with wide spectrum is higher than that of waves with narrow spectrum.

1 Introduction

Descriptions of unusually high waves appearing on the sea surface for a short time (freak, rogue, or killer waves) have been considered as a part of marine folklore for a long time. A number of instrumental registrations have appeared recently making the community to pay more attention to this problem and to reconsider known observations of freak waves: some of them are collected in the paper by Torum and Gudmestad (1990), by Olagnon and Athanassoulis (2001), by Kharif and Pelinovsky (2003), and by Rosenthal (2003). Such unusual waves are also observed in the coastal zone and the probability of their appearance is rather high. One of the first works (Sand et al. 1990) already presents data of freak wave observations in the shallow part of the North Sea (on the depth of 20 m). Chien et al. (2002) report about 140 freak wave events in the coastal zone of Taiwan in the past 50 years (1949–1999) that caused loss of 500 people and destruction of 35 ships. According

I. Didenkulova
Institute of Cybernetics, Tallinn, University of Technology, Tallinn, Estonia
dii@hydro.appl.sci-nnov.ru

I. Didenkulova, E. Pelinovsky, and A. Sergeeva
Institute of Applied Physics, Nizhny Novgorod, Russia

E. Pelinovsky, C. Kharif (eds.) *Extreme Ocean Waves*, 83–94.

Fig. 1 Freak wave attacks the breakwater in Kalk Bay, South Africa, on 26 August 2005

to Didenkulova et al. (2006a), two-third of the freak wave events that occurred in 2005 were observed onshore. Thus, a freak wave attacked the breakwater in Kalk Bay (South Africa) on 26 August 2005 and washed off the breakwater people, and some of them were injured (Fig. 1). Two months later on 16 October 2005, two freak waves induced panic at Maracas Beach (Trinidad Island, Lesser Antilles), when a series of towering waves, many more than 25 feet high (maximal height of 8 m), flooded the beach, carried sea-bathers, venders, and lifeguards, running for their lives.

Thus, analysis of freak waves on a coast is an important task for practice. Here we investigate distribution functions of the runup height and velocity on a beach, assuming that distribution functions in the coastal zone are known and waves do not break. The analytical shallow water theory, described in Spielfogel (1976), Pedersen and Gjevik (1983), Synolakis (1987), Pelinovsky and Mazova (1992), Tadepalli and Synolakis (1994), Carrier et al. (2003), Tinti and Tonini (2005), Kânoğlu and Synolakis (2006), Didenkulova et al. (2006b, 2007a,b) is used as theoretical model. The paper is organized as follows. The theoretical model of the long wave runup is described in Sect. 2. The runup of irregular waves on a plane beach is discussed in Sect. 3. Main results are summarized in Sect. 4.

2 Theoretical Model of the Long Wave Runup

The dynamics of a wave climbing the beach can be described in the framework of the shallow water equations. The simplified geometry of the coastal zone is shown in Fig. 2.

The wave comes onshore from the left. Sketchy, the incident wave is presented as a single crest, but then we consider the incident wave as a continuous function

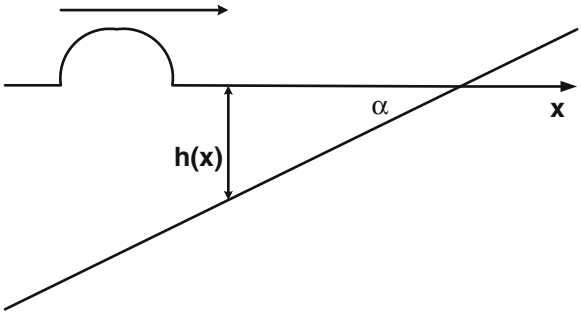

Fig. 2 Definition sketch for the wave runup problem

representing random crests and troughs. The basic equations for water waves in shallow water are ($\eta(x,t)$ is the vertical displacement of the sea level, $u(x,t)$ is the depth averaged velocity of the water flow)

$$\frac{\partial \eta}{\partial t} + \frac{\partial}{\partial x}\left[(h(x)+\eta)\,u\right] = 0,$$
$$\frac{\partial u}{\partial t} + u\frac{\partial u}{\partial x} + g\frac{\partial \eta}{\partial x} = 0, \tag{1}$$

where $h(x) = -\alpha x$. In this case, the nonlinear shallow-water equations (1) can be solved with the use of Riemann invariants and the Legendre (hodograph) transformation (Carrier and Greenspan 1958). Let us introduce the Riemann invariants

$$I_{\pm} = u \pm 2\sqrt{g(h+\eta)} + g\alpha t \tag{2}$$

and rewrite system (1) in the following form:

$$\frac{\partial I_{\pm}}{\partial t} + c_{\pm}\frac{\partial I_{\pm}}{\partial x} = 0, \tag{3}$$

where characteristic speeds are

$$c_{\pm} = \frac{3}{4}I_{\pm} + \frac{1}{4}I_{\mp} - g\alpha t. \tag{4}$$

The system (3)–(4) is still nonlinear, as characteristic speeds $c_{\pm}$ contain time t; however, it can be reduced to linear by excluding the coordinate x. After introducing new variables

$$\lambda = \frac{I_+ + I_-}{2} = u + g\alpha t, \qquad \sigma = \frac{I_+ - I_-}{2} = 2\sqrt{g(h+\eta)}, \tag{5}$$

we obtain the linear wave equation to describe the long wave runup process

$$\frac{\partial^2\Phi}{\partial\lambda^2} - \frac{\partial^2\Phi}{\partial\sigma^2} - \frac{1}{\sigma}\frac{\partial\Phi}{\partial\sigma} = 0, \tag{6}$$

and all physical variables can be expressed through the function $\Phi(\lambda,\sigma)$

$$\eta = \frac{1}{2g}\left(\frac{\partial\Phi}{\partial\lambda} - u^2\right), \qquad u = \frac{1}{\sigma}\frac{\partial\Phi}{\partial\sigma}, \tag{7}$$

$$t = \frac{1}{\alpha g}\left(\lambda - \frac{1}{\sigma}\frac{\partial\Phi}{\partial\sigma}\right), \qquad x = \frac{1}{2\alpha g}\left(\frac{\partial\Phi}{\partial\lambda} - u^2 - \frac{\sigma^2}{2}\right). \tag{8}$$

The physical sense of the variable σ is the total water depth, and $\sigma = 0$ corresponds to the moving shoreline. Various calculations of the wave field and runup characteristics using the Carrier–Greenspan transformation can be found in Spielfogel (1976), Pedersen and Gjevik (1983), Synolakis (1987), Pelinovsky and Mazova (1992), Tadepalli and Synolakis (1994), Carrier et al. (2003), Tinti and Tonini (2005), Kânoğlu and Synolakis (2006), Didenkulova et al. (2006b, 2007a,b). Surprising result concluded here from linear equation (6) is that the extreme runup characteristics (runup and rundown amplitudes, runup velocities) can be calculated in the framework of linear shallow-water theory if the incident wave approaches to the beach from the open sea. Particularly, the runup amplitude $R_{\sin}$ of incident sine wave with amplitude A, wavelength λ, and frequency ω given at the point $x = L$ with the depth h is

$$\frac{R_{\sin}}{A} = \left(\frac{16\pi^2\omega^2 h}{g\alpha^2}\right)^{1/4} = 2\pi\sqrt{\frac{2L}{\lambda}}. \tag{9}$$

Meanwhile, the water oscillation on shore will not have simple sine shape; see Fig. 3 for various values of the breaking parameter $\mathrm{Br} = R_{\sin}\omega^2/g\alpha^2$ (condition $\mathrm{Br} = 1$ corresponds to the wave breaking on shore).

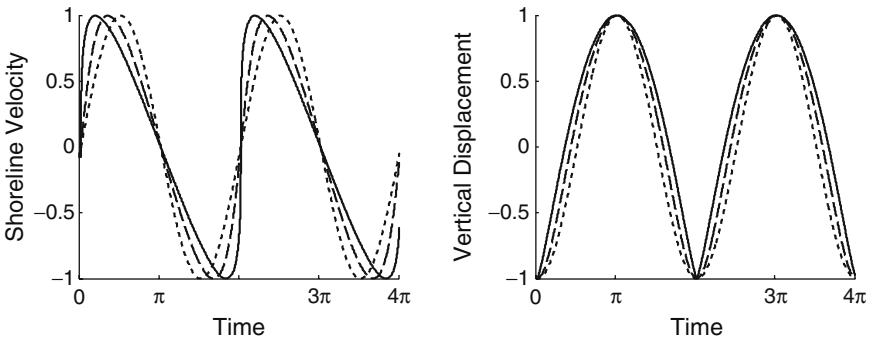

Fig. 3 Velocity and vertical displacement of the moving shoreline for incoming sine wave; the breaking parameter $\mathrm{Br} = 0$ (*dotted line*), 0.5 (*dashed line*), and 1 (*solid line*); time is normalized by wave frequency ω^{-1}, vertical displacement by $R_{\sin}$, and shoreline velocity by $\omega R_{\sin}/\alpha$

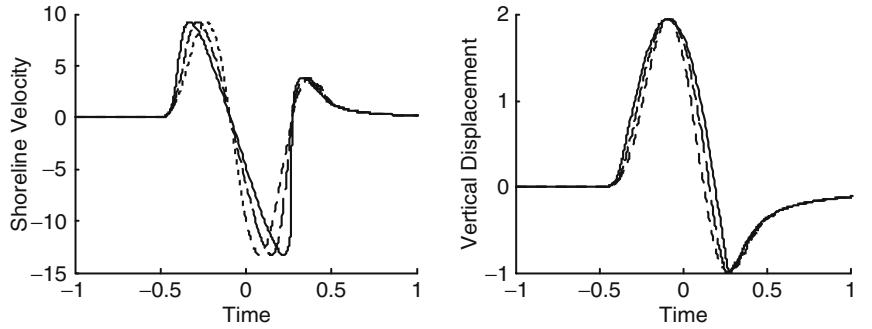

Fig. 4 Velocity and vertical displacement of the moving shoreline for incoming $\sin^4(\omega t)$ pulse; the breaking parameter Br = 0 (*dotted line*), 0.5 (*dashed line*), and 1 (*solid line*); time is normalized by wave frequency ω^{-1}, vertical displacement by $R_{\sin}$, and shoreline velocity by $\omega R_{\sin}/\alpha$

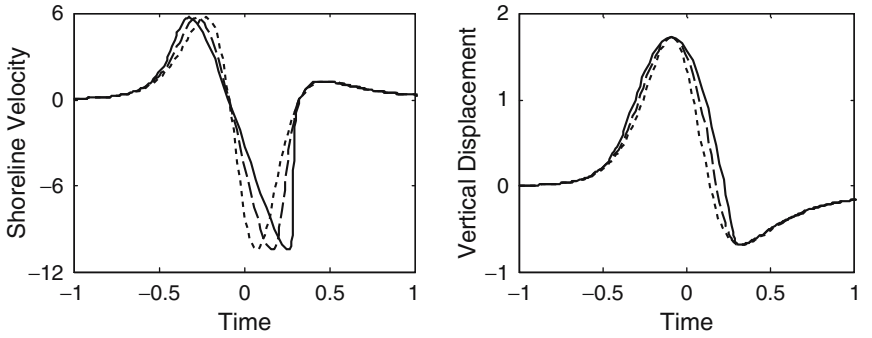

Fig. 5 Velocity and vertical displacement of the moving shoreline for incoming soliton $\mathrm{sech}^2(4t/T_0)$; the breaking parameter Br = 0 (*dotted line*), 0.5 (*dashed line*), and 1 (*solid line*); time is normalized by the duration of the pulse T_0, vertical displacement by $R_{\sin}$, and shoreline velocity by $\omega R_{\sin}/\alpha$

The runup of waves of different types, for instance solitary waves, can be also described by formulas (6)–(8). Water oscillations and velocities on shore for the runup of a sine pulse and a soliton are presented on Figs. 4 and 5 for different values of the breaking parameter Br.

3 Runup of Irregular Waves

Formulas (6)–(8) can be applied to describe the runup of irregular long waves as well. Because of implicity of the Carrier–Greenspan transformation it is rather difficult to calculate wave characteristics. But for calculations of the extreme runup characteristics, the linear approach can be applied (Synolakis 1991; Pelinovsky and Mazova 1992), and in this case we need to find extremes of the Fourier series

$$\eta\,(t,x=0)=\int\left(\frac{16\pi^2 h}{g\alpha^2}\right)^{1/4}\omega^{1/2}A(\omega)\exp\left[\mathrm{i}\left(\omega\,(t-\tau)+\phi\,(\omega)+\frac{\pi}{4}\right)\right]\mathrm{d}\omega, \tag{10}$$

$$u\,(t,x=0)=\frac{1}{\alpha}\int\left(\frac{16\pi^2 h}{g\alpha^2}\right)^{1/4}\omega^{3/2}A\,(\omega)\exp\left[\mathrm{i}\left(\omega\,(t-\tau)+\phi\,(\omega)+\frac{3\pi}{4}\right)\right]\mathrm{d}\omega, \tag{11}$$

where A and ϕ are spectral amplitudes and phases, ω is the basic frequency of the incident wave

$$\eta\,(t,x=L)=\int A(\omega)\exp\left[\mathrm{i}\,(\omega t+\phi\,(\omega))\right]\mathrm{d}\omega, \tag{12}$$

and τ is travel time to the coast. We wish to repeat that series (10)–(11) can be used to calculate positive and negative runup amplitudes but not moments and distribution functions of the water displacement at the shoreline. This approach has been used in Didenkulova et al. (2007a) to study the runup of nonsinusoidal waves.

Now we consider the transformation of irregular waves when they climb a beach and estimate distribution functions of the water displacement at the shoreline assuming distribution functions of the water displacement at the coastal zone to be known and waves do not break.

The ensemble of realizations with random phases ϕ is taken for a numerical simulation of irregular waves. For this purpose we quantize Fourier series (10)–(12) and use real functions, whereupon equations for incoming wave, displacement, and velocity of the shoreline in nondimensional variables can be rewritten as

$$\eta\,(t,x=L)=\sum_{n=1}^{N}A_n\cos\left(\omega_n t+\phi_n\right), \tag{13}$$

$$\eta\,(t,x=0)=\sum_{n=1}^{N}\sqrt{\omega_n}A_n\cos\left(\omega_n t+\phi_n+\frac{\pi}{4}\right), \tag{14}$$

$$u\,(t,x=0)=\sum_{n=1}^{N}\omega_n^{3/2}A_n\cos\left(\omega_n t+\phi_n+\frac{3\pi}{4}\right), \tag{15}$$

where $A_n=\sqrt{2S(\omega_n)\Delta\omega}$ are calculated through the frequency spectrum of incoming wave $S(\omega)$, $\Delta\omega=2\pi/T$ is the sampling rate, T is the size of time calculated domain, and $\omega_n=n\Delta\omega$. Random spectral phases ϕ_n are distributed uniformly at the interval $(0,\ 2\pi)$.

First, let us consider random wave field with Gaussian statistics, where the frequency spectrum of incoming wave $S(\omega)$ is

$$S(\omega)=Q\exp\left[-\frac{(\omega-\omega_0)^2}{2l^2}\right], \tag{16}$$

with the central frequency ω_0 and the spectrum width l. Constant Q in (16) can be found from the condition

$$\sigma^2 = 2\int_0^\infty S(\omega)\mathrm{d}\omega, \tag{17}$$

then

$$Q = \frac{\sigma^2}{\sqrt{2\pi}l\,\mathrm{erfc}(-\omega_0/\sqrt{2}l)}, \tag{18}$$

where

$$\mathrm{erfc}(z) = \frac{2}{\sqrt{\pi}}\int_z^\infty \exp(-t^2)\mathrm{d}t \tag{19}$$

is a complementary error function.

In this case, frequency spectra for the shoreline displacement $S_r(\omega)$ and the shoreline velocity $S_u(\omega)$ are

$$S_r(\omega) = \frac{4\pi L\omega}{c}Q\exp\left[-\frac{(\omega-\omega_0)^2}{2l^2}\right], \tag{20}$$

$$S_u(\omega) = \frac{4\pi L\omega^3}{c\alpha^2}Q\exp\left[-\frac{(\omega-\omega_0)^2}{2l^2}\right]. \tag{21}$$

All these spectra in nondimensional variables for $l = 0.5$ are shown on Fig. 6. It is obvious that spectra for the shoreline displacement $S_r(\omega)$ and the shoreline velocity $S_u(\omega)$ are asymmetric and shifted to the high-frequency area.

Distribution functions for maximal amplitudes (positive and negative) of the wave field, defined as maximum (minimum) between two zero points, are important for applications. Detailed calculations of the distribution functions of the runup amplitudes are given in (Sergeeva and Didenkulova 2005). The Fourier series of $N = 512$ harmonics and sampling rate $\Delta\omega = 0.01$ are used. Spectrum width l is changed from 0.1 to 0.7. All statistical characteristics are obtained with the use of ensemble averaging over 500 realizations.

The occurrence probability of the wave with amplitude A for a Gaussian narrow-band process can be described by Rayleigh distribution (Massel 1996)

$$P(A) = \exp\left(-2A^2\right), \tag{22}$$

where A is the wave amplitude normalized on significant amplitude A_s, which is defined as $A_\mathrm{s} \approx 2\sigma$. For the numerical estimation of positive (negative) amplitude distribution, the statistical "frequency" F (ratio of a number of waves m with fixed amplitude a to a general number of waves)

$$F = \frac{m}{N}, \tag{23}$$

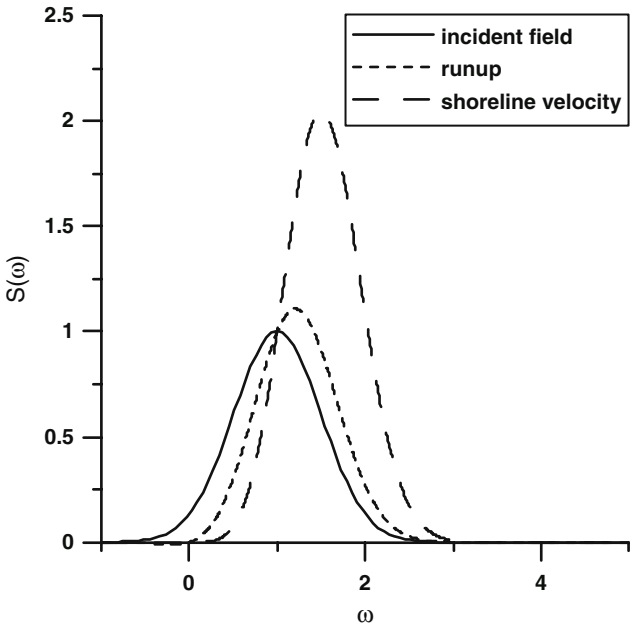

Fig. 6 Incident field, runup, and shoreline velocity spectra for $l = 0.5$

and statistical distribution function of amplitude (occurrence frequency of waves with amplitude A larger than a)

$$P(a) = F(A > a). \tag{24}$$

are calculated. For the narrow-band incident wave field ($l = 0.1$), the distribution functions of the runup characteristics are described by the Rayleigh distribution, as it is expected due to linearity expressions for extreme characteristics. If the spectrum of incident wave is wider ($l = 0.7$), the asymmetry of displacement and velocity spectra increases, but nevertheless distribution functions of the maximal shoreline displacement (Figs. 7 and 8) and the maximal shoreline velocity (Fig. 9) differ from the Rayleigh low weakly.

Knowing spectral and probability distributions of the wave field runup characteristics on a beach can be calculated. Thus the significant runup height of the wave on a beach is

$$R_s = \sqrt{\frac{4\pi\omega_0 L}{c}} A_s F\left(\frac{\omega_0}{l}\right) = 2\pi\sqrt{\frac{2L}{\lambda}} A_s F\left(\frac{\omega_0}{l}\right), \tag{25}$$

where function $F(z)$ describes influence of the incident wave spectrum width

$$F(z) = \sqrt{1 + \frac{\exp(-z^2/2)}{\sqrt{\pi/2}z\,\mathrm{erfc}(-z/\sqrt{2})}}. \tag{26}$$

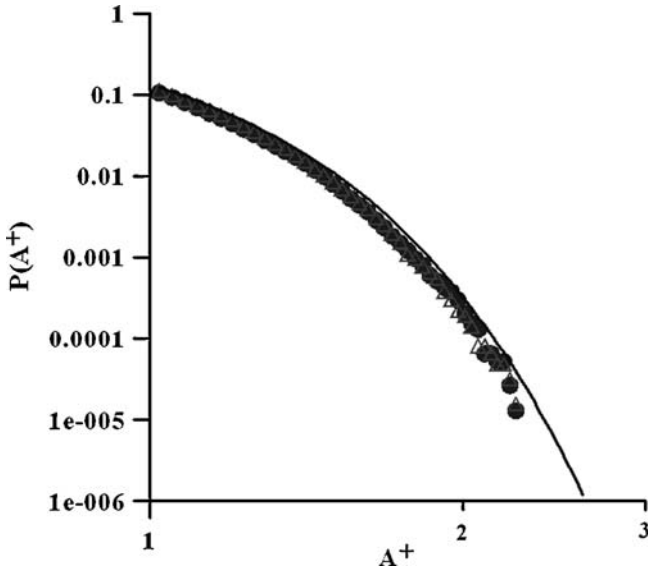

Fig. 7 Distribution functions of maximal positive amplitudes for incident wave (*triangles*) and shoreline displacement (*circles*) with the incident wave spectrum width $l = 0.7$; solid line corresponds to the Rayleigh distribution

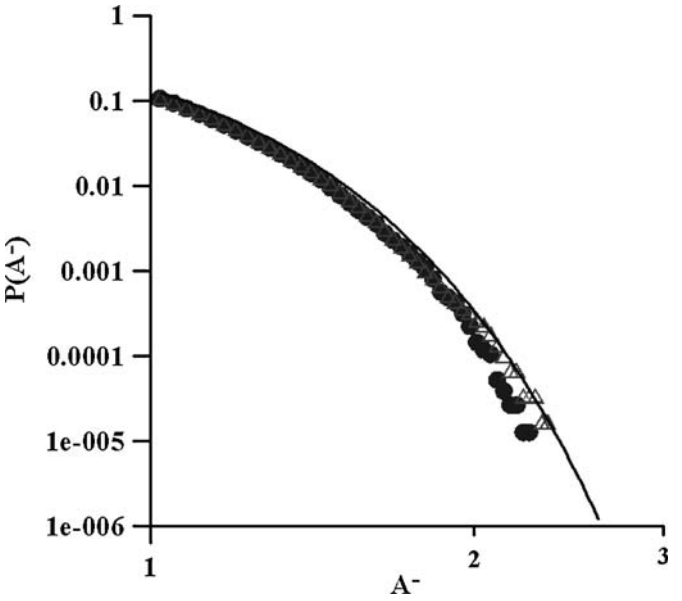

Fig. 8 Distribution functions of maximal negative amplitudes for incident wave (*triangles*) and shoreline displacement (*circles*) with the incident wave spectrum width $l = 0.7$; solid line corresponds to the Rayleigh distribution

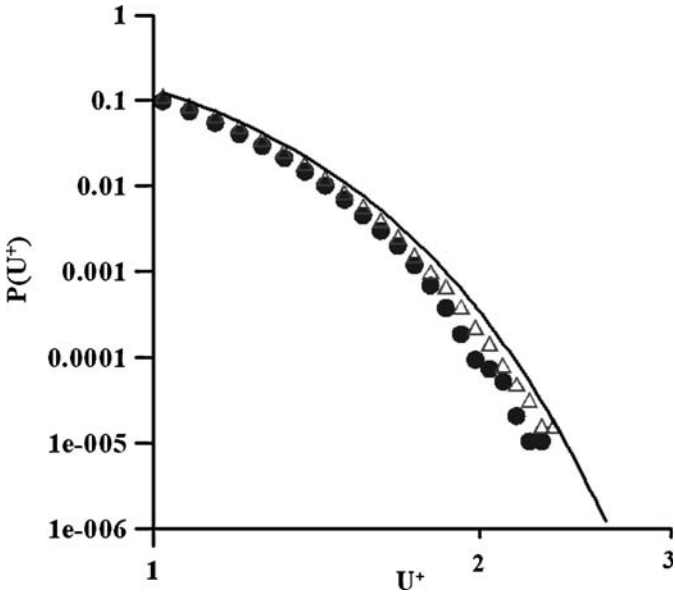

Fig. 9 Distribution functions of maximal velocities for incident wave (*triangles*) and shoreline displacement (*circles*) with the incident wave spectrum width $l = 0.7$; solid line corresponds to the Rayleigh distribution

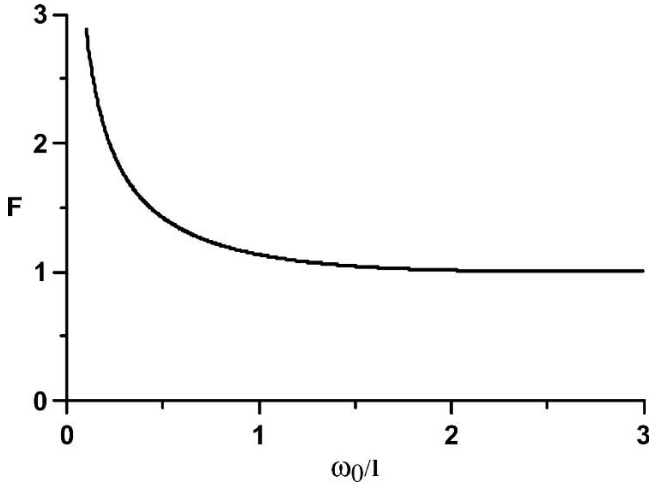

Fig. 10 Function of an influence of the incident wave spectrum width on a runup height of the wave

The function $F(z)$ is shown in Fig. 10. It tends to one $(F = 1)$ for the narrow-band process $(l \ll \omega_0)$ and the significant runup height of the wave can be described by the formula for the runup of a sine wave (Didenkulova et al. 2007b). Significant runup height grows with the increasing of the spectrum width, especially when

$l > \omega_0$. Thus, Gaussian approximation in a problem of the wave runup on a beach works not only for the case of $l \ll \omega_0$ but also for $l < \omega_0$, when distribution function differs from Gaussian.

Previous analysis used the wave field presenting as the superposition of the independent spectral components. Such approach is very popular to describe random water waves. Meanwhile, the wave field in shallow water contains many coherent wave components, and an idea to present it as random assembly of the solitary waves is very popular, see, for instance Brocchini and Gentile (2001). The runup of solitary wave on a plane beach is well studied (Synolakis 1987) and the runup amplitude can be expressed through soliton amplitude

$$\frac{R}{h} = 2.8312 \frac{1}{\sqrt{\alpha}} \left(\frac{A}{h} \right)^{5/4}. \tag{27}$$

In fact, this formula can be derived from (10) taking into account the relation between the soliton amplitude and duration. If the wave field contains random separated solitons, the runup of each individual soliton presents the independent random process, and distribution function of runup amplitude can be found analytically if the distribution function of the soliton amplitudes is known. Assuming for simplicity the Rayleigh distribution for soliton amplitude and using (27), exceedance frequency of runup amplitude is

$$P(R) = \exp\left[-0.378 \alpha^{4/5} \frac{(R/h)^{8/5}}{(A/h)^2} \right], \tag{28}$$

and probability of appearance of big waves on the coast is high. In fact, this formula is valid for independent solitons. More detailed computing of statistical runup characteristics of the realistic "soliton" wave field is performed in Brocchini and Gentile (2001).

So, the wave runup on a plane beach leads to increasing of the probability of the large-amplitude waves, and freak wave phenomenon should be taken into account in the coastal protection.

4 Conclusion

Distribution functions of the maxima wave characteristics at the point of shoreline (displacement and velocity), caused by a wave coming from the open sea, are analyzed in frames of nonlinear shallow water theory. Modeled (Gaussian) spectrum is used for numerical simulations. It is shown that variations of distribution functions for the maximal shoreline displacement and shoreline velocity are weak for $l < \omega_0$. For this case the significant runup height of the wave can be described by the formula for the runup of a sine wave. For the wide-band process, especially for $l > \omega_0$, the significant runup height grows significantly.

Acknowledgments This research is supported particularly by grants from INTAS (06-1000013-9236, 06-1000014-6046), RFBR (08-05-00069, 08-02-00039, 08-05-72011), Marie Curie network SEAMOCS (MRTN-CT-2005-019374), and Scientific School of Corresponding Member of Russian Academy of Science V.A. Zverev.

References

Brocchini M, Gentile R (2001) Modelling the run-up of significant wave groups. Continental Shelf Res 21:1533–1550

Carrier GF, Greenspan HP (1958) Water waves of finite amplitude on a sloping beach. J Fluid Mech 4:97–109

Carrier GF, Wu TT, Yeh H (2003) Tsunami run-up and draw-down on a plane beach. J Fluid Mech 475:79–99

Chien H, Kao C-C, Chuang LZH (2002) On the characteristics of observed coastal freak waves. Coastal Eng J 44(4):301–319

Didenkulova II, Slunyaev AV, Pelinovsky EN, Charif Ch (2006a) Freak waves in 2005. Nat Hazards Earth Syst Sci 6:1007–1015

Didenkulova II, Zahibo N, Kurkin AA, Levin BV, Pelinovsky EN, Soomere T (2006b) Runup of nonlinearly deformed waves on a coast. Doklady Earth Sci 411(8):1241–1243

Didenkulova II, Kurkin AA, Pelinovsky EN (2007a) Run-up of solitary waves on slopes with different profiles. Izvestiya Atmos Ocean Phys 43(3):384–390

Didenkulova I, Pelinovsky E, Soomere T, Zahibo N (2007b) Runup of nonlinear asymmetric waves on a plane beach. In: Kundu A (ed) Tsunami and nonlinear waves. Springer, Berlin Heidelberg New York, pp 173–188

Kânoğlu U, Synolakis C (2006) Initial value problem solution of nonlinear shallow water-wave equations. Phys Rev Lett 97:148501

Kharif C, Pelinovsky E (2003) Physical mechanisms of the rogue wave phenomenon. Eur J Mech B: Fluid 22(6):603–634

Massel SR (1996) Ocean surface waves: Their physics and prediction. World Scientific, Singapore

Olagnon M, Athanassoulis GA (eds) (2001) Rogue waves 2000. Ifremer, France

Pedersen G, Gjevik B (1983) Runup of solitary waves. J Fluid Mech 142:283–299

Pelinovsky E, Mazova R (1992) Exact analytical solutions of nonlinear problems of tsunami wave run-up on slopes with different profiles. Nat Hazards 6:227–249

Rosenthal W (2003) Rogue waves: Forecast and impact on marine structures. GKSS Research Center, Geesthacht, Germany

Sand SE, Hansen NE, Klinting P, Gudmestad OT, Sterndorff MJ (1990) Freak wave kinematics. In: Torum A, Gudmestad OT (eds) Water wave kinematics. Kluwer, Dordrecht, pp 535–549

Sergeeva AV, Didenkulova II (2005) Runup of irregular waves on a plane beach. Izvestiya Russian Acad Eng Sci 14:98–105

Spielfogel LO (1976) Runup of single waves on a sloping beach. J Fluid Mech 74:685–694

Synolakis CE (1987) The runup of solitary waves. J Fluid Mech 185:523–545

Synolakis CE (1991) Tsunami runup on steep slopes: How good linear theory really is. Nat Hazards 4:221–234

Tadepalli S, Synolakis CE (1994) The runup of N-waves. Proc R Soc Lond A 445:99–112

Tinti S, Tonini R (2005) Analytical evolution of tsunamis induced by near-shore earthquakes on a constant-slope ocean. J Fluid Mech 535:33–64

Torum A, Gudmestad OT (eds) (1990) Water wave kinematics. Kluwer, Dordrecht

Symbolic Computation for Nonlinear Wave Resonances

E. Kartashova, C. Raab, Ch. Feurer, G. Mayrhofer, and W. Schreiner

Abstract Extreme ocean waves are characterized by the energy concentration in a few chosen waves/modes. Frequency modulation due to the nonlinear resonances is one of the possible processes yielding the appearance of independent wave clusters which keep their energy. Energetic behavior of these clusters is defined by (1) integer solutions of the resonance conditions, and (2) coupling coefficients of the dynamical system on the wave amplitudes. General computation algorithms are presented which can be used for arbitrary 3-wave resonant system. Implementation in Mathematica is given for planetary ocean waves. Short discussion concludes the paper.

1 Introduction

Resonance is a common thread that runs through almost every branch of physics, and without resonance we would not have radio, television, music, etc. Resonance causes an object to oscillate, sometimes the oscillation is easy to see (vibration in a guitar string), but sometimes this is impossible without measuring instruments (electrons in an electrical circuit). A well-known example with Tacoma Narrows Bridge (at the time it opened for traffic in 1940, it was the third longest suspension bridge in the world) shows how disastrous resonances can be: on the morning of 7 November 1940, the 4-month-old Tacoma Narrows Bridge began to oscillate dangerously up and down, tore itself apart, and collapsed. Though designed for winds of 120 mph, a wind of only 42 mph caused it to collapse. The experts did agree that somehow the wind caused the bridge to resonate, and nowadays, wind tunnel testing of bridge designs is mandatory.

Another famous example is the experiments of Tesla who in 1898 studied experimentally vibrations of an iron column and noticed that at certain frequencies specific

E. Kartashova, C. Raab, Ch. Feurer, G. Mayrhofer, and W. Schreiner
Research Institute for Symbolic Computation (RISC), Johannes Kepler University Linz, Altenbergerstr. 69, 4040 Linz, Austria

E. Pelinovsky, C. Kharif (eds.) *Extreme Ocean Waves*, 95–126.

pieces of equipment in the room would start to jiggle. Playing with the frequency he was able to move the jiggle to another part of the room. Completely fascinated with these findings, he forgot that the column ran downward into the foundation of the building, and the vibrations were being transmitted all over Manhattan. The experiments had started sort of a small earthquake in his neighborhood with smashed windows, swayed buildings, and panicky people in the streets. For Tesla, the first hint of trouble came when the walls and floor began to heave (Cheney 1989). He stopped the experiment as soon as he saw police rushing through the door.

The difference between resonances in a human made system and in some natural phenomena is very simple. We can change the form of a bridge and stop the experiment by switching off electricity but we can not change the direction of the wind, the form of the Earth atmosphere, or the sizes of an ocean. What we can try to do is *to predict* drastic behavior of a real physical system by computing its resonances. While linear resonances in different physical systems are comparatively well studied, to compute characteristics of nonlinear resonances and to predict their properties is quite a nontrivial problem, even in the one-dimensional case. Thus, the notorious Fermi–Pasta–Ulam numerical experiments with a nonlinear *1D*-string (carried out more than 50 years ago) are still not fully understood (Berman and Israilev 2005). On the other hand, nonlinear wave resonances in continuous *2D*-media like ocean, space, atmosphere, plasma, etc. are well studied in the frame of wave turbulence theory (Zakharov et al. 1992) and provide a sound basis for qualitative and sometimes also quantitative analysis of corresponding physical systems. The notion of nonlinear wave interactions is crucial in the wave turbulence theory (Zakharov et al. 2004). Excluding resonances allows to describe a nonlinear wave system statistically by wave kinetic equations and power-law energy spectra of turbulence (Zakharov and Filonenko 1967), and to observe this behavior in numerical experiments (Pushkarev and Zakharov 2000). Direct computations with Euler equations (modified for gravity water waves (Zakharov et al. 2005)) show that the existence of resonances in a wave system yield some additional effects, which are not covered by the statistical description. The role of resonances in the evolution of water wave turbulent systems has been studied profoundly by a great number of researchers. One of the most important conclusions (for gravity water waves) made recently in Tanaka (2007) is the following: *The four-wave resonant interactions control the evolution of the spectrum at every instant of time, whereas nonresonant interactions do not make any significant contribution even in a short-term evolution*.

The behavior of a resonant wave system can be briefly described (Kartashova 1998) as follows: (1) not all waves take part in resonant interactions, (2) resonantly interacting waves form a few independent small wave clusters, such that there is no energy flow between these clusters, (3) including some small but nonzero resonance width into consideration *does not* destroy the clusters. A model of laminated wave turbulence (Kartashova 2006a) allows to describe statistical and resonant regimes simultaneously while methods to compute resonances numerically are presented in Kartashova (2006b) (idea) and in Kartashova and Kartashov (2006, 2007a,b) (implementation). Our main purpose here is to study the possibilities of a symbolic implementation of these general algorithms using the computer algebra system Mathematica.

The implemented software can be executed with local installations of Mathematica and the corresponding method libraries; however, we have also developed a Web interface that allows to run the methods from any computer in the Internet via a conventional Web browser. The implementation strategy is simple and is based on generally available technologies; it can serve as a blueprint for other mathematical software with similar features.

We take as our principal example the barotropic vorticity equation in a rectangular domain with zero boundary conditions, which describes oceanic planetary waves, and show how (a) to compute interaction coefficients of corresponding dynamical systems, (b) to solve resonant conditions, (c) to construct the topological structure of the solution set, and (d) to use the software via a Web interface over the Internet. A short discussion concludes the paper.

2 Mathematical Background

Wave turbulence takes place in physical systems with nonlinear dispersive waves that are described by evolutionary dispersive NPDEs. The role of the evolutionary dispersive NPDEs in the theoretical physics is so important that the notion of dispersion is used for *a physical* classification of PDEs into dispersive and nondispersive. On the one hand, the well-known mathematical classification of PDEs into elliptic, parabolic, and hyperbolic equations is based on the form of equations and can be applied to the second order PDEs on an arbitrary number of variables. On the other hand, the physical classification is based on *the form of solutions* and can be applied to PDEs of arbitrary order and arbitrary number of variables. To construct the physical classification of PDEs, two preliminary steps are to be made: (1) to divide all variables into two groups – time- and space-like variables (t and x, respectively); and (2) to check that the *linear part* of the PDE under consideration has a wave-like solution in the form of Fourier harmonic

$$\psi(x,t) = A \exp \mathrm{i}[kx - \omega t],$$

with amplitude A, wave-number k, and wave frequency ω. The direct substitution of this solution into the linear PDE shows that ω is an explicit function on k, for instance:

$$\psi_t + \psi_x + \psi_{xxx} = 0 \quad \Rightarrow \quad \omega(k) = k - 5k^3.$$

If ω as a function on k is real-valued and such that $\mathrm{d}^2\omega/\mathrm{d}k^2 \neq 0$, it is called *a dispersion function* and the corresponding PDE is called evolutionary dispersive PDE. If the dimension of the space variable x is more than 1, that is, $\vec{x} = (x_1, \ldots, x_p)$, $\vec{k}$ is called the wave-vector and the dispersion function $\omega = \omega(\vec{k})$ depends on the coordinates of the wave-vector. This classification *is not complementary* to a standard mathematical one. For instance, though hyperbolic PDEs normally do not have dispersive wave solutions, the hyperbolic equation $\psi_{tt} - \alpha^2\psi_{xx} - \beta^2\psi = 0$ has them.

In the huge amount of application areas of NPDEs (classical and quantum physics, chemistry, medicine, sociology, etc.), a nonlinear term of the corresponding NPDE can be regarded as small. This is symbolically written as

$$L(\psi) = -\varepsilon N(\psi), \tag{1}$$

where L and N are linear and nonlinear parts of the equation respectively and ε is a small parameter defined explicitly by the physical problem setting. It can be shown that in this case the solution ψ of (1) can be constructed as a combination of the Fourier harmonics with amplitudes A depending on the time variable and possessing two properties formulated here for the case of quadratic nonlinearity:

- **P1.** The amplitudes of the Fourier harmonics satisfy the following system of nonlinear ordinary differential equations (ODEs) written for simplicity in the real form

$$\begin{aligned} \dot{A}_1 &= \alpha_1 A_2 A_3, \\ \dot{A}_2 &= \alpha_2 A_1 A_3, \\ \dot{A}_3 &= \alpha_3 A_1 A_2, \end{aligned} \tag{2}$$

  with coefficients α_j being functions on wave-numbers;
- **P2.** The dispersion function and wave-numbers satisfy the *resonance conditions*

$$\begin{cases} \omega(\vec{k}_1) \pm \omega(\vec{k}_2) \pm \omega(\vec{k}_3) = 0, \\ \vec{k}_1 \pm \vec{k}_2 \pm \vec{k}_3 = 0. \end{cases} \tag{3}$$

The transition from (1) to (2) can be performed by some standard methods (for instance, multiscale method (Nayfeh 1981)), which also yields the explicit form of resonance conditions.

Keeping in mind our main problem – to find a solution of (1) – one has to take care of the initial and boundary conditions. This is done in the following way: the case of periodic or zero boundary conditions yields *integer wave numbers*, otherwise they are real. Correspondingly, one has to find all integer (or real) solutions of (3), substitute corresponding wave-numbers into the coefficients α_j, and then look for the solutions of (2) with given initial conditions.

One can see immediately a big problem that appears as soon as one has to solve a NPDE with periodical or zero boundary conditions. Indeed, dispersion functions take different forms, for instance,

$$\omega^2 = k^3, \;\; \omega^2 = k^3 + \alpha k, \;\; \omega^2 = k, \;\; \omega = \alpha/k, \;\; \omega = m/n(n+1), \ldots, \text{etc.},$$

with $\vec{k} = (m,n)$, $k = \sqrt{m^2+n^2}$, and α being a constant. This means that (3) corresponds to a system of Diophantine equations of many variables, normally 6–9, with cumulative degrees 10–16. Those have to be solved usually for the integers of the order $\sim 10^3$, which means that computations has to be performed with integers of order 10^{48} and more. Original algorithms to solve these systems of equations

have been developed based on some profound results of number theory (Kartashova 2006b) and implemented numerically (Kartashova and Kartashov 2006, 2007a,b).

Further on, an evolutionary dispersive NPDE with periodic or zero boundary conditions is called *three-term mesoscopic system* if it has a solution of the form

$$\tilde{\psi} = \sum_{j=1}^{\infty} A_j \exp \mathrm{i}[\vec{k}_j \vec{x}_j - \omega t]$$

and there exists at least one triple $\{A_{j_1}, A_{j_2}, A_{j_3}\} \in \{A_j\}$ such that **P1** and **P2** keep true with some nonzero coefficients α_j, $\alpha_j \neq 0 \; \forall j = 1,2,3$.

3 Equations for Wave Amplitudes

3.1 Method Description

The barotropic vorticity equation describing ocean planetary waves has the form (Kartashova and Reznik 1992)

$$\frac{\partial \triangle \psi}{\partial t} + \beta \frac{\partial \psi}{\partial x} = -\varepsilon J(\psi, \triangle \psi), \tag{4}$$

with boundary conditions

$$\psi = 0 \quad \text{for } x = 0,\, L_x; \;\; y = 0,\, L_y.$$

Here β is a constant called Rossby number, ε is a small parameter and the Jacobian has the standard form

$$J(a,b) = \frac{\partial a}{\partial x}\frac{\partial b}{\partial y} - \frac{\partial a}{\partial y}\frac{\partial b}{\partial x}.$$

First we give a basic introduction on how a PDE can be turned into a system of ODEs by a multiscale method. Using operator notation, our problem (4) is viewed as a perturbed version of the linear PDE $L(\psi) = 0$. We pick a solution of this equation, say ψ_0, which is a superposition of several waves φ_j, that is, $\psi_0 = \sum_{j=1}^{s} A_j \varphi_j$, each being a solution itself. To construct a solution of the original problem we make the amplitudes time-dependent. As the size of the nonlinearity in (1) is just of order ε, the amplitudes will vary only on time-scales $1/\varepsilon$ times slower than the waves. Hence we define an additional time-variable $t_1 := t\varepsilon$ called "slow time" to handle this time scale. So we look for approximate solutions of (1) that have the following form

$$\psi_0(t, t_1, \vec{x}) = \sum_{j=1}^{s} A_j(t_1) \varphi_j(\vec{x}, t),$$

which for $\varepsilon = 0$ is an exact solution. The exact solution of the equation is written as power series in ε around ψ_0, that is, $\psi = \sum_{k=0}^{\infty} \psi_k \varepsilon^k$. In our computation it is truncated up to maximal order m, which in our case is $m = 1$, that is,

$$\psi(t, t_1, \vec{x}) = \psi_0(t, t_1, \vec{x}) + \psi_1(t, t_1, \vec{x})\varepsilon.$$

Plugging $\psi(t, t_1, \vec{x})$ one has to keep in mind that, since $t_1 = \varepsilon t$, we now have $\frac{\mathrm{d}}{\mathrm{d}t} = \frac{\partial}{\partial t} + \varepsilon \frac{\partial}{\partial t_1}$ due to the chain rule. Equations are formed by comparing the coefficients of ε^k. For $k = 0$ this gives back the linear equation, but we keep the equation for $k = 1$. In particular, for (4) we arrive at

$$\begin{aligned} \frac{\partial \triangle \psi_0}{\partial t} + \beta \frac{\partial \psi_0}{\partial x} &= 0, \\ \frac{\partial \triangle \psi_0}{\partial t_1} + \frac{\partial \triangle \psi_1}{\partial t} + \beta \frac{\partial \psi_1}{\partial x} &= -J(\psi_0, \triangle \psi_0). \end{aligned}$$

To get (2), we have to get rid of all other variables. This is done by integrating against the φ_j's, that is, $\langle ., \varphi_j \rangle_{L^2(\Omega)}$, and averaging over (fast) time, that is, $\lim_{T\to\infty} \frac{1}{T} \int_0^T . \mathrm{d}t$.

3.2 The Implementation

This method was implemented in Mathematica with order $m = 1$ in mind. So it would not be immediately applicable to higher orders without some (minor) adjustments. The ODEs are constructed by the function

```
ODESystem[L(ψ), N(ψ), ψ,
    {x1,..,xn}, t, domain, jacobian, m, s, A, linwav,
    {λ1,..,λp}, paramvalues].
```

Basically this function takes the problem together with the solution of the linear equation as input and computes the list of ODEs for the amplitudes as output. Its arguments are given in more detail:

- `L(ψ), N(ψ)`: Linear and nonlinear part of (1), each applied to a symbolic function parameter. Derivatives have to be specified with `Dt` instead of `D` and the nonlinear part has to be a polynomial in the derivatives of the function.
- ψ: symbol used for function in `L(ψ), N(ψ)`
- `{x1,...,xn}, t`: list of symbols used for space-variables, and symbol for time-variable
- `domain`: The domain on which the equation is considered has to be specified in the form `{{x1,minx1,maxx1}, ..., {xn,minxn,maxxn}}`, where the bounds on x_i may depend on $x_1, \ldots, x_{i-1}$ only.
- `jacobian`: For integration the (determinant of the) Jacobian must also be passed to the function. This is needed in case the physical domain does not coincide with the domain of the variables above, it can be set to `1` otherwise.

- `m, s`: maximal power of ε and number of waves considered
- `A`: symbol used for amplitudes
- `linwav`: General wave of the linear equation is assumed to have separated variables, that is, $\varphi(\vec{x},t) = B_1(x_1)\cdots B_n(x_n)\exp(\mathrm{i}\theta(x_1,\ldots,x_n,t))$, and has to be given in the form
  $\{$`B1(x1),...,Bn(xn), θ(x1,...,xn,t)`$\}$.
- $\{\lambda_1, \ldots, \lambda_p\}$: list of symbols of parameters the functions in `linwav` depend on
- `paramvalues`: For each of the `s` waves explicit values of the parameters $\{\lambda_1,\ldots,\lambda_p\}$ have to be passed as a list of `s` vectors of parameter values.

```
ODESystem[linearpart_,nonlinearpart_,fun_Symbol,vars_List,
    t_Symbol,domain_List,jacobian_,ord_Integer,num_Integer,
    A_Symbol,linwav_List,params_List,paramvalues_List] :=
  Module[{B,theta,eq,k},
    eq = PerturbationEqns[linearpart,nonlinearpart,
                          fun,vars,t,ord];
    eq = PlugInGenericWaveTuple[eq,fun,vars,t,A,B,theta,num]
           /. fun[1]->(0&);
    eq = Table[Resonance2[eq,linwav,vars,t,params,A,B,theta,
                  num,paramvalues,k],
                {k,num}];
    Map[Integrate[Simplify[#,And@@(Function[B,B[[2]]<B[[1]]<
                     B[[3]]]/@domain)]*jacobian,
                  Sequence@@domain]&,
        eq,{2}]
    ]
```

Internally this function is divided into three subroutines briefly described below.

3.2.1 Perturbation Equations, General Form

The first of the subroutines is

`PerturbationEqns[L(ψ), N(ψ), ψ, {x1,...,xn}, t, m]`.

As mentioned before we approximate the solution of our problem by a polynomial of degree m in ε. This subroutine works for arbitrary m. In the first step we construct equations by coefficient comparison. Additional time-variables will be created automatically and labeled `t[1],...,t[m]`. The output is a list of $m+1$ equations corresponding to the powers $\varepsilon^0,\ldots,\varepsilon^m$. The implementation is quite straightforward. First set $\psi = \sum_{k=0}^{m}\psi_k(t,t_1,\ldots,t_m,x_1,\ldots,x_n)\varepsilon^k$ in (1), where $t_k = \varepsilon^k t$, that is, $\frac{\mathrm{d}}{\mathrm{d}t} = \frac{\partial}{\partial t} + \sum_{k=1}^{m}\varepsilon^k\frac{\partial}{\partial t_k}$. Then extract the coefficients of $\varepsilon^0,\ldots,\varepsilon^m$ on both sides and assemble the equations. Finally replace $\varepsilon^k t$ by t_k again.

```
PerturbationEqns[linearpart_,nonlinearpart_,fun_Symbol,
    vars_List,time_Symbol,ord_Integer] :=
  Module[{i,j,e,eq},
```

```
    eq = ((linearpart == -e*nonlinearpart)
           /. {fun->Sum[e^i*fun[i][time,Sequence@@Table[e^j*
                                    time,{j,ord}],Sequence@@
                                    DeleteCases[vars,time]],
                        {i,0,ord}]});
    eq = (eq /. ((Dt[#, __]->0)& /@ Join[vars,{time,e}]));
    eq = (Equal@@#)& /@
            Transpose[Take[CoefficientList[#,e],1+ord]& /@
                        (List@@eq)];
    eq /. Table[e^j*time->time[j],{j,ord}]
    ]
```

3.2.2 Perturbation Equations, Given Linear Mode

In step two we set $\psi_0(t,t_1,\vec{x}) = \sum_{j=1}^{s} A_j(t_1)\varphi_j(\vec{x},t)$ as described earlier. This is done by the function

`PlugInGenericWaveTuple[eq, ψ, {x1,...,xn}, t, A, B, θ, s],`

where the first argument is the output of the previous step. The symbols `B` and θ have to be passed for labeling the shape and phase functions, respectively. The output consists of two parts. The first part of the list formulates the assumption $L(\varphi_j) = 0$ explicitly for each of the waves. This is not used in subsequent computations, but is provided as a way to check the assumption. The second part of the list is the equation corresponding to the coefficients of ε from the previous step, with ψ_0 as above. As the task of this step is so short, the implementation does not need further explanation.

```
PlugInGenericWaveTuple[eq_List,fun_Symbol,vars_List,
  t_Symbol,A_Symbol,B_Symbol,theta_Symbol,num_Integer] :=
  Module[{i,j,waves,n=Length[DeleteCases[vars,t]]},
    waves = Table[A[j][Slot[2]]*
                    Product[B[i][j][Slot[i+2]],{i,n}]*
                    Exp[I*theta[j][Sequence@@Table[Slot[i+2],
                                        {i,n}],Slot[1]]],
                  {j,num}];
    {Table[eq[[1]] /. fun[0]->Function[Evaluate[waves[[j]]]],
           {j,num}],
     Expand /@
          (eq[[2]] /. fun[0]->Function[Evaluate[Total[waves]]])
    }]
```

3.2.3 Time and Scale Averaging

Step three is the most elaborate. Under the assumption that interchange of averaging over time and inner product is justified, an integrand

$$h = \lim_{T\to\infty} \frac{1}{T} \int_0^T \psi_0 \overline{\varphi_k}\, \mathrm{d}t$$

is computed, which when integrated over the domain yields

$$\int_\Omega h = \lim_{T\to\infty} \frac{1}{T} \int_0^T \langle \psi_0, \varphi_k \rangle_{L^2(\Omega)}\, \mathrm{d}t.$$

Resonance conditions posed on the phase functions are explicitly used by

```
Resonance[eq, linwav, {x1,..,xn}, t,
    {λ1,..,λp}, A, B, θ, s, cond, k],
```

which receives the output from the previous step in `eq`. Here `cond` specifies the resonance condition in terms of θ_j, which have to be entered as `θ[j][x1,..,xn,t]`, respectively. The last argument is the index of the wave φ_k in the integral above. Alternatively, `Resonance2` uses explicit parameter settings `paramvalues` for the waves instead of `cond`. This has been necessary because the general `Resonance` does not give useable results (see Sect. 3.3 for more details). The main work in this step is to find out which terms do not contribute to the result. We exploit the fact that oscillating terms vanish when averaged over time by simply omitting those summands of $\langle \psi_0, \varphi_k \rangle_{L^2(\Omega)}$ that have a factor $\exp(\mathrm{i}\theta)$ with some time-dependent phase θ. The code for `Resonance` is not shown here, but is quite similar to `Resonance2`.

```
Resonance2[eq_List,linwav_List,vars_List,t_Symbol,params_List,
    A_Symbol,B_Symbol,theta_Symbol,num_Integer,
    paramvalues_List,testwave_Integer] :=
  Module[{e,i,j,n=Length[DeleteCases[vars,t]]},
    e = Expand[(List@@Last[eq])*
                Exp[-I*theta[testwave][Sequence@@
                                        DeleteCases[vars,t],
                                      t]]];
    e = e /.
         Table[
           theta[j] ->
            (Evaluate[(linwav[[n+1]] /.
                        (Rule@@#& /@
                          Transpose[{params,paramvalues[[j]]}]
                        )
                      ) /. Append[Table[
                                    DeleteCases[vars,t][[i]]
                                      -> Slot[i],
                                    {i,n}],
                                  t -> Slot[n+1]]
                     ]&
            ),
          {j,num}];
```

```
e = MapAt[
      (Function[theta,If[FreeQ[theta,t],theta,0]
               ]
            [Simplify[#]]
      )&,
      e,
      Position[e,Exp[_]]];
e = Equal@@
      (e*Conjugate[A[testwave]][t[1]]*
        Product[Conjugate[B[i]
                          [testwave]
                          [DeleteCases[vars,t][[i]]]
                         ],
                {i,n}]
      ) /.
        Flatten[
          Table[B[i][j] ->
                 Function[
                   Evaluate[DeleteCases[vars,t][[i]]],
                   Evaluate[linwav[[i]] /.
                              (Rule@@#& /@
                                Transpose[
                                  {params,paramvalues[[j]]
                                  }]
                              )]],
               {i,n},{j,num}]]
]
```

The integration of h is done by Mathematica and can be quite time-consuming. So `ODESystem` simplifies the integrand first to make integration faster. Still the expressions involved can be quite complicated. This is the most time-consuming part during construction of the ODEs.

3.3 Obstacles

Mathematica sometimes does not seem to take care of special cases and consequently has problems with evaluating expressions depending on symbolic parameters. We give two simple examples to illustrate this issue:

- Orthogonality of sine-functions.
  Indeed, it holds that

$$\forall m,n \in \mathbb{N} : \int_0^{2\pi} \sin(mx)\sin(nx)\,\mathrm{d}x = \pi\delta_{m,n}.$$

Computing this in Mathematica by

```
Integrate[Sin[m*x]Sin[n*x], {x,0,2π},
    Assumptions → m∈Integers && n∈Integers]
```

yields 0 independently of m,n instead.

- Computation of a limit.
  Mathematica evaluates an expression

$$\forall n \in \mathbb{Z} : \lim_{x \to n} \frac{\sin(x\pi)}{x} = \pi \delta_{n,0}$$

and similar expressions in two different ways getting two different answers. On the one hand

```
Limit[Sin[(m-n)π]/(m-n), m→n,
Assumptions → m∈Integers && n∈Integers]
```

gives 0. On the other hand, however, when the condition $m,n \in \mathbb{Z}$ is not used for computing the result, Mathematica yields the correct answer π, as with

```
Limit[Sin[(m-n)π]/(m-n), m→n].
```

Unfortunately these issues prevented us from obtaining a nice formula for the coefficients in symbolic form by `Resonance`. So we just compute results for explicit parameter settings using `Resonance2`.

3.4 Results

3.4.1 Atmospheric Planetary Waves

For the validation of our program we consider the barotropic vorticity equation on the sphere first. Here numerical values of the coefficients α_i are available (Table 1, Kartashova and L'vov (2007)). The equation looks quite similar

$$\frac{\partial \triangle \psi}{\partial t} + 2\frac{\partial \psi}{\partial \lambda} = -\varepsilon J(\psi, \triangle \psi).$$

However, in spherical coordinates ($\phi \in [-\frac{\pi}{2}, \frac{\pi}{2}]$, $\lambda \in [0, 2\pi]$) the differential operators are different:

$$\triangle = \frac{\partial^2}{\partial \phi^2} + \frac{1}{\cos(\phi)^2}\frac{\partial^2}{\partial \lambda^2} - \tan(\phi)\frac{\partial}{\partial \phi},$$

$$J(a,b) = \frac{1}{\cos(\phi)}\left(\frac{\partial a}{\partial \lambda}\frac{\partial b}{\partial \phi} - \frac{\partial a}{\partial \phi}\frac{\partial b}{\partial \lambda}\right).$$

The linear modes have in this case the following form (Pedlosky 1987):

$$P_n^m(\sin(\phi))\exp\left(\mathrm{i}\left(m\lambda+\frac{2m}{n(n+1)}t\right)\right), \tag{5}$$

where $P_n^m(\mu)$ are the associated Legendre polynomials of degree n and order $m \le n$, so again they depend on the two parameters m and n. Also resonance conditions on the parameters look different in this case.

Now we compute the coefficient α_3 in (2). In Kartashova and L'vov (2007) we find the following equation for the amplitude A_3

$$n_3(n_3+1)\frac{\partial A_3}{\partial t_1}(t_1) = 2iZ(n_2(n_2+1)-n_1(n_1+1))A_1(t_1)A_2(t_1),$$

so $\alpha_3 = 2iZ\frac{n_2(n_2+1)-n_1(n_1+1)}{n_3(n_3+1)}$. Parameter settings and corresponding numerical values for Z were taken from the table below (see Kartashova and L'vov (2007)). For this equation and $s=3$ results produced by our program have the form $c_1\overline{A_3}\dot{A_3} = c_2A_1A_2\overline{A_3}$, so $\alpha_3 = c_2/c_1$.

Testing all resonant triads from Table 1 from Kartashova and L'vov (2007), we see that the coefficients differ merely by a constant factor of $\pm\sqrt{8}$, which is due to the different scaling of the Legendre polynomials. In our computation they were normalized s.t. $\int_{-1}^{1} P_n^m(\mu)^2\,\mathrm{d}\mu = 1$. With three triads, however, results were completely different. Interestingly this were exactly those triads for which no φ_0 appears in the table.

Furthermore, for the other coefficients in (2) our program computes $\alpha_1 = \alpha_2 = 0$ in all tested parameter settings. This fact can be easily understood in the following way. We checked only resonance conditions but not the conditions for the interaction coefficients to be non-zero, which are elaborated enough:

$$m_i \le n_i, \quad n_i \ne n_j \quad \forall i = 1,2,3, \quad |n_1-n_2| < n_3 < n_1+n_2,$$

and

$$n_1+n_2+n_3 \quad \text{is odd.}$$

Randomly taken parameter setting does not satisfy these conditions.

3.4.2 Ocean Planetary Waves

Returning to the original example on the domain $[0,L_x]\times[0,L_y]$, we find explicit formulae for the coefficients in Kartashova and Reznik (1992). According to Sect. 3.3 we can only verify special instances and not general formulae.

Linear modes have now the form (Kartashova and Reznik 1992)

$$\sin\left(\pi\frac{mx}{L_x}\right)\sin\left(\pi\frac{ny}{L_y}\right)\exp\left(i\left(\frac{\beta}{2\omega}x+\omega t\right)\right), \tag{6}$$

with $m,n \in \mathbb{N}$ and $\omega = \frac{\beta}{2\pi\sqrt{(\frac{m}{L_x})^2+(\frac{n}{L_y})^2}}$.

Parameter settings solving the resonance conditions were computed as in Sect. 4. Unfortunately results do not match and we have no explanation for that. In particular, the condition $\frac{\alpha_1}{\omega_1^2}+\frac{\alpha_2}{\omega_2^2}+\frac{\alpha_3}{\omega_3^2}=0$ stated in Kartashova and Reznik (1992) does not hold for the results of our program since we got $\alpha_1=\alpha_2=0$ in all tested parameter settings, just as in the spherical case.

For example, if we try the triad {{2, 4}, {4, 2}, {1, 2}}, where $L_x=L_y=1$, our program computes $\alpha_3=\frac{32\sqrt{5}}{11}\pi\left(\sin(3\sqrt{5}\pi)-\mathrm{i}(1+\cos(3\sqrt{5}\pi))\right)$, whereas the general formula yields $\alpha_3=\frac{19+7\sqrt{5}}{11}\pi\sin(3\sqrt{5}\pi)$. However, if we use a triad with $q=1$, e.g. {{24, 18}, {9, 12}, {8, 6}}, both agree on $\alpha_1=\alpha_2=\alpha_3=0$.

4 Resonance Conditions

The main equation to solve is

$$\frac{1}{\sqrt{\left(\frac{m_1}{L_x}\right)^2+\left(\frac{n_1}{L_y}\right)^2}}+\frac{1}{\sqrt{\left(\frac{m_2}{L_x}\right)^2+\left(\frac{n_2}{L_y}\right)^2}}=\frac{1}{\sqrt{\left(\frac{m_3}{L_x}\right)^2+\left(\frac{n_3}{L_y}\right)^2}}$$

for all possible $m_i,n_i\in\mathbb{Z}$ with the scales L_x and L_y (also $\in\mathbb{Z}$) and then to check the condition $n_1\pm n_2=n_3$. In the following argumentation it will be seen that L_x and L_y can be assumed to be free of common factors. Below we refer to L_x and L_y as to *the scale coefficients*.

The first step of the algorithm implemented in Mathematica is to rewrite the equation to $\frac{1}{\sqrt{\tilde{m}_1{}^2+\tilde{n}_1{}^2}}+\frac{1}{\sqrt{\tilde{m}_2{}^2+\tilde{n}_2{}^2}}=\frac{1}{\sqrt{\tilde{m}_3{}^2+\tilde{n}_3{}^2}}$ and transform it in the following way: we factorize the result of each $\tilde{m}_i{}^2+\tilde{n}_i{}^2$ and obtain with $\rho_1\cdots\rho_r$ being the factors of $m_i^2+n_i^2$ and $\alpha_1\cdots\alpha_r$ their respective powers:

$$m_i^2+n_i^2=\rho_1^{\alpha_1}\cdot\rho_2^{\alpha_2}\cdots\rho_r^{\alpha_r}.$$

We now define *a weight* γ_i *of the wave-vector* (m_i,n_i) as the product of the ρ_j's to the quotient of their respective α_j and 2. The weight q_i will be the name of the product of the ρ_j's, which have an odd exponent:

$$\sqrt{m_i^2+n_i^2}=\gamma_i\sqrt{q_i}.$$

Our equation then can be rewritten as

$$\frac{1}{\gamma_1\sqrt{q_1}}+\frac{1}{\gamma_2\sqrt{q_2}}=\frac{1}{\gamma_3\sqrt{q_3}}$$

and one easily sees that the only way for the equation to possibly hold is $q_1=q_2=q_3=q$ (see Kartashova (2006b) for details). Further, we call q *an index* of

the corresponding wave-vectors. The set of all wave-vectors with the same index is called *a class of index q* and is denoted as Cl_q. Obviously, the solutions of the resonance conditions are to be searched for with separate classes only.

At this point one can also see that only such scales, L_x and L_y, without common factors are reasonable. If they had a common factor, it would cancel out in the equation.

4.1 Method Description

The following five steps are the main steps of the algorithm:

- *Step 1:* Compute the list of all possible indexes q.

  To compute the list of all indexes q, we use the fact that they have to be square-free and each factor of q has to be different from 3 mod 4 (Lagrange theorem). There exist 57 possible indexes in our computational domains $q \leq 300$:

  $$\{1,2,5,10,13,17,26,29,34,37,41,53,58,61,65,73,74,82,85,89,$$
  $$97,101,106,109,113,122,130,137,145,146,149,157,170,173,178,$$
  $$181,185,193,194,197,202,205,218,221,226,229,233,241,257,$$
  $$265,269,274,277,281,290,293,298\}$$

- *Step 2:* Solve the weight equation $\frac{1}{\gamma_1} + \frac{1}{\gamma_2} = \frac{1}{\gamma_3}$.

  For solving the weight equation, we transform it into the equivalent form:

  $$\gamma_3 = \frac{\gamma_1 \gamma_2}{\gamma_1 + \gamma_2}. \tag{7}$$

  The solution triples $\{\gamma_1, \gamma_2, \gamma_3\}$ can now be found by the two for-loops over γ_1 and γ_2 up to a certain maximum parameter and γ_3 is then found constructively with formula (7).
- *Step 3:* Compute all possible pairs (m_i, n_i) – if there are any – that satisfy $m_i^2 + n_i^2 = \gamma_i^2 q$.

  To compute our initial variables m_i, n_i, we use the Mathematica standard function **Sum Of Square Representation[d, x]**, which produces a list of all possible representations of an integer x as a sum of d squares, that is, we can find all possible pairs (a,b) with $d = 2$ such that they satisfy $a^2 + b^2 = x$. Therefore, checking the condition $m_i^2 + n_i^2 = \gamma_i^2 q$ is easy.
- *Step 4:* Sort out the solutions $\{m1, n1, m2, n2, m3, n3\}$ that do not fulfill the condition $n1 \pm n2 = n3$.
- *Step 5:* Check if by dividing m_i by L_x and n_i by L_y there are still exist some solutions.

  Last two steps are trivial.

4.2 The Implementation

Our implementation is quite straightforward and the main program is based on four auxiliary functions shown in the following subsections.

4.2.1 List of Indexes

The function **constructqs[max]** produces the list of all possible indexes q up to the parameter *max*. The first (obvious) q's $sol = \{1\}$ is given and the function checks the conditions starting with $n = 2$. Every time n satisfies the conditions, it is appended to the list *sol*. If one condition fails, the next $n = n + 1$ is considered and so on until n reaches the parameter *max*. Then the list *sol* is returned:

```
Clear[constructqs];

constructqs[n_, sol_List, max_]; n>max := sol (*6*)
constructqs[n_?SquareFreeQ, sol_List, max_]
:= constructqs[n+1, Append[sol, n], max] (*5*)

constructqs[n_?SquareFreeQ, sol_List, max_];
MemberQ[Mod[PrimeFactorList[n], 4], 3]
:= constructqs[n+1, sol, max] (*4*)

constructqs[n_, sol_List, max_]; !SquareFreeQ[n]
:= constructqs[n+1, sol, max] (*3*)
constructqs[1] := {1} (*2*)

constructqs[max_] := constructqs[3, {1}, max] (*1*)
```

4.2.2 Weight Equation

The function **findγs[γmax]** solves the weight equation in the following way. For a fixed γ_1 and γ_2 running between 1 and γmax, it is checked if γ_3 is an integer. If it is, the triple $\{\gamma_1, \gamma_2, \gamma_3\}$ is added to the list *sol*, which is empty at the initial moment. Once γ_2 reaches γmax, it is set to 1 again and the search starts again with $\gamma_1 = \gamma_1 + 1$. This is done as long as both γ_1 and γ_2 are lower than *max*. Finally, the list *sol* is returned:

```
findγs[γmax_, γ1_, γ2_, sol_List];

γ1 > γmax := (Clear[γ3],sol) (*6*)

findγs[γmax_, γ1_, γ2_, sol_List]; (γ1 ≤ γmax && γ2>γmax &&
IntegerQ[γ3=(γ1γ2)/(γ1+γ2)])
:= findγs[γmax, γ1+1, 1, Append[sol, {γ1, γ2, γ3}]] (*5*)

findγs[γmax_, γ1_, γ2_, sol_List];
(γ1 ≤ γmax && γ2>γmax &&
```

```
!IntegerQ[γ3=(γ1γ2)/(γ1+γ2)])
:= findγs[γmax, γ1 + 1, 1, sol] (*4*)

findγs[γmax_, γ1_, γ2_, sol_List];
(γ1 ≤ γmax && γ2 ≤ γmax && IntegerQ[γ3=(γ1γ2)/(γ1+γ2)])
:= findγs[γmax, γ1, γ2+1, Append[sol, {γ1, γ2, γ3}]] (*3*)

findγs[γmax_, γ1_, γ2_, sol_List];
(γ1 ≤ γmax && γ2 ≤ γmax && !IntegerQ[γ3=(γ1γ2)/(γ1+γ2)])
:= findγs[γmax, γ1, γ2 + 1, sol] (*2*)

findγs[γmax_] := findγs[γmax, 1, 1, {}]) (*1*)
```

For **findγs[γmax]** to be executable, the iteration depth of 2^{12} is not sufficient and it was set to ∞.

4.2.3 Linear Condition

The third auxiliary function **makemns** checks whether the linear condition $n_1 \pm n_2 = n_3$ is fulfilled and structures the solution set into a list of pairs $\{\{m_1,n_1\},\{m_2,n_2\},\{m_3,n_3\}\}$:

```
Clear[makemns];

makemns[m1_, n1_, m2_, n2_, m3_, n3_] := {} (*3*)

makemns[m1_, n1_, m2_, n2_, m3_, n3_];
(n1 + n2 == n3 || n1 - n2 == n3) :=
    {{m1, n1}, {m2, n2}, {m3, n3}} (*2*)

makemns[mn1_List, mn2_List, mn3_List] :=
    Cases[Flatten[Table[makemns[mn1[[i,1]], mn1[[i,2]],
       mn2[[j,1]], mn2[[j,2]], mn3[[k,1]], mn3[[k,2]]],
       {i, 1, Length[mn1]}, {j, 1, Length[mn2]},
       {k, 1, Length[mn3]}], 2],
       {{x1_,x2_}, {x3_,x4_}, {x5_,x6_}}] (*1*)
```

The function **makemns** is called three times:

In (*1*) from three lists of arbitrarily many pairs {mi, ni}, a three-dimensional array is made combining entries of the three lists with each other. Each entry calls the same program with the parameters of the current combination of {m1,n1,m2,n2,m3,n3}.

In (*2*) and (*3*) it is decided whether the condition $n1 \pm n2 = n3$ is fulfilled. If it is, a solution {{m1,n1},{m2,n2},{m3,n3}} is written in the array. The table is then flattened to the level 2 in order to have a list of solutions. In the end, all empty lists have to be sorted out, done by the function **Cases**, which keeps only those cases that have the shape {{x1_,x2_},{x3_,x4_},{x5_,x6_}}.

4.2.4 Scale Coefficients

Finally, the function **respectL[sol, Lx, Ly]** divides each component of the solution by the pair $(L_x,\ L_y)$ and sorts out the result if any of the six components does not remain an integer:

```
respectL[sol_List, Lx_, Ly_] :=
    Map[solution[#]&,
       Cases[Map[#/{Lx, Ly}&,
       Map[#[[1]]]&, sol], {2}], {{_Integer, _Integer},
      {_Integer, _Integer}, {_Integer,  _Integer}}]]
```

The function **respectL[sol, Lx, Ly]** gets as an input the list of the form {solution[{{m1,n1},{m2,n2},{m3,n3}}],...} and returns the list of the same form.

4.3 Results

All solutions in the computation domain $m,n \leq 300$ have been found in a few minutes. Notice that computations in the domain $m,n \leq 20$ by direct search without introducing indexes q and classes Cl_q took about 30 min. A direct search in the domain $m,n \leq 30$ has been interrupted after 2 h, since no results were produced.

The number of solutions depends drastically on the scales L_x and L_y, some data are given below (for the domain $m,n \leq 50$):

$(L_x = 1, L_y = 1)$: 76 solutions;
$(L_x = 3, L_y = 1)$: 23 solutions;
$(L_x = 6, L_y = 16)$: 2 solutions;
$(L_x = 5, L_y = 21)$: 2 solutions;
$(L_x = 11, L_y = 29)$: no solutions (search up to 300, for both *qmax* and γmax).

Interestingly enough, in all tried possibilities, only an odd q yield solutions.

5 Structure of the Solution Set

5.1 Method Description

The graphical way to present 2D-wave resonances suggested in Kartashova (1998) for three-wave interactions is to regard each 2D-vector $\vec{k} = (m,n)$ as a node (m,n) of integer lattice in the spectral space and connect those nodes which construct one solution (triad, quartet, etc.). Having computed already all the solutions of (3) in Sect. 4, now we are interested in the structure of resonances in spectral space. To each node (m,n) we can prescribe an amplitude $A(m,n,t_1)$ whose time evolution can be computed from the dynamical equations obtained in Sect. 3. Thus, solution

set of resonance conditions (3) can be thought of as a collection of triangles, some of them are isolated, some form small groups connected by one or two vertices. Corresponding dynamical systems can be reconstructed from the structure of these groups. For instance, a single isolated triangle corresponding to a solution with wave vectors $(m_1,n_1)(m_2,n_2)(m_3,n_3)$ and wave amplitudes $\{(A1,\ A2,\ A3)\}$ corresponds to the following dynamical system:

$$\begin{aligned}
\dot{A_1} &= \alpha_1 A_2 A_3,\\
\dot{A_2} &= \alpha_2 A_1 A_3,\\
\dot{A_3} &= \alpha_3 A_1 A_2,
\end{aligned}$$

with α_i being functions of all m_i, n_i (see Sect. 3).

If that two triangles share one common vertex $\{(A1,\ A2,\ A3),(A3,\ A4,\ A5)\}$, then the corresponding dynamical system is

$$\begin{aligned}
\dot{A_1} &= \alpha_1 A_2 A_3,\\
\dot{A_2} &= \alpha_2 A_1 A_3,\\
\dot{A_3} &= \alpha_{3,1} A_1 A_2 + \alpha_{3,2} A_4 A_5,\\
\dot{A_4} &= \alpha_4 A_3 A_5,\\
\dot{A_5} &= \alpha_5 A_3 A_4.
\end{aligned}$$

If two triangles have two vertices in common $\{(A1,\ A2,\ A3),(A2,\ A3,\ A4)\}$, then the dynamical system is quite different:

$$\begin{aligned}
\dot{A_1} &= \alpha_1 A_2 A_3,\\
\dot{A_2} &= \alpha_{2,1} A_1 A_3 + \alpha_{2,2} A_3 A_4,\\
\dot{A_3} &= \alpha_{3,1} A_1 A_2 + \alpha_{3,2} A_2 A_4,\\
\dot{A_4} &= \alpha_4 A_2 A_3 = \frac{\alpha_4}{\alpha_1}\dot{A_1}.
\end{aligned}$$

Using the fourth equation, the formulae for $\dot{A_2}$ and $\dot{A_3}$ can be simplified to

$$\begin{aligned}
\dot{A_4} &= \frac{\alpha_4}{\alpha_1}\dot{A_1} \Rightarrow A_4 = \frac{\alpha_4}{\alpha_1}A_1 + \beta_1,\\
\dot{A_2} &= A_1 A_3 \left(\alpha_{2,1} + \frac{\alpha_{2,2}\alpha_4}{\alpha_1}\right) + \frac{\alpha_4\beta_1}{\alpha_1},\\
\dot{A_3} &= A_1 A_2 \left(\alpha_{3,1} + \frac{\alpha_{3,2}\alpha_4}{\alpha_1}\right) + \frac{\alpha_4\beta_1}{\alpha_1}.
\end{aligned}$$

This means that *qualitative dynamics* of the three-term mesoscopic system depends *not on the geometrical structure* of the solution set but on its *topological structure*. Constructing the topological structure of the solution set, we do not consider concrete values of the solution but only the way how triangles are connected. In any finite spectral domain we can compute all independent wave clusters and

write out corresponding dynamical systems; thus obtaining complete information about energy transfer through the spectrum. Of course, *quantitative* properties of the dynamical systems depend on the specific values of m_i, n_i (for instance, values of interaction coefficients α_i, magnitudes of periods of the energy exchange among the waves belonging to one cluster, etc.).

5.2 Implementation

To construct the topological structure of a given solution set we need first to find all groups of connected triangles. This is done by the following procedure:

```
FindConnectedGroups[triangles_List] :=
 Block[{groups = {}, tr = triangles, newgroup},
   While[Length[tr] > 0,
     {newgroup, tr} =
       FindConnectedTriangles[{First[tr]}, Rest[tr]];
     groups = Append[groups, newgroup];
   ];
   groups
 ];

FindConnectedTriangles[grp_List,triangles_List]:=
 Module[{points,newGrpMember,tr=triangles},
   points=Flatten[Apply[List,grp,2],1];
   newGrpMember=Cases[tr, _[___,#1,___]]&/@points;
   (tr=DeleteCases[tr, _[___,#1,___]])&/@points;
   newGrpMember=Union[Join@@newGrpMember];
   If[Length[newGrpMember]==0,
     {grp,tr},
     newGrpMember=FindConnectedTriangles[newGrpMember,tr];
     {Join[grp,First[newGrpMember]],
      newGrpMember[[2]]}
    ]
 ];
```

The function `FindConnectedGroups` expects a list of triangles as input, and three different types for data structure can be used. The first type is just a list of three pairs, where each pair contains the coordinates of a node, for example, `{{1,2},{3,4},{5,6}}`. An alternative type is like the type before just with another head symbol instead of list, for example,

```
Triangle[{1,2},{3,4},{5,6}].
```

The function also works for vertex numbers instead of coordinates, for example, `Triangle[1,2,3]`. In every case, the function returns a partition of the input

list where all elements of a list are connected and elements of different lists have no connection to each other.

The function `FindConnectedTriangles` is an auxiliary function, which has two parameters. The first list contains all connected triangles. The second list contains all other triangles that are possibly connected to one of the triangles in the first list. The function `FindConnectedTriangles` returns a pair of lists: the first list contains all triangles that are connected to the selected triangles, the second list contains all the remaining.

The input list for `FindConnectedTriangles` is a list of three-element lists. Before we can use the results produced in Sect. 4 as an input we have to transform the data. This can be easily done by

```
TransformSolution[sol_List]:=
  Flatten[Rest/@sol]/.solution[trs:{___List}]->trs.
```

Some remarks on the implementation

The function `FindConnectedGroups` selects a triangle, which is not yet in a group and calls the function `FindConnectedTriangles`. Since the returned first list always contains at least one triangle, the length of the list `tr` decreases in every loop call, hence the `FindConnectedGroups` terminates. The question left is how to find all triangles connected with a certain triangle. This has been done in the following way. First we search for all triangles that share at least one node with this triangle. Then we restart the search with all triangles found. For efficiency reasons it is better to perform the search with all triangles we found in one step together. If in one step no further triangles are found then we are ready and return the list of connected triangles and the remaining list. In each step we remove all triangles we found from the list of triangles that are not declared as connected. This increases the speed because the search is faster if there are less elements to compare. More important, this prevent us to search in loops and find some triangles more than once. In general, search in a loop can be the reason for a termination problem but due to shrinking the list of triangles to search for in every step the termination can be guaranteed.

5.3 Results

In Fig. 1 the geometrical structure of the solution set is shown, for the case m_i, $n_i \leq 50$ and $L_x = L_y = 1$.

Below we show all the topological elements of this solution set.

1. Twenty-one groups contain only one triangle (obviously, they have isomorphic dynamical systems):

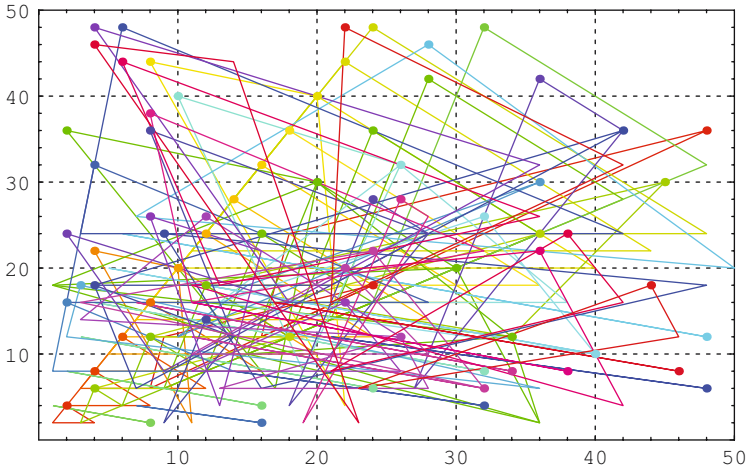

Fig. 1 The geometrical structure of the result in domain $D = 50$

$\{\{3,18\},\{36,6\},\{2,12\}\}$ $\{\{4,46\},\{14,44\},\{23,2\}\}$
$\{\{6,44\},\{36,26\},\{13,18\}\}$ $\{\{6,48\},\{42,24\},\{3,24\}\}$
$\{\{8,26\},\{16,22\},\{13,4\}\}$ $\{\{9,24\},\{48,18\},\{16,6\}\}$
$\{\{14,28\},\{28,14\},\{7,14\}\}$ $\{\{18,36\},\{36,18\},\{9,18\}\}$
$\{\{22,16\},\{26,8\},\{11,8\}\}$ $\{\{22,20\},\{28,10\},\{11,10\}\}$
$\{\{22,44\},\{44,22\},\{11,22\}\}$ $\{\{22,48\},\{42,32\},\{21,16\}\}$
$\{\{24,18\},\{9,12\},\{8,6\}\}$ $\{\{26,28\},\{28,26\},\{19,2\}\}$
$\{\{28,42\},\{42,28\},\{21,14\}\}$ $\{\{28,46\},\{50,20\},\{7,26\}\}$
$\{\{36,22\},\{42,4\},\{11,18\}\}$ $\{\{36,30\},\{15,18\},\{10,12\}\}$
$\{\{38,24\},\{42,16\},\{21,8\}\}$ $\{\{44,18\},\{46,12\},\{23,6\}\}$
$\{\{48,36\},\{18,24\},\{16,12\}\}$

2. Further nine groups also contain one triangle, but in each triangle two points coincide (again, they have isomorphic dynamical systems):

$\{\{8,2\},\{8,2\},\{1,4\}\}$ $\{\{16,2\},\{16,2\},\{7,4\}\}$
$\{\{16,4\},\{16,4\},\{2,8\}\}$ $\{\{24,6\},\{24,6\},\{3,12\}\}$
$\{\{32,8\},\{32,8\},\{4,16\}\}$ $\{\{34,8\},\{34,8\},\{7,16\}\}$
$\{\{46,8\},\{46,8\},\{17,16\}\}$ $\{\{48,6\},\{48,6\},\{21,12\}\}$
$\{\{48,12\},\{48,12\},\{6,24\}\}$

3. There exist two groups with two triangles each (by observation of the geometrical pictures it is easy to determine that both have isomorphic dynamical systems):

$\{\ \{\{2,24\},\{18,16\},\{9,8\}\},\quad \{\{4,48\},\{36,32\},\{18,16\}\}\ \}$
$\{\ \{\{12,26\},\{26,12\},\{3,14\}\},\ \{\{26,12\},\{28,6\},\{13,6\}\}\ \ \}$

4. Two further groups consist of two triangles each, but the common point is contained twice in one triangle (the dynamical systems are isomorphic, but different from the two groups above):

$$\{\ \{\{24,22\},\{32,6\},\{3,16\}\},\ \ \{\{32,6\},\{32,6\},\{11,12\}\}\ \}$$
$$\{\ \{\{8,38\},\{32,22\},\{11,16\}\},\ \{\{38,8\},\{38,8\},\{11,16\}\}\ \}$$

5. As we can see by inspecting their geometrical structures, further seven groups are not isomorphic to any group found above:

$$\{\ \{\{6,12\},\{12,6\},\{3,6\}\},\quad \{\{12,24\},\{24,12\},\{6,12\}\},$$
$$\{\{24,48\},\{48,24\},\{12,24\}\}\ \}$$

$$\{\ \{\{2,16\},\{14,8\},\{1,8\}\},\quad \{\{4,32\},\{28,16\},\{2,16\}\},$$
$$\{\{32,4\},\{32,4\},\{14,8\}\}\ \}$$

$$\{\ \{\{2,4\},\{4,2\},\{1,2\}\},\quad \{\{4,8\},\{8,4\},\{2,4\}\},$$
$$\{\{8,16\},\{16,8\},\{4,8\}\},\quad \{\{16,32\},\{32,16\},\{8,16\}\}\ \}$$

$$\{\ \{\{4,22\},\{10,20\},\{11,2\}\},\quad \{\{8,44\},\{20,40\},\{22,4\}\},$$
$$\{\{10,20\},\{20,10\},\{5,10\}\},\quad \{\{20,40\},\{40,20\},\{10,20\}\}\ \}$$

$$\{\ \{\{10,40\},\{26,32\},\{19,8\}\},\quad \{\{26,32\},\{38,16\},\{13,16\}\},$$
$$\{\{32,26\},\{40,10\},\{13,16\}\},\quad \{\{40,10\},\{40,10\},\{5,20\}\}\ \}$$

$$\{\ \{\{4,18\},\{14,12\},\{7,6\}\},\quad \{\{8,36\},\{28,24\},\{14,12\}\},$$
$$\{\{12,14\},\{14,12\},\{9,2\}\},\quad \{\{24,28\},\{28,24\},\{18,4\}\},$$
$$\{\{36,42\},\{42,36\},\{27,6\}\},\quad \{\{42,36\},\{21,18\},\{4,18\}\}\ \}$$

$$\{\ \{\{2,36\},\{20,30\},\{17,6\}\},\quad \{\{4,6\},\{6,4\},\{3,2\}\},$$
$$\{\{8,12\},\{12,8\},\{6,4\}\},\quad \{\{12,18\},\{18,12\},\{9,6\}\},$$
$$\{\{16,24\},\{24,16\},\{12,8\}\},\quad \{\{18,12\},\{9,6\},\{4,6\}\},$$
$$\{\{20,30\},\{30,20\},\{15,10\}\},\quad \{\{20,30\},\{34,12\},\{1,18\}\},$$
$$\{\{24,36\},\{36,24\},\{18,12\}\},\quad \{\{30,20\},\{36,2\},\{1,18\}\},$$
$$\{\{32,48\},\{48,32\},\{24,16\}\},\quad \{\{34,12\},\{36,2\},\{15,10\}\},$$
$$\{\{36,24\},\{18,12\},\{8,12\}\},\quad \{\{45,30\},\{34,12\},\{12,18\}\}\ \}$$

Geometrical interpretation of all topological elements is given below. In cases when there exist more then one element with given structure, wave numbers are written at the picture corresponding to the element chosen for presentation.

5.4 Important Remark

To compute all nonisomorphic subgraphs algorithmically is a nontrivial problem. Indeed, all isomorphic graphs presented in previous section are described by similar dynamical systems, only magnitudes of interaction coefficients α_i vary. However, in the general case graph structure thus defined does not present the dynamical system

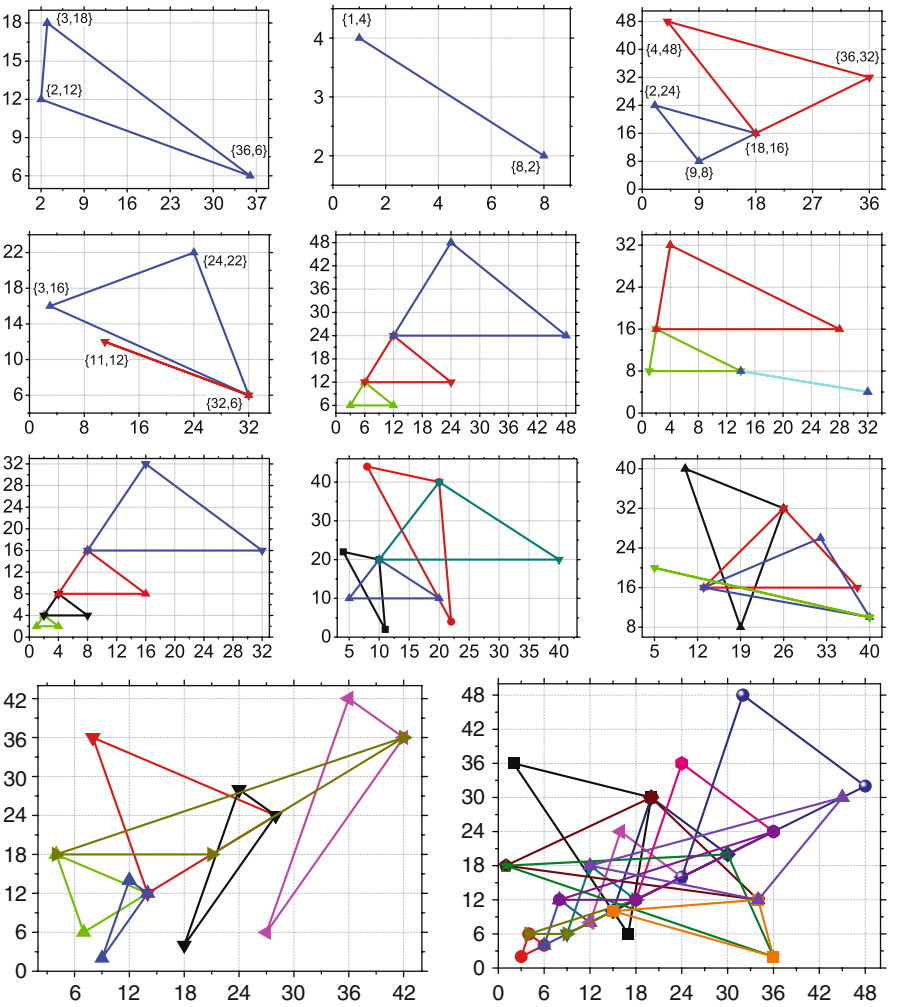

unambiguously. Consider Fig. 2 below where two objects are isomorphic *as graphs*. However, the first object represents four connected triads with dynamical system

$$(A_1, A_2, A_3),\ (A_1, A_2, A_5),\ (A_1, A_3, A_4),\ (A_2, A_3, A_6), \tag{8}$$

while the second three connected triads with dynamical system

$$(A_1, A_2, A_5),\ (A_1, A_3, A_4),\ (A_2, A_3, A_6). \tag{9}$$

This problem has been solved in Kartashova and Mayrhofer (2007) by introducing hypergraphs of a special structure; the standard graph isomorphism algorithm used by Mathematica has been modified in order to suit hypergraphs.

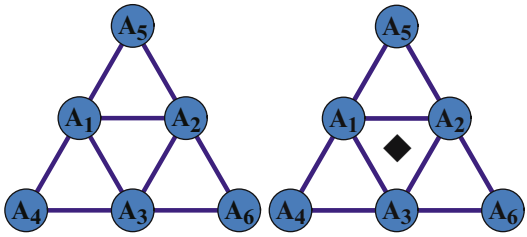

Fig. 2 Example of isomorphic graphs and nonisomorphic dynamical systems. The left graph corresponds to the dynamical system (8) and the graph on the right to the dynamical system (9). To discern between these two cases we set a placeholder inside the triangle not representing a resonance

6 A Web Interface to the Software

The previous sections have presented implementations of various symbolic computation methods for the analysis of nonlinear wave resonances. These implementations are written in the language of the computer algebra system Mathematica, which provides an appealing graphical user interface (GUI) for executing computations and presenting the results. For instance, the pictures shown in Sect. 4.3 were produced by converting the computed hypergraphs to Mathematica plot structures that can be displayed by the GUI of the system.

However, to run these methods the user needs an installation of Mathematica on the local computer with the previously described methods installed in a local directory. These requirements make access to the software difficult and hamper its wide-spread usage. To overcome this problem, we have implemented a Web interface such that the software can be executed from any computer connected to the Internet via a Web browser without the need for a local installation of mathematical software.

This implementation follows a general trend in computer science, which turns away from stand alone software (that is installed on local computers and can be executed only on these computers via a graphical user interface) and proceeds towards *service-oriented software* (Gold et al. 2004) (that is installed on remove server computers and wraps each method into a service that can be invoked over the Internet via standardized Web interfaces). Various projects in computer mathematics have pursued middleware for *mathematical web services*, see for instance MathBroker (2007), MONET (2004), Baraka and Schreiner (2006). On the long term, it is thus envisioned that mathematical methods generally become remote services that can be invoked by humans (or other software) without requiring local software installations.

However, even without sophisticated middleware it is nowadays relatively simple to provide (for restricted application scenarios) web interfaces to mathematical software by generally available technologies. The web interface presented in the following sections is deliberately kept as simple as possible and makes only use of such technologies; thus it should be easy to take this solution as a blueprint for

other mathematical software with similar features. In particular, the web interface is quite independent of Mathematica as the system underlying the implementation of the mathematical methods; the same strategy can be applied to other mathematical software systems such as Maple, MATLAB, etc.

6.1 The Interface

Figure 3 shows the web interface to some of the methods presented in the previous sections. Its functionality is as follows:

Create Solution Set: The user may enter a parameter D in the first (small) text field and then press the button "Create Solution Set." This invokes the method `CreateSolutionSet`, which computes the set of all solutions whose values are smaller than or equal to D. This set is written into the second (large) text field in the form

$$\{\texttt{Solution}[x_1, y_1, z_1], \ldots, \texttt{Solution}[x_n, y_n, z_n]\}.$$

Plot Topology: The user may enter into the second (large) text field a specific solution set (or, as show above, compute one), and then press the button "Plot Topology." This first invokes the method `Topology`, which computes the topological structure of the solution set as a list of hypergraphs and then calls the

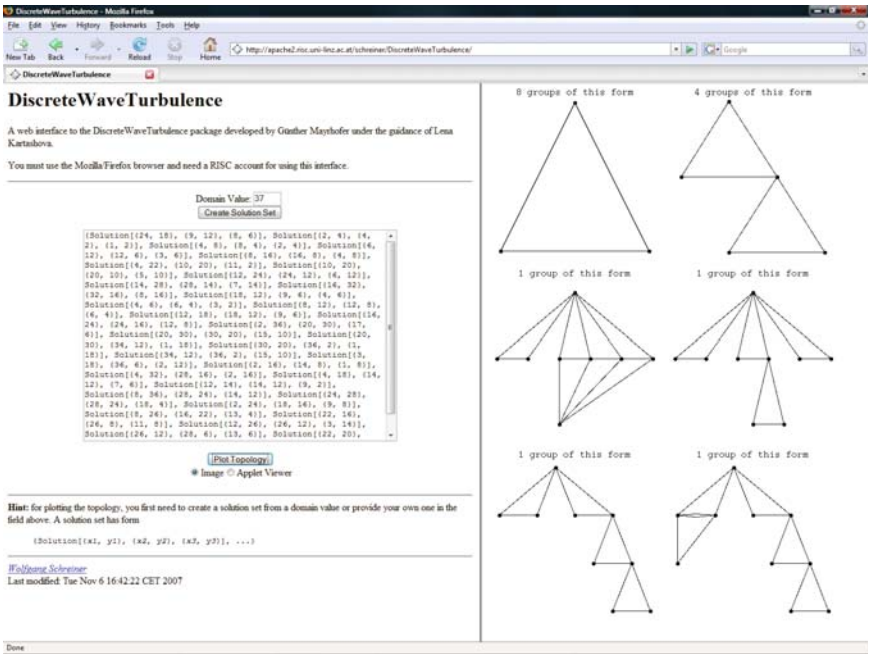

Fig. 3 Web interface to the implementation

method `PlotTopology`, which computes a plot of each hypergraph. The results are displayed in the right frame of the browser window.

The web interface is available at the URL

`http://www.risc.uni-linz.ac.at/projects/alisa`
(Button "Discrete Wave Turbulence")

To run the computations, an account and a password are needed.

6.2 The Implementation

The web interface is implemented in PHP, a scripting language for producing dynamic web pages (The PHP Group 2007). PHP scripts can be embedded into conventional HTML pages within tags of form `<php?...?>`; when a Web browser requests such a page, the Web server executes the scripts with the help of an embedded PHP engine, replaces the tags by the generated output, and returns the resulting HTML page to the browser. With the use of PHP, thus programs can be implemented that run on a web server and deliver their results to a client computer which displays them in a web browser. The web interface to the discrete wave turbulence package is implemented in PHP as sketched in Fig. 4 and described below (the parenthesized numbers in the text refer to the corresponding numbers in the figure).

Create Solution Set: The browser frame `input` on the left side contains essentially the following HTML input form:

```
<form target="textarea"
    action="https://apache2.../CreateSolutionSet.php"
    method="post">
  <input name="domain" size="3">
  <input type="submit" value="Create Solution Set">
</form>
```

This form consists of an input field `domain` to receive a domain value and a button to trigger the creation of the solution set. When the button is pressed, (1) a request is sent to the web server which carries the value of `domain`; this request asks the server to deliver the PHP-enhanced web page `CreateSolutionSet.php` into the target frame `textarea`, which is displayed internally to `input`.

The file `CreateSolutionSet.php` has essentially the content

```
<?php
  $math="/.../math";
  $cwd="/.../DiscreteWaveTurbulence";
  $domain = $_POST['domain'];
  $mcmd =
    "SetDirectory[\"" . $cwd . "\"]; " .
    "Needs[\"DiscreteWaveTurbulence`SolutionSet`\"]; " .
    "sol=DiscreteWaveTurbulence`SolutionSet`CreateSolutionSet[".
```

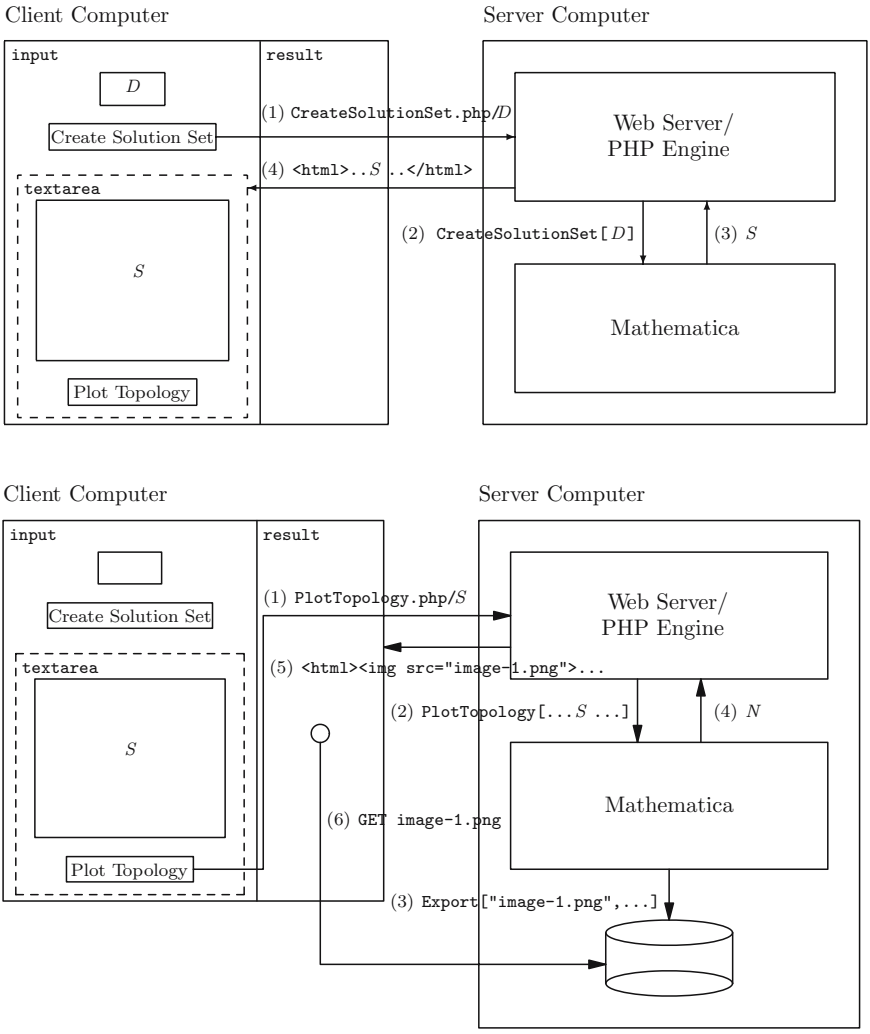

Fig. 4 Implementation of the web interface

```
      $domain . "]; ";
$command="$math -noprompt -run '" . $mcmd .
   "Print[StandardForm[sol]]; Quit[];'";
$result = shell_exec("$command");
echo
  ...
  "<textarea  name=\"sol\" cols=\"60\" rows=\"20\">" .
  htmlspecialchars($result) .
  "</textarea>" .
 ...;
?>
```

After setting the paths `$math` of the Mathematica binary and `$cwd` of the directory where the `DiscreteWaveTurbulence` package is installed, the script sets the local variable `$domain` to the value of the input field `domain`. Then the Mathematica command `$mcmd` is constructed in order to load the file `SolutionSet.m` and execute the command `CreateSolutionSet` to compute the solution set. Now the system command `$command` is constructed to (2) invoke Mathematica, which calls the previously constructed command, and (3) prints its result to the standard output stream, which is captured in the variable `$result`. From this, the script contstructs the HTML code of the result document, which is (4) delivered to the Web browser.

Plot Topology: The browser frame `textarea` contains essentially the following HTML input form:

```
<form target="result"
    action="https://apache2..../PlotTopology.php"
    method="post">
  <textarea name="sol" cols="60" rows="20">...</textarea>
  <input type="submit" value="Plot Topology">
  </center>
</form>
```

This form consists of the textarea field `sol` to receive the solution set and a button to trigger the plotting of the topology of this set. When the button is pressed, (1) a request is sent to the web server which carries the value of `sol`; this request asks the server to deliver the PHP-enhanced web page `PlotTopology.php` into the target frame `result` on the right side of the browser.

The file `CreateSolutionSet.php` has essentially the content

```
<?php
  $math="/.../math";
  $basedir ="/.../DiscreteWaveTurbulence";
  $baseurl ="http://apache2/.../DiscreteWaveTurbulence";
  $sol = $_POST['sol'];
  ... // create under $basedir a unique subdirectory $dir
  $mcmd =
    "SetDirectory[\"$basedir/$dir\"]; " .
    "Needs[\"DiscreteWaveTurbulence`Topology`\"]; " .
    "Needs[\"DiscreteWaveTurbulence`SolutionSet`\"]; " .
    "top=DiscreteWaveTurbulence`Topology`Topology[$sol]; " .
    "plots=DiscreteWaveTurbulence`Topology`PlotTopology1[top];";
  $command="/usr/bin/Xvnc :20 & export DISPLAY=:20; " .
    "export MATHEMATICA_USERBASE=$basedir/.Mathematica; " .
    "$math -run '" . $mcmd .
    "Print[ExportList[plots,\"$image\"]]; Quit[];'";
  $result = shell_exec("$command | tail -n 1");
  for ($i=0;$i<$result;$i++)
    echo "<img src=\"$baseurl/$dir/image-$i.png\"/>";
?>
```

For holding the images to be generated later, the script creates a unique directory `$basedir/$dir`, which is served by the web server under the url

`$baseurl/$dir`. The script extracts the solution set `$sol` from the request and sets up the Mathematica command to compute its topological structure and generate the plots from which ultimately the image files will be produced.

For this purpose, however, Mathematica needs an X11 display server running; since a Web server has no access to an X11 server, we start the virtual X11 server Xvnc (RealVNC Remote Control Software 2007) as a replacement and set the environment variable `DISPLAY` to the display number on which the number listens; Mathematica will subsequently send X11 requests to that display, which will be handled by the virtual server. Likewise, Mathematica needs access to a `.Mathematica` configuration directory; the script sets the environment variable `MATHEMATICA_USERBASE` correspondingly.

With these provisions, we can (2) invoke first the command to compute the plots and then the (self-defined) command `ExportList` to generate for every plot an image in the previously created directory. For this purpose the command uses (3) the Mathematica command `EXPORT[`*`file`*`,`*`plot`*`,"PNG"]`, which converts *plot* to an image in PNG format and writes the image to *file*. `ExportList` returns the number of images generated, which is (4) written to the standard output stream which in turn is captured in the variable `$result`. From this information, the script generates an HTML document, which contains a sequence of `img` elements referencing these images. After this document has been (5) returned to the client browser, the browser (6) requests the referenced images with `GET` messages from the web server.

6.3 Extensions

As an alternative to the display of static images, the Web interface also provides an option "Applet Viewer" with somewhat more flexibility. If this option is selected, Mathematica is instructed to save all generated plots as files in the standard representation. The generated HTML document then embeds (rather than `img` elements) a sequence of `applet` elements that load instances of the "JavaView" applet (The JavaView Project 2007). These applets run in the Java Virtual Machine of the Web browser on the client computer, load the plot files from the web, and visualize them in the browser. Rather than just displaying static images, the viewer allows to perform certain manipulations and transformations of the plots such as scaling, rotating, etc. While this additional flexibility is not of particular importance for the presented methods, they may in the future become useful for others.

To limit access to the software, respectively, to the computing power of the server computer, it may be protected by authentication mechanisms. For example, on the Apache Web server, it suffices to provide in the installation directory of the software a file `.htaccess` with content

```
<Files "*.php">
  SSLRequireSSL
  AuthName "your account"
```

```
    AuthType Basic
    Require valid-user
</Files>
```

With this configuration, the user is asked for the data of a valid account on the computer running the Web server; other authentication mechanisms based, for example, on password files may be provided in a similar fashion.

7 Discussion

Summing up all the results obtained, we would like to make some concluding remarks.

- In general, coefficients α_i can be computed symbolically by hand and only numerically by Mathematica (see Sect. 3.3); at present we are not aware of the possibility to overcome this problem.
- For the known case of spherical barotropic vorticity equation, values of coefficients α_i coincide with known form of the literature for all triads except three. These three triads, though satisfying resonant conditions, are known to be special from the physical point of view in the following sense (see Kartashova and L'vov (2007) for details). Though resonance conditions are fulfilled for the waves of these triads, they, so to say, do not have a place in the physical space to interact and their influence (if any) on the dynamics of the wave system has to be studied separately from all other waves. Our results might indicate that also the coefficients α_i of these triads have to be defined in some other way compared to other resonant triads. For instance, another way of space-averaging has to be chosen.
- The results of Sect. 3.4.2 show that analytical formulae given in Kartashova and Reznik (1992) for α_j *are not correct*.
- The results of Sect. 4.3 show a crucial dependence of the number of solutions on the form of the boundary conditions. In particular, some boundary conditions (for example, $(L_x, L_y) = (11, 29)$) yield *no solutions*, which is of most importance for physical applications. From the mathematical point of view, an interesting result has been observed: in all our computations (i.e., for $m, n \leq 300$) indexes corresponding to nonempty classes turned out to be *odd.* It would be interesting to prove this fact analytically because if it is true, we can reduce the computational time.
- The algorithm presented in Sect. 4 has been implemented before numerically in Visual Basic, and our purpose here was to show that it works fast enough also in Mathematica. The algorithms presented in Sects. 3 and 5 *have never been implemented before*, the whole work is usually done by hand and some mistakes as in Kartashova and Reznik (1992) are almost unavoidable: it takes sometimes a few weeks of skillful researchers to compute interaction coefficients of dynamical systems for one specific wave system.

- All the algorithms presented above can easily be modified for the case of a four-term mesoscopic system. The only problem left is a procedure to establish all nonisomorphic topological elements for a quadruple graphs, similar to the procedure given in Kartashova and Mayrhofer (2007) for a triangle graphs. The structure of quadruple graphs is much more complicated while some mechanisms of energy transfer in the spectral space do exist (Kartashova 2007) that are absent in three-term mesoscopic systems. A complete classification of quadruple graphs is still an open question but in a given spectral domain it can be done directly (a very time consuming operation).
- We have developed a Web interface for the presented methods, which turns the implementations from only locally available software to Web-based services that can be accessed from any computer in the Internet that is equipped with a Web browser. The presented implementation strategy is simple and is based on generally available technologies; it can be applied as a blueprint for a large variety of mathematical software. In particular, the results are not bound to the current Mathematica implementation but can be adapted to any other computer algebra system (e.g., Maple) or numerical software system (e.g., MATLAB) of similar expressiveness.
- At present, an explicit form of eigen-modes (5) and (6) is used as one of the input parameters for our program package. Theoretically, at least for some classes of linear partial differential operators and boundary conditions, computing eigen-modes can also be performed symbolically based on the results in Rosenkranz (2005). If this were done, not an eigen-mode but boundary conditions would play role of input parameter.

Acknowledgements Authors acknowledge the support of the Austrian Science Foundation (FWF) under projects SFB F013/F1301 "Numerical and symbolical scientific computing," P20164-N18 "Discrete resonances in nonlinear wave systems," and P17643-NO4 "MathBroker II: Brokering Distributed Mathematical Services."

References

Baraka R, Schreiner W (2006) Semantic querying of mathematical web service descriptions. Third international workshop on web services and formal methods (WS-FM 2006), Vienna, Austria, 8–9 September 2006

M. Bravetti et al. (eds) Lecture notes in computer science, vol. 4184. Springer, Berlin Heidelberg New York, pp 73–87

Berman GP, Israilev FM (2005) The Fermi-Pasta-Ulam problem: Fifty years of progress. Chaos 15(1):015104–015118

Cheney M (1989) Tesla man out of time. Dorset Press, New York

Gold N, Mohan A, Knight C, Munro M (2004) Understanding service-oriented software. IEEE Software 21(2):71–77

Kartashova EA (1998) Wave resonances in systems with discrete spectra. In: Zakharov VE (ed) Nonlinear waves and weak turbulence. Advances in the Mathematical Sciences (AMS), pp 95–129

Kartashova E (2006a) A model of laminated turbulence. JETP Lett 83(7):341–345

Kartashova E (2006b) Fast computation algorithm for discrete resonances among gravity waves. Low Temp Phys 145(1–4):286–295
Kartashova E (2007) Exact and quasi-resonances in discrete water-wave turbulence. Phys Rev Lett 98(21):214502
Kartashova E, Kartashov A (2006) Laminated wave turbulence: Generic algorithms I. Int J Mod Phys C 17(11):1579–1596
Kartashova E, Kartashov A (2007a) Laminated wave turbulence: Generic algorithms II. Comm Comp Phys 2(4):783–794
Kartashova E, Kartashov A (2007b) Laminated wave turbulence: Generic algorithms III. Phys A Stat Mech Appl 380:66–74
Kartashova E, L'vov VS (2007) A model of intra-seasonal oscillations in the Earth atmosphere. Phys Rev Lett 98(19):198501 (featured in Nat Phys (2007) 3(6):368)
Kartashova E, Mayrhofer G (2007) Cluster formation in mesoscopic systems. Phys A Stat Mech Appl 385:527–542
Kartashova EA, Reznik GM (1992) Interactions between Rossby waves in bounded regions. Oceanology 31:385–389
MathBroker II (2007) Brokering distributed mathematical services. Reseach Institute for Symbolic Computation (RISC). http://www.risc.uni-linz.ac.at/projects/mathbroker2
MONET (2004) Mathematics on the Web. The MONET Consortium, April 2004. http://monet.nag.co.uk
Nayfeh AN (1981) Introduction to perturbation techniques. Wiley, New York
Pedlosky J (1987) Geophysical fluid dynamics. Springer, Berlin Heidelberg New York
Pushkarev AN, Zakharov VE (2000) Turbulence of capillary waves – theory and numerical simulations. Physica D 135:98–116
RealVNC Remote Control Software (2007) VNC Free Edition 4.1. http://www.realvnc.com/products/free/4.1
Rosenkranz M (2005) A new symbolic method for solving linear two-point boundary value problems on the level of operators. J Symb Comp 39:171–199
Tanaka M (2007) On the role of resonant interactions in the short-term evolution of deep-water ocean spectra. J Phys Oceanogr 37:1022–1036
The JavaView Project (2007) JavaView – Interactive 3D geometry and visualization. http://www.javaview.de
The PHP Group (2007) PHP: Hypertext preprocessor. http://www.php.net
Zakharov V, Dias F, Pushkarev A (2004) One-dimensional wave turbulence. Phys Rep 398:1–65
Zakharov VE, Filonenko NN (1967) Weak turbulence of capillary waves. J Appl Mech Tech Phys 4:500–515
Zakharov VE, Korotkevich AO, Pushkarev AN, Dyachenko AI (2005) Mesoscopic wave turbulence. JETP Lett 82(8):491
Zakharov VE, L'vov VS, Falkovich G (1992) Kolmogorov spectra of turbulence. Series in nonlinear dynamics. Springer, Berlin Heidelberg New York

Searching for Factors that Limit Observed Extreme Maximum Wave Height Distributions in the North Sea

Gerrit Burgers, Frits Koek, Hans de Vries, and Martin Stam

Abstract The probability that individual waves are much larger than the significant wave height is studied in a large set of observations. It is investigated whether steepness and shallow water effects are limiting factors for extreme wave heights. The relation between observations and a model freak wave index is examined.

Measurements from two locations in the North Sea are used, one with a depth of 80 m, and another with a depth of 20 m. The data consist of the significant wave height, wave period and maximum wave height of 20-min records. The total amount of the records covers several years. The freak wave model index from the European Centre for Medium-Range Weather Forecasts (ECMWF) wave model is collocated with the observations.

The instrumental data show Rayleigh like distributions for the ratio of maximum wave height to significant wave height. Our analysis is limited by uncertainties in the instrumental response in measuring maximum wave height. The data indicate that steepness is a limiting factor for extreme wave height. At the shallow water location, extreme waves are not more frequently observed than at the deep water location. The relation between the freak wave index of the ECMWF wave model and enhanced extreme wave probability is studied.

1 Introduction

During the All Saints Day storm of November 2006, a waverider buoy recorded extreme individual waves of 17 and 20 m, around twice the significant wave height at the time (Fig. 1). For the same storm, the ECMWF (European Centre

G. Burgers
Royal Netherlands Meteorological Institute, P.O. Box 201, NL-3730 AE De Bilt, The Netherlands
burgers@knmi.nl

F. Koek, H. de Vries, and M. Stam
Royal Netherlands Meteorological Institute, De Bilt, The Netherlands
koek@knmi.nl, jwdv@knmi.nl, and stam@knmi.nl

E. Pelinovsky, C. Kharif (eds.) *Extreme Ocean Waves*, 127–138.

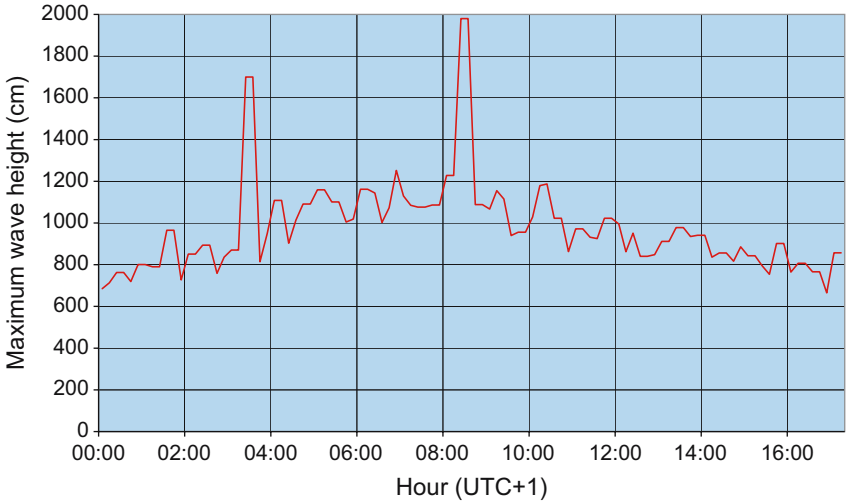

Fig. 1 Registration of maximum wave height at Schiermonnikoog Island (SMN) at (53°35N, 6°10E) during the night of 1 November 2006

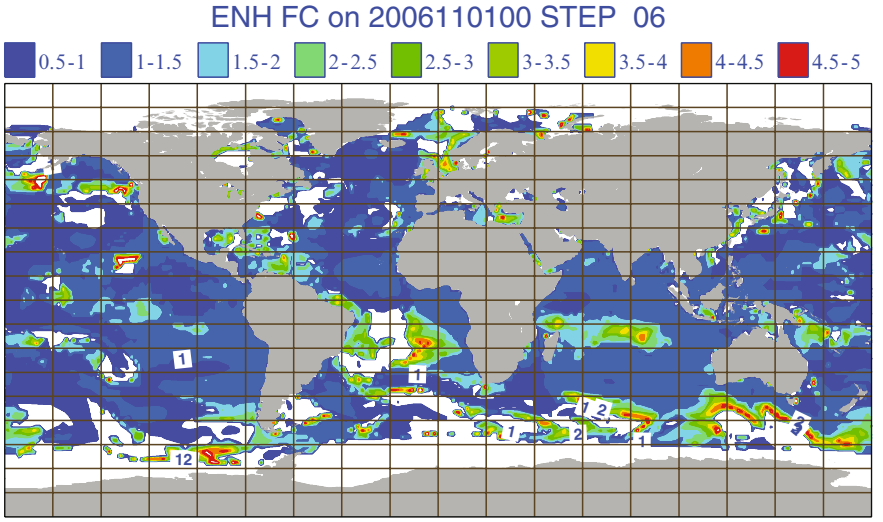

Fig. 2 WAM enhancement factor. This factor gives the ratio of the WAM model estimate to the standard linear model probability for waves with a height more than twice the significant wave height

for Medium-Range Weather Forecasts) wave model WAM indicated an enhanced probability of extreme waves in the North Sea, see Fig. 2. For a water depth of 20 m, a 20-m wave would be quite exceptional. Whether the record is correct remains unclear: analysis of the buoy by the manufacturer showed that the measurement is not reliable in these conditions (Datawell 2006), and in the same storm, damage

was reported at a platform more than 15 above sea level (Bojanowski 2007). But the buoy has been in place for years, so in principle we can determine multi-year return times for wave extremes.

In this chapter, we study the following questions: how exceptional are extreme waves in long records? Can the WAM model identify conditions with enhanced extreme wave probability? More precisely, we focus on the ratio $r = H_{\max}/H_s$, where H_s is the significant wave height and $H_{\max}$ the maximum wave height in a 20-min record, and from the WAM model we use the BFI index (Janssen 2003). Our study differs from the one by Holliday et al. (2006) in that we do use the 20-min record summary information instead of individual wave records, and that we have used data that accumulate to a much longer time. However, because various instruments and algorithms have been used, the interpretation as one single dataset is problematic.

Standard linear wave theory (see e.g. the textbook of Holthuijsen (2007) or the introduction by Berg and Rhome (2005)) gives rise to a Rayleigh distribution for wave height (Appendix). Freak waves are sometimes defined as waves that are higher than twice the significant wave height. According to the Rayleigh distribution, about one in 3,000 waves is a freak wave. For waves with a period of about 10 s, this is of the order of once every 8 h. In practice, of course, usage of the term freak wave is often restricted to cases where the absolute value is exceptionally high. Over the last few years, several mechanisms have been proposed, that give rise to enhanced extreme wave distribution compared with standard Rayleigh theory (Janssen 2003; Mori and Janssen 2006). In Fig. 3, which is discussed in Appendix A, such an enhanced extreme wave distribution is compared with the standard Rayleigh distribution. On the one hand, the WAM model index is based on a non-linear effect that enhances the extreme wave height distribution. On the other hand, for very large r, when

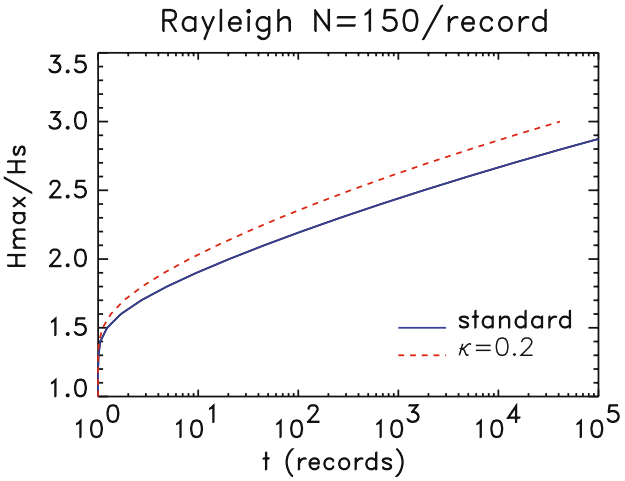

Fig. 3 Rayleigh and Janssen distribution of $H_{\max}/H_s$ of the return time of the ratio of $H_{\max}/H_s$ of maximum wave height over significant wave height. Time is measured in 150-wave records. The *thick line* is the Rayleigh distribution, the *dashed line* distribution according to Janssen theory for the case that the kurtosis of the sea surface $\kappa = 0.2$, corresponding to BFI $= 0.33$

steepness becomes a limiting factor, non-linear effects will lead to a suppression with respect to the Rayleigh distribution. Moreover, in shallow water, the behaviour might be quite different. So it is interesting to examine the behaviour of the observed distribution.

In Sect. 2, we discuss the observational dataset as well as the WAM model index. In Sect. 3, we present and analyse maximum wave height distributions, including a comparison between model results and observations. It is clear from the results that the maximum wave height as measured by an instrument depends on the sensor used. In Sect. 4, we give a discussion of the results, and in Sect. 5, we present the conclusions.

2 Data Sources

2.1 North Sea Data

The data consist of reports of the Meetnet Noordzee (MNZ), a network of measuring instruments at a number of platforms and buoys in the North Sea set up by the Dutch authorities in cooperation with platform operating companies. In this chapter, we use data from the AUK platform located in the central North Sea at (56°24N, 0°02E) and a depth of 80 m, and from the wave buoy near the coast of Schiermonnnikoog Island (SMN) in the north of the Netherlands at (53°35N,6°10E) and a depth of 20 m.

A report consists of a set of wave parameters extracted from a 20-min record, the frequency of the reports is 3 h. In this chapter, in addition to significant wave height and wave period, also the maximum wave height of the record is used. The MNZ data for wave height and wave period have been monitored for years by the Royal Netherlands Meteorological Institute (KNMI), and we know them to be reliable.

The measurements have been made by several types of instruments (Table 1). The radars operate from fixed platforms and measure surface elevation with a frequency

Table 1 Overview of instruments used in this study at the locations of Auk at 56°24N, 0°02E and Schiermonnikoog Island (Schier) at 53°35N, 6°10E

Label	Location	Type	Period
1	Auk	Waverider	19840326–19861010
2	Auk	Saab radar	19860413–19870714
A2	Auk	Saab radar	19930616–19990625
A3	Auk	Wavec	19901024–19991109
AUK1	Auk	Saab radar	20000204–20050928
AUK2	Auk	Wavec	20010718–20010925
AUK2	Auk	Directional waverider	20020621–20030731
4	Schier	Wavec	19901024–19930331
W4	Schier	Wavec	19931101–19991109
SMN1	Schier	Wavec	19931109–20031216
SMN1	Schier	Directional waverider	20020220–20070831

of 5.12 Hz. Wave buoys calculate wave data on the basis of acceleration measurements. The sample frequency is 1.28 Hz. A linear time-domain filter is used to reconstruct a wave height record, and to estimate the maximum wave height from these accelerations. The number of waves (from the estimated zero-upcrossing period) in a record falls typically in the range 150–200. The results of Sect. 3 show that wave buoys give systematically lower estimates for the maximum wave height than the radar estimates, and that there are significant differences between the various combinations of buoys and filters that have been used over the years.

Quality control included rejection of duplicates and the rejection of gross errors. For example, for the radar altimeter, some short periods with on average unrealistically high values were skipped. There are some features of the dataset we cannot explain. For example, there seems to be a preference for 'nice' values of the ratio $H_{\max}/H_{\mathrm{s}}$ such as 1.5 or 2. We have not been able to trace what part of the processing is responsible for this feature.

2.2 WAM Model BFI

The Benjamin Feir index *BFI* proposed by Janssen (2003) is a measure of the strength of the effect of non-linear interactions on wave height distribution. Non-linear effects are stronger if (1) waves are steeper, and (2) the wave spectrum is more narrow allowing for waves to travel longer together. For a narrow-band spectrum the definition of the BFI is

$$\mathrm{BFI} = \frac{\sqrt{2} k m_o^{1/2}}{(\sigma/\omega)}, \tag{1}$$

where k denotes the dominant wave number, ω the frequency of the spectrum, σ the spectral width, and $m_o^{1/2} = 0.25 H_{\mathrm{s}}$ the amplitude of the spectrum. In the numerator, $k m_0^{1/2}$ is the steepness, and the denominator is the narrowness of the spectrum.

For general spectra, the above expression for the spectral width is rather ambiguous, and Janssen (2003) uses the following expression for the BFI:

$$\mathrm{BFI} = \sqrt{2\pi} k m_o^{1/2} Q_p, \tag{2}$$

with

$$Q_{\mathrm{p}} = \frac{2}{m_0^2} \int \mathrm{d}\omega \omega E^2(\omega) \tag{3}$$

where $E(\omega)$ is the spectral density.

The BFI was added as an output parameter to ECMWF's wave model in the fall of 2003. Since then all model forecasts have been archived and from these archives BFI and significant wave height have been extracted from 6 October 2003 until 31 December 2006 in 6-hourly steps for model grid points near platform AUK and Schiermonnikoog.

3 Results

The first quantity we consider is the return period of $r = H_{\max}/H_s$ for the deep-water station AUK. In Fig. 4, this quantity is plotted as a function of return time (in units of 20-min records), for various instruments and periods. It appears that the differences between the instruments and periods are large. The radar altimeter values are close to those which one would expect from a Rayleigh, the wave-buoy data are generally lower.

For situations where the average steepness (H_s/λ) is large, steepness may be a limiting factor. First, we check in Fig. 5, which gives a plot of $H_{\max}$ vs. T if wave heights do not exceed the limiting steepness line of $H = \lambda/7$. This figure shows that it is not uncommon that the steepness approaches the limiting steepness.

If steepness is a limiting factor, then one would expect that for a given significant wave height, longer periods that go with less steep waves would lead to an enhanced probability of high values of r. Figure 6, where the average value of r for records with $H_s \approx 4m$ is plotted as a function of T, gives some evidence for this fact.

Now we turn to the shallow water results. In Fig. 7, the return periods for the shallow-water station Schiermonnikoog (SMN) are shown. Comparing these results to the deep water-data of AUK is hampered by the fact that different stations and periods are hard to compare. Even when matching periods and instruments, there remain problems: the SMN1 Wavec is much lower than the AUK2 Wavec, while the SMN W4 is only slightly lower than the AUK A3. We checked that this also holds when we restricted the comparison to periods that both instruments yielded data, (not shown). We note that period of the W4 vs. A3 comparison is much

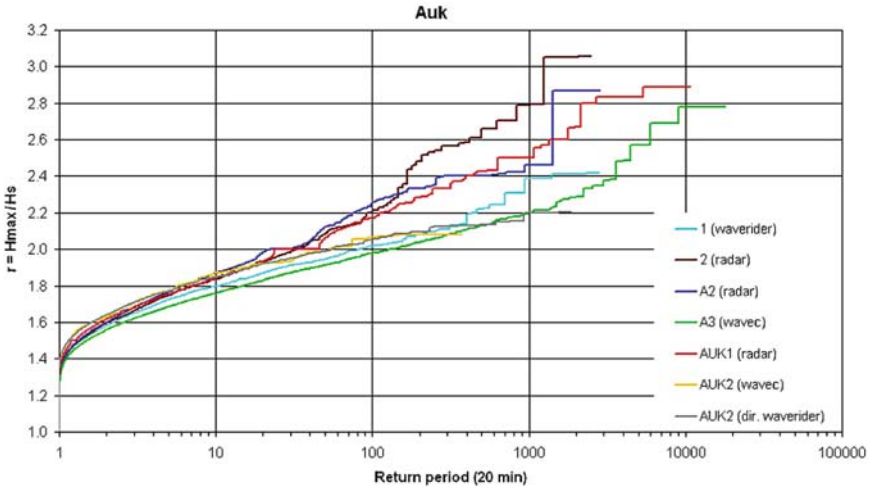

Fig. 4 Return times at the deep water station AUK. Time is measured in 20-min records. The labels refer to different instruments and periods, see Table 1

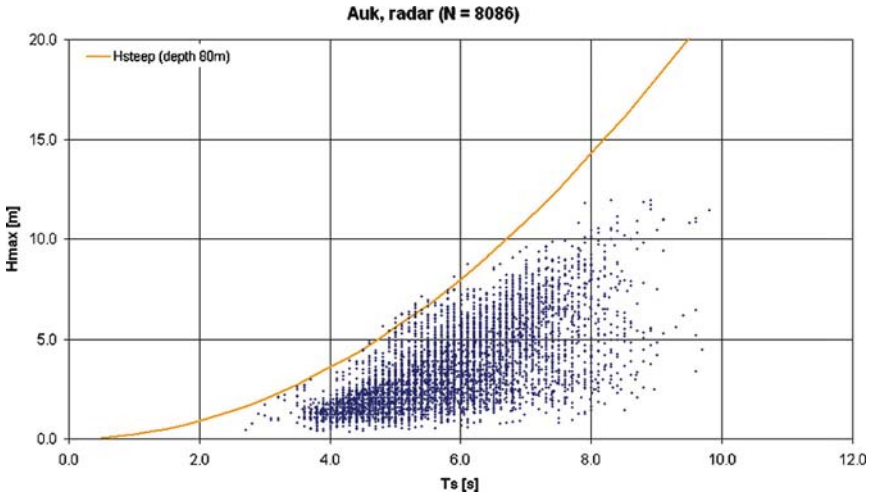

Fig. 5 Scatter plot of maximum wave height $H_{\max}$ vs. mean period T in deep water for the radar measurements at AUK

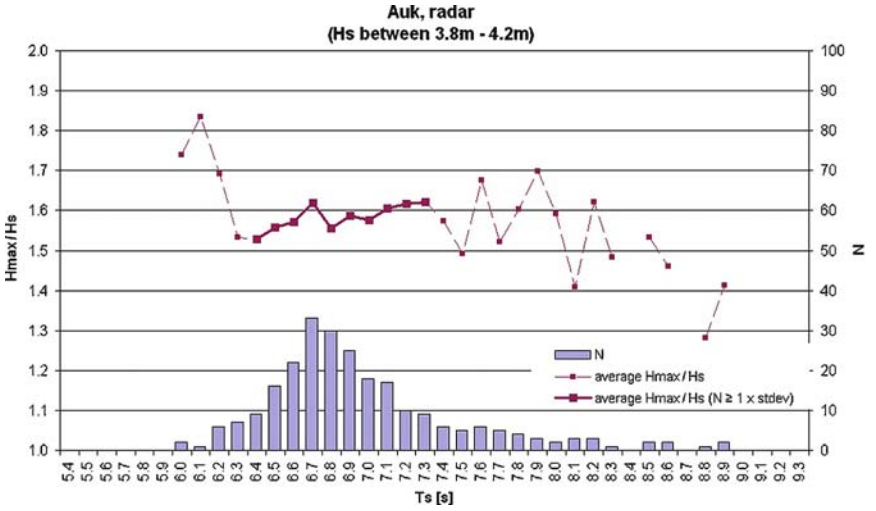

Fig. 6 The ratio $r = H_{\max}/H_{\mathrm{s}}$ as function of the mean period T, for radar measurements at AUK. The *histogram* indicates the number of data in each bin. The *solid line* connects the average value of r for bins with 9 or more entries

longer (19931101–19991109) than the period of the AUK2 vs. SMN1 comparison (20010718–20010925). What we can conclude is that there is no indication that outside the surf zone, values of r are higher in shallow water than in deep water

For this shallow water location, the constant steepness line (yellow) in a H-T diagram has a different shape than for deep water. Figure 8, which gives a plot of

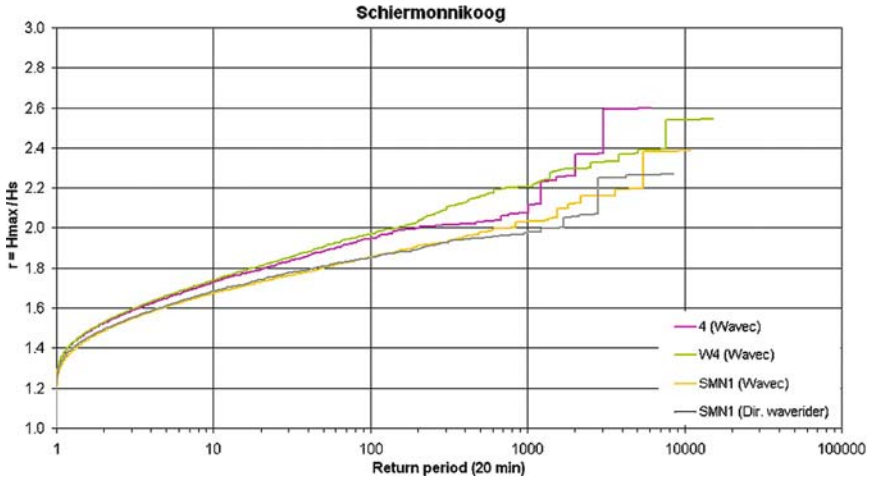

Fig. 7 Return times at the shallow water station Schiermonnikoog Island (SMN). Time is measured in 20-min records. The labels refer to different instruments and periods, see Table 1

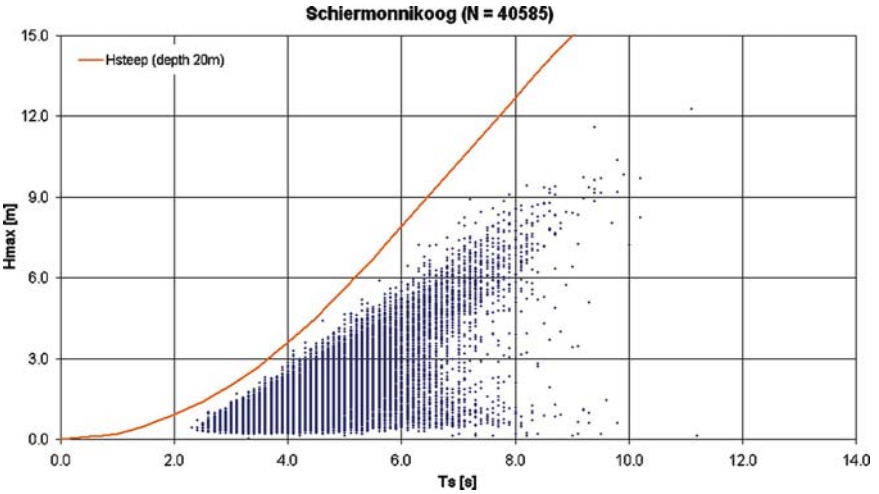

Fig. 8 Scatter plot of maximum wave height $H_{\max}$ vs. mean period T at the shallow water station Schiermonnikoog Island (SMN)

$H_{\max}$ vs. T for SMN, shows that for this station maximum wave heights are not as close to yellow line as for deep water waves. We checked in plots of H_s against steepness, see Figs. 9 and 10, that although the general picture that high waves are more often steep than low waves remains valid, for waves with $H_S > 2m$, the limiting steepness at the shallow water location decreases with significant wave height, while it stays roughly constant at the deep-water location.

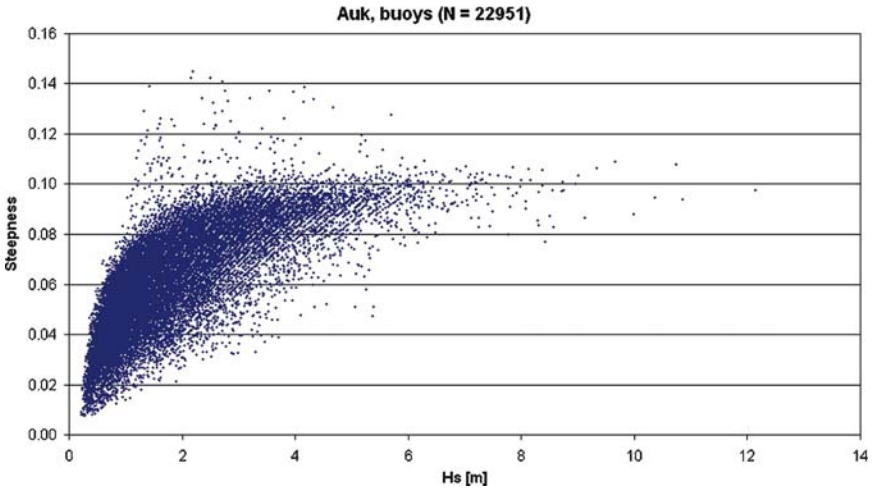

Fig. 9 Scatterplot of wave steepness vs. H_s at the deep water station AUK

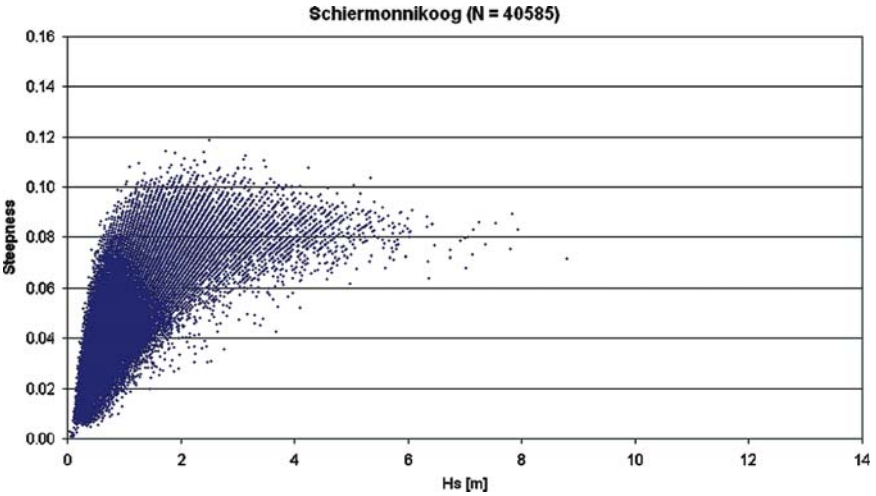

Fig. 10 Scatterplot of wave steepness vs. H_s at the shallow water station Schiermonnikoog Island

Finally, we checked whether there is a relation between the BFI index of WAM of the ECMWF and the probability of high r values. To this end, average values of r have been collocated with the model BFI. The results are shown in Fig. 11 for AUK and Fig. 12 for SMN. During the period for which the model BFI was available, there were many more observations at the shallow water station than at the deep water station. The data for the deep water station AUK do not exclude a relation between high r observations and high WAM model BFI indices. For the shallow water location, there is hardly a correlation between high r observations and high WAM model BFI indices.

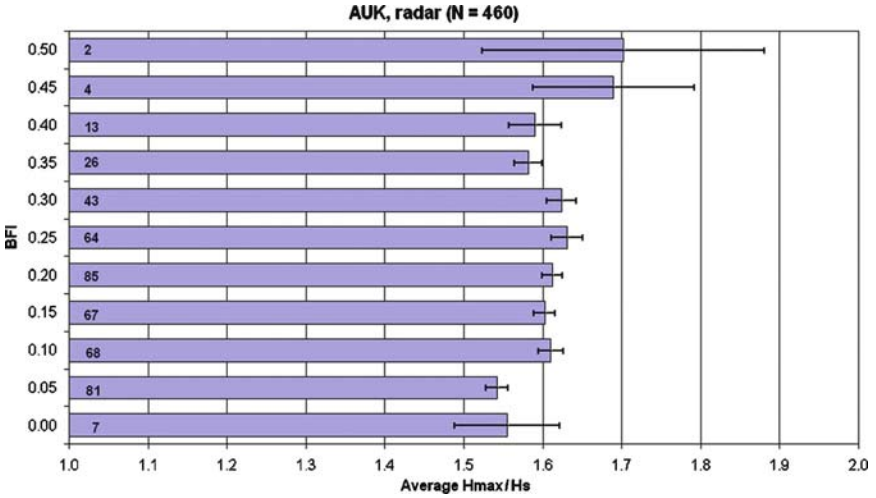

Fig. 11 Model BFI vs. measured $H_{\max}/H_{\mathrm{s}}$ in deep water at AUK. Observations have been binned according to model BFI, the number of observations is indicated by the *black number* in each bar. The length of the bar gives the average value of r for that bin, and the *black line* indicates the standard deviation

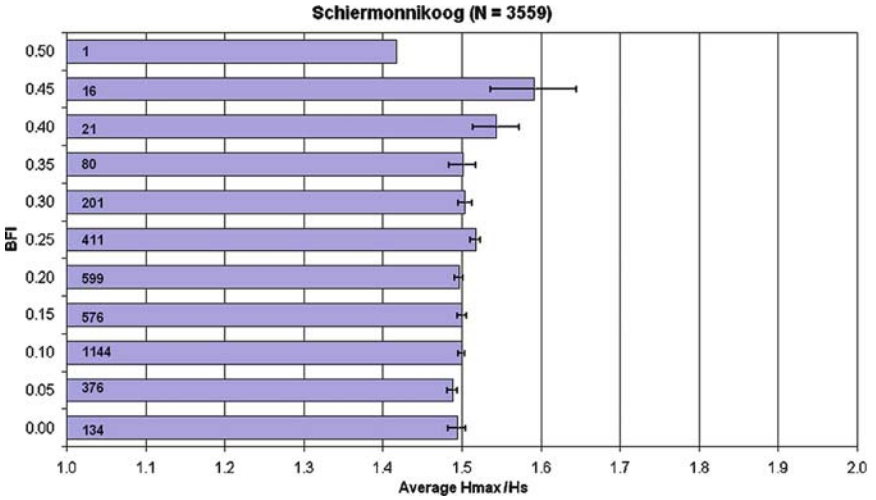

Fig. 12 Model BFI vs. measured $H_{\max}/H_{\mathrm{s}}$ in shallow water at SMN. Observations have been binned according to model BFI, the number of observations is indicated by the *black number* in each bar. The length of the bar gives the average value of r for that bin, and the *black line* indicates the standard deviation

4 Discussion

From the measurements it appears that there are systematic differences between the various instruments. Because the radar has a higher sampling frequency, and makes a more direct measurement than the accelerations measured by the buoys,

we consider the radar measurements to be more reliable. Additional confidence in the radar results comes from the fact that they are close to those predicted by standard Rayleigh theory. Apparently, the frequency of around 1 Hz of accelerations by the buoys is not sufficient for capturing maximum wave heights well, making that the buoy results are systematically below the radar results. That differences between various periods are so large indicates that not only the instrument but also the processing algorithm has a large impact on the distribution of the measurements. This makes a comparison of the deep water station with the shallow water station far from straightforward. What remains is a number of series of several months of data. The most obvious result is that there is no change in behaviour for timescales ranging from hours to months. There is neither evidence for an enhanced tail because of non-linear enhancement effects nor for a damped tail because of limiting steepness effects. Considering subclasses, steepness may have an effect: there is some indication that given the significant wave height and the period, extreme waves are more likely in case long periods. In shallow water, wave energy can converge and give rise to high waves. But our results do not indicate a higher probability of extreme waves in shallow water than in deep water. If any, we observe the opposite effect: extreme waves are less likely in shallow water. We do find a clear difference in plots of steepness vs. wave height between deep water and shallow water: in deep water, there is a limiting steepness that does not depend on wave height, in shallow water, this limit decreases with wave height, probably because of bottom friction effects.

For deep water, Janssen theory expects an increase of the mean value of r of the order of 0.1 if the BFI is varied from 0 to 0.5 (Peter Janssen, personal communication). Such an increase is compatible with our results for the deep water station AUK in Fig. 11. Janssen theory does not expect a correlation between BFI and r in shallow water, because in shallow water conditions for four-wave interactions differ from deep water. This is confirmed by our shallow water results in Fig. 12.

5 Conclusion

The analysis has been hampered by the fact that the instruments report approximations for maximum wave height, and that those approximations differ between different instruments and observing periods. Our main result is that the instrumental data are consistent with a Rayleigh like extreme wave distributions up to return periods of many months. There is slight indication that for long waves steepness can be a limiting factor for maximum wave height. In shallow water, there is some evidence that extreme waves are less common than in deep water. The distributions of wave height vs. steepness in shallow water and deep water are different, which may be related to the overall damping effect of bottom friction that causes a reduction of significant wave height in shallow water. As expected, in shallow water, there is no relation between the WAM model BFI and the probability of extreme waves. For deep water, such a relation cannot be ruled out.

Acknowledgement We thank Peter Janssen for valuable and stimulating discussions.

APPENDIX: Rayleigh Distribution

According to linear wave theory, see e.g. Holthuijsen (2007), the probability $p(r)$ that an individual wave has a height $H = rH_s$ is given by

$$p(r) = \exp(-r^2). \tag{4}$$

From this expression it follows the probability $P(\bar{r})$ that in a series of N waves all waves have $r < \bar{r}$ is

$$P(\bar{r}) = (1 - p(\bar{r}))^N. \tag{5}$$

The exact number of waves in a 20-minute record is not determined. In the North Sea, periods are shorter than in the open ocean and vary from 5 to 10 s, in very severe storms the dominant period can be higher. So a typical number of waves in a 20-min record is about 150. In Fig. 3, return maximum wave height as a function of the number of records is plotted as a solid line. The maximum wave height ratio r reaches a value of 2 for about 20 records (about 6 h) and increases slowly with the number of records. Even for 10^5 records, that is about 4 years, r is below 3.

For comparison, a distribution that follows from the theory of Mori and Janssen (2006) is shown as well (dotted line). The case shown corresponds to a BFI of 0.33. In Janssen theory, the BFI is directly related to κ, the kurtosis of the sea surface, by $\kappa = (\pi\sqrt{3})BFI^2$, so the case of Fig. 3 corresponds to $\kappa = 0.2$.

References

Berg R, Rhome J (2005) Expecting the unexpected wave: How the national weather service marine forecasts compare to observed seas. Mar. Weath. Log 49:4–7

Bojanowski A (2007) Monsterwellen bedrohen Schiffe im Nordatlantik http:\\www.spiegel.de\wissenschaft\natur\0,1518,470 359,00.html

Datawell (2006) Versnellingswaarden: Detectie en reparatie van extreme versnellingswaarden. Datawell internal report. Datawell BV, Haarlem, The Netherlands

Holliday N, Yelland M, Pascal R, Swail V, Taylor P, Griffitchs C, Kent E (2006) Were extreme waves in the Rockall trough the largest ever recorded? Geophys Res Lett 33:L05613 doi:10.1029/2005GL025238

Holthuijsen L (2007) Waves in oceanic and coastal waters. Cambridge University Press, Cambridge, UK, pp 404

Janssen P (2003) Nonlinear four-wave interactions and freak waves. J Phys Ocean 33:863–884

Mori N, Janssen P (2006) On kurtosis and occurence probability of freak waves. J Phys Ocean 36:1471–1483

Extremes and Decadal Variations of the Northern Baltic Sea Wave Conditions

Tarmo Soomere

Abstract Average wave conditions, their seasonal cycle and decadal variations, and extreme wave storms in the northern Baltic Sea are studied on the basis of long-term time series from Almagrundet (1978–2003) and Vilsandi (1954–2005), and wave statistics from the middle of the northern Baltic Proper. The typical wave periods are 3–4 s in coastal areas and 4–6 s on the open sea. The monthly mean wave height varies from about 0.4 (0.5) m in April–July to 0.8 (1.3–1.4) m in January at Vilsandi (Almagrundet). The annual mean wave height varied insignificantly in the 1960s–1970s, considerably increased in the 1980s, was at highest in the mid-1990s, and rapidly decreases in 1998–2005. Significant wave heights $H_S \geq 4$ m occur with a probability of about 1%. Extreme wave conditions with $H_S \geq 7$ m have been registered five times since 1978. The records overlook 2–3 such cases. The overall recorded maximum H_S is 7.8 m. The estimated maximum of H_S was 9.5 m in cyclone Gudrun in January 2005.

1 Introduction

The complexity of physics and dynamics of the Baltic Sea extend far beyond the typical features of many other water bodies of comparable size (e.g. Alenius et al. 1998). The combination of a relatively small size and vulnerability of its ecosystem makes this region extremely susceptible with respect to climate changes and shifts. Numerous changes of the forcing conditions and of the reaction of the water masses of the Baltic Sea have been reported during the latter decade. The apparently increasing storminess in the Baltic Sea has already caused extensive erosion of depositional coasts (Orviku et al. 2003), although the changes in the wave climate have been found marginal, at least, until the mid-1990s (WASA Group 1995; Mietus and Storch 1997).

T. Soomere
Institute of Cybernetics at Tallinn University of Technology, Tallinn, Estonia
soomere@cs.ioc.ee

E. Pelinovsky, C. Kharif (eds.) *Extreme Ocean Waves*, 139–157.

Very rough seas measured twice in December 1999 reinforced the discussion whether the wave conditions in the Baltic Sea have become rougher compared with the situation a few decades ago. The exceptional storm Erwin/Gudrun of January 2005 highlighted inadequate awareness of extreme wave properties (Soomere et al. 2008) and of the height and spatial extent of extreme water levels (Suursaar et al. 2006).

Recognition of the wave climate changes, in particular, changes of extremes, presumes a thorough knowledge of the typical and extreme wave conditions The global wave data set KNMI/ERA-40 Wave Atlas (09.1957–08.2002, Sterl and Caires 2005) allows the production of reliable wave climatology for open ocean conditions, based on 6-hourly means of wave properties over an average of $1.5^\circ \times 1.5^\circ$ areas. This resolution is too sparse for the Baltic Sea conditions.

The wave properties in the Baltic Sea can be modelled with the use of local models, because the waves from the rest of the World Ocean practically do not affect this water body. The pattern of dominant winds (Mietus 1998; Soomere and Keevallik 2001) and the geometry of the Baltic Sea suggest that the highest and longest waves occur either at the entrance of the Gulf of Finland, off the coasts of Saaremaa, Hiiumaa, and Latvia, or along the Polish coasts. Wave data from the northern parts of the Baltic Sea Proper thus adequately represent both the average and the roughest wave situations in the region.

Wave statistics for the Baltic Proper has been recently estimated with the use of the second-generation spectral wave model HYPAS and wind data from 1999 to 2000 (Jönsson et al. 2002, 2005; Danielsson et al. 2007). The overall picture of wave activity follows the above-described wind pattern. Several numerical wave studies are performed for the southern part of the Baltic Sea (e.g. Gayer et al. 1995; Paplińska 1999; Blomgren et al. 2001). Valuable wave data and statistics are presented in sources published in the former USSR (Rzheplinsky 1965; Rzheplinsky and Brekhovskikh 1967; Davidan et al. 1978, 1985; Lopatukhin et al. 2006a, b).

Yet the information about long-term changes of wave properties is fragmentary in the Baltic Sea. This water body is characterised by extremely complex geometry, highly varying wind fields, extremely rough wave conditions at times, extensive archipelago areas with specific wave propagation properties, and the ice cover during a large part of each year. The quality of wind information only allows reasonable reproduction of wave patterns since 1990s. Although third generation wave models (e.g. Komen et al. 1994) have been implemented for the northern Baltic Sea at the turn of the millennium (e.g. Tuomi et al. 1999; Soomere 2001), wave statistics based on such models is available only for limited areas (Soomere 2003, 2005).

An adequate long-term simulation of the Baltic Sea wave fields is still missing. Also, no comprehensive description of the wave climate or statistical estimates of extreme wave conditions exists in the whole Baltic Proper.

The central goal of this study is to present a systematic description of the basic properties of average and extreme wave conditions and to depict their durable changes in the northern Baltic Proper on the basis of available long-term wave measurements and numerical simulations of a specific event. The wave patterns in the

Gulf of Finland (an elongated basin with a length of about 400 km and a maximum width of about 135 km) are frequently connected with those in the Proper, and are addressed to some extent as well.

The analysis is mostly based on instrumental measurements in 1978–2003 at Almagrundet (located near the western coast of the northern Baltic Proper) and on visual observations from the island of Vilsandi in 1954–2003 (the eastern coast of the Baltic Proper). To a limited extent, data from waveriders in the middle of the northern Baltic Proper and from Bogskär are used. The results predominantly represent Type A statistics in terms of the classification of Kahma et al. (2003): almost no corrections have been made to compensate for missing values, for the uneven distribution of data (except for the use of daily mean wave heights for certain parameters), or for ice cover. Modelled data are used in the estimates of extreme waves in windstorm Gudrun in January 2005.

2 Wave Climate in the Northern Baltic Proper

2.1 Data from Almagrundet, Bogskär and from the Open Sea

Contemporary wave measurements were launched in the northern Baltic Sea in the framework of wave power studies at the end of the 1970s near the lighthouse of Almagrundet and south of Öland. A waverider buoy was simultaneously deployed near Hoburg, south of Gotland. The measurements were mostly performed during a few years (Mårtensson and Bergdahl 1987), but went on longer at Almagrundet.

The data from Almagrundet (1978–2003, 59°09′N, 19°08′E, Fig. 1, Broman et al. 2006) form the longest instrumentally measured wave time series in this region. The above-discussed anisotropy of the Baltic Sea wave fields has caused some discussion about whether the data correctly represent the open-sea wave conditions (Kahma et al. 2003). Almagrundet is a 14 m deep shoaling area about 10 nautical miles south-east of Sandhamn in the Stockholm archipelago. It is sheltered from a part of dominating winds. The fetch length for winds from the south-west, west, and north-west is quite limited. Yet the data constitute one of the most valuable data sets for the Baltic Sea.

An upward-looking echo-sounder from Simrad was placed at a depth of about 30 m in 1978 (Mårtensson and Bergdahl 1987) and was active until mid-September 1995 at Almagrundet. An analogous device from WHM was installed in a neighbouring location at a depth of 29 m in 1992 and produced usable data in 1993–2003 (Broman et al. 2006). The position of the water surface was sampled during 640 s each hour. Wave components with periods of less than 1.5 s as well as the data probably reflecting wave interference and breaking waves and possibly very steep waves were discarded (Mårtensson and Bergdahl 1987). Single waves were identified on the basis of the classical zero-downcrossing method (IAHR 1989). An estimate of the significant wave height $H_{1/3}$ (the average height of 1/3 of the highest waves) was

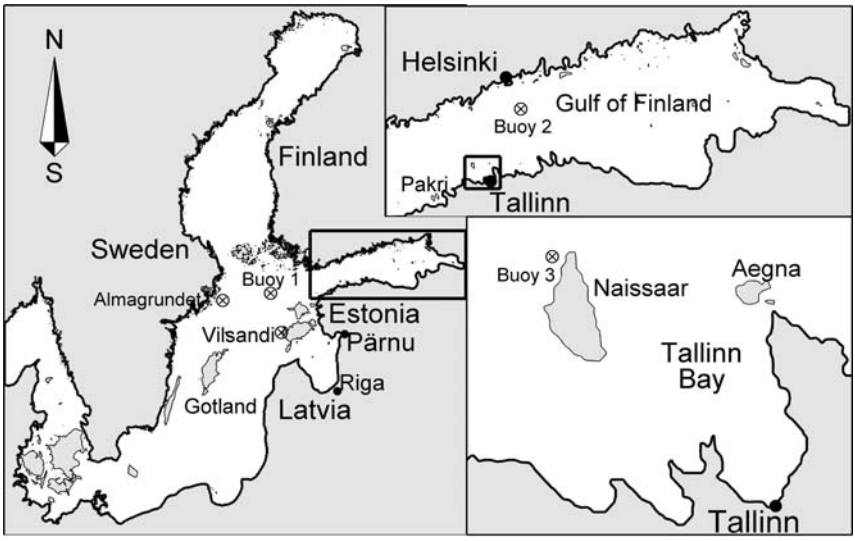

Fig. 1 Wave measurement sites, marked by *crossed circle*, at Almagrundet, at the Island of Vilsandi, in the northern Baltic Proper (buoy 1), near Helsinki (buoy 2) and at the Island of Naissaar (buoy 3)

found from the 10th highest wave H_{10} in a record of N waves under the assumption that wave heights are Rayleigh distributed:

$$H_{1/3} = \frac{H_{10}}{\sqrt{\frac{1}{2}\ln\frac{N}{10}}}.$$

The set of 95,458 measurements in 1978–1995 reliably describes the wave properties (Broman et al. 2006). Later 46,671 recordings in 1993–2003 have certain quality problems. The overall behaviour of the wave height apparently follows the sea state; yet the data contain a number of modest but still evidently unrealistic peaks. As the values of wave period are also unreliable, Broman et al. (2006) recommend considering the data as merely indicative.

A non-directional waverider was operated in 1983–1986 near Bogskär at 59°28.0′ N, 20°21.0′ E (Kahma et al. 2003). The wave properties were measured hourly. The total measuring time is 14,630 h, or about 2 years of uninterrupted measurements. The measuring times, however, are concentrated in the autumn season and thus well represent the wave climate during relatively windy months.

A directional waverider was deployed in the northern Baltic Proper at a depth of about 100 m (buoy 1 in Fig. 1, 59°15′ N, 21°00′ E) in September 1996 and operated since then during the ice-free seasons (Kahma et al. 2003). This device as well as contemporary spectral wave models estimate the significant wave height as $H_S = 4\sqrt{m_0} \approx H_{1/3}$, where m_0 is the zero-order moment of the wave spectrum (the total variance of the water surface displacement, e.g. Komen et al. 1994). These

data are the most representative of the Baltic Sea wave fields; however, to date, this time series is not long enough for determining the climatological values of wave properties (Guide 2001).

Directional wave measurements in the Gulf of Finland in 1990–1991, 1994, and from November 2001 (59°57.9′N, 25°14.1′E, water depth about 60 m, buoy 2 in Fig. 1) during the ice-free seasons have considerably increased the awareness of wave conditions in semi-enclosed sub-basins of the Baltic Sea (Kahma and Pettersson 1993; Pettersson 2001; Kahma et al. 2003). Hardly any instrumental wave data are available from the coastal areas of Estonia and Latvia, except for sporadic measurements made with pressure-based sensors (Soomere 2005).

2.2 Visual Observations from the Island of Vilsandi

A reasonable source of the open sea wave information form visual observations from the ships (Hogben et al. 1986). Wave climate changes estimated from data observed from merchant ships are consistent with those shown by the instrumental records (Gulev and Hasse 1998, 1999). Visual observations from the coast are less frequently used for wave climate studies. Although such observations frequently represent only wave properties in the immediate vicinity of the observation point (Orlenko et al. 1984), have a poor temporal resolution, may give a distorted impression of extreme wave conditions, have many gaps caused by inappropriate weather conditions or by the presence of ice, etc., the data are one of the few sources for detecting the long-term changes of wave climate.

The coastal site adequately reflecting the open sea wave conditions (except for easterly winds) is located at the Island of Vilsandi (58°22′59″N, 21°48′55″E, Fig. 1). Wave observations were performed there starting from 1954 up to three times a day. The interval between subsequent observations is often much longer than the typical saturation time of rough seas in the northern Baltic Proper (about 8 h, Soomere 2001) or the duration of wave storms (that seldom exceeds 10 h, Broman et al. 2006; Lopatukhin et al. 2006b). The data, however, well represent the general features of the Baltic Sea wave fields: relatively low overall wave activity, short wave periods, and substantial seasonal variation of wave conditions (Soomere and Zaitseva 2007).

The observer noted the five highest waves during a 5-min time interval and filed the highest single wave H_{max} and the mean height H of these waves at Vilsandi. Given the typical wave periods in the coastal zone 3–4 s (Broman et al. 2006), the height H is approximately equal to the average height of 2.5–3% of the highest waves. As the observers' estimates well represent the significant wave height (Gulev and Hasse 1998, 1999), we shall interpret H as an estimate of the significant wave height and shall use it whenever given in the data set. Only when this measure is missing, H_{max} is used instead. As the difference between H and H_{max} is about 6% in average (Soomere and Zaitseva 2007), doing so apparently has a fairly minor influence on climatological values of wave heights.

The wave period was found as an arithmetic mean from three consecutive observations of passing time of 10 waves each time. Since the visually observed wave periods are only a few tenths of seconds shorter than the peak periods (Gulev and Hasse 1999), the results are interpreted as estimates of the peak period. All obviously erroneous, ambiguous, or inconsistent entries in the observation diaries were omitted in the analysis of Soomere and Zaitseva (2007). At least one sensible observation of the wave height has been made on 15,038 days (coverage 79%). Most of the gaps occur from January to March apparently owing to the presence of sea ice.

2.3 Wave Climate

2.3.1 Wave Statistics in the Northern Baltic Sea

The wave climate of the northern Baltic Sea is relatively mild (Table 1). The overall average of the significant wave height at the open sea may slightly exceed the one estimated from Almagrundet data, but apparently it is close to 1 m.

The overall average wave height calculated from the entire Vilsandi data set is much smaller. The excess proportion of calms at Vilsandi ($>$30%, Soomere and Zaitseva 2007) is evidently due to the absence of observable waves in many cases of easterly winds. Removing a fraction of calms from this set is therefore roughly equivalent to ignoring data inadequately reflecting the open sea wave fields in such wind conditions. If the number of calms is reduced to 6% from the total number of recordings (the level typical for the northern Baltic Proper, Fig. 2), the average wave height at Vilsandi is 0.74 m.

The wave heights at Almagrundet in 1993–2003 (WHM data) may be slightly overestimated because of certain small, but evidently unrealistic peaks. The analysis of the Vilsandi data relies on the daily average wave height

The probability distributions of the occurrence of different wave heights at Almagrundet, Bogskär, and on the open sea (Fig. 2) resemble the Rayleigh distribution. This distribution at Vilsandi resembles analogous distributions for wave heights in semi-sheltered bays of the Baltic Sea (Soomere 2005).

Table 1 Basic properties of wave fields at Almagrundet and Vilsandi

Data set	Overall average wave height	Median wave height	Most frequent	
			wave height	wave period
Almagrundet 1978–95 (1993–2003)	0.876 (1.04)	0.7 (0.73)	0.25–0.5	3 (–)
Vilsandi 1954–2005 (6% calms kept)	0.575 (0.74)	0.3 (0.5)	$<$0.25 (0.25–0.5)	3 (3)
Bogskär 1982–1986	–	–	0.5–0.75	5
Northern Baltic Proper	–	–	0.25–0.5	5

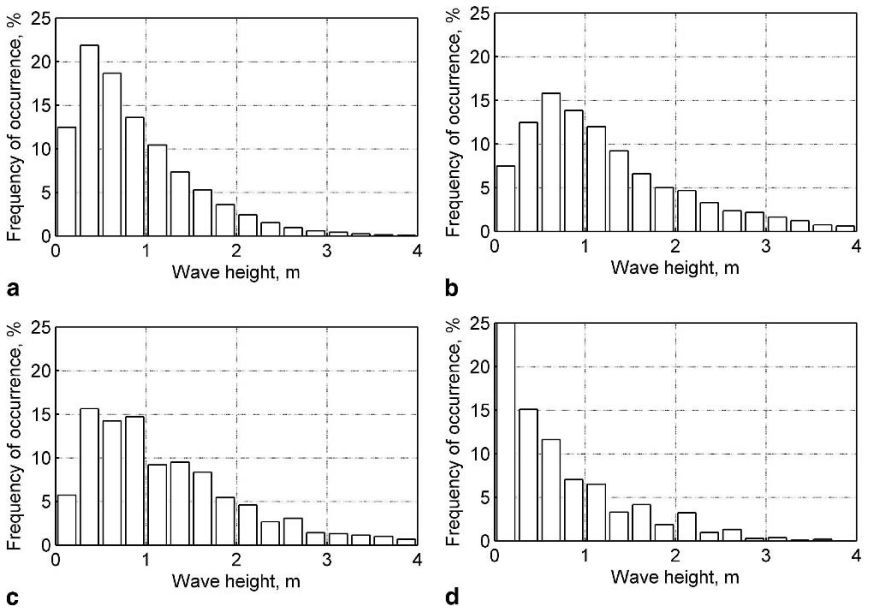

Fig. 2 Frequency of occurrence of wave heights at (**a**) Almagrundet 1978–1995, (**b**) Bogskär 1982–1986, (**c**) at buoy 1 in the northern Baltic Proper, (**d**) at Vilsandi

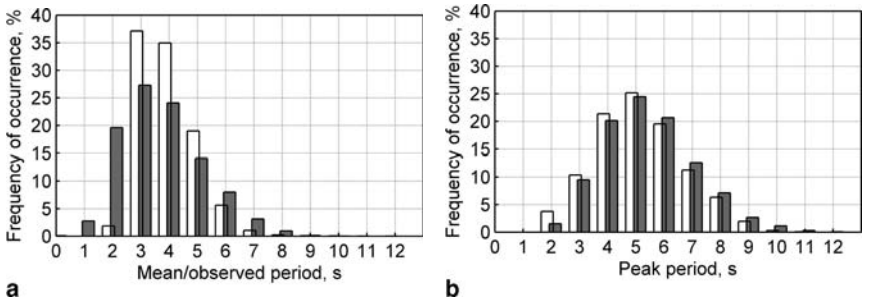

Fig. 3 Frequency of occurrence of wave periods: (**a**) Almagrundet 1978–1995 (*white bars*) and Vilsandi 1954–2005 (*filled bars*), (**b**) Bogskär 1982–1986 (*white bars*) and buoy 1 in the northern Baltic Proper 1996–2000 (*filled bars*)

Most frequently waves with periods of 4–6 s dominate in the middle of the Baltic Proper whereas in the coastal regions waves with periods of 3–4 s predominate (Fig. 3). Wave periods about 5–6 s also occur with an appreciable frequency in the coastal areas. Periods up to 7 s are still common on the open sea. This difference in periods apparently comes from a relatively large number of short-fetched wave conditions at sheltered measurement sites.

The joint distributions of wave heights and periods (Fig. 4) suggest that the proportion of relatively steep seas is quite large in the Baltic Sea. Periods of 2–3 s usually correspond to wave heights well below 1 m whereas waves with periods of 4–5 s

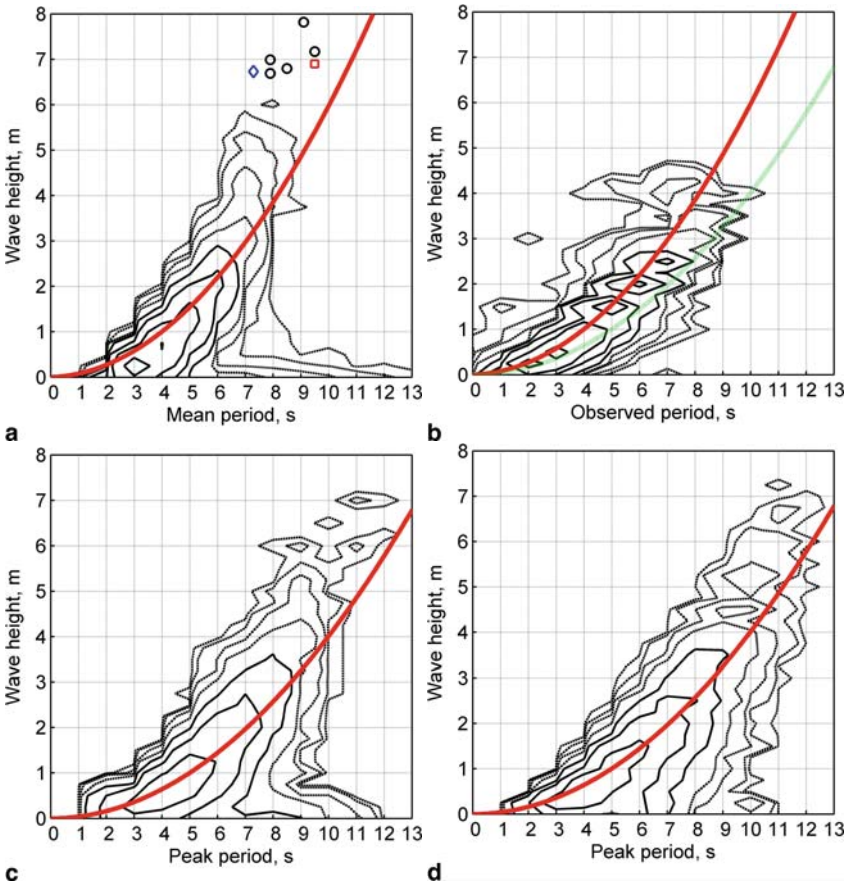

Fig. 4 Scatter diagram of wave heights and periods: (**a**) Almagrundet 1978–1995, (**b**) Vilsandi in 1954–1994, (**c**) Bogskär 1982–1986, (**d**) buoy 1 in the northern Baltic Proper. The wave height step is 0.25 m and the period step is 1 s. The range of periods is shown on the horizontal axis: 2 s stands for $1.5 \le T_p < 2.5$ s, 3 s stands for $2.5 \le T_p < 3.5$ s, etc. Isolines for the probability of occurrence of 0.0033%, 0.01%, 0.033%, 0.1% (*dashed lines*), 0.33%, 1%, 3.3%, and 10% (*solid lines*) are plotted. Wave conditions with $H_{1/3} > 6.5$ m at Almagrundet are shown as follows: *circles* – the January 1984 storm, *diamond* – a storm in January 1988, *square* – a storm in August 1989. The *bold line* indicates saturated wave conditions with a Pierson-Moskovitz spectrum. The *bold grey line* in panel (**b**) indicates saturated wave situation in terms of the peak period

have a typical height of about 1 m. Periods 6–7 s usually correspond to wave heights of about 1.5–2 m. In coastal areas, dominating periods are 7–8 s only when wave heights are about 3 m or higher. Even longer waves are infrequent. Mean periods over 8 s (peak periods ≥ 10 s) dominate either in very rough seas (wave heights over 4 m) or in remote low swell conditions when the wave heights are well below 1 m. For example, at Almagrundet the mean period never exceeded 9.5 s in very rough seas and was about 10 s in one case of rough seas with $H_{1/3} \sim 4$ m. Even in the final

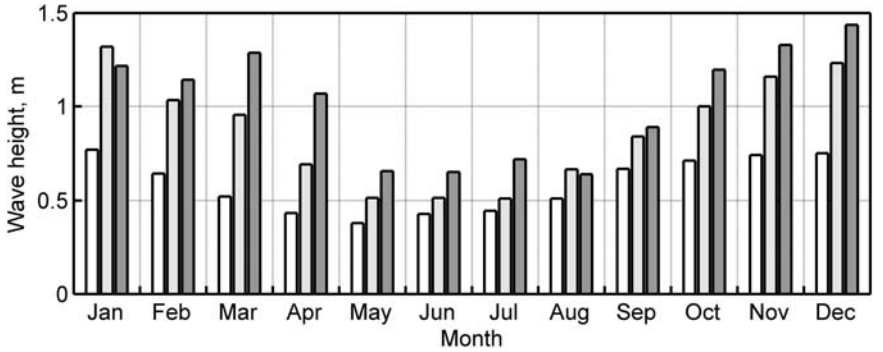

Fig. 5 Annual variation of the monthly mean wave height at Vilsandi 1954–2005 (*white bars*, based on the daily mean wave height) and at Almagrundet 1978–1995 (*light grey bars*) and 1993–2002 (*dark grey bars*)

stage of the January 1984 storm when $H_{1/3} \sim 7$ m, the mean period was below 10 s. At the location of buoy 1, the peak period of about 12 s has been registered about twice a year and at Bogskär roughly once in two years.

The annual variation in the monthly mean wave height matches the similar variation of the wind speed (Mietus 1998). It is impressive at Almagrundet: from about 0.5 m during summer to 1.3–1.4 m in winter (Fig. 5). It is somewhat less pronounced at Vilsandi: from about 0.4 m during summer to about 0.8 m in winter.

The highest monthly mean wave height occurs from November to January at Almagrundet. Another wave height maximum may occur at Almagrundet in March (Broman et al. 2006). It is apparently connected with easterly winds during late winter and early spring (Mietus 1998), and the influence of which is not detectable at the sheltered observation site of Vilsandi. The highest wave activity at Vilsandi generally occurs in January, but during October to December a comparable wave activity is observed. The calmest period is the late spring and summer months from May to July–August whereas a well-defined minimum in May is visible in Vilsandi data.

2.3.2 Extreme Conditions

Estimates of extreme wave conditions with the use of the WAM model forced by homogeneous wind patterns suggest that the significant wave height generally does not exceed 8–8.5 m in the northern Baltic Proper (Soomere 2001). This estimate is confirmed by Lopatukhin et al. (2006a).

Seas in which $H_S > 7$ m are extremely rough in the Baltic Sea basin. This threshold was not reached at Bogskär in 1982–1986. Waves of this height cannot be observed from Vilsandi, because the depth of the observation area is about 4 m. The most ferocious storm (the only one during which $H_{1/3} \geq 7$ m was registered at the site) occurred at Almagrundet on 13–14 January 1984 when $H_{1/3}$ reached

7.82 m and the highest single wave was 12.75 m high[1] (Broman et al. 2006). This is, formally, the largest significant wave height ever recorded in the northern Baltic Sea[2]. The wave periods remained fairly modest ($T_m = 9.1$ s, $T_p = 10.7$ s).

The wave height reached $H_{1/3} = 6.9$ m in a relatively short but violent storm in August 1989 and $H_{1/3} = 6.73$ m in another severe storm on 30 January 1988 at Almagrundet. The significant wave height on the open sea apparently exceeded 7 m during these events. No reliable data are available for a severe storm in January 1993.

The significant wave height exceeding 7 m has been recorded only four times by buoy 1: twice in December 1999 (whereas $H_{1/3}$ was about 6 m at Almagrundet, Kahma et al. 2003), on 22 December 2004 [when the roughest wave conditions $H_S = 7.7$ m, and the highest single wave (14 m) were recorded for this site, see http://www.fimr.fi] and on 9 January 2005 during windstorm Gudrun (Soomere et al. 2008). The peak periods during these events slightly exceeded 12 s.

Rough seas with the (observed or measured) wave heights over 4 m occurred with a probability of 0.2% (about once a year) at Vilsandi, of 0.42% in 1978–1995 at Almagrundet, of 1% at Bogskär, and of 1.4% at buoy 1. Such seas usually occur several times a year, each time during a few hours.

2.3.3 Gulf of Finland

The average and, in particular, the maximum wave heights in the Gulf of Finland are much smaller than in the Baltic Proper. The 'memory' of wave fields is relatively short, and the changes in the wind field are fast reflected in the wave pattern. As a consequence, the wave fields in smaller sub-basins (such as Tallinn Bay or Narva Bay) mimic the changes of the open-sea winds (Soomere 2005; Laanearu et al. 2007).

On the basis of data from 1990–1991 and 1994, the maximum H_S occurring once in 100 years in the Gulf of Finland was estimated to be 3.8 m and the corresponding single wave height 7.1 m. Wave conditions with $H_S > 4$ m occur extremely seldom (Alenius et al. 1998; Pettersson 2001). The peak periods in rough seas (with $H_S \sim 4$ m) are 8–9 s (Kahma and Pettersson 1993).

Recent data show that considerably rougher seas may occur in this area. In November 2001, seas with $H_S = 5.2$ m and $T_P \approx 11$ s occurred (Pettersson and Boman 2002). Wave systems with $T_P \geq 10$ s, however, usually correspond to penetration of long-period swell of moderate height into the gulf (cf. Broman et al.

[1] The significant wave height, calculated directly from the wave spectrum, was $H_S = 7.28$ m.

[2] The Almagrundet data set contains several contradicting extreme wave data. A severe storm that affected nearly the whole Baltic Proper caused $H_{1/3} = 7.83$ m, formally the all-highest of the data set, in March 1997. Since H_S estimated from the wave spectrum was 5.7 m and the highest single wave reached 10.24 m, this value of $H_{1/3}$ evidently overestimates the wave conditions. An extremely high single wave (12.79 m) was recorded on 25 December 1996 when $H_{1/3} = 6.37$ m. Still the significant wave height, estimated from the wave spectrum, was only 3.8 m (Broman et al. 2006).

2006). Only a few observations reveal such long periods: $T_P \approx 11$ s occurred only three times in 1990–1994 and during a short time in another very strong storm in November 2001 (Pettersson 2001).

The average wave directions are often concentrated along the gulf axis (Pettersson 2001), although the wind directions are more evenly spread (Soomere and Keevallik 2003). This phenomenon is attached to the slanting fetch conditions in which the wind direction is oblique to the coastline (The SWAMP Group 1985, Chap. 8). Shorter waves are usually aligned with the wind, while somewhat longer and higher waves (that often dominate the wave field) propagate along the gulf axis (Holthuijsen 1983; Kahma and Pettersson 1994; Pettersson 2004).

3 Interannual and Long-Term Variations

The most intriguing question is whether any long-term changes in the wave activity can be identified in the Baltic Proper. The total duration of the measurements is about 25 years at Almagrundet and 52 years at Vilsandi. The series thus are long enough to extract climatological trends (Guide 2001).

The overall course of wave activity (Fig. 6) reveals a quasiperiodic variation. The interval between subsequent periods of high or low wave activity is about 25 years. The sea was comparatively calm at the end of the 1950s, became slightly rougher in 1965–1975, and calmer again at the end of the 1970s. A rapid increase in the annual mean wave height occurred from the mid-1980s until the mid-1990s. The increase was well over 1% per annum depending on the particular choice of the time interval and the site (Almagrundet 1979–1992: 1.3%; 1979–1995: 1.8%; Vilsandi 1979–1995 as high as 2.8% per annum). This trend follows the analogous trends for the southern Baltic Sea. Its magnitude is comparable with the one reported for the North Atlantic (Bacon and Carter 1991; Kushnir et al. 1997), but it is much faster

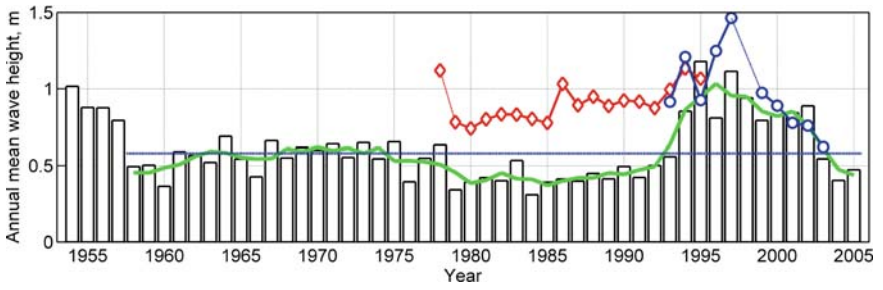

Fig. 6 The annual mean wave height at Vilsandi 1954–2005 (*bars, grey line*: 3-year moving average since 1958) and at Almagrundet 1978–1995 (*diamonds*) and 1993–2003 (*circles*). The *horizontal line* indicates the overall mean wave height at Vilsandi in 1958–2005. Notice that Almagrundet data from 1978 reflect only windy months November and December (Broman et al. 2006) and that the wave heights in 1954–1957 probably are overestimated at Vilsandi (Soomere and Zaitseva 2007). Data from Almagrundet for 1998 are missing

than in the North Sea (where it was $<1\%$ per annum, Gulev and Hasse 1999; Vikebo et al. 2003). The overall increase of wave heights is consistent with the increase of wind speed over the northern Baltic Sea (Broman et al. 2006) that is frequently associated with the increasing storminess since the middle of the twentieth century (Alexandersson et al. 1998).

This trend only existed during about 1.5 decades and was replaced by a drastic decrease of the mean wave height since 1997. The relevant data from Almagrundet were even estimated as doubtful by Broman et al. (2006), because the annual mean wind speed continued to increase and intensification of beach processes was reported along the downwind side of the coasts (Orviku et al. 2003). Although the mean wind speed does not necessarily exactly match the average wave height, it is intuitively clear that a larger wind speed generally causes greater wave activity. The match of the long-term variation of wave properties at Almagrundet and Vilsandi suggests that both data sets adequately reflect the changing wave situation.

The drastic changes of the mean wave height on the background of the gradual increase of the mean wind speed (Broman et al. 2006) suggest that the local wave generation conditions have substantially changed within relatively short time intervals. In particular, the overall wave activity was exceptionally high at Almagrundet in 1996–1997, but the wind data from Utö (a small island in the northern Baltic Proper that well represents the open-sea wind conditions, Soomere 2003) suggest that these years were relatively calm.

4 Extremes During Windstorm Gudrun

4.1 The Storm and Waves

The above estimates for extreme wave conditions turned out to be inadequate when windstorm Gudrun, an extratropical cyclone, also known as Erwin in Ireland, the United Kingdom, and Central Europe, attacked northern Europe on 7–9 January 2005 (Carpenter 2005). It reached the power of a hurricane, according to the Saffir-Simpson hurricane scale (Simpson and Riehl 1981), in the North Sea region. In the Baltic Sea, it remained slightly below the hurricane level; yet it was one of the strongest storms in Denmark, Sweden, Latvia, and Estonia for at least 40 years. It caused widespread property damage, exceptionally high coastal floods along the Western Estonian coast and in the Gulf of Finland, and loss of 18 lives (Carpenter 2005; Suursaar et al. 2006; Bengtsson and Nilsson 2007). Substantial beach destruction occurred on exposed coasts (Orviku 2006).

The coastal wind data suffered from failures of meteorological equipment during Gudrun (Suursaar et al. 2006). Forecast winds from the German Weather Forecast Service (DWD, Deutscher Wetterdienst), the Danish Meteorological Institute (DMI), and the Finnish Institute of Marine Research (FIMR) suggest that the maximum wind speed on the open sea (Fig. 7) was 28–29 m s^{-1}. Forecasts released on 6–7 January predicted the windstorm maximum to hit the entrance of the Gulf of

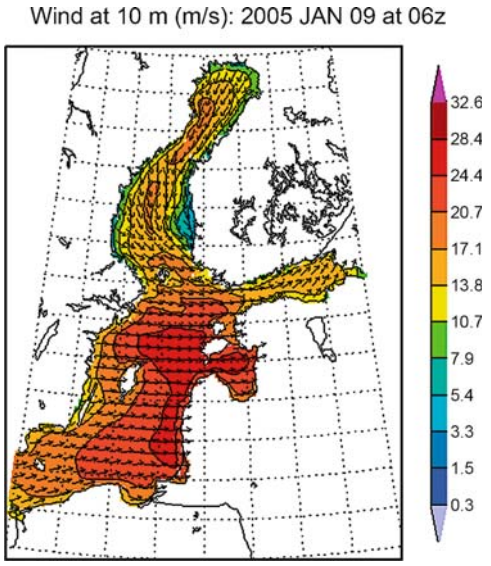

Fig. 7 Modelled wind speed (m/s) and direction (arrows) 10 m above water surface at 06:00 GMT on 9 January in the DMI 54-h forecast valid at 00:00 GMT on 9 January. Courtesy of the Danish Meteorological Institute

Finland. The significant wave height was forecast to exceed 10 m at buoy 1, to reach 11–12 m at the latitudes of the Gulf of Finland, and to be >6 m in the central part of this gulf (Soomere et al. 2008). Such wave conditions were considerably rougher than during any other storm in the northern Baltic Sea in the history of contemporary shipping (K. Kahma, personal communication on 8 January 2005). The area with the largest wind speeds crossed the Baltic Sea somewhat more southwards than originally forecast (Soomere et al. 2008) and the wave conditions were not so rough.

Buoy 1 adequately reflects extreme wave conditions in the case of SW winds, but the Gudrun's strongest winds were from W-WSW and occurred between Gotland and Saaremaa. The wave sensors therefore were located much northwards from the maximum of the wave storm. Even with these non-ideal conditions for wave generation and detection of the roughest seas, the significant wave height reached $H_S = 7.16$ m at 03:00 and 07:00 GMT on 9 January and was close to 7 m during about 12 h. The peak period T_P exceeded 10 s for nearly 24 h and was about 11–12 s at the wavestorm maximum.

Very long (T_p up to 12 s) and high ($H_S > 4$ m) waves also occurred in the Gulf of Finland during Gudrun. The significant wave height was close to 4 m in the early morning of 9 January and exceeded 3 m during the rest of this day at buoy 2. The peak periods were over 10 s during almost the whole day and reached 11–12 s at noon. The wave height was about 4 m in the morning of 9 January at the location of buoy 3 (a pressure sensor mounted north-westwards from the Island of Naissaar in 14 m deep water at 59°37.1′N, 24°29.1′E, see Fig. 1), and reached 4.5 m, the second highest instrumentally registered wave height in the central part of the gulf, at 09:00 GMT. The peak periods were ∼12 s during about 10 h (Soomere et al. 2008).

The occurrence of long and high waves in the interior of the Gulf of Finland is an important feature of this storm. The maximum wind speed in the northernmost part of the Baltic Proper and at the entrance of the gulf apparently was about 20–24 m s^{-1} (Fig. 7) and well below 20 m s^{-1} during a large part of the storm in the gulf (see also coastal data in Suursaar et al. 2006). Storms with a wind speed of about 20 m s^{-1} may excite peak periods about 12 s only if the fetch length is $\geq$600 km and the wind duration $\geq$18 h (Rosenthal 1986). Although growth curves of Kahma and Calkoen (1992) suggest that somewhat shorter duration ($\sim$15 h) and fetch ($\sim$350 km) are sufficient for generation of such seas, it is still probable that some other factors eventually contributed to the occurrence of the observed wave system in the Gulf of Finland. For example, topographic refraction caused by the coastal slopes of the entrance of the gulf may gradually redirect a part of waves propagating from the southern parts of the Baltic Proper.

4.2 Modelled Wave Fields

The operational centres of DWD, DMI, and FIMR run the wave model WAM cycle 4 (Komen et al. 1994) on a regular rectangular grid in shallow water mode without data assimilation. The models use different sources of hourly to three-hourly forecast winds at the standard height of 10 m above the surface level from different atmospheric models. The land-sea masks, bathymetry, computational grid, spatial and temporal resolution, and spectral range of the wave models are different as well (Soomere et al. 2004, 2008). The mesh size varies from $1/10^\circ$ along latitudes and $1/6^\circ$ along longitudes (the DWD model) down to $0.08^\circ \times 0.08^\circ$ (the FIMR model). The DWD and FIMR models use 24 equally spaced wave propagation directions whereas the DMI model uses 12 directions. The DWD and DMI models employ 25 frequency bands from 0.04177 in 10% steps. The FIMR model uses an extended range of 35 bands up to 1.073 Hz. The models have demonstrated reasonable performance in both typical and extreme wave conditions. For example, the mean relative error of the forecast of the maximum wave height in the five strongest storms is about 15% for 13 buoys operated by the DMI.

The models well reproduced the course of wave properties during windstorm Gudrun. The overall maximum of H_S at buoy 1 was overestimated by about 6% by the FIMR model and by 12–20% by the models of the DWD and the DMI (Table 1, Soomere et al. 2008). The wave models mostly followed the measured sea state (somewhat overpredicted the wave heights and underpredicted the wave periods) also in the Gulf of Finland.

4.3 Maximum of the Wave Storm

The overall maximum H_S during this storm is estimated by Soomere et al. (2008) by means of correcting the overall maximum of the modelled H_S with the use of

Table 2 Relative errors of operational wave models and the estimated overall maximum of the significant wave height in the Baltic Sea during windstorm Gudrun

Model	Overall maximum at buoy 1	Overprediction (m)	Relative error (%)	Modelled overall maximum of H_S (m)	Estimated overall maximum of H_S (m)
FIMR	7.6	0.44	5.8	10.2	9.6
DMI	8.96	1.80	20	11.7	9.4
DWD	8.17	1.01	12.4	10.95	9.59

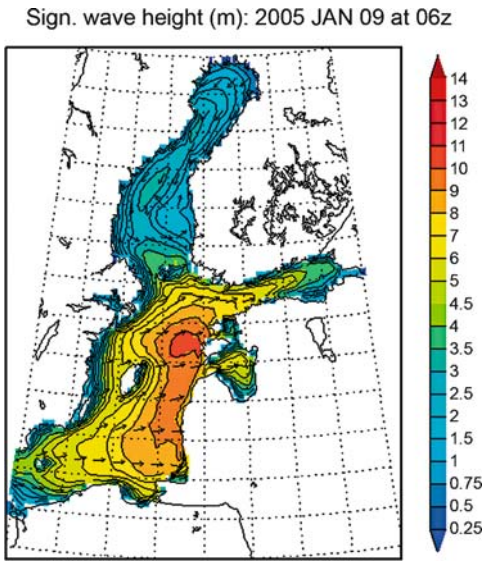

Fig. 8 Modelled significant wave heights (m) and wave propagation directions (*arrows*) at 06:00 GMT on 9 January in the DMI 54-h forecast valid at 00:00 GMT on 9 January. Courtesy of the Danish Meteorological Institute

the relative errors of the models calculated from observed data (Table 2). Doing so presumes that the wave models adequately represent the spatial patterns of wave properties and that the relative errors of the models are roughly the same over the entire area of intense waves. Since a large part of properties of the wave fields during Gudrun were located within the 'corridors' formed by outputs of the three models, a reasonable estimate of this maximum eventually lies between the values defined by these models.

The overall maximum $H_S \approx 9.5$ m during windstorm Gudrun evidently occurred about 200 km south-eastwards from buoy 1, off the coast of Saaremaa (about 57 °N, 20.4 °E, Fig. 8). Such wave conditions are much rougher than those expected to happen once in a century (Lopatukhin et al. 2006a). Waves were also remarkably long: peak periods up to 13 s were forecast (and eventually occurred) in the eastern part of the sea (Soomere et al. 2008).

The described procedure can be applied to the Gulf of Finland only based on results from buoy 2, because buoy 3 was located at a considerably smaller depth at a distance of >10 km from the closest model point. The significant wave height evidently reached 5 m in the gulf but most probably did not exceed the historical maximum $H_S = 5.2$ m.

5 Discussion

The most surprising outcome from the above analysis is that no overall increase of the average wave height has occurred in the northern Baltic Proper within the second half of the twentieth century. The annual mean wave height considerably increased in the 1980s and was exceptionally high in the mid-1990s, but quickly decreased starting from about 1997.

The long-term behaviour of the mean wave height matches neither the gradual increase of the mean wind speed nor the behaviour of the annual amplitude of the monthly mean sea level at the eastern coast of the Baltic Sea. This amplitude drastically increased in the 1970s and the 1980s at the Finnish coasts, and decreased again at the end of the twentieth century. Also, the short-term water level variability had a local minimum in the 1960s, increased until the 1980s, and then decreased until the end of the century (Johansson et al. 2001). The mismatch of the changes of the wind, wave, and water level dynamics in the northern Baltic Proper is a highly interesting feature and needs further investigation.

The qualitative match of the long-term variations of average wave properties at Almagrundet and at Vilsandi proves that decadal changes in the dominating wind directions cannot cause such long-term changes. Consequently, variations of certain other properties of the wind fields such as the duration of winds from different directions or changes in wind patterns related to the shifts of the trajectories of cyclones (Suursaar et al. 2006) may play a crucial role in the forming of long-term variations of the Baltic Sea wave fields.

Extreme wave conditions with $H_S \geq 7$ m were first observed in January 1984 in the northern Baltic Sea. Later on such seas occurred probably 1–2 times in late 1980s, once in 1990–1995, and four times since 1996. The frequency of extreme wave storms, therefore, has been largely unchanged during the last 30 years: they occur roughly twice a decade.

The strong reaction of the water surface is the most interesting feature of windstorm Gudrun that excited very high and long waves, although the maximum sustained wind speed was not exceptional and the wind direction was not particularly favourable for wave generation. Wave conditions with $H_S \sim 9.5$ m are much rougher than could be expected, based on the existing wave statistics (Lopatukhin et al. 2006a, b). Remarkably, long and high waves also appeared in the interior the Gulf of Finland, in an area which generally is sheltered from long waves. Given the rapid decrease of the mean wave height in 1997–2005, this event suggests that the decrease is accompanied by certain nontrivial changes of the forcing patterns.

It might be speculated that a future storm of the same strength and duration, but corresponding to more favourable wave generation conditions (e.g., a strong and large cyclone travelling in the NNE direction), may create even higher waves. Since only a few cyclones do so (Suursaar et al. 2006), such a 'perfect storm' is not likely to occur. However, if it did happen, it probably would excite even rougher wave conditions at the entrance of the Gulf of Finland and off the south-western coast of Finland than Gudrun did near Saaremaa. The possibility of such rough seas within the existing climatological conditions is of paramount importance for navigational safety and design of offshore structures.

The future climate changes are quite likely to modify factors controlling the volume of the water body, the mean temperature, salt water inflow conditions, the overall transport scheme of waters, the distribution of upwelling and downwelling patterns, the location of areas of the largest wave intensity and wave-induced mixing (Myrberg et al. 2007), and therefore the vertical and horizontal distribution of salinity, temperature, and other decisive constituents of the local ecosystem. In particular, the increased sea surface temperature leads to the reduction of ice cover in the northern parts of the sea. The potential increase of wind stress at sea-surface during relatively windy winter months may lead to further changes of wave climate; in particular, to enhancing of the extremes in wave heights and sea levels. Timely detection of such changes is a major challenge for scientists. Launching of adaptation measures is an accompanying challenge of decision-makers.

Acknowledgements Financial support of the Estonian Science Foundation (Grant 7413), EU-supported INNOVE project 1.0101-0208, Marie Curie RTN network SEAMOCS (MRTN-CT-2005-019374), and Marie Curie ToK project CENS-CMA (MC-TK-013909) is gratefully acknowledged.

References

Alenius P, Myrberg K, Nekrasov A (1998) Physical oceanography of the Gulf of Finland: a review. Boreal Env Res 3:97–125

Alexandersson H, Schmith T, Iden K, Tuomenvirta H (1998) Long-term variations of the storm climate over NW Europe. Glob Atmos Ocean Syst 6:97–120

Bacon S, Carter DJT (1991) The wave climate changes in the North-Atlantic and North Sea. Int J Climatol 11: 545–558

Bengtsson A, Nilsson C (2007) Extreme value modelling of storm damage in Swedish forests. Nat Hazards Earth Syst Sci 7:515–521

Blomgren S, Larsson M, Hanson H (2001) Numerical modelling of the wave climate in the southern Baltic Sea. J Coastal Res 17:342–352

Broman B, Hammarklint T, Rannat K, Soomere T, Valdmann A (2006) Trends and extremes of wave fields in the north-eastern part of the Baltic Proper. Oceanologia 48:165–184

Carpenter G (2005) Windstorm Erwin/Gudrun – January 2005. Speciality Practice Briefing, Issue No 2: pp 14. http://www.guycarp.com/portal/extranet/pdf/Speciality_Briefing_170105.pdf. Accessed 12 December 2007

Danielsson A, Jonsson A, Rahm L (2007) Resuspension patterns in the Baltic proper. J Sea Res 57:257–269

Davidan IN, Lopatoukhin LI, Rozhkov VA (1978) Wind sea as a probabilistic hydrodynamic process. Gidrometeoizdat, Leningrad [In Russian]
Davidan IN, Lopatoukhin LI, Rozhkov VA (1985) Wind waves in the world oceans. Gidrometeoizdat, Leningrad [In Russian]
Gayer G, Günther H, Winkel N (1995) Wave climatology and extreme value analysis for the Baltic Sea area off the Warnemünde harbour entrance, Deutsche Hydrographische Zeitschrift 47:109–130
Gulev SK, Hasse L (1998) North Atlantic wind waves and wind stress fields from voluntary observing ship data. J Phys Oceanogr 28:1107–1130
Gulev SK, Hasse L (1999) Changes of wind waves in the North Atlantic over the last 30 years. Int J Climatol 19:1091–1117
Holthuijsen LH (1983) Observations of the directional distribution of ocean wave energy in fetch limited conditions. J Phys Oceanogr 13:191–207
Hogben N, Da Cunha NMC, Oliver GF (1986) Global Wave Statistics. Unwin Brothers, London
IAHR working group on wave generation and analysis (1989) List of sea-state parameters. J Waterw Port Coast Ocean Eng 115:793–808
Johansson M, Boman H, Kahma KK, Launiainen J (2001) Trends in sea level variability in the Baltic Sea. Boreal Env Res 6:159–179
Jönsson A, Broman B, Rahm L (2002) Variations in the Baltic Sea wave fields. Ocean Eng 30:107–126
Jönsson A, Danielsson A, Rahm L (2005) Bottom type distribution based on wave friction velocity in the Baltic Sea. Continent Shelf Res 25:419–435
Kahma K, Calkoen CJ (1992) Reconciling discrepancies in the observed growth of wind-generated waves. J Phys Oceanogr 22:1389–1405
Kahma K, Pettersson H (1993) Wave statistics from the Gulf of Finland. Internal report 1/1993. Finnish Institute of Marine Research, Helsinki [In Finnish with English summary]
Kahma K, Pettersson H (1994) Wave growth in a narrow fetch geometry. Glob Atmos Ocean Syst 2:253–263
Kahma K, Pettersson H, Tuomi L (2003) Scatter diagram wave statistics from the northern Baltic Sea. MERI – Report Series of the Finnish Institute of Marine Research 49:15–32
Komen GJ, Cavaleri L, Donelan M, Hasselmann K, Hasselmann S, Janssen PAEM (1994) Dynamics and modelling of ocean waves. Cambridge University Press, Cambridge
Kushnir Y, Cardone VJ, Greenwood JG, Cane, MA (1997) The recent increase of North Atlantic wave heights. J Clim 10:2107–2113
Laanearu J, Koppel T, Soomere T, Davies PA (2007) Joint influence of river stream, water level and wind waves on the height of sand bar in a river mouth. Nordic Hydrol 38:287–302
Lopatukhin LI, Mironov ME, Pomeranets KS, Trapeznikov ES, Tshernysheva ES (2006a) Estimates of extreme wind and wave conditions in the eastern part of the Gulf of Finland. Proc BNIIG 245:145–155
Lopatukhin LI, Bukhanovsky AV, Ivanov SV, Tshernyshova ES (2006b) Handbook of wind and wave regimes in the Baltic Sea, North Sea, Black Sea, Azov Sea and the Mediterranean. Russian Shipping Registry, Sankt-Petersburg, pp 450 [In Russian]
Mårtensson N, Bergdahl L (1987) On the wave climate of the Southern Baltic. Report Series A: 15. Department of Hydraulics, Chalmers University of Technology, Göteborg
Mietus, M (co-ordinator) (1998) The climate of the Baltic Sea Basin, Marine meteorology and related oceanographic activities. Report No. 41. World Meteorological Organisation, Geneva
Mietus M, von Storch H (1997) Reconstruction of the wave climate in the Proper Baltic Basin, April 1947–March 1988, GKSS Report 97/E/28, Geesthacht
Myrberg K, Soomere T, Leppäranta M, Nekrasov A (2007) Recent advances in the physical oceanography of the Gulf of Finland. In Isemer H–J (ed) Fifth study conference on BALTEX, Kuressaare, Saaremaa, Estonia, 4–8 June 2007, International BALTEX Secretariat, Publication No. 38, Geesthacht, Germany, pp 19–22
Orlenko LR, Lopatukhin LI, Portnov GL (eds) (1984) Studies of the hydrometeorological regime of Tallinn Bay. Gidrometeoizdat, Leningrad [In Russian]

Orviku K (2006) Developmental ties between Järve-Mändjala beach and Nasva harbour, Proc Estonian Maritime Acad 3:7–18

Orviku K, Jaagus J, Kont A, Ratas U, Rivis R (2003) Increasing activity of coastal processes associated with climate change in Estonia. J Coast Res 19:364–375

Paplińska B (1999) Wave analysis at Lubiatowo and in the Pomeranian Bay based on measurements from 1997/1998 – comparison with modelled data (WAM4 model). Oceanologia 41:241–254

Pettersson H (2001) Directional wave statistics from the Gulf of Finland 1990–1994. MERI – Report Series of the Finnish Institute of Marine Research 44:1–37 [In Finnish with English summary]

Pettersson H (2004) Wave growth in a narrow bay. PhD Thesis, Finnish Institute of Marine Research, Contributions No. 9, Helsinki

Pettersson H, Boman H (2002) High waves and sea level during the November storm. Annual report 2001, Finnish Institute of Marine Research, Helsinki, p. 7

Rosenthal W (1986) Wind waves and swell. In: Sündermann J (ed) Oceanography, vol. 3C. Landolt-Börnstein: Numerical Data and Functional Relationships in Science and Technology–New Series, Springer, pp 17–36

Rzheplinsky GV, Brekhovskikh YuP (1967) Wave atlas for Gulf of Finland, Gidrometeoizdat, Leningrad [In Russian]

Rzheplinsky GV (ed) (1965) Wave and wind atlas for the Baltic Sea. Tallinn [In Russian]

Simpson RH, Riehl H (1981) The hurricane and its impact. Lousiana State University Press, Baton Rouge

Soomere T (2001) Wave regimes and anomalies off north-western Saaremaa Island. Proc Estonian Acad Sci Eng 7:157–173

Soomere T (2003) Anisotropy of wind and wave regimes in the Baltic Proper. J Sea Res 49:305–316

Soomere T (2005) Wind wave statistics in Tallinn Bay. Boreal Env Res 10:103–118

Soomere T, Behrens A, Tuomi L, Nielsen JW (2008) Wave conditions in the Baltic Proper and in the Gulf of Finland during windstorm Erwin/Gudrun. Nat Hazards Earth Syst Sci 8:37–46

Soomere T, Dick S, Gästgifvars M, Huess V, Nielsen JW (2004) Project plan for implementation of interfacing between Baltic scale models to local (coastal area) models. http://www.boos.org/fileadmin/user_upload/PAPA_Reports/PAPA_ImplementationInterfacingBalticScaleToLocalModels.pdf, 22 pp. Accessed 9 December 2007

Soomere T, Keevallik S (2001) Anisotropy of moderate and strong winds in the Baltic Proper. Proc Estonian Acad Sci Eng 7:35–49

Soomere T, Keevallik S (2003) Directional and extreme wind properties in the Gulf of Finland. Proc Estonian Acad Sci Eng 9:73–90

Soomere T, Zaitseva I (2007) Estimates of wave climate in the northern Baltic Proper derived from visual wave observations at Vilsandi. Proc Estonian Acad Sci Eng 13:48–64

Sterl A, Caires S (2005) Climatology, variability and extrema of ocean waves – the web-based KNMI/ERA-40 wave atlas. Int J Climatol 25:963–977. doi: 10.1002/joc.1175

Suursaar Ü, Kullas K, Otsmann M, Saaremäe I, Kuik J, Merilain M (2006) Cyclone Gudrun in January 2005 and modelling its hydrodynamic consequences in the Estonian coastal waters. Boreal Env Res 11:143–159

The SWAMP Group (1985) Ocean wave modelling. Plenum Press, New York

Tuomi L, Pettersson H, Kahma K (1999) Preliminary results from the WAM wave model forced by the mesoscale EUR-HIRLAM atmospheric model. MERI – Report series of the Finnish Institute of Marine Research 40:19–23

Vikebo F, Furevik T, Furnes G, Kvamsto NG, Reistad M (2003) Wave height variations in the North Sea and on the Norwegian Continental Shelf 1881–1999. Continent Shelf Res 23:251–263

WASA Group (1995) The WASA project: changing storm and wave climate in the northeast Atlantic and adjacent seas? In Proceedings of Fourth International Workshop on Wave Hindcasting and Forecasting, Banff, Canada, October 16–20, pp. 31–44; also: GKSS Report 96/E/61

WMO (2001) Guide to the applications of marine climatology. WMO Publication 781, Geneva

Extreme Waves Generated by Cyclones in Guadeloupe

Narcisse Zahibo, Irina Nikolkina, and Ira Didenkulova

Abstract Cyclones produce some harm by terrific wind speed, abnormal precipitations, and sea motion. Historically, storm surge inundation has been the most destructive and murderous. The extreme waves caused by cyclones on the coast of Guadeloupe for a whole historic period are discussed. The first documented sea damage during hurricane passage in Guadeloupe occurred in 1642. Data of extreme waves induced by hurricanes from 1928 to 2007 in Guadeloupe are collected and discussed. The heights of extreme waves for Caribbean and Atlantic coasts are compared; the most dangerous regions are also evaluated.

1 Introduction

Cyclones known as hurricanes in North Atlantic and typhoons in North Pacific are categorized according to their maximum wind speed and lowest central pressure. In the Atlantic, the Saffir–Simpson Scale (SSS) is used to classify most of the tropical cyclones that exceed the intensities of "tropical depressions" and "tropical storms." It is a scale with the range of 1–5 based on wind speed that shows expected damage to structures, the effects of storm surge, and flooding (Table 1).

N. Zahibo and I. Nikolkina
Laboratory of Tropical and Atmospheric Physics, Department of Physics, University of Antilles Guyane, Guadeloupe (F.W.I.), France
nzahibo@bakanik.univ-ag.fr

I. Nikolkina and I. Didenkulova
Department of Applied Mathematics, Nizhny Novgorod State Technical University, Nizhny Novgorod, Russia
irina.nikolkina@caramail.com

I. Didenkulova
Institute of Applied Physics, Nizhny Novgorod, Russia
Institute of Cybernetics, Tallinn, Estonia
dii@hydro.appl.sci-nnov.ru

E. Pelinovsky, C. Kharif (eds.) *Extreme Ocean Waves*, 159–177.

Table 1 Saffir–Simpson hurricane scale

Category	Wind speed (km h^{-1})	Storm surge (m)
Tropical depression	0–62	0
Tropical storm	63–117	0–0.9
1	119–153	1.2–1.5
2	154–177	1.8–2.4
3	178–209	2.7–3.7
4	210–249	4–5.5
5	>250	>5.5

Various data of tropical storms and hurricanes in the Atlantic can be found now in sites (NTC; UNISYS; Hurricanecity). The Atlantic tropical cyclones that resulted in great loss of life during 1492–1996 are introduced and discussed in Rappaport and Fernandez-Partagas (1997). Recently, Pielke et al. (2003) discussed the hurricane vulnerability in Latin America and the Caribbean after catastrophic Hurricane Mitch, which caused deaths of more than 10,000 people and resulted in property damage at a valuation of more than $8.5 billion in Honduras and Nicaragua.

The French West Indies located in the Lesser Antilles, North Atlantic has a huge experience of tropical cyclones. The most detailed catalogue of cyclone activity in Martinique and Guadeloupe was compiled by Saffache et al. (2002, 2003) based on historical documents. This data was used by Zahibo et al. (2007) to obtain the statistical analysis of cyclone characteristics in Guadeloupe.

Cyclones produce some harm by terrific wind speed, abnormal precipitations, and sea action. Historically, storm surge inundation has been the most destructive and murderous. One of the most catastrophic recent natural disasters occurred in Bangladesh in 1970; where more than 300,000 people were lost in storm surge flooding during a powerful cyclone (Wolshon et al. 2005). Storm surges are created by large wind speed (in cyclones category 1–5 SSS wind speed is less than 33 m s^{-1}) and high atmospheric pressure fall (the maximum value of 5 h Pa in the Atlantic was recorded in September 1966 when Hurricane Inez went over Guadeloupe).

A storm surge history is rather extensive; thus on 10 March 1899 during cyclone Mahina (the most fatal natural disaster in Australian history) an extreme wave occurred. Just before the eye of the cyclone passed overland to the north, a tidal wave (caused by storm surge), variously reported as either 13 m or 48 ft (14.6 m) high, swept inland for about 5 km, destroying anything that was left of the Bathurst Bay pearling fleet along with the settlement. The analysis of this event made by Nott and Hayne (2000) suggested that marine inundations have not exceeded 3–5 m elevation.

The analysis of the storm surge (up to 28 ft height) on American coast during Katrina passage has been produced under the direction of the Federal Emergency Management Agency (Knabb et al. 2005). Afterwards, numerical simulation was performed for forecasting storm surges propagating up the Mississippi River (Reed and Stucky 2005). Nowadays, the Atlantic Storm Surge and Tsunami System is a work in progress, NOAA (O'Reilly et al. 2006).

Recently, Atlantic has been struck by a destructive event of category 5. The Hurricane Dean was formed on 13 August 2007 over west coast of Africa. This powerful

tropical cyclone is considered as the most intense event in the Atlantic basin since Hurricane Wilma that occurred in 2005. Dean fell on the Lesser Antilles on the night of 16th to 17th of August, 2007. The field survey has been performed by authors in August 2007 in Guadeloupe after the attack of the Hurricane Dean.

The extreme waves caused by cyclones on the coast of Guadeloupe for a whole historic period are discussed here. The paper is organized as follows. Data of extreme waves induced by the last Hurricane Dean in Guadeloupe is given in Sect. 2. Analysis of available historical data of storm surges is made in Sect. 3. The main conclusions are summarized in Sect. 4.

2 Extreme Waves Induced by Hurricane Dean

2.1 Cyclone General Information

The Hurricane Dean crossed the center of an Antillean arc on 16–17 August 2007. After traversing the channel Sainte-Lucie (south of Martinique), Dean reached to the third stage of SSS; its average maximal wind speed was in the order of 160–180 km h^{-1} with blasts of 200 km h^{-1}. Between 4 a.m. and 7 a.m. the center of the hurricane passed several kilometers to south of Martinique (15 km to Sainte-Anne, 30 km to Airport Lamentin) (Communique meteorogique de presse, 2007), see satellite image and Guadeloupe map in Figs. 1 and 2.

Two deaths were caused by Dean in Martinique: an old man died because of cardiac seizure and another man died because of a very strong wind. Great damages occurred in French territories, trees were overthrown and root out (particularly cocowood of Faula au Vauclin, South-east of Martinique; and Sainte-Anne, South of Martinique), roads were destroyed, some beaches of white sand in Sainte-Anne and Diamant disappeared under the water. But the most considerable damage occurred to bananas (100% of production in Martinique and 80% in Guadeloupe), tropical fruits, and sugar-cane (70% of production in Martinique) (Sergent, 2007), see Fig. 3.

The Guadeloupe archipelago was 200 km far from the center of the hurricane; since hurricane winds reached its maximum strength at 10–100 km from the center, wind speed was not so violent there. The highest wind speed was observed in the South: on the island Marie-Galante (119 km h^{-1}) and Les Saintes (126 km h^{-1}) (Damase, 2007). In general, maximum wind speed in Guadeloupe was less than 100 km h^{-1} on the plain and about 175 km h^{-1} on the mountain Soufriere (Communiqué météorologique de presse, 2007). According to SSS these wind speed values correspond to storm surges of 0.09–2.4 m height in Grande-Terre and Basse-Terre, respectively.

The wave height was about 6–10 m; surge waves were measured in Basse Poine, North Atlantic of Martinique (10.4 m), and in the channel Sainte-Lucie (9 m). In the vicinity of Guadeloupe surge waves were estimated to be 6–8 m, in the channel of Les Saintes the heights exceeded 7 m (Communiqué météorologique de presse, 2007).

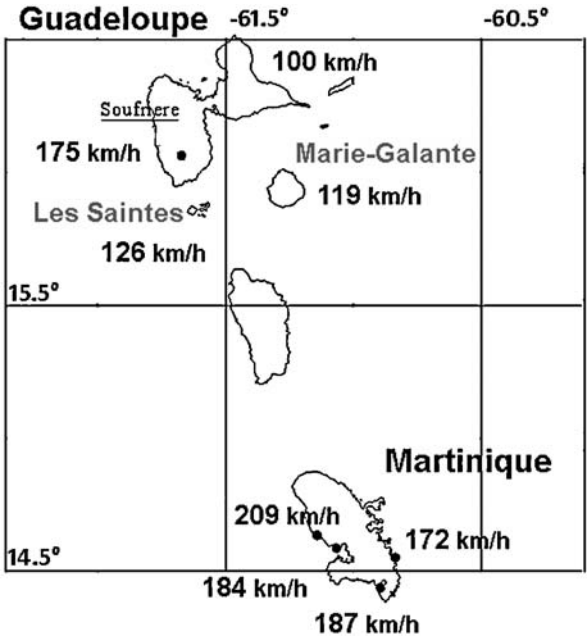

Fig. 1 Observed wind speed during hurricane passage

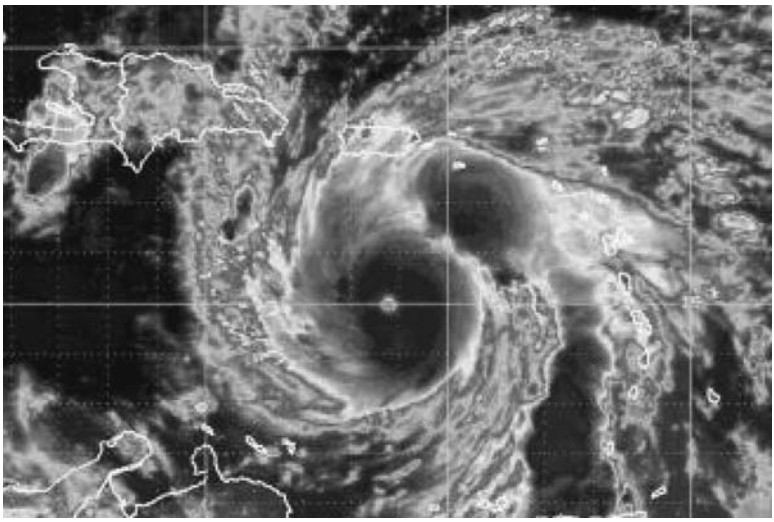

Fig. 2 Hurricane Dean category 4 in the Caribbean, satellite image 17 August 2007, 5.15 a.m. GMT (Les cyclones, typhons et autres ouragans, 2007)

Fig. 3 About 80% of bananas were damaged in Guadeloupe

Field survey of the Guadeloupe Island was carried out 2 days after hurricane passage by a survey team from the University of Antilles Guyane: Prof. Narcisse Zahibo, MSc student Irina Nikolkina and Dr. Ira Didenkulova, which lasted for four days (19–22 August 2007).

As hurricane passed from 200 km to the south from Guadeloupe (channel Sainte-Lucie, south of Martinique), particular damage was caused on the southern shore of Guadeloupe. The most damaged areas were observed from North West to South of Basse-Terre and from South to South East of Grande-Terre. The expedition started in Sainte-Rose (north-west of Basse-Terre) and finished in Sainte-Anne (south-east of Grande-Terre).

2.2 Severely Damaged Territories

Authors performed the field survey and suggested that Grande-Terre was especially damaged by storm surges. This amplification could be caused by bottom topography as the beaches in Grand-Terre are the flattest. The most damaged territories were located in the northern coast of the Caribbean shore, St Anne, St Félix, and Petit-Havre. The main harm observed in Grande-Terre during the field survey included soil degradation, inundation (Sainte-Anne), destruction of littoral buildings (Petit Havre), and debris of marine origin up to 50–60 m inshore (Saint-Felix). North-western part of Basse-Terre was damaged mainly by wind, as it reached its maximum speed near the volcano Soufriere (Communiqué météorologique de presse, 2007). The field survey results showed that the most significant damage was caused

in north and north-western parts of Basse-Terre (Vieux-Habitants, Sainte-Rose, Malendure, Vieux-Habitants). Here is the short description of the observed damage.

2.3 Gosier

In Center of Gosier the main beach was inundated with the marine (sea shells, algae, grass-wrack) and anthropogenic (plastic bottles, bauchles) origin materials (Fig. 4). The small beach near the central park was covered with sea-grass on a horizontal distance of more than 5 m (Fig. 5). The central square of Gosier, which is situated on the sea shore, was cluttered up with the rubbish of all sorts (Fig. 6). The horizontal distance covered with the sea garbage exceeded 10 m. A berth to get to an island Ile de Gosier was totally destroyed by the hurricane, and stone plates near the berth were broken (Fig. 7).

2.4 Saint Félix

In Anse du Mont, Saint-Félix, garbage of marine origin was drifted in the water 100 m offshore (Fig. 8). Anse Canot was over covered by sea-grass along a distance more than 40 m inland (Fig. 9), and trees were uprooted. This beach was washed away, and thickness of a depredated layer exceeded 20 cm. The beach degradation can be seen in Fig. 9.

Fig. 4 Local people gathering cockle-shell and sea plants, Gosier

Fig. 5 A small beach covered with sea-grass, Gosier

Fig. 6 Garbage on the central square, Gosier

Fig. 7 Destroyed berth, Gosier

Fig. 8 Yachts and sea garbage in Marina Saint-Felix (Anse du Mont)

Fig. 9 Beach of Saint-Felix (Anse Canot): before the hurricane, February 2007 (*left*); after the Hurricane Dean, August 2007 (*right*)

2.5 Petit Havre

According to an eye-witness, in the bay Petit Havre the wave of 6 m height (Lapinard, 2007) destroyed a berth (Fig. 10). The small beach is totally ruined (Fig. 11), sea garbage and rubbish of anthropogenic origin materials covered the shore. The hurricane uprooted the trees and bent a stone more than 1 m height. Along the beach of Petit Havre the soil was washed away for a distance about 45 m (Fig. 12). A summerhouse and a table were broken and the trees were root out because of beach degradation (Fig. 13). A metallic frame (probably a part of local berth) was dragged by the waves.

2.6 Sainte-Anne

The local newspaper declaimed on the first day after the hurricane passage "The Sainte-Anne beach doesn't exist any more; the road, parking – everything is covered

Fig. 10 Destroyed berth in Petit Havre

Fig. 11 The beach of Petit Havre: January, 2006 (*left*) and August, 2007 (*right*)

Fig. 12 Beach degradation

Fig. 13 Consequences of the hurricane: broken table (*left*), inclined summerhouse (*right*)

Fig. 14 Sainte-Anne beach: before the hurricane, December 2005 (*left*); after the Hurricane Dean, August 2007 (*right*)

with sand up to apartment houses," see Fig. 14 (Lapinard, 2007). The destroyed berth (Fig. 15) and several tired up palms (Fig. 16) were observed. The diameter of a rhizome is comparable with human height, mounts to 1.8 m with 30–40 cm thickness. A layer of degraded soil was in 40 cm thickness (Fig. 17). The small hidden beach Village Artisanal de Sainte-Anne near the main road was covered by sea-grass (Fig. 18). The grass was spread out to a distance of 50 m.

Fig. 15 Destroyed berth, Sainte-Anne

Fig. 16 Fallen palms, Sainte-Anne

Fig. 17 Soil degradation, Sainte-Anne

Fig. 18 Sea grass on a small beach, Sainte-Anne

Fig. 19 Community of Marine Capture Fisheries was heavily damaged (Vieux-Habitants)

2.7 Basse-Terre Region

In Vieux-Habitants, run-up of severe storm surges of 3–4 m and heavy winds were observed (Figs. 19 and 20). The beach in Malendure was covered by sea-grass, placed out to several meters (Fig. 21). According to a local paper, some damage was caused in the beach Sainte-Claire, Goyave (Fig. 22), sea damage was drifted 30–40 m offshore, and terrific storm surges were recorded in Vieux-Habitants (Fig. 23) (Lapinard, 2007).

Fig. 20 Storm surges in Vieux-Habitants (France-Antilles Guadeloupe, samedi 18 et dimanche 19 août 2007)

Fig. 21 Extreme left sea-grass several meters inshore in Malendure (on the left photo: a member of expedition Ira Didenkulova)

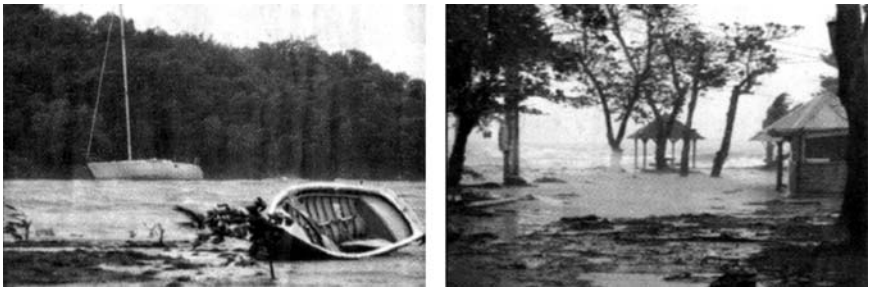

Fig. 22 Data of hurricane destruction in Sainte-Claire, Goyave (destroyed beach)

2.8 Tide-Gauge Data

Since 1984, the network of tide-gauges exits in Guadeloupe. It consists of six mareographs nowadays (two of them are nonworking), Fig. 23 (Etude du risque tsunami en Guadeloupe, 2006). According to the report of the Volcanic and Seismic

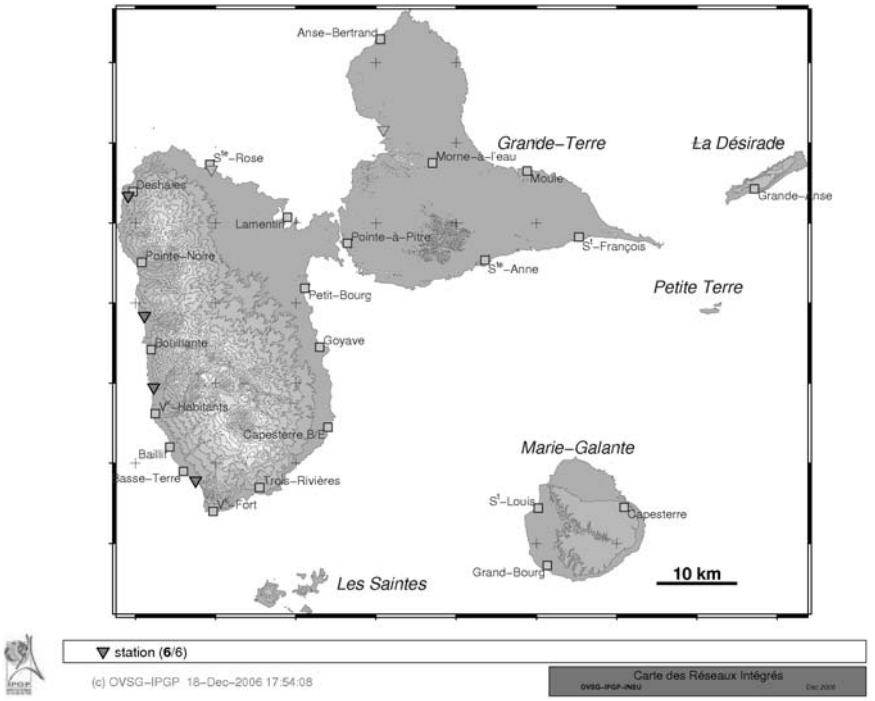

Fig. 23 The location of the tide-gauges in Guadeloupe (triangles and squares indicate actual tide-gauges and planned stations, respectively)

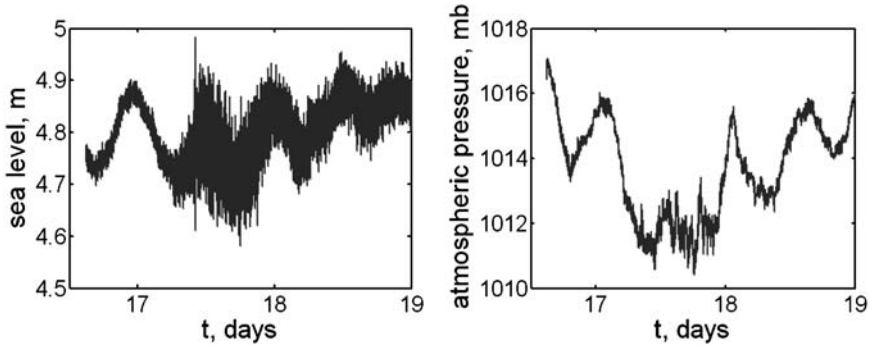

Fig. 24 Records of sea level and atmospheric pressure taken in August, 2007 in Deshaies

Observatory of Guadeloupe, the tide-gauges, which are available now, are located in average depth of about 2 m in Deshaies, Bouillante, Vieux-Habitants and Gourbeyre. The port in Deshaies was the only place where the tide-gauge record was available (Fig. 24). According to the record, storm surges in Deshaies reached 3 m height.

The field survey results mark that, being nowadays well-protected by stone constructions, Deshaies was slightly damaged by wind and not by sea waves. However,

there was some water inside the mareograph (about 2 m above mean water level). This statement is in a good agreement with data from the western part of Basse-Terre (Vieux-Habitants), where storm surges of 3–4 m height were observed. Apparently, the amplitude of storm surges might have had similar order in all Basse-Terre.

The atmospheric pressure is in an obvious correlation with sea waves; here we observe so-called rule of reverse barometer (Lamb, 1932). The experience of the Volcanic and Seismic Observatory of Guadeloupe in 2006 showed that normally the short-term atmospheric pressure variations have an order of 5 mb that causes sea level variations of 5 cm (Etude du risque tsunami en Guadeloupe, 2006). During the cyclone passage the short-term atmospheric pressure variations of 7 mb were accompanied by sea level variations of about 40 cm.

Because of the large distance between the hurricane eye and Guadeloupe (200 km), all mentioned phenomena were recorded by tide-gauge several hours after hurricane passage.

The locations and amplitudes of the storm surges are given in Fig. 25. According to Fig. 25, the Caribbean coast, especially south of Grande-Terre and west of Basse-Terre, was damaged significantly.

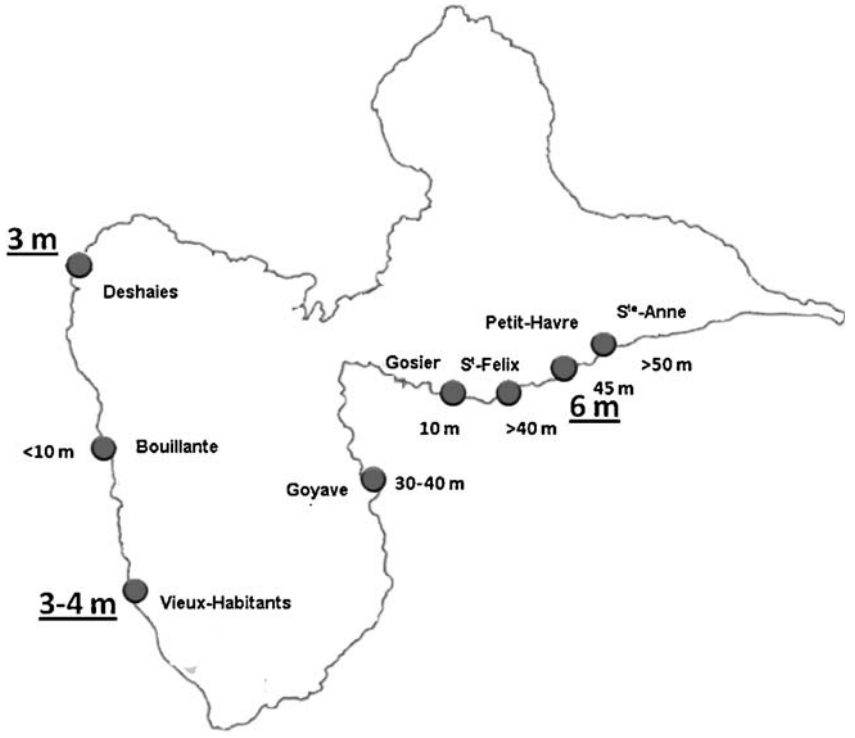

Fig. 25 Locations and amplitude of storm surges produced by Hurricane Dean (run-up height, big underlined letters; run-up length, small letters)

3 Historical Data of Storm Surges

The first mentioned sea-damage during hurricane passage in Guadeloupe occurred in 1642. "Dead fish was partly dug in sand along the whole shore of Basse-Terre; here a refugee was found from its natural world <the sea>." In Table 2, events are presented in the chronicle order. Here we give some description found in Saffache (2003). Figure 26 presents data of extreme waves in Guadeloupe from 1928 to 2007. Here we use only presided data for storm surge locations for several cyclones; the description does not include the name of district, but a storm surge height for the whole island is given. Thus, the terrible cyclone of 1928 (category 4) produced extreme waves of 15 m height; the famous Hurricane Hugo (category 4) that traversed the island from east to west causing huge damage by wind caused "small storm surges" ("modest houle" in French). This phenomenon is discussed in Pagney and Dalby (1991), where the authors suggested that the coast morphology could have reduced storm surge. During 2000–2006, cyclones produced extreme waves less than 2.5 m, except Hurricane Fabian (category 3) when 4 m storm surges were reported.

Table 2 Damaging cyclones in Lesser Antilles

Date	Cyclone	Category	Storm surge (m)	Location
1928		4	15	Guadeloupe coast
1966	Inez	3	"Probable storm surge"	Saint-François, Pointe-a-Pitre and Sainte-Rose
1979	David	4	4–5	Saint-François
1989	Hugo	4	"Minor storm surge"	Guadeloupe coast
1995	Luis	4	"Strong storm surge"	Moule, Port-Louis, Malendure, Deshaies and Bouillante
1995	Marilyn	1	4–6	Caribbean coast of Grande-Terre and on the shore of Basse-Terre, between Capesterre and Petit-Bourg
1998	Bonnie	TS	1.5–2	South-east of Guadeloupe
1998	Danielle	2	2–2.5	Atlantic coast (east-north-east and north-east)
1999	Jose	2	4–5	South-east of Guadeloupe
1999	Lenny	TS	4–5	Caribbean coast
			3	Deshaies
2000	Joyce	TS	2	Guadeloupe coast
2001	Chantal	TS	"Storm surge"	Guadeloupe coast
2003	Fabian	4	4	Guadeloupe coast
2003	Isabel	4	2.5	Guadeloupe coast
2004	Ivan	3	"Minor storm surge"	Guadeloupe coast
2007	Dean	4	6–8	Petit Havre (Gosier)
			3	Deshaies
			3–4	Vieux-Habitants

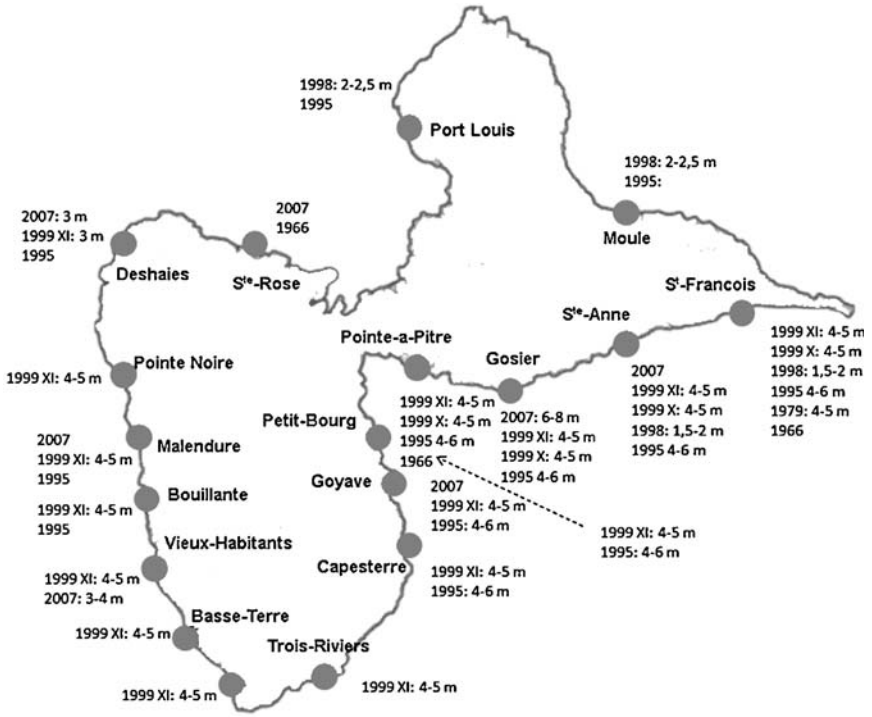

Fig. 26 Locations and dates of extreme waves in Guadeloupe in 1928–2007

The most important storm surges were recorded in 2007 (6–8 m, Petit-Havre), in 1995 (4–6 m, Caribbean coast of Grande-Terre and south-eastern coast of Basse-Terre), and in 1999 (4–5 m, Caribbean coast).

Both Atlantic and Caribbean coasts of the island are exposed to extreme waves; the mean value of storm surge height for the Atlantic coast (2.2 m) is twice lower than that for the Caribbean one (4.4 m). The most dangerous regions are observed in the southern shore of Grande-Terre: Gosier, Sainte-Anne, and Saint-François.

The maximum runup was recorded in 1999 during Hurricane Lenny (category 4), when waves of 3 m height in Deshaies flooded a local boulevard up to 200 m inland. In 2007, after Dean passage, runup length in Anse du Mont, Gosier, reached 100 m.

4 Conclusion

Since 1928, several terrific hurricanes have occurred in the Caribbean, and extreme waves produced by these cyclones damaged Guadeloupe. The tide-gauge record of the first storm surge (hurricane Dean, August 2007) was presented and analyzed.

According to it, the atmospheric pressure is in an obvious correlation with storm surges; here we observe so-called rule of reverse barometer.

The maximal storm surges in Guadeloupe reached 15 m and were produced by hurricane in 1928. The most important storm surges were recorded in 2007 (6–8 m, Petit-Havre), in 1995 (4–6 m, Caribbean coast of Grande-Terre and south-eastern coast of Basse-Terre), and in 1999 (4–5 m, Caribbean coast). Both Atlantic and Caribbean coasts of the island felt extreme waves, and the mean value of storm surge height for the Atlantic coast (2.2 m) is twice lower than that for the Caribbean one (4.4 m). The most dangerous regions are located in the southern shore of Grande-Terre: Gosier, Sainte-Anne, and Saint François.

Acknowledgements Authors are grateful to M F. Beauducel from Observatoire Volcanologique et Sismologique de Guadeloupe de l'Institut de Physique du Globe de Paris for tide-gaude data. This research is supported particularly by grants from INTAS (06-1000014-6046), RFBR (08-05-00069, 08-02-00039, 08-05-72011), Marie Curie network SEAMOCS (MRTN-CT-2005-019374), and Scientific School of Corresponding Member of Russian Academy of Science V.A. Zverev.

References

Communiqué météorologique de presse, le 21 août 2007 a 12h00 locales, Direction Interrégionale Antilles-Guyane, Meteo France

Damase M.A (2007) Catastrophe naturelle ou pas? Damase M . France-Antilles: le quotidien d'information de la Guadeloupe, N 11251, p 2

Etude du risque tsunami en Guadeloupe (2006) Installation de marégraphes permanents pour l'analyse des effets liés a l'activitè volcanique, Institut de physique du globe de Paris, Observatoire Volcanologique et sismologique de Guadeloupe. Rapport final–décembre 2006, http://tempetetropicale.blogspot.com/2007/08/tude-du-risque-tsunami-en-guadeloupe.html

Knabb RD, Rhome JR, Brown DP (2005) Tropical cyclone report Hurricane Katrina 23–30 August 2005, National Hurricane Center, 20 December 2005 http://www.nhc.noaa.gov/pdf/TCR-AL122005_Katrina.pdf

Lamb H (1932) Hydrodynamics, 6th edn. Cambridge University Press, Cambridge, London

Lapinard YJ (2007) Cyclone Dean en images / Lapinard YJ, Mercader H (2007) France-Antilles: le quotidien d'information de la Guadeloupe. N 11244. P 4–5

Les cyclones typhons et autres ouragans (2007). http://youpifrance.blogspot.com/2007/08/les-cyclones-typhons-et-autres-ouragans.html

Nott J, Hayne M (2000) How high was the storm surge from tropical cyclone Mahina? Aust J Emerg Manage (Autumn):11–13

O'Reilly C, Macaulay P, Parkes G (2007) Atlantic Storm Surge and Tsunami Warning System. http://www.quebec2007.ca/pdf/salle205c/seance30/articles/c_oreilly.pdf

Pagney P, Dalby M A (1991) propos de l'ouragan Hugo. Les phénomènes cycloniques et les Petites Antilles françaises. Les risques cycloniques et les Petites Antilles françaises. Les cyclones et l'archipel guadeloupéen. S.1., S.N. p 53

Pielke RA Jr, Rubiera J, Landsea C, Fernandez CML, Klein R (2003) Hurricane vulnerability in Latin America and the Caribbean: Normalized damage and loss potentials. Nat Hazards Rev 4(3):101–113

Rappaport EN, Fernandez-Partagas J (1997) The deadliest Atlantic tropical cyclones, NOAA Technical Memorandum NWS NHC 47:1492–1996. http://www.nhc.noaa. gov/pastdeadly.shtml

Reed DB, Stucky BE (2005) Forecasting Hurricane storm surge on the Mississippi river. Solutions to coastal disasters :52–60

Saffache P, Marc J-V, Cospar O (2002) Les cyclones en Martinique: Quatre siècles cataclysmiques. IBIS Rouge Editions, Martinique

Saffache P, Marc J-V, Huyghes-Belrose V (2003) Les cyclones en Guadeloupe: Quatre siècles cataclysmiques. IBIS Rouge Editions, Martinique, p 276

Sergent D (2007) Aux Antilles, le cyclone Dean a ravage les bananeraies / Sergent D. La Croix, N 37829, p 7

Wolshon B, Urbina E, Wilmot C, Levitan M (2005) Review of policies and practices for hurricane evacuation. I. Transportation planning, preparedness, and response. Nat Hazards Rev, ASCE/August:129–142

Zahibo N, Pelinovsky E, Talipova T, Rabinovich A, Kurkin A, Nikolkina I (2007) Statistical analysis of cyclone hazard for Guadeloupe, Lesser Antilles. Atmos Res 84:13–29

An Analytical Model of Large Amplitude Internal Solitary Waves

Nikolay I. Makarenko and Janna L. Maltseva

Abstract The problem on steady internal waves in a weakly stratified two-layered fluid is studied analytically. We consider the model with homogeneous fluid in the lower layer and with exponentially stratified fluid in the upper layer. The long-wave approximation is constructed by means of implementing a scaling procedure with a small Boussinesq parameter. Extreme configurations of solitary waves such as broad table-top waves are discussed.

1 Introduction

It is well known at present (Helfrich and Melville 2006; Pelinovsky et al. 2007) that ocean internal waves can exhibit huge magnitude comparable with total fluid depth. One of the most interesting extreme forms of nonlinear internal waves is intimately related with the broadening effect. Broadening occurs when the phase speed of solitary wave is close to the propagation speed of smooth internal bore. Turner and VandenBroeck (1988) found this effect numerically by calculation of interfacial table-top solitary waves in a two-fluid system.

Two-layer approximation is a standard model of sharp pycnocline in a stratified fluid. In this description, the density is constant in each layer but has a discontinuity at interface. At the same time, in several cases, one should take into account slight continuous stratification of fluid layer in spite of the density jump at interface. In this chapter, we consider a theoretical model of strongly nonlinear interfacial waves in a two-layer fluid, which has a constant density in lower layer, and the density depends exponentially on the height in upper layer. The newly proposed model equation generalizes the models suggested by Ovsyannikov et al. (1985) and Miyata (1985) for a system with constant densities in both layers, as well as the "2.5-layer"

N.I. Makarenko and J.L. Maltseva
Lavrentyev Institute of Hydrodynamics, Novosibirsk 630090, Russia
makarenko@hydro.nsc.ru, maltseva@hydro.nsc.ru

E. Pelinovsky, C. Kharif (eds.) *Extreme Ocean Waves*, 179–189.

model considered by Voronovich (2003). We demonstrate that perturbed model is well consistent with the known results about table-top waves in the perfect two-fluid system. We have also found the range of parameters where continuous stratification in upper layer essentially affects the shape of solitary waves. In this view, the resulting model takes into account the influence of weak stratification outside of the pycnocline.

The method of derivation involves asymptotic analysis of the Dubreil-Jacotin – Long equation, which is equivalent to the fully nonlinear Euler equations. Long-wave scaling procedure uses small Boussinesq parameter, which characterizes small slope of the density profile in upper layer. Our method combines approaches suggested originally by Ovsyannikov and Miyata for a two-layer fluid with expansion procedure developed by Long (1965) and Benney and Ko (1978) in the case of continuous stratification. Previously, this method was used in theoretical study of table-top solitary waves and internal bores in a weakly stratified fluid without homogeneous layers (Makarenko 1999; Maltseva 2003). Lamb and Wan (1998) investigated numerically flat-crested waves in a continuously stratified fluid, and Grue et al. (2000) observed breaking and broadening of such solitary waves in laboratory experiments.

2 Basic Equations

We consider a 2D motion of inviscid inhomogeneous two-layered fluid, which is weakly stratified under gravity. The Euler equations describing steady flows are

$$\begin{aligned} &\rho(uu_x + vu_y) + p_x = 0,\\ &\rho(uv_x + vv_y) + p_y = -\rho g,\\ &u_x + v_y = 0, \quad u\rho_x + v\rho_y = 0, \end{aligned} \tag{1}$$

where ρ is the fluid density, u and v are the velocity components, p is the pressure, and g is the gravity acceleration. The flow is confined between the flat bottom $y = -h_1$ and the rigid lid $y = h_2$ (Fig. 1), and the interface $y = \eta(x)$ separates the layers (the value $\eta = 0$ gives equilibrium level of this interface).

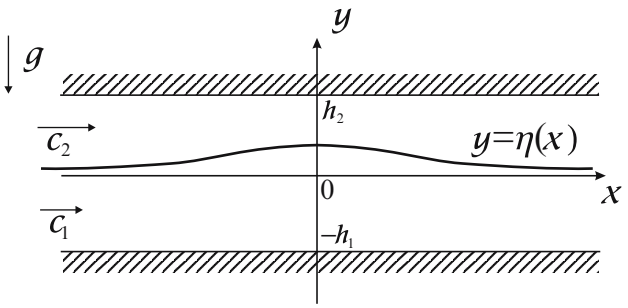

Fig. 1 Scheme of motion

We introduce the stream function ψ as usually by $u = \psi_y$, $v = -\psi_x$, so the mass conservation implies the dependence $\rho = \rho(\psi)$, and the pressure p can be found from the Bernoulli equation

$$\frac{1}{2}|\nabla\psi|^2 + \frac{1}{\rho(\psi)}p + gy = b(\psi).$$

It is supposed that the fluid velocity (u,v) tends to the upstream velocity $(c_j,0)$ as $x \to -\infty$ where c_j is the wave speed with respect to j-th layer ($j = 1,2$). In this case, boundary conditions at the bottom, at the interface, and at the lid take the forms, respectively

$$\psi = -c_1 h_1 \ \ (y = -h_1), \qquad \psi = 0 \ \ (y = \eta), \qquad \psi = c_2 h_2 \ \ (y = h_2). \tag{2}$$

It is well known (Yih, 1980) that the system (1) can be reduced to the Dubreil-Jacotin – Long (DJL) equation for a stream function

$$\rho(\psi)\Delta\psi + \rho'(\psi)\left(gy + \frac{|\nabla\psi|^2}{2}\right) = H'(\psi).$$

Here the function $H(\psi) = \rho(\psi)b(\psi)$ involves the Bernoulli function $b(\psi)$ and the density $\rho(\psi)$, which are specified by the condition $\rho(\psi) = \rho_\infty(\psi/c_j)$ in j-th layer. In this chapter, we consider the upstream density profile

$$\rho_\infty(y) = \begin{cases} \rho_1 & (-h_1 < y < 0), \\ \rho_2 \exp(-N^2 y/g) & (0 < y < h_2), \end{cases} \tag{3}$$

where $N = \text{const}$ is the Brunt – Väisälä frequency, and the constants ρ_1 and ρ_2 are such that $\rho_2 < \rho_1$. The special case $N = 0$ gives a familiar two-fluid system with a piece-wise constant fluid density ρ and the Bernoulli function b. In general case $N \neq 0$, the function $b(\psi)$ is constant in lower layer $-h_1 < y < \eta(x)$ only, $b(\psi) = c_1^2/2$. At the same time, we have in upper layer $\eta(x) < y < h_2$

$$b(\psi) = \frac{1}{2}c_2^2 + \frac{g\psi}{c_2} + \frac{g^2}{N^2}\left(1 - e^{\frac{N^2\psi}{gc_2}}\right).$$

As a consequence, we obtain the Laplace equation for a stream function in the homogeneous layer

$$\psi_{xx} + \psi_{yy} = 0, \tag{4}$$

and ψ should satisfy the nonlinear equation

$$\psi_{xx} + \psi_{yy} = \frac{N^2}{gc_2}\left\{g\left(y - \frac{\psi}{c_2}\right) + \frac{1}{2}\left(\psi_x^2 + \psi_y^2 - c_2^2\right)\right\} \tag{5}$$

in the exponentially stratified layer. Note that Voronovich (2003) used the linear Helmholtz equation

$$\psi_{xx} + \psi_{yy} + \frac{N^2}{c^2}(\psi - cy) = 0 \qquad (c = c_1 = c_2), \tag{6}$$

which is a simplified version of (5). By this approach, the nonlinearity appears due to interfacial boundary condition

$$[\rho(\psi)(|\nabla\psi|^2 + 2gy - 2b(\psi)] = 0, \qquad y = \eta(x), \tag{7}$$

where the square brackets mean the discontinuity jump. The condition (7) provides continuity of the pressure p everywhere in the flow domain. As Long (1965) noted, nonlinear inertial terms of (5) are significant in the case when perturbation method uses several parameters in addition to small quantity $\Delta\rho/\rho$. Therefore, we take into account all the nonlinearities appearing from exact Euler equations. In addition, we reformulate the condition (7) by taking into account conservation of total momentum due to the flow force integral

$$\int_{-h_1}^{h_2} (p + \rho\,\psi_y^2)\,\mathrm{d}y = \text{const}.$$

Excluding the pressure p by the Bernoulli equation, we obtain the relation

$$\rho_1 \int_{-h_1}^{\eta(x)} \left(c_1^2 + \psi_{1y}^2 - \psi_{1x}^2 - 2gy\right)\mathrm{d}y + \rho_2 \int_{\eta(x)}^{h_2} e^{-\frac{N^2\psi_2}{gc_2}} \times \left\{ c_2^2 + \psi_{2y}^2 - \psi_{2x}^2 - \frac{2g^2}{N^2}\left(e^{\frac{N^2\psi_2}{gc_2}} - 1\right) + 2g\left(\frac{\psi_2}{c_2} - y\right)\right\}\mathrm{d}y = C, \tag{8}$$

where the constant C depends on parameters of upstream flow as follows:

$$C = \rho_1 g h_1^2 + 2\rho_1 c_1^2 h_1 + 2\rho_2 c_2^2 h_2 + 2\rho_2 g\left(\frac{c_2^2}{N^2} + \frac{g^2}{N^4}\right)\left(1 - \frac{N^2 h_2}{g} - e^{-\frac{N^2 h_2}{g}}\right).$$

It is easy to check by direct calculation that the integral relation (8) is equivalent to the boundary condition (7), which is rather simple. However, (8) provides more effectively the derivation of model describing solitary waves of finite amplitude.

3 The Model Equation

To formulate approximate model in a dimensionless form, we introduce now some certain scales and parameters. The density profile (3) is clarified by the Boussinesq parameters σ and μ defined by the formulae

$$\sigma = \frac{N^2 h_2}{g}, \qquad \mu = \frac{\rho_1 - \rho_2}{\rho_2}. \tag{9}$$

Here the constant σ characterizes the slope of density profile in a continuously stratified layer, and μ is the dimensionless density jump at interface. As usual, both these parameters are small in the case of slight stratification. However, we expect that the interfacial mode dominates modes of internal waves in stratified layer, when $\mu \gg \sigma$. Therefore, we fix the constant μ and use the parameter σ as the perturbation parameter.

Further, we define the densimetric Froude number F_j as the scaled phase speed c_j in j-th layer,

$$F_j^2 = \frac{\rho_j c_j^2}{g(\rho_1 - \rho_2)h_j} \quad (j = 1,2). \tag{10}$$

The pair $F = (F_1, F_2)$ is a distinctive mark for a two-fluid system in the presence of a velocity jump at a sharp interface. We demand the difference between c_1 and c_2 to be moderate in order to avoid the Kelvin – Helmholtz instability, at least in accordance with long-wave limit criteria (Ovsyannikov et al. 1985):

$$|c_1 - c_2| < \sqrt{\frac{g(\rho_1 - \rho_2)(\rho_1 h_2 + \rho_2 h_1)}{\rho_1 \rho_2}}.$$

In addition to the Froude numbers F_j, we use also the parameter λ given by the formula

$$\lambda^2 = \left(\frac{Nh_2}{c_2}\right)^2 = \frac{\sigma g h_2}{c_2^2} = \frac{\sigma}{\mu F_2^2}.$$

The constant λ characterizes the inverse densimetric Froude number defined for a continuously stratified fluid in upper layer. Finally, the parameter $r = h_1/h_2$ is the layer thickness ratio for the fluid at rest.

The derivation procedure involves the slow independent variable $\xi = \sqrt{\sigma}x/h_2$, the dimensionless variables $(\bar{y}, \bar{\eta}) = (y, \eta)/h_2$ and the stream function $\psi = c_j h_j \bar{\psi}$ $(j = 1,2)$, scaled separately in j-th layer. We are seeking for the function $\bar{\psi}$ expanded in powers on σ as

$$\bar{\psi} = \psi^{(0)} + \sigma\,\psi^{(1)} + O(\sigma^2),$$

where the coefficients $\psi^{(k)}$ are determined by the equations (4) and (5) under boundary conditions (2) transformed to appropriate dimensionless form. Thus, in lower layer $-r < y < \eta$ we obtain the coefficients

$$\psi^{(0)} = \frac{y - \eta}{r + \eta}, \qquad \psi^{(1)} = -\frac{1}{6}\left(\frac{1}{r+\eta}\right)_{\xi\xi}\left\{(y+r)^3 - (r+\eta)^2(y+r)\right\}$$

(bar is omitted in notations of dimensionless variables here and later). Respectively, in upper layer $\eta < y < 1$ the coefficients of perturbation series are

$$\psi^{(0)} = y - \eta\,\frac{\sin\lambda(1-y)}{\sin\lambda(1-\eta)},$$

$$\psi^{(1)} = \frac{\sin\lambda(1-y)}{2\lambda}\left(\frac{\eta}{\sin\lambda(1-\eta)}\right)_{\xi\xi}\left\{(1-\eta)\cot\lambda(1-\eta)-(1-y)\cot\lambda(1-y)\right\}$$
$$+\frac{1}{6}\eta^2\left\{\frac{\sin\lambda(\eta-y)+\sin\lambda(1-\eta)-\sin\lambda(1-y)}{\sin^3\lambda(1-\eta)}\right.$$
$$\left.+\frac{\sin^2\lambda(1-y)}{\sin^2\lambda(1-\eta)}-\frac{\sin\lambda(1-y)}{\sin\lambda(1-\eta)}\right\}$$
$$+\frac{\eta(\eta-y)}{2}\frac{\sin\lambda(1-y)}{\sin\lambda(1-\eta)}.$$

Finally, we use the dimensionless version of integral relation (8) in the form

$$\mu r^3F_1^2\int_{-r}^{\eta}\left(\psi_y^2-\sigma\psi_\xi^2\right)\mathrm{d}y+\int_{\eta}^{1}e^{-\sigma\psi}\left\{\mu F_2^2(1+\psi_y^2-\sigma\psi_\xi^2)-2\sigma^{-1}\left(e^{\sigma\psi}-1\right)\right.$$
$$\left.+2\left(\psi-y\right)\right\}\mathrm{d}y$$
$$=(1+\mu)\eta^2-\mu rF_1^2(\eta-r)+2\mu F_2^2+2\left(\lambda^{-2}+\sigma^{-2}\right)\left(1-\sigma-e^{-\sigma}\right).$$

Substituting the power expansion for ψ and truncating the terms $O(\sigma^2)$, we obtain the nonlinear ordinary differential equation for the wave shape $\eta(x)$, which depends on dimensionless variables x with scale unit h_2:

$$\left(\frac{\mathrm{d}\eta}{\mathrm{d}x}\right)^2=\frac{\eta^2\left(A_0+A_1\eta+A_2\eta^2+A_3\eta^3\right)}{B_0+B_1\eta+B_2\eta^2+B_3\eta^3+B_4\eta^4}. \tag{11}$$

Here the coefficients A_j and B_j are trigonometric polynomials depending on $s_n=\sin n\lambda(1-\eta)$ and $c_n=\cos n\lambda(1-\eta)$ with integer or half-integer n,

$$A_0=18r\lambda\,s_1^2\left\{\left[2(F_1^2-1)-\sigma F_2^2\right]s_1^2+\lambda F_2^2s_2\right\},$$
$$A_1=2\lambda\,F_2^2\left\{s_1^2\left[\lambda(9-2\sigma r)s_2-s_1^2(6r\lambda^2+9\sigma)\right]\right.$$
$$\left.-2s_{1/2}^2\left[r\sigma\lambda s_1+3r\sigma\lambda^2(1+2c_1)\right]\right\}-36\lambda\,s_1^4,$$
$$A_2=4\lambda^2F_2^2s_{1/2}^2\left\{3\sigma\lambda(r-1)(1+2c_1)-4\left(3\lambda s_1^2+\sigma s_2\right)c_{1/2}^2-\sigma s_1\right\},$$
$$A_3=12\lambda^3\sigma F_2^2s_{1/2}^2(1+2c_1),$$
$$B_0=12\lambda r^3F_1^2s_1^4+9rF_2^2(2\lambda-s_2)s_1^2,$$
$$B_1=9F_2^2\left\{r\lambda(2\lambda-s_2)s_2-\left[2(r-1)\lambda+s_2\right]s_1^2\right\},$$
$$B_2=9\lambda F_2^2\left\{\lambda\left[r(s_1^2-3)+2\right]s_2+4s_1^4+2r\lambda^2-2(r\lambda^2+3)s_1^2\right\},$$

$$B_3 = -9\lambda^2 F_2^2 \left\{ (c_1^2+2)s_2 + 2\lambda(r-1)c_1^2 \right\},$$

$$B_4 = -18\lambda^3 F_2^2 c_1^2.$$

Note that λ in above formulas is $\lambda = O(\sqrt{\sigma})$ for a fixed $F_2 \neq 0$. This is the case when continuous stratification disappears in upper layer as $\sigma \to 0$. In such a way, the (11) reduces to the equation

$$\left(\frac{\mathrm{d}\eta}{\mathrm{d}x}\right)^2 = \frac{3\eta^2\left[\eta^2 + \left(F_2^2 - rF_1^2 - 1 + r\right)\eta + r\left(F_1^2 + F_2^2 - 1\right)\right]}{r^3F_1^2(1-\eta) + F_2^2(r+\eta)}. \qquad (12)$$

as $\lambda \to 0$. This simplified version of model equation was earlier obtained by Ovsyannikov et al. (1985) and, in the case $c_1 = c_2$, by Miyata (1985) (Choi and Camassa, 1999) for a two-fluid system with constant density in the both layers. Recently, this model was thoroughly compared and validated with experimental observations and numerical calculations of solitary waves in the framework of fully nonlinear Euler equations (Camassa et al. 2006).

For a fixed $\lambda \neq 0$ and small $\sigma > 0$, the Froude number F_2 has the order $F_2 = O(\sqrt{\sigma})$, and the (11) takes the limiting form

$$r^3F_1^2\,\eta_x^2 = 3\eta^2\left(r(F_1^2-1) - \eta\right) \qquad (13)$$

as $\sigma \to 0$. This is the Boussinesq – Rayleigh equation known as the model of surface solitary waves in homogeneous fluid layer with dimensionless depth r. In the case under consideration, the Froude number $F_1 = c_1/\sqrt{g_1 h_1}$ is defined by the reduced gravity acceleration $g_1 = (\rho_1 - \rho_2)g/\rho_1$. This curious analogy also agrees with the (12), which results to (13) as $F_2 \to 0$.

4 Solitary Waves

Parametric range of solitary waves is obtained as the domain in (F_1, F_2)-plane being supercritical with respect to the spectrum of small amplitude sinusoidal waves determined by linearized (2), (4), (5), and (7). The dispersion relation of linear waves is

$$\Delta(k;F) = 0,$$

where k is a dimensionless wave-number and the function Δ is defined by the formula

$$\Delta = F_1^2 rk\sqrt{\sigma}\coth rk\sqrt{\sigma} + F_2^2\left(\sqrt{\lambda^2 - \frac{\sigma^2}{4} - k^2\sigma}\cot\sqrt{\lambda^2 - \frac{\sigma^2}{4} - k^2\sigma} - \frac{\sigma}{2}\right) - 1.$$

This dispersion relation determines real wave-numbers k if and only if the Froude point $F = (F_1, F_2)$ belongs to the shaded area on the Fig. 2.

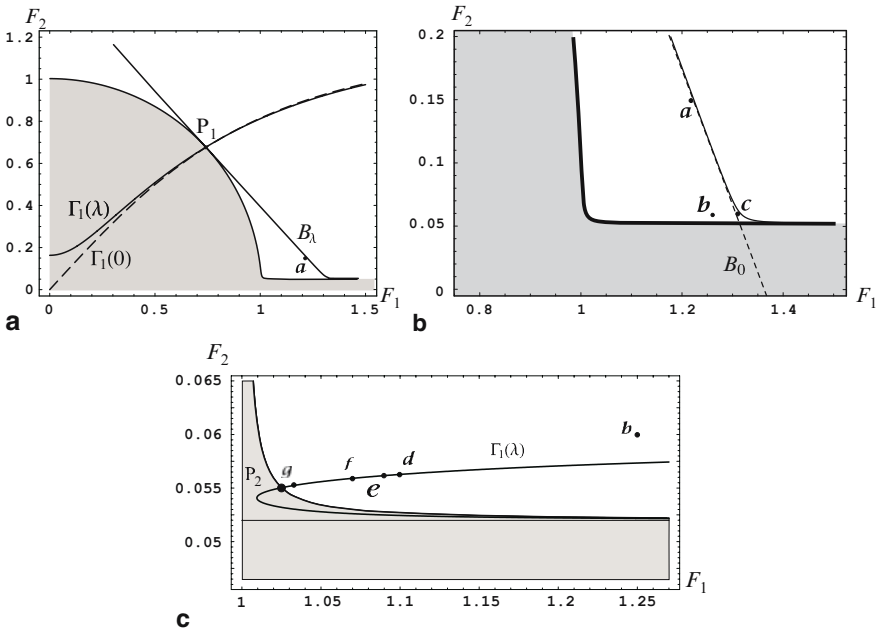

Fig. 2 The spectrum and supercritical domain: $\sigma = 0.00008$, $\mu = 0.003$, $r = 1.2$

The boundary of this spectral domain is determined by the equation

$$F_1^2 + F_2^2 \left(\sqrt{\frac{\sigma}{\mu F_2^2} - \frac{\sigma^2}{4}} \cot \sqrt{\frac{\sigma}{\mu F_2^2} - \frac{\sigma^2}{4}} - \frac{\sigma}{2} \right) = 1. \tag{14}$$

Note that a perfect two-fluid system with constant densities ρ_1 and ρ_2 in the layers has one-modal spectrum bounded by the unit circle $F_1^2 + F_2^2 = 1$. The curve (14) transforms to this circle in a weak-stratification limit $\sigma \to 0$ by fixing μ. However, it is clear that this transformation from a nonbounded spectral domain to compact spectrum is not uniform in F_1 as $\sigma \to 0$.

Equation (11) has solitary-wave solutions when the point (F_1, F_2) is located between the spectrum and the curve B_λ, which gives the broadening limit of internal waves. The line $\sqrt{r}F_1 + F_2 = \sqrt{1+r}$ (the dashed line on Fig. 2b) is the bore diagram for (12), and it gives a limit form of the curve B_λ as $\lambda \to 0$. Small amplitude solitary waves bifurcate from upstream flow at the spectrum boundary (14), these waves are described by weakly nonlinear version of the (11)

$$\eta_x^2 = \eta^2 \left[\gamma_0 + \gamma_1 \eta + O(\eta^2) \right]. \tag{15}$$

Here the lowest-order coefficient γ_0 is positive in supercritical domain $\Delta(0;F) > 0$ since

$$\gamma_0 = \frac{3\Delta(0;F)}{r^2 F_1^2 + F_2^2} + O(\sigma^2),$$

and the coefficient $\gamma_1(F, \lambda)$ depends on parameters F_j and λ in a complicated way.

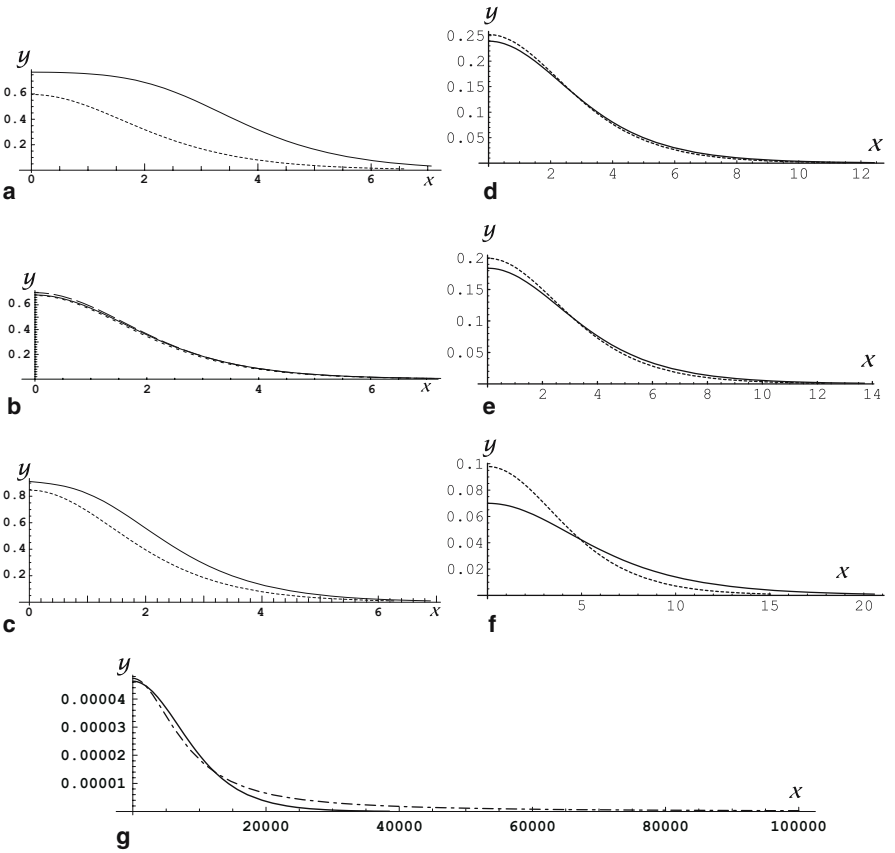

Fig. 3 Profiles of solitary waves

The Fig. 2b presents an enlarged fragment of Fig. 2a near the positive semiaxis OF_1. This is a thin spectral layer for the perturbed problem, and it has the thickness $O(\sqrt{\sigma})$ and therefore disappears as $F_1 > 1$ and $\sigma \to 0$. Similarly, Fig. 2c illustrates scaled fragment of Fig. 3b, which is located close to the Froude point $F = (1,0)$. Branches of the curve $\Gamma_1(\lambda):\ \gamma_1(F,\lambda) = 0$ shown on Fig. 2a and c indicate where the balance of nonlinearities η^3 and η^4 is possible in the (15). It is really true in the vicinity of the point P_1 with the coordinates $F_1 = r/\sqrt{(1+r)r} + O(\lambda)$ and $F_2 = 1/\sqrt{1+r} + O(\lambda)$. This is the same effect as the balance of quadratic and cubic nonlinearities in the KdV–mKdV model (Kakutani and Yamasaki 1978).

In contrast, the neighborhood of the point P_2 with coordinates

$$F_1 = 1 + \frac{1}{2\pi}\sqrt{\frac{\sigma}{r\mu}} + O(\sigma), \qquad F_2 = \frac{1}{\pi}\sqrt{\frac{\sigma}{\mu}} + \frac{\sqrt{r}\sigma}{\pi^2\mu} + O(\sigma^{3/2})$$

demonstrates one more case of exotic behavior of solitary waves. For example, when the point F belongs to the curve $\Gamma_1(\lambda)$ then the fractional scaling of variables $x = \sigma^{1/4} x_0$, $\eta = \sigma^{1/2}\eta_0$ leads from (11) to model equation

$$\left(\frac{\mathrm{d}\eta_0}{\mathrm{d}x_0}\right)^2 = \eta_0^3 \frac{R^2 + 3R(\pi\eta_0 + R)^3 - 3(\pi\eta_0 + R)^4}{r^3(\pi\eta_0 + R)^4 + 3r^2/(2\pi^2\mu^2)} \qquad (R = \sqrt{r/\mu}). \tag{16}$$

This equation describes solitary waves with power decay as $|x_0| \to \infty$ (not exponential decay because of multiplier η_0^3 at right-hand side).

The Fig. 3a–f presents the profiles of solitary waves calculated for (11)–(13). Here the solid line corresponds to the (11), the dashed line corresponds to the (12), and the dotted line corresponds to the (13). The point (a) gives the broad plateau-shape solitary wave, which is precisely described by (11) and (12). The point (b) demonstrates the location of Froude point (F_1, F_2) where all the equations (11)–(13) are in good agreement. The point (c) is out of validity range of (12) but the solitary wave solution for the equation (11) still exists here. The points (d)–(f) demonstrate how the (13) loses its accuracy by moving along the curve $\Gamma_1(\lambda)$. Solitary wave for (11) seems to be broadening on the Fig. 3d–f. Indeed, it is the lost of exponential decay near the point P_2. The Fig. 3g illustrates good agreement of (11) (solid line) and (16) (dashed line) for the point (g); here (13) fails to approximate at all.

Conclusion

In this chapter, we have considered the problem on permanent internal waves at the interface between a homogeneous layer and exponentially stratified layer in a two-fluid system. An ordinary differential equation describing large amplitude solitary waves has been obtained using the long-wave scaling procedure. This equation extends the model suggested by Ovsyannikov et al. (1985) and Miyata (1985) for a two-layer fluid with two homogeneous layers. Parametric range of solitary waves is characterized, including extreme regimes such as broad plateau-shape solitary waves.

Acknowledgements This work was supported by RFBR (grant No 07-01-00309), INTAS–SB RAS (grant No 06-1000013-9236), and Interdisciplinary Program of SB RAS (Project No 113). N.I.M. acknowledges also the support by RFBR–CNRS (grant No 07-01-92212).

References

Benney DJ, Ko DRS (1978) The propagation of long large amplitude internal waves. Stud Appl Math 59:187–199

Camassa R, Choi W, Michallet H, Rusås PO, Sveen JK (2006) On the realm of validity of strongly nonlinear asymptotic approximations for internal waves. J Fluid Mech 549:1–23

Choi W, Camassa R (1999) Fully nonlinear internal waves in a two-fluid system. J Fluid Mech 396:1–36

Grue J, Jensen A, Rusås PO, Sveen JK (2000) Breaking and broadening of internal solitary waves. J Fluid Mech 413:181–217

Helfrich KR, Melville WK (2006) Long nonlinear internal waves. Annu Rev Fluid Mech 38:395–425

Kakutani T, Yamasaki N (1978) Solitary waves on a two-layer fluid. J Phys Soc Jpn 45:674–679

Lamb K, Wan B (1998) Conjugate flows and flat solitary waves for a continuously stratified fluid. Phys Fluid 10:2061–2079

Long RR (1965) On the Boussinesq approximation and its role in the theory of internal waves. Tellus 17(1):46–52

Makarenko NI (1999) Conjugate flows and smooth bores in a weakly stratified fluid. J Appl Mech Tech Phys 40(2):249–257

Maltseva JL (2003) Limiting forms of internal solitary waves. JOMAE Trans ASME 125(1):76–79

Miyata M (1985) An internal solitary wave of large amplitude. La Mer 23(2):43–48

Ovsyannikov LV, Makarenko NI, Nalimov VI, et al. (1985) Nonlinear problems of the theory of surface and internal waves. Nauka, Novosibirsk [in Russian]

Pelinovsky EN, Polukhinan O, Slyunaev A, Talipova T (2007) Internal solitary waves. In: Grimshaw R (ed) Solitary waves in fluids, WIT Press, Southhampton, pp 85–110

Turner REL, VandenBroeck J-M (1988) Broadening of interfacial solitary waves. Phys Fluid 31: 2486–2490

Voronovich AG (2003) Strong solitary internal waves in a 2.5- layer model. J Fluid Mech 474:85–94

Yih CS (1980) Stratified flows. Academic Press, NY

Index

Z